ISSN 0236-2945

LIGHT & ENGINEERING

Volume 25, Number 4, 2017

Editorial of Journal
"Light & Engineering" (Svetotekhnika), Moscow

Dear Colleagues,
Authors and Co-authors!
Dear Friends!

We wish you a Year
that is filled with all the
Fragrance of Roses,
Illuminated with all the LIGHTS
of the world and be blessed with
all the Smiles on the Planet.

We wish you all the best,
great work to reach your fondest goals,
and when you're done, sweet rest.
We hope this year will be the year
when all your dreams come true!

Warmest wishes for a
Happy holiday season
and a wonderful New Year!
Happy New Year 2018!

LIGHT & ENGINEERING

СВЕТО ТЕХНИКА

Moscow, 2017

Editorial Office:

VNISI, Rooms 327 and 334
106 Prospekt Mira, Moscow 129626, Russia
Tel: +7.495.682.26.54
Tel./Fax: +7.495.682.58.46
E-mail: lights-nr@inbox.ru
http://www.sveto-tekhnika.ru

Light & Engineering" is an international scientific Journal subscribed to by readers in many different countries. It is the English edition of the journal "Svetotekhnika" the oldest scientific publication in Russia, established in 1932.

Establishing the English edition "Light and Engineering" in 1993 allowed Russian illumination science to be presented the colleagues abroad. It attracted the attention of experts and a new generation of scientists from different countries to Russian domestic achievements in light and engineering science. It also introduced the results of international research and their industrial application on the Russian lighting market.

The scope of our publication is to present the most current results of fundamental research in the field of illumination science. This includes theoretical bases of light source development, physiological optics, lighting technology, photometry, colorimetry, radiometry and metrology, visual perception, health and hazard, energy efficiency, semiconductor sources of light and many others related directions. The journal also aims to cover the application illumination science in technology of light sources, lighting devices, lighting installations, control systems, standards, lighting art and design, and so on.

"Light & Engineering" is well known by its brand and design in the field of light and illumination. Each annual volume has four issues, with about 80–140 pages per issue. Each paper is reviewed by recognized world experts.

To promote the work of the Journal, the editorial staff is in active communication with Thomson Scientific (Citation index) and other international publishing houses and agencies, such as Elsevier and EBSCO Publishing.

CONTENTS

VOLUME 25 **NUMBER 4** **2017**

LIGHT & ENGINEERING

Light & Engineering
Vol. 25, No. 4, pp. 4-17, 2017

Svetotekhnika
No. 2, 2017, pp. 13–22

USE OF LIGHT IN THE EXPLORATION AND RESEARCH OF THE SEAS AND OCEANS

Oleg V. Kopelevich

The Institute of Oceanology of P.P. Shirshov of RAS, Moscow
E-mail: oleg@ocean.ru

ABSTRACT

The article considers the problems and opportunities associated with the use of visible radiation in the study of seas and oceans. Sea water is a light-scattering environment, and in most important cases scattering prevails over absorption. Therefore, for theoretical evaluations of spreading sunlight and radiation of artificial sources in an underwater environment, one should use solutions of integro-differential equation of radiation transfer, which has required the development of various special methods. A measurement of the light field parameters in an underwater environment also presents considerable difficulties caused primarily by weather conditions, which are cloud cover and surface waves. The theory of underwater vision has its own specific characteristics, especially when observation of underwater objects takes place through a turbulent sea surface. An interesting example relating to this problem is given in the review. Another example illustrates modern possibilities of underwater vision at the greatest ocean depths. Light as an instrument to study and monitor the marine environment has important advantages and even distinct preferences in comparison with other methods. One of them is the ability of light to penetrate the sea surface with small losses (unlike microwave radiation and sound), which allows applying remote light probing of the ocean subsurface layer (from boats, aircrafts and satellites). With the appearance of lidar using laser pulses for probing and with the development of satellite observations, remote optical methods are becoming more and more widespread.

Keywords: light, light-scattering environment, radiation transfer theory, photometry, spreading of the solar radiation, underwater visibility, lidars, satellite observations

1. INTRODUCTION

This review is dedicated to use of visible radiation (further – light) when exploring seas and oceans. The author hopes that the problems under consideration will be interesting to the readers of Light & Engineering Journal, and primarily to those interested not only in design and technological development of lighting installations, their introduction and operation, but also in the study of light distribution in various environments, in measurement of light characteristics, its energy transformation into other energy types, as well as in light use for other purposes besides illumination [1]. It is pertinent to note here that both, the founder of photometry Frenchman Pierre Booger and the creator of the modern photometry Soviet scientist A.A. Gershun, considered the "sea" subject in their work. Booger measured transparency of sea water under laboratory conditions, proposed empirical formulae of the dependence of the reflectance factor on the incidence angle when light reflects from the water's surface, concluded an exponential law of light weakening when it passes through an absorbing environment, developed the theory of object visibility in a turbid medium and applied it to calculate a limit depth of visibility for drowned objects [2]. A.A. Gershun was an author of the first-ever monograph on sea optics "Transparency and Colour

of the Sea"[3]. He was engaged in underwater illumination and in more common theoretical and experimental problems of photometry of turbid media [4, p. 85–103; 397–400; 430–438].

As an environment for light distribution, sea water has an important feature which determines the science of ocean optics. This is a light-scattering environment, and in most important cases the scattering prevails in comparison with absorption. Photons in the water, on average, undergo a greater number of scattering events than of absorption. Therefore, to describe light interactions with the marine environment, the multiple scattering theory or the radiation transfer theory should be used. This theory has rather universal character and, in general, it is applicable to atmospheric optics and in astrophysics, as well as in neutron transport theory. However, a specific characteristic of sea water's optical properties causes certain limitations to the transport theory results obtained in other fields using hydro-optics. Optical characteristics of sea water are the main factor determining light distribution in water from both of natural and of artificial sources.

Optical phenomena in the seas and oceans were of interest to sailors in ancient times. The approach of making optical measurements directly in the sea was first implemented by a Russian fleet captain O.E. Kotzebue. He was the one to begin to estimate the transparency of ocean water, measuring the depth at which sinking objects disappear from view. The interest in sea optics grew with developments in underwater exploration and the submarine fleet. The main issues which were pursued were detection and masking of underwater objects, visibility under water and use of underwater photo equipment. Light modes at various depths are of interest to marine biologists as well, because light modes influence the process of photosynthesis and the production of primary biota in seas and oceans.

The possibilities of an instrumental studies of light distribution principles in water environments rapidly expanded in the 1920s after photographic plates were replaced with photocells. Along with photometers to measure underwater illuminance, immersed transparency metres and scattering metres came to be used. Natural hydro optical studies became comprehensive: in sea expeditions, both photometric values (surface and underwater illuminance, as well as luminance), and the optical characteristics of water were simultaneously measured.

An important milestone in this field in the 1920s was an explanation of sea colour; in 1922, independently from each other and almost at the same time, Indian physicist Ch. Raman [5] and Soviet scientist V.V. Shuleikin [6] showed that water colour can be explained by a cumulative action of selective absorption and scattering. The importance of this discovery is confirmed now by the wide use of satellite colour scanners, which are amongst the most popular satellite measuring instruments due to their economic efficiency and to a wide range of information that can be obtained. The era of satellite colour scanners began in 1978, when the Coastal Zone Colour Scanner (CZCS) was enabled on the American NIMBUS-7 satellite. And at present, satellite observations are the main instruments used to study and monitor seas and oceans.

Another scientific and technological achievement determining a new stage in the development of the ocean optics was the creation of pulse lasers in the 1960s, radiating short powerful light pulses, which led to the emergence an entire area of study in hydro-optics: the learning principles of forming a non-stationary underwater light fields and the development of laser probing methods of the water medium.

In this review we are limited to a short summary of the three main aspects of the use of light in seas and ocean exploration: (1) light mode in water density created by solar radiation; (2) underwater visibility with natural and artificial illumination, including through a turbulent sea surface; (3) use of light to study and monitor the marine environment.

2. MARINE ENVIRONMENT LIGHT MODE CREATED BY SUNLIGHT

In the early stages of exploring the seas and oceans, only the water's surface layer illuminated by sunlight only was accessible to mankind. And today, when divers penetrate into the deepest ocean, this layer is still important. Shallow waters and coastal areas are still the most accessible to people. The surface layer is also important due to the fact that primary products develop within it: this is the photosynthesis layer. Biologists call it the photo layer (the illuminated layer), and the depth accepted to be its lower boundary is where photosynthetic active radiation (PAR – spectral interval 400–700 nm) is 1 % of the surface radiation. In most clear ocean

waters the depth of the photo layer can exceed 100 m.

2.1. Theoretical evaluations of solar radiation expansion in a water environment

Radiometric values expressed in energy units will be referred to as [7]: F is radiation flux, $\underline{E}$ is irradiance and L is radiance.

Because of multiple scattering, the entire photo layer is saturated with sunlight, which sines on a selected point of observation from all directions. The surface for analysis can be real (sea surface or sea floor), or arbitrary; irradiance or luminance can be calculated for a randomly focused surface in any selected point of a marine environment.

Optical properties of sea water are described by a set of optical characteristics, which includes parameters of absorption $a(\lambda)$, scattering $b(\lambda)$, weakening $c(\lambda)$ (sum of absorption and scattering factors ($c = b+a$)), as well as scattering indicatrix $P(\theta, \lambda)$. The latter characterises an angular distribution of once scattered light.

Derivative values are also used: the probability of photon survival (also known as "single scattering albedo") $w(\lambda)$ equal to the relation of scattering and absorption factors ($w = b/c$); factors of scattering forward b_f (into the front hemisphere: scattering angle θ is from 0 to 90^0) and back b_b (θ is from 90 to 180^0), asymmetry parameter $K = b_f/b_b$.

Scattering factors b, b_f, b_b, absorption a and weakening c have dimension [m^{-1}], scattering indicatrix $P(\theta)$ is measured in $srad^{-1}$, and photon survival probability w is a dimensionless value.

Precise and comprehensive definitions of the listed characteristics can be found in monographs [8–9].

An important feature of the sea water scattering indicatrix is its big elongation in the incident beam direction; the asymmetry coefficient is as a rule greater than 10, and in some regions it is even more than 100. This feature plays an important role in light distribution.

In a homogeneous environment, the weakening of a directed beam of light depending on the distance is described by a simple formula:

$$F(l) = F(0)\cdot\exp(-c\cdot l), \qquad (1)$$

where $F(0)$ is initial value of radiation flux, $F(l)$ is the value of the flux after passing l distance within the environment. The cl value is called optical thicknesst, and $e^{-c} = F(1)/F(0)$ value corresponding to transmission of a directed light beam by a layer of unit thickness is the transparency (usually measured in percent).

Formula (1), which reflects the exponential nature of a directed beam weakening, depending on the distance, represents Booger's law. S.I. Vavilov showed that in an absorbing environment, Booger's law is correct when weakening intensity of incident luminous flux by 10^{19} times. However in a scattering environment, such as sea water and atmosphere, Booger's law has limitations: it is only applicable to narrow-band beams and in the interval, where single scattering prevails ($t = cl \ll 1$). In case the distance from a radiation source increases in a strongly scattering (poorly absorbing) environment, multiple scattering dominates, and, instead of using Booger's law to describe radiation spreading in such environment, one should use the radiation transfer equation [8].

In its simplest configuration, the transfer equation looks like:

$$dL / dl = -cL + \\ + b\int_{4\pi} L(\theta',\varphi')\cdot \hat{P}(\theta,\theta')d\Omega', \qquad (2)$$

where dL/dl in the left part of the equation is change of luminance dL in the direction under consideration along an infinitesimal way section dl; the first term of the right part shows luminance reduction at a single interaction with the environment (formula (2) without the second term is Booger's law in differential form).

The second term takes into consideration a luminance increase in the given direction due to the scattering of radiation coming from other directions corresponding to zenith and azimuth angles q', $'j$.

Equation (2) is an integral differential equation which is complex to solve, however there are effective numerical methods developed.

Description of strict and various approximate methods of the transfer equation solution can be found in [8].

Among most applicable numerical methods are the Monte-Carlo method, *DISORT* and *Hydrolight*.

An advantage of the Monte-Carlo method is that it is applicable for any geometry, illumination conditions, spatial distribution of optical characteristics, etc. A disadvantage is its significant computing time.

An advanced method of discrete ordinates *DISORT* (Discrete Ordinates Radiative Transfer) is implemented as a computer program to solve the radiation transfer equation in a plane-parallel environment applicable both for visible, ultra-violet, infrared and microwave radiation. This method is widely used in programs which calculate radiation transfer in the atmosphere. Generalisation of the *DISORT* for the ocean-atmosphere system with a smooth interface is described in [10]. And the used approach is generalised for a wavy sea surface case in [11].

Hydrolight is a commercial program for numerical solution of the radiation transfer equation in a plane-parallel environment [12]. It allows computing spectral luminance distributions at a given depth in water thickness both for descending, and for ascending radiation fluxes, taking into account reflection from the sea floor, as well as under and over the sea surface. In the last case, for a pre-set luminance distribution of direct and diffuse radiation incident on the surface, radiation luminance distribution reflected from a wavy sea surface is also calculated. Other input parameters for the calculation are spectral absorbing and scattering properties of sea water with an arbitrary distribution by depth, characteristics of the sea floor and wavy sea surface. Details of the used method for solving the transfer equation can be found in book [13].

An advantage of the *Hydrolight* program over the Monte-Carlo method is that it calculates the listed characteristics much quicker with the same accuracy. The difference is especially noticeable for ascending radiation luminance, where for sea water within the Monte-Carlo method, we need to start form a very large number of photons (10^7 and more) to provide the required degree of accuracy of the results because of a strong elongation of the scattering indicatrix. A simplified version of the *Hydrolight* program named *EcoLight* only computes irradiances and does it 30–100 times quicker than *Hydrolight*.

The weakening of the solar radiation flux with increasing depth is also approximately described by exponential law:

$$E_d(z) = E_d\left(0^-\right) \times \exp\left(-K_d z\right), \tag{3}$$

where $E_d(z)$ is irradiance created by descending solar radiation flux at z depth; $E_d(0^-)$ is irradiance directly under the surface; K_d is diffuse weakening factor of descending solar radiation (in the Russian body of literature, it is often called vertical weakening factor of underwater irradiance from the top).

If K_d changes with depth, then the exponential curve index, the following integral should be written in (3):

$$E_d(z) = E_d\left(0^-\right) \times \exp\left(-\int_0^z K(z)dz\right). \tag{3a}$$

Formulas (3) and (3a) are also applicable for irradiance $E_u(z)$ created at z depth by ascending solar radiation flux but instead of the K_d factor, one should use K_u factor for ascending solar radiation; $K_u \neq K_d$.

Both factors depend on the optical properties of sea water (primarily, on absorption and on scattering back factors), as well as on an angular structure of descending and/or ascending luminous fluxes.

For K_d factor, one can use an approximate formula [14]:

$$K_d = 1.04 D_0 \left(a + b_b\right), \tag{4}$$

where $D_0 = \left(1-g\right)/\cos\theta_{0w} + 1{,}197g$, a and b_b are absorption and scattering back factors; θ_{0w} is the refraction angle of direct solar rays, g is a portion of diffuse radiation of the whole radiation flux incident on the surface. All values hereafter are functions of the radiation wavelength λ.

g value is close to 0 for clear atmosphere and for when the sun is high (in zenith) and is equal to 1 without direct solar rays in the event of a clouded sky, or of a dust storm. In the first case D_0 =1, in the second it is equal to 1.197. The biggest value of D_0 corresponds to a clear atmosphere case at a maximum possible refraction angle of direct solar rays q_{0w} = 48.3°. D_0 value in this case is close to 1.5.

It can be seen that in general, the K_d value significantly depends on the sun's altitude and on the state of the atmosphere. Nevertheless, given that D_0=*1.2* and if we neglect b_b value in (4) in comparison with

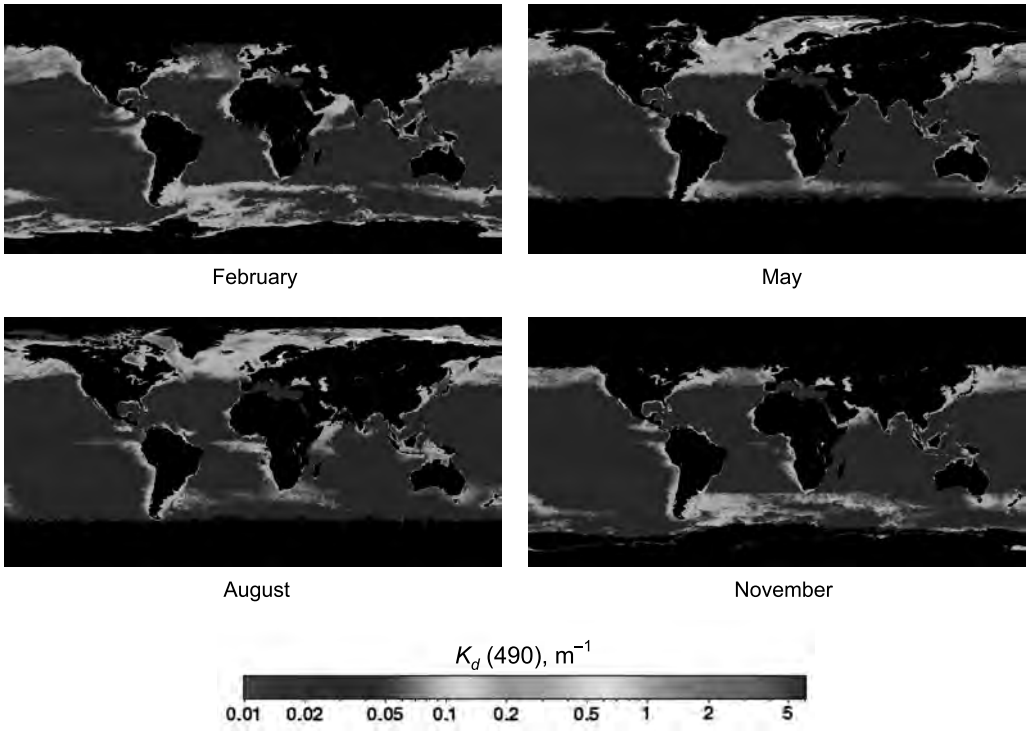

Fig. 1. Average monthly spatial distributions of diffuse weakening factor of underwater irradiance K_d *(490)* according to the *VIIRS* satellite colour scanner data averaged during the 2012–2016 period

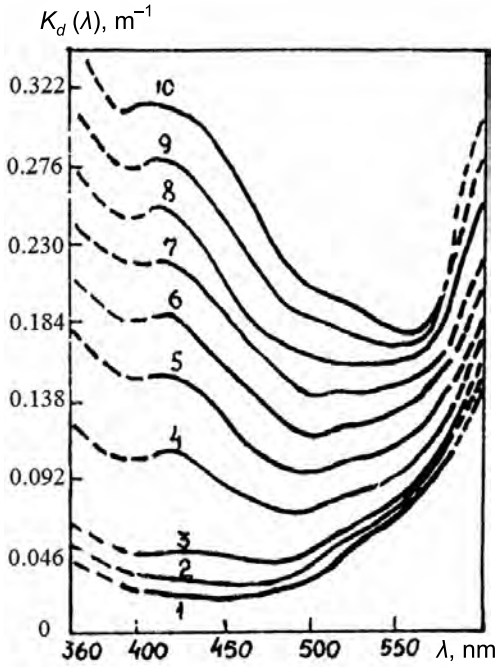

Fig. 2. Spectral dependences of the diffuse weakening factor of underwater irradiance $K_d(\lambda)$ depending on K_d *(500)* value. Figures at the curves correspond to the following K_d *(500)* values: 1–0.028; 2–0.034; 3–0.046; 4–0.069; 5–0.092; 6–0.115; 7–0.138; 8–0.161; 9–0.184; 10–0.207 m^{-1} (the values are derived from data [8, p. 276])

a (which is quite acceptable for most of sea and ocean water), then the obtained approximate formula for the K_d calculation is suitable for most cases: $K_d \cong 1{,}25 \cdot a$.

Fig. 1 shows average monthly spatial distributions of underwater irradiance diffuse weakening factor K_d *(490)* for wavelength of 490 nm for February, May, August and November according to the VIIRS satellite colour scanner averaged for the 2012–2016 period [15]. It can be seen that this value changes drastically depending on the region: from ~0.01 m^{-1} to several units. In addition, this value is subject to noticeable seasonal variations.

2.2. Spectral distributions of underwater irradiance and solar radiation penetration depths limits

The diffuse weakening factor K_d depends on λ – radiation wavelength, and this dependence is pronounced in the spectrum visible interval, Fig. 2, [8, p.276]. K_d*(500)* depends on the absorption factor absolute value, and as it can be seen from Fig. 2, K_d (λ) dependences corresponding to different values of the absorption factor, differ from each other in the short-wave spectrum part most obviously. These changes are primarily connected with the

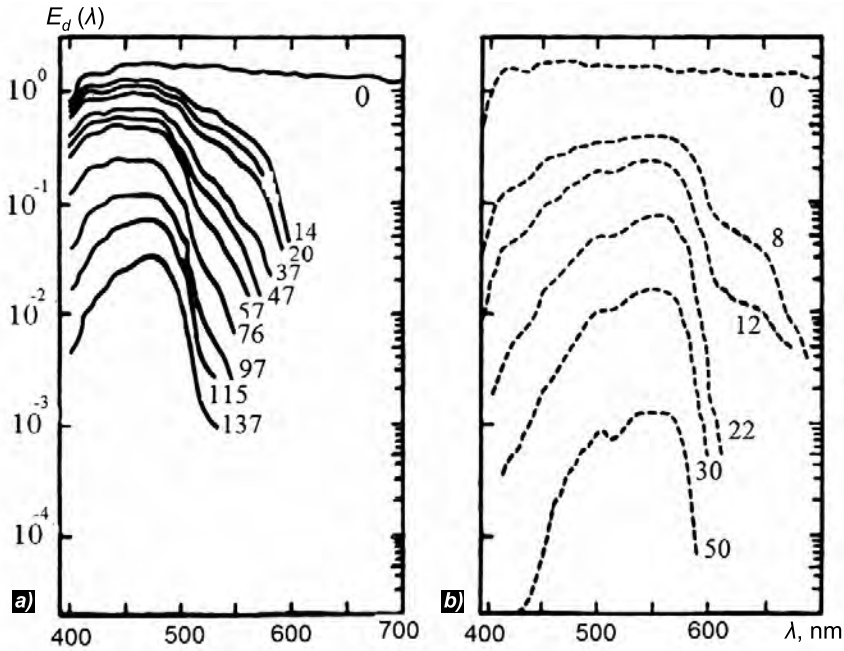

Fig. 3. Change of spectral distribution of underwater irradiance $E_d(\lambda)$ with depth in different waters: a – Sargasso Sea, b – near Senegal. Figures at the curves are the horizons, m [8, p. 269]

change in concentration of coloured organic substances in different waters.

According to (2), changes of $K_d(\lambda)$ spectral values lead to changes in the spectral distribution of underwater irradiance $E_d(\lambda, z)$ with the depth, and this change happens differently in various water types [8, p.269]. It can be seen from Fig. 3 that water acts as a colour filter: directly under the surface (at a depth of 0 m) irradiance spectral distribution corresponds to the solar spectrum, and this distribution narrows with depth depending on the spectral dependence of $K_d(\lambda)$ factor. The general property of all types of sea water is a strong weakening of the red spectrum interval with increasing depth, caused by water absorption. The disappearance of red light from the luminous flux spreading into sea depth can result in unexpected chromatic effects under water. One such effect is colourfully described in book [16], when a diver wounds a large leerfish with a harpoon at a depth of several tens of metres: "The blood was green! Bewildered with this spectacle, I swam up closer looking at the stream, with which life was leaving the heart of the fish. The blood was an emerald green. We exchanged looks of wonder. How many times had we swam among the leerfish but we never suspected that they had green blood. Holding the harpoon firmly with his astonishing trophy, Didi went up. At a depth of fifty five feet, the blood became brown. At twenty feet – it was already pink, and on the surface it was spreading in scarlet streams".

A difference in the absolute values of the K_d factor results in an abrupt difference of the light mode change with depth. In clear ocean water the transmission maximum, E_d value decreases by an order of magnitude at a depth of approximately 100 m, and in turbulent coastal water it decreases by approximately three orders of magnitude already at a depth of 50m (Fig. 3).

Many researchers have asked the question: at what depth does sunlight disappears completely. This question in particular was considered by Pierre Booger, who believed that the sun becomes completely invisible if its light is weakened by 900 billion times. Simple evaluations show that in clear ocean water, such weakening happens at a depth of approximately 600 m.

Photo multipliers, which are modern optical detectors capable to catch even separate photons, and at a depth of 1000m in transparent water will record approximately one photon per second. Only one photon of every 10^{24} hitting the sea surface will reach a depth of 1200 m; here a sensitive photo multiplier would record a photon approximately once a day; at a depth of 1500 m it would be once every 300 years! It is unlikely that a single sunlight photon has reached the bottom of the Mariana Trench during the whole history of mankind.

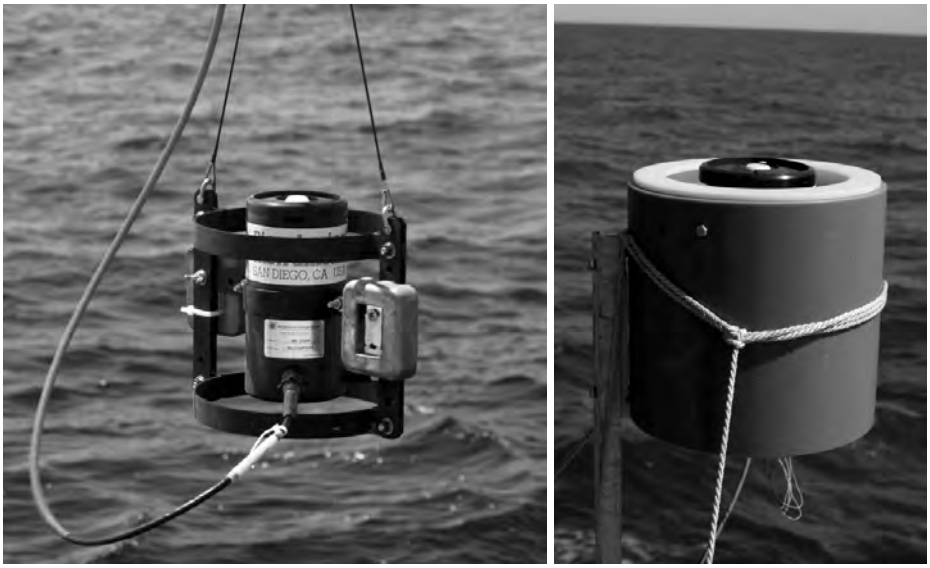

Fig. 4. A measuring instrument of light mode on the sea surface and in water thickness. On the left is an immersed detector, on the right is a deck-based detector

2.3. Measurement of solar radiation parameters on sea surface and in water thickness

Previous sections have shown that at present theoretical light mode calculations in marine environment can generate quite reliable results, provided that the optical characteristics of sea water and illumination conditions are known. Certainly we cannot do without direct measurements of light field parameters: which are at least necessary to check the accuracy of various theoretical models. However, measurements of these parameters under the conditions of sea expeditions usually pose considerable difficulties. In our opinion, to measurement of optical characteristics of sea water is simpler and more reliable; they can be measured in a laboratory, unlike light field parameters.

Measurement difficulties are primarily connected with weather conditions: cloudiness, rolling, surface waves. The latter create high-frequency fluctuations in underwater irradiance, which need to be separated from the average values for data processing. An analysis of the technological difficulties in light field parameter measurement can be found in [8, chapter.9]. The book also describes the devices developed up until the 1980s. In this review we will give examples of modern developments. Only irradiance measuring instruments fall within the scope of this article.

Over the last years, the Institute of Oceanology of Russian Academy of Sciences (IO RAS), uses a light mode metre (LMM) to measure irradiance from the top (E_d) and from the bottom (E_u) [17]. It was created to measure surface and underwater irradiances based on four-channel radiometers developed by the American company *Biospherical Instruments Inc.* The measuring system includes two detectors, each of which provides irradiance measurement in spectral channels 443, 490, 555 and 625 nm (half width of 10 nm) with an error of more than 5 %, Fig. 4. A special cosinusoidal collector provides cosine accuracy of ± 2 % and ± 10 % in angle intervals of (0–65) ^{o} and (65–85) ^{o} respectively.

A deck-based spectral radiometer (Fig. 4) was installed on the flat deck of a boat and equipped with a "vertical stabiliser" to avoid influence of rolling on the irradiance measurements. During the boat's journey, a continuous registration of spectral surface irradiance was made from a deck-based module using four wavelengths during all daylight hours. The dynamic irradiance range of the deck-based detector is equal to (10^{-2} – 30) W/m^2.

The underwater radiometer was submerged from the board using a cable in kevlar braid to a depth of 100 m. Dynamic interval of irradiance measurements was (10^{-4} – 30) W/m^2. The device was equipped with water depth and temperature detectors. The underwater module measurements can be taken both in a continuous probing mode, and at stable horizons. The sampling frequency of irradiance channels in the probing mode was 5 Hz, and in the sample mode it was equal to (1/60) min. To measure underwater irradiance from the bottom

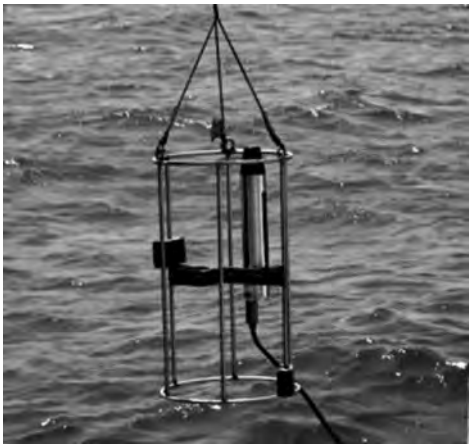

Technical characteristics:

- Dynamic range of the channel of measurement of a spectral irradiance is (3–0,0003) W/ m^2 •nm;
- Spectral range of measurements is (320–1100) nm;
- Spectral resolution is 3 nm;
- The maximum depth of immersion (on cable length) is 100 m;
- Time of selection of an average spectrum (it is set by the operator) is from 0,1s up to 24 h;

The device is calibrated 26.01.2015 by the TRIOS company according to the NIST standards.

Fig. 5. Hyper spectral *RAMSES* radiometer of TRIOS Company development [19]

E_u and to determine the diffuse weakening coefficient K_u, the underwater module was turned over with the collector down. Using a developed auxiliary module installed on the housing of the underwater radiometer, it was possible to take measurements autonomously, without a cable.

Algorithms and correspondent software were developed to calculate spectral values of the surface irradiance [18] and spectral coefficients of diffuse reflection [17].

At the IO RAS, a hyper spectral radiometer *RAMSES* developed by the German company *TRIOS* is also used, Fig. 5. Measurements using this device are taken at discrete horizons, and the depth is determined by means of a built-in depth detector. To measure underwater irradiance from bottom the $E_{u,}$ the underwater module is turned over with the collector down. More detailed information on this device can be found on the *TRIOS* Company website [19].

An interesting system for the measurement of luminance of ascending radiation and irradiance from the top in eight spectral channels is proposed by *SAtlantic* American company [20] (Fig. 6). Two versions are available: a buoy version and a freely incident platform (to isolate the device from the boat's movements, which can lead to the data distortion). In order to work in the buoy version, a detachable float is installed, Fig. 6; in this configuration, luminance and irradiance measurements can be

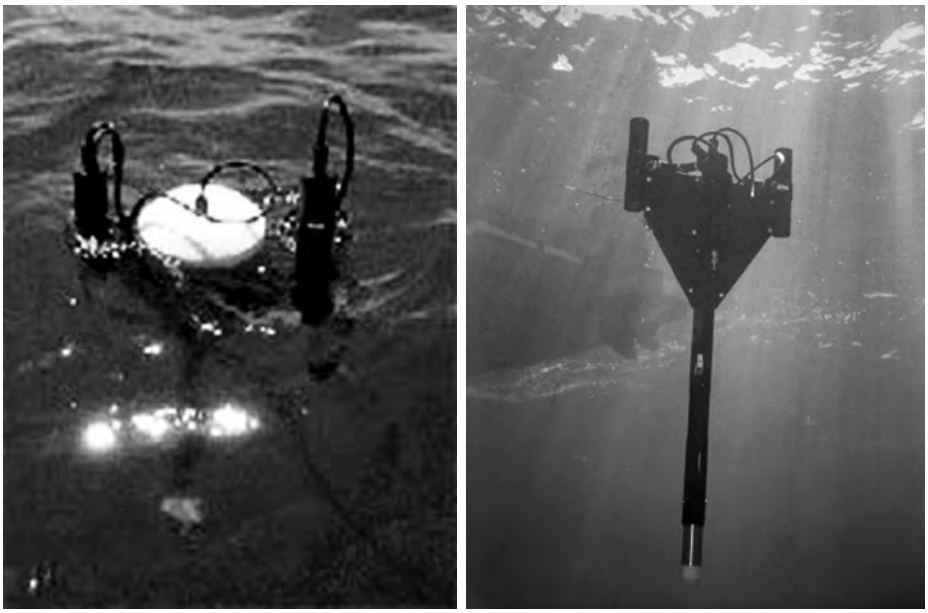

Fig. 6. The *Profiler II* measuring system developed by *SATLANTIC* Company [20] to measure luminance of ascending radiation and irradiance from the top in eight spectral channels. On the left is an example to measure in the buoy version; on the right – to measure in the free fall mode

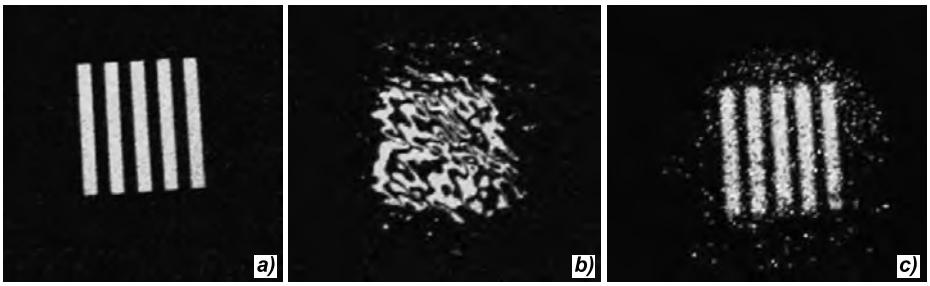

Fig. 7. Images of self-luminescent azimuth mark through the water surface in a laboratory pool: (a) is an initial image through a smooth surface, (b) is an image through a wavy surface (exposure is 1/400 s), (c) is a restored image [24]

performed directly under the sea surface (only 5 cm lower than the surface).

When working in the "free fall" mode, the float is removed, and the probe measures vertical profiles of the characteristics, sinking under its own weight. Other detectors can be installed on the probe, along with luminance and irradiance measuring instruments: those measuring temperature and electrical conductivity, depths, tilt angle, fluorescence and light scattering.

3. UNDERWATER VISIBILITY WITH NATURAL AND ARTIFICIAL ILLUMINATION

Observation of underwater objects is one of the most important directions in the exploration of the world's oceans. To achieve it in practice, various observation systems have been developed and created: onboard ship systems, underwater carrier systems, aircraft systems and satellite systems. The underwater vision theory is based on the theory of radiation transfer but has its own specific character. At present, books and review articles are published, in which basic the provisions of the modern theory of vision are summarised, calculation methods of image, visibility range and resolution parameters of various vision systems are described at natural and artificial illumination [21, 22]. In 2006, the first-ever monograph on the theory of vision through a wavy sea surface was published [23]. The publications mentioned contain practically all important bibliographic references, and the readers who are interested in underwater vision, will be able to find descriptions of various aspects of the problem within them. In our review, we will only provide two interesting examples, one of which addresses the problem of improving image quality when observing an underwater object through a wavy water surface, and another illustrates the modern possibilities of underwater vision at the greatest ocean depths.

3.1. Correction of underwater object images distortion by surface waves

The sea surface is disturbed into wave form by exposure to the wind can be presented as consisting of separate elementary sites with a random inclination. Radiation reflected from an underwater object when passing through the surface, is refracted on these sites and significantly distorted. This problem partly can be solved by averaging (accumulation) a large number of images, provided that the accumulation time considerably exceeds the maximum period of the wave. However, in real aircraft vision systems, which operate at a high movement speed, such averaging is impossible, and we have to deal with "instant" images.

An example of distorting an instant image of a self-luminescent azimuth mark through a wavy water surface in a laboratory pool (exposure was 1/400 s) is shown in Fig. 7.

The idea of correcting a distorted instant image is based on the use of information on spatial distribution of slopes. In experiment [24], the results of which are presented in Fig. 7, such information was obtained from a glare pattern of a wavy surface illuminated with a wide parallel beam (at a known direction and incidence angle). The surface was illuminated with red light, and the object – with green. Processing the glare pattern allowed obtaining a slope value in the neighbourhood of mirror points, which are within the surface area responsible for image distortion. For each instant image, the obtained information was used to correct separate fragments of the image, and the correction of the whole image was implemented by a summation (accumulation) of a series of partly corrected instant images. A result of the performed correction pre-

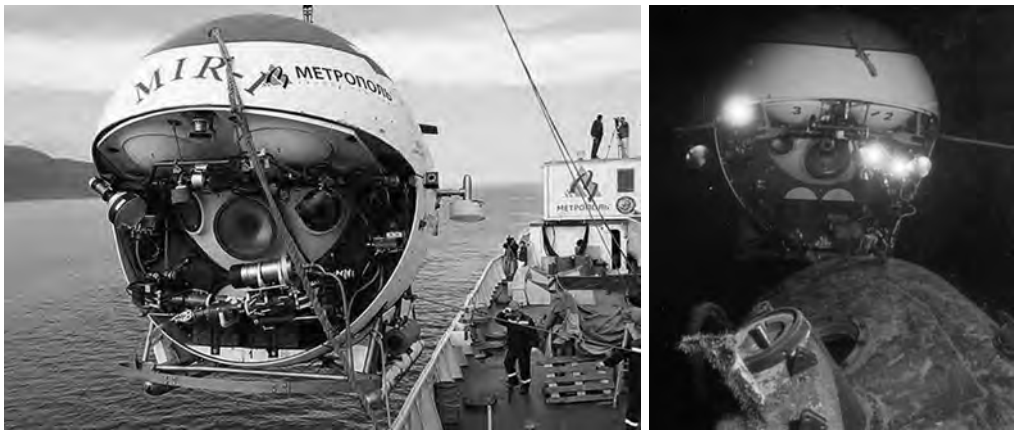

Fig. 8. Deep-water manned vehicle Mir: on the left – before immersion, on the right – investigation of a sunken submarine, Atlantic Ocean, depth is 5400 m

sented in Fig. 7c vividly demonstrates a the possibility of correcting images distorted by surface wind waves.

3.2. Deep-water observations using manned vehicles

In the IO RAS, two deep-water manned vehicles (DWMV) are operated: Mir-1 and Mir-2 with an immersion depth of to 6 km [25]. The vehicles are equipped with powerful underwater luminaires (Fig. 8), which make it possible to conduct visual observations of underwater objects, as well as photo- and video- and recordings. The Mir vehicles enabled important scientific discoveries, studies and video recordings of six objects, which sank at a depth of approximately 5400 m. In 1991 and 1995 using the Mir vehicles, shootings took place of the legendary ship Titanic, sunken at a depth of 3800 m. In the immersion process, the Titanic vessel was studied. During the accident, Titanic went down in two pieces and they now lie at a distance of 600 m apart. Unique filming was carried out. As a result, the *IMAX TITANICA* film and the renowned Hollywood film Titanic were created. Live television broadcasting of a video signal was undertaken at a depth of 3800 m, using a fibre-optical cable stretching to the ocean surface and then via a satellite to land. These operations were performed three times, and during one of them, people around the world watched a transmission from the Titanic within 2.5 hours of filming for the *Discovery* channel.

The Mir DWMV supported several other famous film projects, including: *"Bismarck", "Aliens of the Deep", "Ghost of the Abyss"*, etc.

Unique scientific research was undertaken during an expedition to the lake Baikal in July and August 2008. The Mir vehicles made 52 descents. Scientists taking part in these studies managed to find oil-bearing rocks, seismogenic grounds and new microorganisms.

The Mir vehicles and onboard scientific crew also descended to the hydrothermal fields of the Atlantic and Pacific oceans. They gathered a large body of unique scientific data, which allowed estimating the scales of the global hydrothermal system, deposits of mining formation in some regions, studying their chemical composition, investigating biological diversity of the hydrothermal systems, etc..

4. USE OF LIGHT TO STUDY AND MONITOR SEA ENVIRONMENT

Use of light to study and monitor sea environment has important advantages, and in some cases is superior to other methods. Among them are: the possibility to study without damaging the investigated environment, a practically inertia-free, high spatial resolution, potentially great scope and variety of the obtained information. Optical probes are widely used (transparency meters, nephelometers, fluorimetres) to study spatial distribution of suspensions, phytoplankton, a coloured organic substance, and hydrodynamic processes.

Unlike microwave radiation and sound, light passes through the sea surface without significant losses, which makes it possible to study the ocean subsurface layer distantly (from a boat, or a onboard a plane, as well as from satellites).

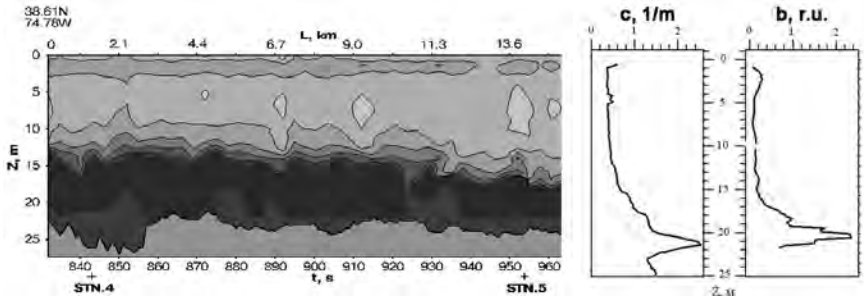

Fig. 9. Measurements using aircraft lidar of IO RAS. On the left – spatial distribution of a weighed substance (relative units) according to aircraft lidar shooting over a shallow Atlantic shelf near the east coast of the USA. (Vertically is depth in metres also computed according to the polarisation lidar data. A 16-kilometre section site is presented. Along the lower scale is time in seconds. Crosses (+) show position of stations 4 and 5, where reference optical measurements were performed.) Vertical profiles are comparison results: computed according to lidar (on the right) and measured *in situ* with benthonic nepheloid layer at a depth of ≈ 21 m (on the left)

4.1. Use of laser radiation

Since the early 1970s, in specialised expeditions of the IO RAS, natural experiments to study the principles of pulse laser radiation expansion in ocean waters and to study the possibilities to use laser pulses for probing water environment were made. It was found that laser beams could penetrate water thickness rather deeply: in an experiment with clear ocean water performed using a specially developed underwater bench, laser signal sent from a research vessel, was registered at a depth of more than 300 m; irradiance weakening relative to the surface was by a factor of 11.

To determine the characteristics of the surface layer water, lidar began to be used (*Lidar is Light Detection and Ranging).* Lidar was developed simultaneously in two directions: the so-called "time" lidars and fluorescent lidars. The first are based on measurement and on the subsequent processing of the time dependence of an "echo signal", which results from the backward scattering of the probing pulse spreading in the water thickness. The principle studies in this field in the USSR were performed by specialists from the Institute of Physics in Minsk and of the Institute of Applied Physics in Nizhny Novgorod. The type are based on the measurement and analysis of the spectral characteristics of backward scattering pulses, which are caused by quantitative and qualitative composition of fluorescing components of sea water and by combination (Raman) scattering – this was first explored by spe-

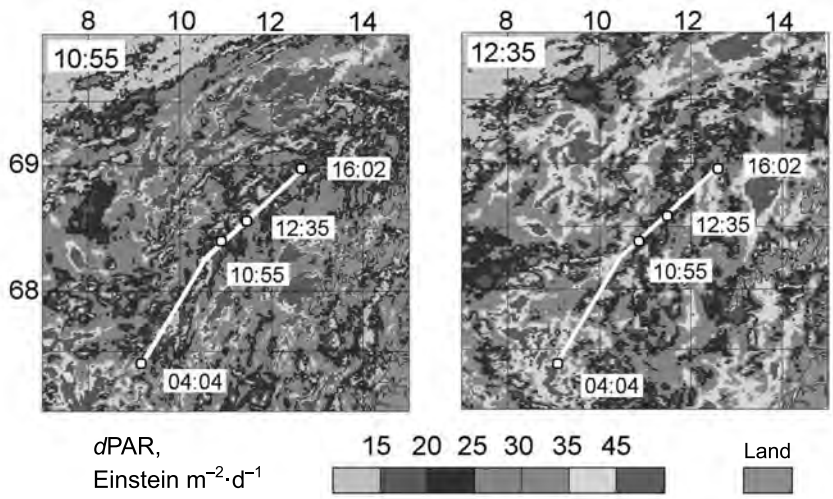

Fig. 10. Comparison of spatial distributions of daytime exposition of photosynthetically active radiation (400–700 nm) computed according to the *MODIS-Aqua* satellite scanner using IO RAS algorithm on August 1, 2014 at 10:55 am *GMT* (on the left) and at 12:35 pm *GMT* (on the right). The white line shows route of the boat, and figures nearby show the beginning (4:04 a.m.) and the end (4:02 p.m.) of the PAR measurements, as well as the boat position during the satellite flight [31]

Table 1. Main characteristics of the ocean and atmosphere, computed using data from satellite colour scanners [30]

Parameter	Use
Spectral coefficient of water thickness luminance	An indicator of the processes in the surface layer (such as expansion of river runoff, impurities of various origin, mesoscale whirlwinds, frontal zones, etc.)
Concentration of chlorophyll	Characterises the biomass of phytoplankton; it is a key parameter to calculate primary products of oceans and seas
Characteristics of atmospheric aerosol	They influence transmission of solar and egressing radiation, as well as cloud microphysics
Parameters of clouds	It is the most important meteorological factor
Surface spectral irradiance	An important factor determining primary products and thermal ocean balance
Factor of underwater irradiance vertical weakening	A key characteristic to calculate the light mode in water thickness, ocean albedo and bulk absorption of solar energy in the surface layer
Primary products	Characterises ocean biological resources, influences global carbon flows in the atmospheric and ocean system
Absorption factor of a painted organic substance	Determines light absorption in water, characterises the concentration of painted organic substances and water quality in coastal areas; it is one of monitoring parameters
Scattering factor of sea suspension	Determines water thickness albedo, characterises concentration of suspension in water; one of monitoring parameters

cialists from Moscow State University. Information on lidar methods for studying the structure of the top ocean layer from aircraft carriers can be found in review [26].

An example of measurement from an aircraft polarising lidar (APL) developed in the IO RAS is given in Fig. 9. The measurements were carried out during the Russian-American lidar experiment from a plane laboratory of NASA in 1996 [27]. Along with aircraft measurements, direct determinations of the vertical structure were performed from a boat. As it can be seen in Fig. 9, a good coincidence of vertical profiles is observed. Such measurements were also made from a boat using a ship version of the polarising lidar [28].

Measurements by means of APL also allow computing values of diffuse weakening factor of underwater irradiance K_d in the sea subsurface layer and constructing its spatial distribution [29].

4.2. Satellite observations of ocean colour

The first satellite scanner of ocean colour was started in 1978 on the NIMBUS-7 satellite, and for almost eight years of its work in the orbit, it transmitted a huge scope of information on the quantitative characteristics of various sea and ocean colours, depending on biological productivity of water and on other factors. At present, satellite colour scanners using solar radiation and not needing active sources, provide information on the dynamic processes in the surface layer (in particular, the expansion of river runoff), allow estimating chlorophyll concentration and light mode in water thickness, concentration of suspension and of painted organic substances, water quality in coastal areas, etc. (Table 1 [30]).

Fig. 10 shows spatial distributions of daytime exposition of the photosynthetic active radiation (PAR, (400–700) nm) computed according to the *MODIS-Aqua* satellite scanner data using an algorithm developed at the IO RAS [18]. In the quoted paper, calculation results using the IO RAS algorithm [31] and using the standard NASA algorithm [32] are compared with the results of continuous ship measurements (each 10 min.) using LMM (see section 1.3), which were carried out during an expedition of the Professor Shtokman research vessel along a route from Kaliningrad to Arkhangelsk at the end of July and begin-

ning of August 2014. The results of the performed comparison showed that both algorithms provide quite an acceptable evaluation accuracy applied to one day and 100 sq.km: without abrupt cloudiness changes, the error was equal to (5–35)% for the NASA algorithm and to (2–22)% for the IO RAS algorithm. It should be noticed that IO RAS algorithm makes it possible to estimate not only surface but also underwater irradiance at various depths in the subsurface layer [33].

5. CONCLUSION

Due to achievements in modern engineering, new opportunities arise for the use of light during exploration of the seas and oceans. New colour scanners with improved spectral characteristics and a higher spatial resolution are available. Possibilities of pilotless drones for studying and monitoring sea subsurface layer and ocean coastal areas are not yet fully developed. Possibilities of creating underwater lidars to carry out optical remote probing within the sea environment are considered. People have already reached the bottom of the Mariana Trench, and deep-water manned vehicles work at depths of 6 km. Underwater sailplanes (gliders) have been developed with an autonomous sailing range of thousands of kilometres. They can also be installed with optical measuring instruments. The era of exploring the seas and oceans using light continues.

REFERENCES

1. Reference book on lighting engineering / Under the editorship of Yu.B. Aizenberg. The 3rd revised edition, Moscow: Znak, 2006. 972 p.

2. Gershun A.A. An essay on the history of photometry / Selected works on photometry and lighting engineering. Moscow: The State publishing house of physical and mathematical literature, 1958, pp. 9–48.

3. Gershun A.A., Yanishevsky Yu.D. Transparency and colour of the sea /Leningrad: Naval Forces Naval Academy Edition 1941.

4. Gershun A.A. Selected works on photometry and lighting engineering. Moscow: The State publishing house of physical and mathematical literature. 1958. 548 p.

5. Raman, C.V. On the molecular scattering of light in water and the colour of the sea // Proc. R. Soc. London, Ser. A. 1922, Vol.101, pp. 64–79.

6. Shuleykin V. On sea chromaticity // Bulletin of the Institute of physics and biophysics, 1922, Vol. 2, pp. 119–136.

7. GOST 7601–78 Physical optics, Gosstandart of the USSR, 1979, 27 P.

8. Ocean optics. Vol.1, Physical optics of the ocean// Nauka, Moscow, 1983, 372 P.

9. Shifrin K.S. Introduction into ocean optics / Leningrad: Gidrometeoizdat, 1983, 278 P.

10. Jin, Z., Stamnes, K. Radiative transfer in nonuniformly refracting layered media: atmosphere-ocean system // Appl. Optics, 1994, Vol. 33, pp. 431–442.

11. Sheberstov, S.V., Nabiullina, M.V., Lukianova, E.A. Numerical Modelling of Radiative Transfer in Ocean-Atmosphere system with wind-roughened surface // Proc. of the 2nd Int. Conf. "Current Problems in Optics of Natural Waters". St- Petersburg, 2003, pp. 90–95.

12. HYDROLIGHT 5.2, ECOLIGHT 5.2 – Sequoia Scientific [Internet resource] URL: http://www.sequoiasci.com/wp-content/uploads/2013/07/HE52UsersGuide.pdf.

13. Mobley, C.D. Light and Water: Radiative Transfer in Natural Waters / San Diego: Academic Press, 1994. 592 P.

14. Gordon, H.R. Can the Lambert–Beer law be applied to the diffuse attenuation coefficient of ocean water? // Limnol. Oceanogr. 1989, Vol.34, No. 8, pp. 1389–1409.

15. OceanColorWeb // Data – Level 3 Browser [Internet resource]. URL: http://oceancolor.gsfc.nasa.gov.

16. Cousteau J. – I., Dumas F. In the world of silence / Moscow: Molodaya Gvardiya, 1957, 224 P.

17. Khrapko, A.N., Kopelevich, O.V., Burenkov, V.I. et al. New instrument for measuring surface and underwater irradiances // Proc. of 5th Int. Conf. on Current Problems in Optics of Natural Waters (ONW '2007). Nizhnii Novgorod, 2007, pp. 271–275.

18. Vazyulya, S.V., Kopelevich, O.V., Sheberstov, S.V., Artemiev, V.A. Estimation of sea surface solar radiation at 400–700 nm using satellite ocean color data, and its validation by ship data // Optics Express, 2016, Vol 24, No. 6, pp. A604-A611.

19. RAMSES Hyperspectral Radiance and Irradiance Sensors / ramses_en.pdf. [Internet recource]. URL: http://www.trios.de.

20. Free-Falling Optical Profiler [Electronic resource]. URL: http://satlantic.com/profiler.

21. Dolin L.S., Levin I.M. Handbook on the theory of underwater vision / Leningrad: Gidrometeoizdat, 1991, 229 P.

22. Dolin L.S., Levin I.M. Theory of underwater visibility // Fundamental and applied hydrophysics, 2015, Vol.8, #2, pp. 22–35.

23. Dolin, L.S., Gilbert, G.D., Levin, I.M., Luchinin, A.G. Theory of imaging through wavy sea surface / N. Novgorod: Institute of Applied Physics, 2006, 180 P.

24. Savchenko V.V., Osadchiy V. Yu., Levin I.M. Correction of underwater object images distorted by surface waves // Oceanology, 2008, Vol. 48, #6, pp. 843–846.

25. Ocean.Ru- Laboratory of scientific operation… [Internet resource].URL: http://ocean.ru›content/view/52/45/.

26. Goldin Yu. A., Luchinin A.G. Aircraft lidar methods of studying vertical structure of optical characteristics of the ocean top layer // In: Subsurface ocean layer. Physical processes and remote probing. N. Novgorod: IAP RAS, 1999. Vol.2, pp. 345–381.

27. Vasilkov, A.P., Goldin, Yu.A., Gureev, B.A. et al. Airborne polarized lidar detection of scattering layers in the ocean // Applied Optics. 2001, Vol. 40, No. 24, pp. 4353–4364.

28. Goldin Yu. A., Gureev B.A. Ventskut Yu.I. Polyarisation lidar for probing ocean water thickness from a boat / In: Comprehensive studies of the World Ocean – the Meridian, Atlantic Ocean project. Moscow: Nauka, 2008, pp. 179–188.

29. Goldin, Y.A., Vasilev, A.N., Lisovskiy, A.S., Chernook, V.I. Results of Barents Sea airborne lidar survey // Proc. SPIE, 2007, Vol. 6615, 66150E.

30. Kopelevich O.V. Optical properties of ocean and sea water // In: World Ocean, Vol. 2, Physics, chemistry and biology of the ocean. Precipitation forming in the ocean and interaction of Earth geospheres. Moscow: Scientific world, 2014, pp. 58–82.

31. Kopelevich O.V., Burenkov V.I., Vazyulya S.V., et al. PAR balance evaluation in Barents Sea according to the satellite colour scanner SeaWiFS // Oceanology, 2003, #6, pp. 834–845.

32. NASA, “OceanColourWEB”. [Internet resource]. URL: http://oceancolor.gsfc.nasa.gov/.

33. Kopelevich, O.V., Sheberstov, S.V., Burenkov, V.I. et al. Assessment of underwater irradiance and absorption of solar radiation at water column from satellite data // Proc. SPIE, 2007, Vol. 6615, 661507.

***Oleg V. Kopelevich*,**
Dr. of phys-math science, graduated from the Moscow Institute of Physics and Technology, an engineer and physicist. At present, he is a head of the laboratory of the Ocean Optics of the Institute of Oceanology of P.P. Shirshov of the Russian Academy of Sciences

Light & Engineering
Vol. 25, No. 4, pp. 18-23, 2017

Svetotekhnika
No. 4, 2017, pp. 19–28

SPACE RETROREFLECTOR ARRAYS

Andrei L. Sokolov, Alexander S. Akentyev, and Vladimir D. Nenadovich

Joint-Stock Company "Scientific and Production Corporation "Systems of Precise Instrument Making" (JSC "SPC "SPIM"), Moscow
E-mail: alsokolov@bk.ru

ABSTRACT

The main geodetic target-satellites of double-sided pulse laser range are considered. An updated ring retroreflector array for the GLONASS navigation spacecraft is presented. The main characteristics of the Pyramid compact retroreflector array for low-orbital satellites are considered.

Keywords: corner reflector, retroreflector arrays, spacecraft, geodetic target-satellites

1. INTRODUCTION

All modern navigation and geodetic spacecrafts (SC) are equipped with corner reflectors (CR), which form so-called retroreflector arrays (RA) [1–5]. These are needed to reflect range measuring system rays back to the radiation source in order to measure distance to the SC precisely and then to correct parameters of the orbit and of co-ordinates of the optical-laser station, as well as to calibrate ground-based radio engineering measuring facilities [6–9].

CRs are unique optical devices, which change direction of incident rays to opposite, irrespective of the incidence angle. Fig. 1 shows ray trace in a CR and also several CRs fixed in a metal glass, which are made in Precision Systems and Instruments Research-and-production Corporation JSC. In total there are tens of thousands of such CRs in space.

Currently, one of the main instruments for the provision of a high precision geocentric co-ordinates of GLONASS tracking stations is a laser station network measuring the distance to special geodetic satellites, which should have a submillimeter target error (uncontrollable additive to the systematic measurement correction) and zero signature (absence of pulse configuration and duration distortion). The measurement of ranges to such satellites is also necessary for space geodesy, geodynamics and navigation, including studying the Earth's gravitation field, influence of non-gravitation forces on SC orbit stability, etc.

In most cases, passive geodetic target-satellites, Fig.2, for high-precision laser range measuring are

Fig. 1. Corner reflectors in a frame produced in PCI RPC JSC

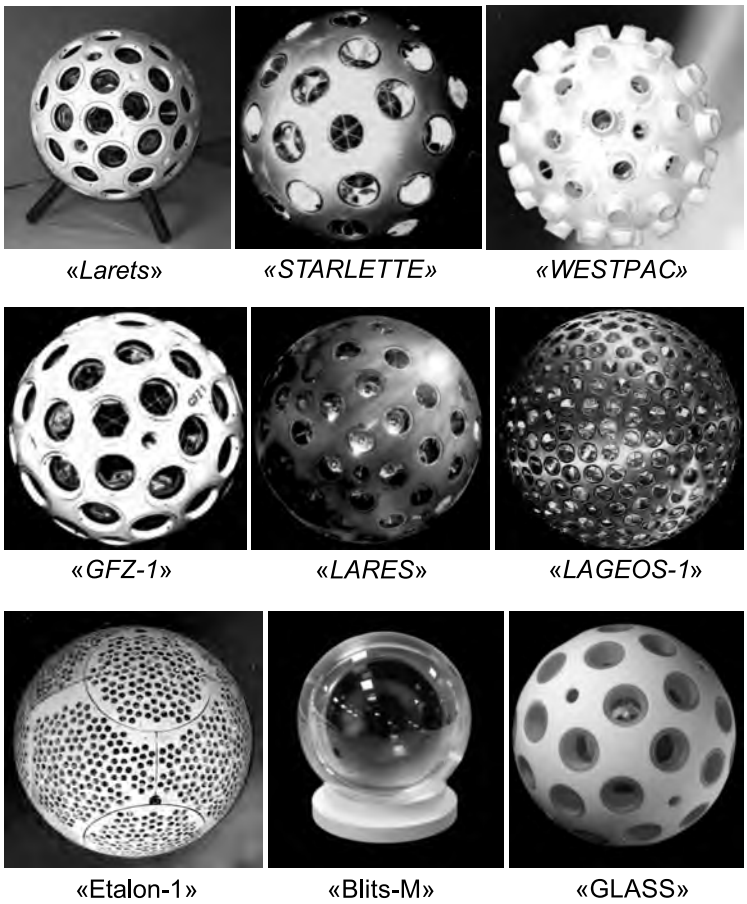

Fig. 2. Passive target-satellites – spherical RAs (are shown not to scale)

heavy metal spheres, on the surface of which between 60 and 2,142 CRs are installed. Over the last decades, from 60 to 2142 CRs were manufactured and placed into orbits the following satellites to address fundamental and applied tasks: LAGEOS-1 (the USA, 1976), LAGEOS-2 (the USA, Italy, 1992), STARLETTE (France, 1975), STELLA (1993, France), ETALON-1 (the USSR, 1989), ETALON-2 (the USSR, 1989), GFZ-1 (Germany, Russia, 1995), Larets (Russia, 2003), WESTPAC (Russia, 1998), "LARES" (Italy, 2012) and many others. The orbit altitude of the Etalon-1,2 satellites is 19100 km, CR number is 2142 pieces, diameter is 1294 mm and mass is 1300 kg.

If an object onto which CR is placed moves, *velocity aberration* occurs. This causes the ray to deviate at an angle of $2 \cdot u/c$, where u is the tangential component of the object movement velocity, and c is light velocity, Fig. 3. Laser ray deviation depends on the satellite orbit height and can reach ten angular seconds at small heights, which means a displacement of the light spot centre over the Earth surface by tens or hundreds of metres from the transmitter.

Therefore, for a successful operation of a ranging system, one should aim for the reflected laser beam energy to be concentrated at a certain distance from the optical axis.

2. BLITS SC

Multielement RAs have a considerable target error and a non-zero signature, which interferes with achieving measurement accuracy at the sub-millimetre level. Besides, the interaction of the Earth's magnetic field with vortex currents induced in the satellite metal body slows down its own rotation to a complete stop, which reduces measurement accuracy.

These disadvantages can be overcome by implementing satellites as spherical glass lenses focusing the incident plain wave on their opposite surface with a reflecting coating [10]. In this case, laser ray's optical path inside the sphere does not depend on the arrival angle and signal configuration as well, as duration are not distorted.

With that end in view, PSI RPC JSC has developed and manufactured Blits-M SC (Fig. 3), which

provides a sub-millimetre target error with zero signature and diffusion equivalent surface area of about 10^6 m^2 to obtain precise measuring data for geodetic support of the GLONASS system. BLITS-M SC is a spherical glass optical system consisting of an inner sphere and two external meniscuses 220 mm in diameter and 17 kg in mass combined. To improve ballistic quality and power engineering of the satellite taking into account the height of orbit, it was necessary to increase its size in comparison with the previous BLITS SC structure, which came to an end in 2013 after collision with a space debris at a height of 832 km. The greater the radius of the sphere, the more the mass relative to the cross-section area and laser radiation energy reflected by the satellite.

However, the main factors increasing the radiant intensity towards the receiver is an optimal reduction of spherical aberration, the layer ratio of curvature radius and thickness for a given wavelength, refractive indices of the satellite glass and temperature. This allows forming a reflection indicatrix (far field diffraction pattern (FFDP)) with a maximum possible intensity of the reflected radiation for deviation angles from the optical axis within an interval of 6–8″ taking into account the chromatic aberration phenomenon.

One of the key criteria for the choice of structure is BLITS-M SC's lifetime maintenance over a ten year period.

In order to achieve this, the satellite's structure includes radiation-resistant glass K108 (for the external meniscuses) and TF105 (for the inner sphere), and a heat-resistant structure is developed.

Generally, the satellite's average temperature while in an orbit is negative and is equal to approximately minus 25 °C. However, when moving along this orbit, for every two hours of exposure to the Sun's radiation with various light incidence angles and can appear to be into Earth shadow. The BLITS-M SC rotation axis is perpendicular to the orbit plane, and rotation speed is from 5 to 10 revolutions per minute in order that the satellite is alternately directed to the laser station by the transmitting and reflecting hemispheres. Aluminium reflection coating causes considerable heating, temperature drops and irregularities in temperature distribution. Therefore, one of the external meniscuses of the BLITS-M SC has an interference dielectric coating.

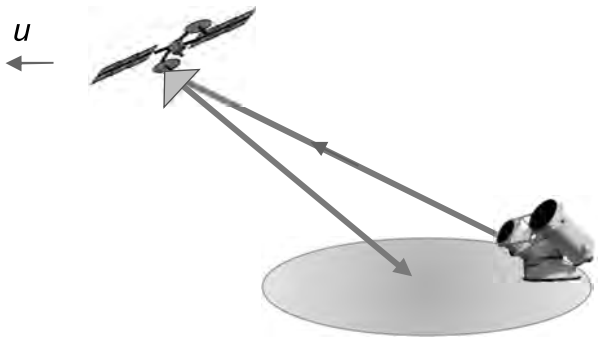

Fig. 3. Effect of the velocity aberration: a reflected ray is deviated at an angle depending on the satellite speed

To achieve the target function, it was necessary to select BLITS-M SC's orbit height properly. Factors determining orbit choice are residual atmosphere influence, space debris and exposure of space radiation (high-energy elementary particles and UV radiation of the Sun). The higher the orbit, the more stable it is, and the less atmospheric influence and space debris density there is. At heights of more than 1500 km, probability of collision with space large debris is very low.

Conversely, space radiation increases with height above 1500 km and with proximity to the Van Allen radiation belts; the number of high-energy electrons and protons capable to cause an external meniscus degradation increases.

As a result of the performed studies, the BLITS-M SC orbit height is selected to be optimum: circular, near-polar and close to 1500 km. BLITS-M SC as a payload together with SC GONETS group is planned to be placed into orbit in 2018.

3. REFLECTION INDICATRIX OF A CORNER REFLECTOR

If a plain wave is incident on a CR, then in the far-field region, a diffraction pattern is formed, its type depends on many factors: CR size, dihedral angles production accuracy, on reflecting edge coating type, etc. The ray can pass inside the CR by six different ways, depending on which of the six sectors of the input edge it comes to [1–5]. Each of three reflections is characterised by a phase difference between orthogonal components of vector ***E*** (linear phase anisotropy). And in this case, the planes of ray incidence on the edges do not coincide. The incidence angle of each CR edge is equal to arctg $\sqrt{2} \approx 54°$, and the angle between the edge incidence planes is equal to $\alpha = \pm 60°$. To descript CR polar-

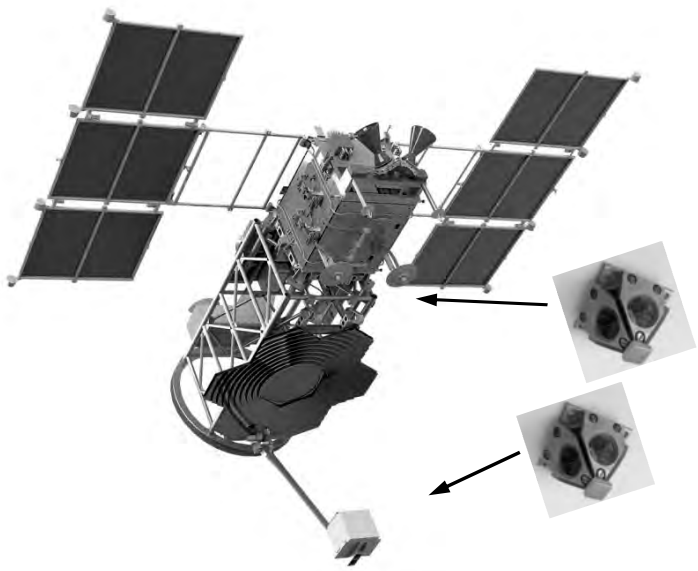

Fig. 4. SC Lomonosov. (RA "Pyramid" in number of two pieces is shown in an increased scale)

ising properties, one should consider six resulting Jones matrices for different combinations of the ray trace, taking into account co-ordinate system turns and phase difference δ on the reflecting edges. Each CR sector is characterised by certain amplitude-phase transmission factors for $\boldsymbol{E}$ vector orthogonal components. As a result of light reflection, six coherent beams are formed. Therefore, it is necessary to take into consideration their various polarisation states, expansion when distributing in space and far field region interference [1–5].

The far field diffraction pattern (FFDP) of the reflected radiation significantly depends on the phase difference of orthogonal components when reflecting, which is determined by CR edge coating type and has the appearance of several spots (FFDP leaves). In that specific case, it is Airy's diffraction pattern with angular width of the central maximum between the first zeroes $2\gamma \approx 2.44 \cdot \lambda/D$, where D is the CR aperture diameter.

Formation of a required phase difference is provided by phase difference change between orthogonal components of electric vector when reflecting. A coating with *any* phase difference can be designed based on thin dielectric layers deposited on the reflecting CR edges [11, 12]. The first dielectric layer being adjacent to the prism surface should have a refractive index higher than the prism material, for example $n = 2$. Upon contact of the last layer with air, total internal reflection always takes place, so losses are ideally absent (but unlike CR without a coating, multibeam interference leads to an additional phase difference between orthogonal components).

4. A RING RETROREFLECTOR ARRAY OF LARGER CORNER REFLECTORS WITH A TWO-LEAFED REFLECTION INDICATRIX

In the GLONASS-K SC, a *ring* retroreflector array consisting of three CR ranks with uncovered edges is used. As it is shown in p. 3, far field diffraction pattern of reflected radiation looks like one central and six peripheral spots in case of total internal light reflection from CR edges. A special turn of every CR in the panel plane allows obtaining an intensity ring, which is formed by side spots of every CR. As the RA diffraction pattern is formed by all CRs, the photons reflected from all CRs come to the receiver device. At inclinations, CR panels appear to be located at different distances from the receiver. At operation angles of radiation incidence of 8–10°, the response signal elongates up to a value of 600–700 ps. It means that root-mean square deviation (RMSD) of a single-unit range measurement is on the average equal to 60 mm instead of the required 6–8 mm.

The problem of decreasing a single measurement random error (RMSD) with simultaneous increase of the reflected signal energy directed to the laser range measuring system, can be solved due to a ring RA consisting of two-spot CRs of an increased size. The two-spot diffraction pattern is formed due

to a controlled change of one of the dihedral angles. Angular size of each spot depends on CR dimensions: the greater the CR, the higher the energy concentration in the spot. Such CR edges should be covered with a special dielectric coating in order on the one hand, to generate a necessary reflection indicatrix, and on the another hand, to reduce its thermal distortions. Ǎn optimum far field diffraction pattern is provided by choice of CR size within (42–48) mm and of camber angle between the reflecting edges within (2.2–2.5)″. At an angular distance between side leaves equal to the angular aberration double value, one of the spots comes to the reflected signal receiver exactly (Fig. 2). This allows reducing energy losses, which arise if reflection indicatrix has one wide or seven narrow leaves [1–6].

For a ring RA (RRA), use of 36 CRs is required, which are separated relative to each other by some angle, for example by 10° so that all lines connecting side leaves are directed to the RRA geometrical centre. Then for a certain RRA orientation, two CRs, which are at opposite sides of this RA, reflect the receiver direction. In this case, RMSD of the RA geometrical centre determination is equal to the root of squares sum of two signal RMSD, i.e. for initial pulse duration of 50ps, it is $18 \cdot \sqrt{2} = 25$ps irrespective of the incidence angle.

5. "PYRAMID"

The compact RA "Pyramid" developed in JSC “SPC “SPIM” is a pyramidal structure of four CRs with common vertex (Fig. 4). Its mass is only 30 g and cross size does not exceed 40 mm.

To achieve the required energy and precision characteristics, it is necessary that an optimum reflection indicatrix is provided by RA design parameters. Presence of velocity aberration leads to the fact that the optimum receiving direction differs from the reflection indicatrix axis and depends on the satellite speed, i.e. on its orbit altitude. For low-orbital satellites, velocity aberration average value [6] is about 8″. It means that the indicatrix should be somehow expanded, for example by reducing CR size. However in doing so, the aperture decreases, and the received laser radiation energy as a whole decreases. When increasing CR number, both effective diffusion surface, and probability of radiation reflexion from two and more CRs increase.

If distances from the laser transmitter to separate CRs in the RA are different, delayed response occurs, which is leads to a target error.

The incidence angle for the all four CRs in the SC flight zenith area is about 54 °, CR aperture decreases and has an oval configuration. As a result, diffuse effective surface for the radiation reflected from CRs is minimal and does not exceed several thousand square metres. In the event the satellite’s location is slightly higher than visible horizon line at $\beta = 27°$, this surface area is from 42000 to 10000 m^2. At the same time, the distance to the satellite is minimal just in zenith area and maximal, when the satellite is located slightly higher than visible horizon line. As photoelectron number recorded by photodetectors of the ground quantum-and-optical system is proportional to the fourth degree of the distance to the satellite, an increase of CR aperture when reducing SC inclination angle, compensates for the increase in distance. As a result, the photoelectron number is maximal within zenith observation angle area $\theta_{zen} = 40$ °.

Zenith area range measurement maximum error arises when radiation is incident simultaneously on several CRs due to the different optical length of the ray within the two CRs. Minimum target errors take place in case, when radiation is incident on two CRs but optical lengths of the ray path inside them are identical. The measurement error as a whole when measuring range to SC with RA "Pyramid" does not exceed 0.5 mm.

Two compact RA "Pyramid" manufactured at SPP RPC JSC were placed onboard of Lomonosov SC (Fig. 4). The satellite was launched into a solar-synchronous orbit of 500 km height in April, 2016 with a scientific equipment of the Moscow State University of M.V. Lomonosov to study phenomena in upper atmosphere.

Each RA is a pyramid consisting of four corner reflectors with common vertex and is capable to reflect laser pulses from the whole lower hemisphere. One RA is placed on the satellite body, and another is on an extension rod at a distance about 2 m. The measurements performed in a single-electron mode allowed observing two tracks at a distance depending on the satellite orientation relative to the laser station at the observation moment.

Despite the small size, RAs provided a sufficient area of the diffuse equivalent surface. According to the evaluation (comparative measurements were made using Stella and Lageos satellites), the surface

was equal to 0.2–0.5 million m^2. The space experiment results allow recommending this system to be installed at low-orbit spacecrafts in order to determine their orientation and to perform any additional monitoring deployment of the spacecraft components in space.

CONCLUSION

Space RAs are an important onboard segment of the optical-laser facilities necessary for space geodesy, geodynamics and navigation, including the study of gravitation Earth field, influence of non-gravitation forces on the spacecraft (SC) orbit stability and other scientific purposes.

REFERENCES

1. Korotayev V. V., Pankov E.D. Polarising properties of corner reflectors // Optical-mechanical industry, 1981, #1, pp. 9–12.

2. Denisyuk G. V., Korneev V.I. Formation of fine-grain image using corner reflectors based on the total internal reflection phenomenon // Optical-mechanical industry,1982, #9, pp.1–3.

3. Sadovnikov M.A., Sokolov A.L. Spatial polarising structure of radiation formed by corner reflectors with non-metallised edges // Optics and spectroscopy, 2009, T. 107, #2, pp. 213–218.

4. Sadovnikov M.A, Sokolov A.L., Shargorodsky V.D. Aalysis of diffusion equivalent surface of corner reflectors with various edge coating // Achievements of modern radio electronics, 2009, #8, pp. 55–62.

5. Ishchenko E. F., Sokolov A.L. Polarising optics (manual). The second edition – Moscow.: Fizmatlit, 2012, 446p.

6. Degnan John J. Millimeter Accuracy Satellite Laser Ranging: A Review // Contribution of Space Geodesy to Geodynamics: Technology, 1997, Vol. 25, pp. 133–162.

7. Vasilyev V. P., Shargorodsky V.D. A precise satellite laser range measuring based on lasers with a high pulse frequency // Electromagnetic waves and electronic systems, 2007, #7, pp. 6–10.

8. Arnold D. URL: http://ilrs.gsfc.nasa.gov/about/reports/other_publications.html (addressing date: 03.2017: 03.2017).

9. Sadovnikov M.A. Necessary conditions to achieve submillimetric accuracy of measurements in the satellite laser range measuring // Electromagnetic waves and electronic systems, 2009, #12, pp. 13–16.

10. Belov M. S., Vasilyev V.P., Gashkin I.S., Parkhomenko N.N., Shargorodsky V.D.

Spherical lens as a satellite target for precise laser range measuring // Electromagnetic waves and electronic systems, 2007, #7, pp. 11–14.

11. Sokolov A. L., Murashkin V.V. Diffraction polarising and optical elements with radial symmetry // Optics and spectroscopy, 2011, V. 111, pp. 900–907.

12. Sokolov A.L. Formation of polarization-symmetrical beams using cube-corner reflectors // J. Opt. Soc. Am. A., 2013, Vol. 30, # 7, pp. 1350–1357.

13. Sokolov A.L. Optical vortices with axisymmetric polarization structure // Optical Engineering, 2017, Vol. 56 (1), pp. 014109–1 – 014109–8.

Andrei L. Sokolov,
Doctor of Technical Science, Associate Professor, graduated from the Moscow Power Institute in 1981. At present, he is the Chief of the Science and Technology Complex of Systems of Precise Instrument Making Scientific and Production Corporation JSC

Alexander S. Akentyev,
an engineer, graduated from the Moscow Power Institute in 2014. At present, he is an engineer at Systems of Precise Instrument Making Scientific and Production Corporation JSC and a postgraduate student of the Moscow Power Institute, MPEU

Vladimir D. Nenadovich.,
an engineer, graduated from the Moscow Power Institute in 2013. At present, he is an Engineer of Systems of Precise Instrument Making Scientific and Production Corporation JSC and postgraduate student of the Moscow Power Institute, MPEU

Light & Engineering
Vol. 25, No. 4, pp. 24-31, 2017

Svetotekhnika
No. 3, 2017, pp. 17–22

EVALUATION OF ILLUMINATION QUALITY BASED ON SPATIAL-ANGULAR LUMINANCE DISTRIBUTION

Vladimir P. Budak, Victor S. Zheltov, Tatiyana V. Meshkova, and Renat Sh. Notfullin

The Moscow Power Engineering Institute, National Research University (NRU), Moscow
E-mail: budakvp@gmail.com

ABSTRACT

A new approach to the formulation of an illumination quality criterion based on an analysis of spatial-angular luminance distribution and of the properties of human sight is considered in this article. As part of the research, an experimental installation was developed to determine comfort and discomfort areas, which are inseparable from an assessment of illumination quality. A method for computer simulation of spatial-angular luminance distribution, based on local evaluations Monte-Carlo method is shown, which in future can facilitate moving from a preset illuminance distribution simulation to a preset quality simulation.

Keywords: local evaluations of Monte-Carlo method, spatial-angular luminance distribution, discomfort, illumination quality criterion

1. INTRODUCTION

The development of computer facilities and mathematical simulation methods has performed a real revolution in design of illumination installations (II). At the end turn of the twenty-first century, exhausting engineering calculations gave way to II computer simulation. These made it possible not only to design according to preset normalised quantitative data, but also to see a "photorealistic" picture of an installation, which was not yet in existence. On the whole, II design to match preset quantitative characteristics has been achieved in today's illumination practice, but designing to preset quality characteristics is and idea not as developed for today's lighting community. Besides, currently formulated quality characteristics have some key disadvantages. In a real engineering practice, a quality indicator is only expressed when calculating an integrated discomfort index *UGR*. If at the beginning of II simulation methods and software development, such a situation was natural, with the emergence of new methods [1] of the global illumination equation (GIE) simulation [2], totally new opportunities arise, not just for illuminance distribution calculation in a diffuse approximation but for the calculation of spatial-angular luminance distribution.

This allows to once again raise the question of an illumination quality index and of II design according to preset quality indices.

2. SIMULATION OF SPATIAL-ANGULAR LUMINANCE DISTRIBUTION USING LOCAL EVALUATIONS OF MONTE-CARLO METHOD

Modern lighting practice and normalized standards have grown out of the possibility to simulate illuminance taking into account multiple reflections, and out of the possibility to simulate luminance for direct light only without accounting for reflections. Based on this assumption, only in external illumination, and in particular in architectural and road illumination, the luminance characteristic as perceived by the human eye is normalised. One should notice that the *DIALux* and *Relux* programs generally used for II design, simulate illuminance distribution in the diffuse approximation.

With such an approach, the finite elements method simulates the luminous emittance equation [9], which is a GIE consequence [2] in the diffuse approximation.

GIE is an integral equation of the second kind

$$L(\mathbf{r},\hat{\mathbf{l}}) = L_0(\mathbf{r},\hat{\mathbf{l}}) + \\ + \frac{1}{\pi}\int L(\mathbf{r},\hat{\mathbf{l}}')\sigma(\mathbf{r};\hat{\mathbf{l}},\hat{\mathbf{l}}')\left|(\hat{\mathbf{N}},\hat{\mathbf{l}}')\right| d\hat{\mathbf{l}}', \quad (1)$$

where $L(\mathbf{r},\hat{\mathbf{l}})$ is luminance in $\mathbf{r}$ point in direction $\hat{\mathbf{l}}$, $\sigma(\mathbf{r};\hat{\mathbf{l}},\hat{\mathbf{l}}')$ is bidirectional reflection function (reflection or transmission), L_0 is direct luminance component, directly from sources, $\hat{\mathbf{N}}$ is normal in $\mathbf{r}$ point to a scene surface element.

It should be noted that at present, a new software product *DIALux Evo*, the cornerstone of which is the GIE simulation based on photon cards [10], and this fact allows simulating spatial-angular luminance distribution. However *DIALux Evo* has not found its level in engineering practice yet.

Within this article, we propose to apply local evaluations of the Monte-Carlo method for GIE calculation. The local evaluations method traces its roots to atomic physics [11] and continues its development in optics of the atmosphere and ocean [12]. GIE can be written down as a space integral and expanded into Neumann series, every term of which can be represented as a certain multiple space integral. Each term of the latter can be approximately presented as a random node quadrature, i.e. Monte-Carlo method.

After some transformations, the obtained expansion can be written down as follows [1]:

$$L(\mathbf{r},\hat{\mathbf{l}}) = L_0(\mathbf{r},\hat{\mathbf{l}}) + \\ + \frac{1}{N}\sum_{i=1}^{N}\left(\frac{1}{\pi}\frac{L_0(\mathbf{r}_{1i},\hat{\mathbf{l}}_{1i})}{p_1(\mathbf{r}_{1i},\hat{\mathbf{l}}_{1i})}\frac{\sigma(\mathbf{r};\hat{\mathbf{l}}_{1i},\hat{\mathbf{l}})G(\mathbf{r}_1,\mathbf{r})}{p_2(\mathbf{r}_{1i},\hat{\mathbf{l}}_{1i}\to\mathbf{r},\hat{\mathbf{l}})} + \right. \\ + \frac{1}{\pi^2}\frac{L_0(\mathbf{r}_{1i},\hat{\mathbf{l}}_{1i})}{p_1(\mathbf{r}_{1i},\hat{\mathbf{l}}_{1i})}\frac{\sigma(\mathbf{r}_{2i};\hat{\mathbf{l}}_{1i},\hat{\mathbf{l}}_{2i})G(\mathbf{r}_{1i},\mathbf{r}_{2i})}{p_2(\mathbf{r}_{1i},\hat{\mathbf{l}}_{1i}\to\mathbf{r}_{2i},\hat{\mathbf{l}}_{2i})}\times \\ \left.\times\frac{\sigma(\mathbf{r};\hat{\mathbf{l}}_{2i},\hat{\mathbf{l}})G(\mathbf{r}_{2i},\mathbf{r})}{p_2(\mathbf{r}_{2i},\hat{\mathbf{l}}_{2i}\to\mathbf{r},\hat{\mathbf{l}})} + \ldots\right), \quad (2)$$

where $p_1(\mathbf{r}_{1i},\hat{\mathbf{l}}_{1i})$, $p_2(\mathbf{r}_{1i},\hat{\mathbf{l}}_{1i}\to\mathbf{r},\hat{\mathbf{l}})$ are initial and transitional probability densities determining position of random nodes [12].

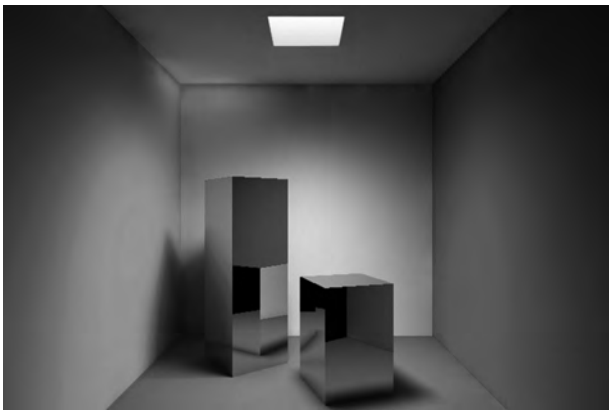

Fig. 1. Example of visualization of the space-angular luminance distribution by local estimates of the Monte Carlo method for the *Cornell Boxes* reference scene

As $p_2(\mathbf{r}_{1i},\hat{\mathbf{l}}_{1i}\to\mathbf{r},\hat{\mathbf{l}})$ is only determined by two sequential random nodes, the expression can be interpreted as a Markov's chain. As a result of creating the Markov's chain, the transition nucleus for studied points $\mathbf{r},\hat{\mathbf{l}}$ at each chain stage can be estimated. Accumulating the statistics will directly obtain the luminance at preset points along the preset directions [1]. Such an evaluation can be called a local evaluation similarly to evaluations in atmospheric optics [12].

Let us formulate an algorithm of the local evaluation. In the first stage, the studied points and directions $\mathbf{r},\hat{\mathbf{l}}$ in a scene are recorded. Then a light source is randomly selected and an arbitrary direction of the ray output from the source is determined. Source sampling with a probability proportional to its luminous flux, and the choice of direction according to the source of luminance distribution, or to the luminous intensity curve will be most effective. After this, the obtained ray is traced until crossing with an object. Further, for each of the studied points, the GIE nucleus is calculated and the statistics collected. After the statistics have been accumulated, averaged and normalised, we directly obtain luminance in the preset points along the preset directions. And in this method, a diffuse-directed reflection model can be used, for example, Phong's model [13].

For the first time, an algorithm similar to the local evaluations, was formulated in [14] as applied to visualisation in computer graphics within a phenomenological approach and was named *Instant Radiosity*. The absence of a strict mathematical argumentation for the computer graphics algorithm is not a disadvantage in most cases as the main ob-

jective of this is a "photorealistic" visualization but not exact luminance values. As to the light engineering component, the situation different: it is important here to have unbiased values of luminance for its analysis. The algorithm proposed in [14] was earlier considered in [11], and its mathematical argumentation is given in [1]. Fig. 1 shows an example of luminance distribution calculation in the *Cornell Boxes* master scene.

Thus, local evaluations allow simulating direct luminance in a preset point and along a preset direction.

Knowing luminance distribution at each point of the illumination scene, one can calculate any characteristic of the light field. Most interesting is the calculation of a value characterising illumination quality according to a preset level of visual work, and corresponding to the ideas of light design for scene illumination. Deriving such a criterion would allow computerising the optimisation of the lighting installation calculation. Even better if the program prompts a set of optimum illumination versions giving the designer a final choice of the light environment in the scene.

2. CRITERION OF ILLUMINATION QUALITY

The results of our research allow distinguishing between several factors influencing visual discomfort, and hence illumination quality as a whole:

- spatial-angular luminance distribution;
- visual adaptation;
- spectral composition of the light source radiation;
- exposition time.

It follows from the experiments that the first two factors have the most significant impact, whereas influence of the spectral composition of the light source radiation and of the exposition time require separate research.

There is no definition of illumination quality in the modern edition of the Dictionary of the International Illumination Commission. Therefore, we propose our own: *illumination can be considered high quality, if it increases visual working capacity of a person and does not interfere with compliting the tasks set within an illumination scene*.

Current quantitative illumination characteristics are as a rule normalised as one digit. In an ideal scenario, quality characteristics should be also normalised as separate digits.

An objective was set for this research project: to formulate illumination quality evaluation as one integral value for an arbitrary illumination scene with a known luminance distribution for each point in space in each direction.

Discomfort is influenced by the relation of the source luminance to the background luminance [6], i.e. by contrast. And there is a contrast threshold, after which a feeling of discomfort appears. In our opinion, it is exactly the relationship of the contrast to the threshold exactly can serve as a criterion of illumination quality. In the event of continuous a spatial-angular luminance distribution over the illumination scene, a natural contrast generalisation is the relation of the luminance distribution gradient over the observation field to an average luminance over the luminance field. With an increase of the gradient, a boundary between the glare source and the background becomes more circumscribed, and illumination quality decreases respectively. Further, it can be assumed that a change in luminance direction does not influence illumination quality, and therefore we take into consideration an absolute gradient value. Having selected a space point within the scene (room) and an observation direction, one can determine generalised contrast in the scene point:

$$K(x,y)=\frac{\left|\mathrm{grad}L(x,y)\right|}{\bar{L}},$$
$$\bar{L}=\frac{1}{A}\int_{(A)}L(x,y)p(x,y)dxdy,\ \ A=\int_{(A)}dxdy, \tag{3}$$

where x, y are co-ordinates of a point on the scene projection, L is luminance in the point of the observation direction, $\bar{L}$ is average luminance over the vision field, $p(x, y)$ is a weight function accounting for various contributions to the eye's reaction of the points located in the middle of the visual field and on the periphery, because the density of cones is greatest at the visual axis [7].

Coordinates x, y in a synthesised image are directly connected with the sighting direction $\hat{\mathbf{l}}$ for spatial-angular luminance distribution $L(\mathbf{r},\hat{\mathbf{l}})$ from when assigning a sighting point of the scene, or a specific point in light design, which is the same, as well as the camera focus of the scene visualization.

Fig. 2. Example of setting the weight coefficient *p* for different fields of view

In this regard, *A* can be interpreted as a visualisation frame area, or as solid angle of the camera's visual field.

The distribution of cones over the retina can be considered proportional to 1/θ2, where θ is the angle of sight [8]. Respectively, the added function *p* should be proportional to this value, or can be preset in a tabular way, for example as shown in Fig. 2.

As *Q*, the criterion of illumination quality, we use generalised contrast $K(x, y)$ weight-averaged over the field (equation):

$$Q = \frac{1}{AK_{thr}} \int K(x,y)\, p(x,y) dxdy, \qquad (4)$$

where K_{thr} is the threshold contrast value.

It should be noted that in most practical lighting tasks, we are concerned with illumination not of the whole scene but only of some of its parts. So in indoor illumination, operation surfaces illuminance is normalized, but not illuminance of passages. When illuminating a sports ground, primarily its playing field should be illuminated. Moreover, designers often form areas of accenting illumination to create some light rhythm in the illumination of the scene. Thus one more additional weight coefficient h ($0 \le h(x, y) \le 1$), should be introduced. This coefficient takes into consideration lighting tasks, and it is equal to 1 in the working area and to 0 for points insignificant for illumination quality. Selection of coefficient $h(x, y)$ values corresponds to algorithms of fuzzy logics [15]. An example of $h(x, y)$ coefficient set is briefly shown in Fig. 3.

Hence, expression for the quality criterion calculation will be as follows:

$$Q = \frac{1}{AK_{thr}} \int K(x,y)\, p(x,y) h(x,y) dxdy. \qquad (5)$$

The obtained expression can be used for the evaluation of illumination quality by one digit, if the evaluation is carried out by means of the software, when luminance distribution for all scene points is known in any direction.

It should be noted that the quality criterion undoubtedly needs an experimental calibration test, however in our opinion, there is no necessity of its ultraprecise determination: first, visual perception dispersion reaches scores of percents, and secondly, this criterion is only necessary for optimizing the choice of the illumination design model giving a final decision the light designer.

3. EXPERIMENTAL DETERMINATION OF DISCOMFORT LUMINANCE AT THE COMFORT – DISCOMFORT BOUNDARY

Illumination quality characteristics are directly connected with the observer determining feelings of comfort or discomfort. And the observer's evaluation is subjective and can change from one observer to another in a very wide range. It is commonly supposed that discomfort glare is an unpleasant sensation in case of non-uniform luminance distribution or high level luminance in the visual fild $L(\mathbf{r}, \hat{\mathbf{l}})$. The glare phenomenon makes difficult reading indications of devices. It degrades visibility of the observed objects and causes a premature fatigue of the visual analyzer. In this respect, the added criterion *Q* allows estimating illumination discomfort in a scene from a stable scenery spot but discomfort determination requires a study of K_{thr}. – characteristics of the human eyes threshold.

As part of this research, at the Light and Engineering Chair of the Moscow Power Institute NRU, a study was conducted to estimate the discomfort sensation caused by a glare source in the observer's field of vision. Luckiesh and Guth's experiment [3] from 1949 on finding a boundary value of the discomfort glare was used as a basis for this experiment,. During the experiment, dependences of this parameter on the main factors were revealed.

Within Luckiesh and Guth's experiment, an expanded visual field of uniform luminance was si-

Fig. 3. Example of determining the weight coefficient *h*, taking into account the lighting task

mulated using two-thirds of an 80-inch (2 m) photometric sphere with a lamp located near its centre to provide a uniform illuminance field. Light sources were located behind round openings in the sphere surface. These openings were provided for sources of a bright light. The observer was located on a chair, so that his head was exactly in the centre of the sphere.

An evaluation of the glare sensation was made at a short-term emergence of the source in the observer's field of vision under the condition of a uniform background luminance distribution. Background luminance was considered to be equal to adaptation luminance. The experiment included cycles of three one-second "switched on" periods with intervals equal to 1 between them with a subsequent five-second pause between the cycles. The observers themselves determined the number of experiment cycles sufficient for a luminance evaluation *in the visual field at the border between comfort and discomfort (BCD).*

In total, fifty observers took part in the experiment. They adjusted the initial luminance to determine their own BCD criterion.

In order to determine the discomfort glare boundary value and its dependences on the main factors, Luckiesh and Guth performed one more series of experiments. In this series, background luminance values (1, 10 and 100 foot lambert (1 foot lambert = 10.764 lx)), angular size of the light source (in an interval from 0.0001 to 0.126 sr), and light source position were changed (in an interval from 0 to 100° relative to the vision line along vertical, horizontal, and diagonal). Only ten observers participated in these experiments. The dependence of BCD luminance dependence, location and number of glare sources in the observer field of vision was also determined.

According to the results of the Luckiesh and Guth experiment, the BCD luminance value was equal to 3103 cd/m^2, if adaptation luminance was – 31.4cd/m^2, and the light source diameter was equal to 3.76 cm. The light source was placed on the observers' vision line at a distance of 1 m from the observer. Fig. 4 shows BCD luminance value distribution depending on the observer number.

With pressing concerns for energy saving and energy efficiency, light emitting diodes and lighting devices based on LEDs become the main sources of light. Light emitting diode (LED) illumination is applied everywhere, and discomfort from glare of small size light sources is a topical problem [4].

Besides, the small size and various optical characteristics of LEDs and LED matrices allow simulating glare light sources of any size and configuration using imitation of light spots on a desktop, or blinding headlights of an oncoming vehicle.

For more advanced and modern studies of BCD luminance, an experimental installation was developed at the Lighting Engineering Chair of the Mos-

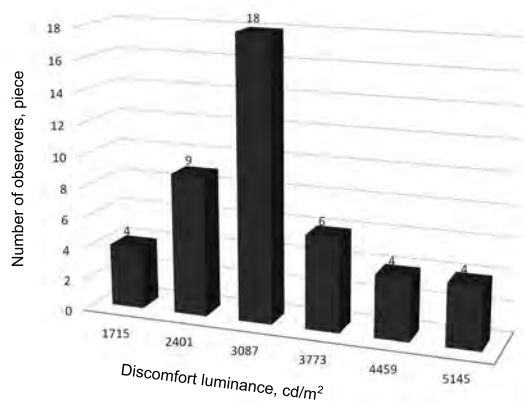

Fig, 4. Distribution of brightness values of the GCD ("standard BCD brightness").

Fig. 5. Experimental installation

cow Power Institute. As the base of the installation, a metal sheet painted with white powder paint was used. On this sheet, plates on which cards of LED's various location were mounted. At the sheet centre, a round card with three LEDs of 0.3 W was placed. Around them, larger rectangular cards imitating glare light sources were mounted. Chromatic temperature of the installed LEDs was equal to 5000 K. Switching on the cards in various modes was performed from a control unit, by means of which light source luminous fluxes could be adjusted. The experimental installation was located at a height of 0.75 m from the floor, so that the central card was at the observer's eyes level. The experimental installation is shown in Fig. 5.

In process of developing and improving the experimental technique, a need to instal an opaque cloth for a greater light diffusion was revealed. In order to change the chromaticity towards a lower chromatic temperature, the LEE Filters 204 full C.T *ORANGE* filter was installed. And to simulate one light source of 3.76 cm diameter, a diffusion light filter was applied. General illumination and respectively, background luminance indoors, was created using six controlled built-in LED luminaires. The installation was controlled by means of toggle-switches, and for each light source (composite or single-unit) its own switch was provided for. Calibration of the experimental installation was made using luminance metre *Konika Minolta LS-110*.

To develop the discomfort scale, five main Hopkinson's criteria were used [5]: noticeable, acceptable, uncomfortable, inconveniently and intolerable. In the process of training the sensation determination technique, it was revealed that the interpretation for the participants was unevident, and some criteria were determined as an interval of luminance values.

Therefore, after researching various scales, selection of optimum easily understood definitions of each criterion, together with carrying out visual work during the experiment, the following scale of discomfort was selected: hardly noticeable; indifferently; acceptable; uncomfortable; inconveniently; insufferably.

Luminance of the glare source was first adjusted by the protocol administrator, then by the participant using a built-in light controller. The experiment's results showed that when participants were adjusting luminance there was less data scattering in comparison with the adjustment made by the administrator.

As it is not possible to adjust general illumination in the classroom from 0 to 100 %, during the experiment background luminance (adaptation luminance) was equal to 75 cd/m^2. The observer was placed on a chair in front of the installation at a distance of 1 m from it. In total, 63 answers for each criterion were obtained. Looking at the experiment results, the discomfort luminance value of 3350 cd/m^2 was obtained, which was different from the value obtained by Luckiesh and Guth by 300 cd/m^2 upward.

Such a difference in BCD luminance values was obtained due to some engineering limitations, because of which it was impossible to reproduce completely the Luckiesh and Guth's experiment conditions in the experimental environment of the existing installation. The main reasons of the difference in results are as follows:

• Background luminance in the MEI installation was almost twice as high as that declared in the

Luckiesh and Guth's experiment: 75 and 34 cd/m^2 respectively;

• The assumed chromatic temperature of the thermal light sources used in the Luckiesh and Guth's experiment (2700–3000 K) considerably differs from chromatic temperature of the LEDs used in the MEI installation (5000 K);

• In Luckiesh and Guth's installation, one test light source was used, and in the MEI installation, light sources of different sizes were formed using single-unit LED of various arrangements.

Based on the performed experiment, we have managed to determine that radiation chromaticity influences the BCD luminance value. BCD luminance also depends on a number and configuration of glare light sources in the observer's field of vision. During the primary experiment, only three LEDs were merged into one (light source diameter = 3.76 cm) at high luminance values corresponding to painful ("intolerable") sensations, and when BCD luminance determining, they could not been perceived by the eye as a source equivalent to one light source of a bigger diameter.

After the experimental installation was upgraded in response to the results of the initial study, all BCD dependences qualitatively coincided with the Luckiesh and Guth's, which confirms that the developed technique was correct. In our opinion, a numerical coincidence cannot be achieved: as it follows from the description of measured results, to achieve this it would have been necessary to completely reproduce their installation, but there were no need to do this.

The original study carried out all measurements using an incandescent lamp, whereas this experiment used much more modern and current LED sources.

CONCLUSION

Through this research, a new integrated approach to the study and determination of a new illumination quality criterion is proposed, which is based on the spatial-angular luminance distribution. A transition from designing according to a preset illuminance distribution, to designing according to a preset quality is already an obvious trend. This transition has become possible due to the development of the computer facilities and mathematical methods of GIE simulation. As a result, it is impossible to formulate a new quality criterion without experimental research because of the lack of a physically appropriate model of luminance perception by the human eye.

As a result of this study, an algorithm of luminance spatial-angular distribution calculation was proposed and implemented, taking into account multiple specular reflections, which is essential when determining discomfort in an illumination scene. An experimental installation for studying discomfort was created and the experiments performed by Luckiesh and Guth were replicated.

The proposed approach for the formulation of a quality criterion based on an integral evaluation of spatial-angular luminance distribution is a good starting point to develop a program package of II design according to a preset illumination quality.

REFERENCES

1. Budak, V., Zheltov, V., Notfulin, R., Chembaev, V. Relation of Instant Radiosity Method with Local Estimations of Monte Carlo Method // WSCG. 2016, pp. 189–197.

2. Kajiya, J.T. The rendering equation // Computer Graphics (Proc. SIGGRAPH'86). 1986, V. 20, #. 4, pp. 143–150.

3. Luckiesh, M., Guth, S.K. Brightness in the visual field at borderline between comfort and discomfort // Illuminating Engineering. 1949, V.44, #. 11, pp. 650–670.

4. Wout Van Bommel, V. Lighting Tomorrow: What's Hot? // Light & Engineering, 2010, #2, V.18, pp.5–9.

5. Hopkinson, R.G. Evaluation of Glare // Illuminating Engineering. 1957.V. 52, #. 6, pp. 305–321.

6. Scheir, G.H., Hanselaer, P., Bracke, P., Deconinck, G., Ryckaert, W. Calculation of the Unified Glare Rating based on luminance maps for uniform and non-uniform light sources // Building and Environment. 2015, V.84, pp. 60–67.

7. Lombardo, M., Lombardo, G., Lomoriello, D.S., Ducoli, P., Stirpe, M., Serrao, S. Interocular symmetry of parafoveal photoreceptor cone density distribution // Retina. 2013, V. 33, #8, pp. 1640–1649.

8. Larson, G.W. et al. A visibility matching tone reproduction operator for high dynamic range scenes // IEEE Transactions on Visualization and Computer Graphics.1997, V.3, # 4, pp. 291–306.

9. Goral, C., Torrance, K.E., Greenberg, D.P., Battaile, B. Modeling the interaction of light between diffuse surfaces // Computer Graphics. 1984. V. 18, No. 3, pp. 213–222.

10. Christensen, N. J., Jensen, H. W. A Practical Guide to Global illumination and Photon Maps // Proc. SIGGRAPH, 2000.

11. Kalos, M.H. On the Estimation of Flux at a Point by Monte Carlo // Nuclear Science and Engineering. 1963, V.16, No.1, pp. 111–117.

12. Monte-Carlo method in atmospheric optics / Under the editorship of G.I. Marchuk. Novosibirsk: Nauka, 1976.

13. Phong Bui Tuong. Illumination for Computer Generated Pictures // CACM. 1975, Vol. 18, No. 6, pp. 311–317.

14. Keller, A. Instant radiosity // Proc. SIGGRAPH, 1997. P. 49–56.

15. Batyrshin I.Z. Main operations of fuzzy logic and their generalisations. Kazan: Otechestvo, 2001, 102 p.

Vladimir P. Budak,
Prof., Dr. of technical science, graduated from MPEI in 1981, Professor of Light and Engineering Chair in National and Research University “MPEI”

Victor S. Zheltov,
Ph.D., graduated from MPEI Light and Engineering Chair in 2005

Tatiyana V. Meshkova,
an ingineer, graduated from MPEI Light and Engineering Chair in 2010, post graduate at the same chair in National and Research University “MPEI”, Chief of the Project Department “NTS”

Renat Sh. Notfullin,
programmer, graduated from National and Research University “MPEI” Light and Engineering Chair in 2016

Light & Engineering
Vol. 25, No. 4, pp. 32-40, 2017

Svetotekhnika
No. 3, 2017, pp. 10–16

LED DRIVERS AND DISCHARGE LAMPS CONTROL GEARS: PRESENT STATE AND FUTURE DEVELOPMENT

Mikhail E. Klykov[1] and Tatyana A. Agafonova[2]

[1] «VNISI» Ltd, Moscow;
[2] «VINITI RAS», Moscow
E-mail: mikhail.klykov@mail.ru

ABSTRACT

A review of up-to-date LED drivers and discharge lamps control gears is presented. Opportunities for further development are characterised. Circuit solutions are classified, and examples of principal diagrams are provided.

Key words: control gears, drivers, discharge lamps, LEDs (light emitting diodes), light sources, electric current sources, voltage sources, regulation

1. DISCHARGE LAMPS CONTROL GEARS

Depending on components, the control gears for discharge lamps may be electromagnetic or electronic.

1.1. Electromagnetic control gears (ballasts)

The control gears combine chokes, transformers, and capacitors. The current here is close to sinusoidal and alternates at the power line frequency of 50 or 60 Hertz. Electromagnetic ballasts are simple, inexpensive, manufactured for decades, and hence are highly durable.

A unified diagram of the control gear is presented in Fig.1. It comprises a coil ballast L (to stabilize lamp current), compensating capacitor C (to compensate reactive power), and ignitor (starter for fluorescent lamps, pulse-igniter for high-pressure gas-discharge lamps (mercury, sodium, metal-halide, etc.).

Average data for ballasts of various lamp types are given in Tables 1–3 in [1].

Due to its simplicity, durability, and low cost, this wiring diagram has been used to operate discharge lamps in alternate current (AC) supply lines for more than sixty years. But over the last 10–15 years electronic ballasts have provided strong competition.

Electronic ballasts

Although they are simple, durable, and low cost, electromagnetic ballasts have some disadvantages: significant weight, dimensions, power losses, as well as limited functional abilities that do not allow a light source to fit optimally with its power supply, thus making some operating and switching modes impossible. As a result, discharge lamps flicker too much (since phosphor radiation and gas discharge have low inertia, the instant luminous flux closely follows the half sine wave of an instant power of a lamp at 50 Hz frequency). Furthermore, there are problems associated with eliminating audible noise and regulating lamp current. The sinusoidal current alternating at 50 Hz frequency provided by magnetic ballast is not optimal for obtaining high values of luminous efficiency and service time. The supply of a discharge lamp by a current with rectangular shape or of higher frequency (>20 KHz) provided by an electronic ballast almost completely eliminates output pulsation and increases lamp service time. In the case of fluorescent lamps,

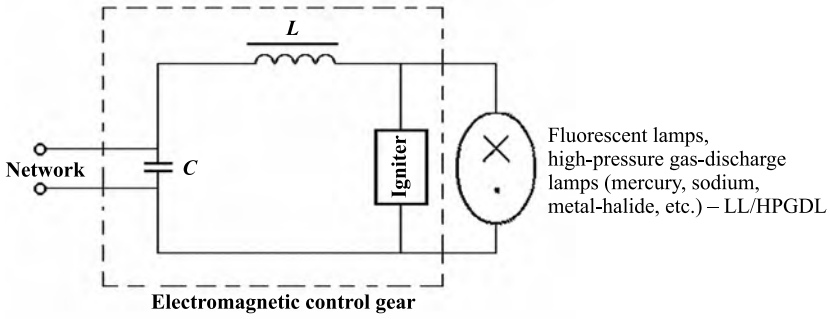

Fig. 1. Generalised scheme of electromagnetic control gears

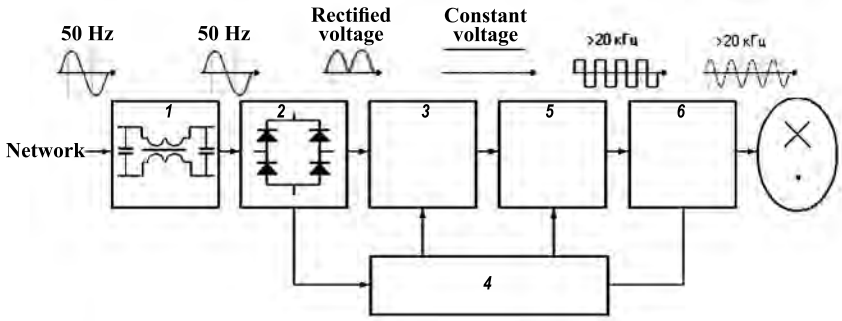

Fig. 2. Structural scheme of high-frequency electronic ballasts: 1 – radio-interference filter, 2 – rectifier, 3 – power factor corrector, 4 – control unit, 5 – inverter, 6 – output unit

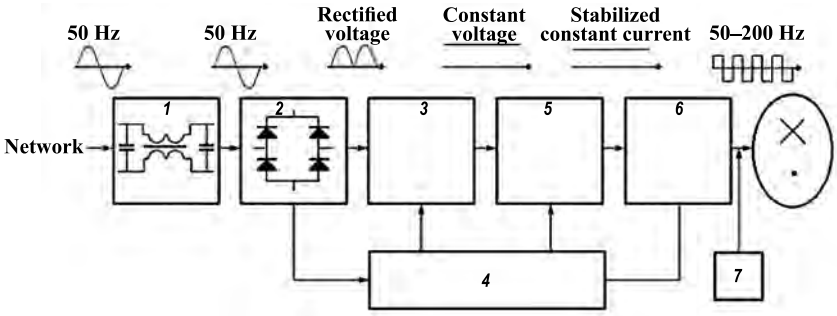

Fig. 3. Structural scheme of low-frequency gears with a rectangular shape of output voltage: 1 – radio-interference filter, 2 – rectifier, 3 – power factor corrector, 4 – control unit, 5 – current stabiliser, 6 – inverter, 7 – igniter

electronic ballast increases lamp output (efficiency) by 10–25 %.

Structural diagrams of electronic ballasts are provided in Figs. 2 and 3.

• The diagram in Fig.2 is designed mostly to feed the fluorescent lamps by high-frequency current (higher than 20 kHz). It is rarely used in HID circuits, because of the problems related to acoustic resonance. The scheme contains the following main parts.

Radio-interference filters (the Π-shape or double Π-shape filters consisting of chokes and capacitors) are used to suppress high-frequency noise made by electronic ballast in the mains;

Rectifier unit: this is used when the ballast operates with an AC power supply.

Power factor corrector: this is used in case of AC power supply. It provides the shape of an input current being close to sinusoidal, raises the power factor to nearly 1, and decreases harmonic distortions of input current. The active power factor correcting units, namely transistor pulse regulators based on voltage increasing or decreasing converters (Figs. 4a and 4b), are the most promising. Both schemes of correctors contain transistors *T*, diodes *VD*, chokes L, capacitors *C* and controlling integral chips (IMC) located in the control unit *4*. In addition to correcting power factor and shaping sinusoi-

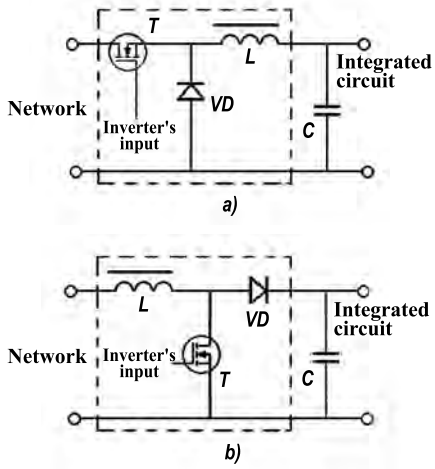

Fig. 4. Schemes of active power factor corrector based on decreasing (*a*) or increasing (*b*) pulse regulators

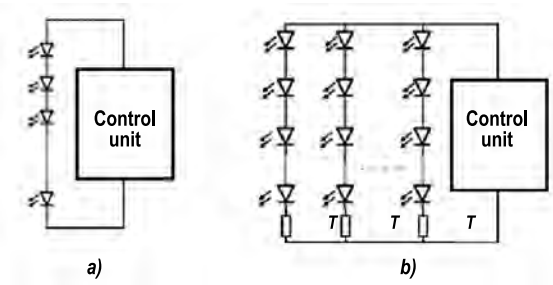

Fig. 5. Connections between LEDs and drivers

dal input current the above-mentioned schemes may stabilise and regulate a rectified line voltage.

Invertor: this is designed to invert constant voltage into alternate voltage with a frequency higher than 20 kHz (exceeding audible range). It comprises transistors **operating** in half-bridge or bridge circuits.

Control unit: usually comprises a chip that controls the transistors in both power factor corrector and inverter modes.

Output unit: adjusts output characteristics of an inverter with starting and operating characteristics of a discharge lamp. As a rule, the output unit comprises resonance LC-circuit where a choke is connected serially while a capacitor – in parallel with a lamp. In switching mode the scheme provides a start of a lamp, and in running mode – stabilisation of lamp current.

The wiring diagram shown in Fig.3 is commonly used in electronic ballasts for metal-halide and high-pressure sodium lamps. Acoustic resonance problem are overcome here by operating at frequencies "free" from that effect, namely at 50–200 Hz, that is at low frequencies. Besides, for linearisation of dynamic current-voltage characteristic of a discharge lamp a rectangular shape current is applied. In contrast to the high-frequency scheme (Fig.2) the low-frequency scheme (Fig.3) has an additional block – current stabilizer made by the scheme of a high-frequency pulse regulator, while the inverter serves to change polarity of lamp current periodically (at frequency of 50–200 Hz) so that electrodes could operate symmetrically and cataphoresis is prevented. In several cases the inverter performs the ignition function for a discharge lamp, hence a separate igniter is not required.

2. LED DRIVERS

Since the rated power of a single LED is low, light-emitting diodes are usually grouped and then

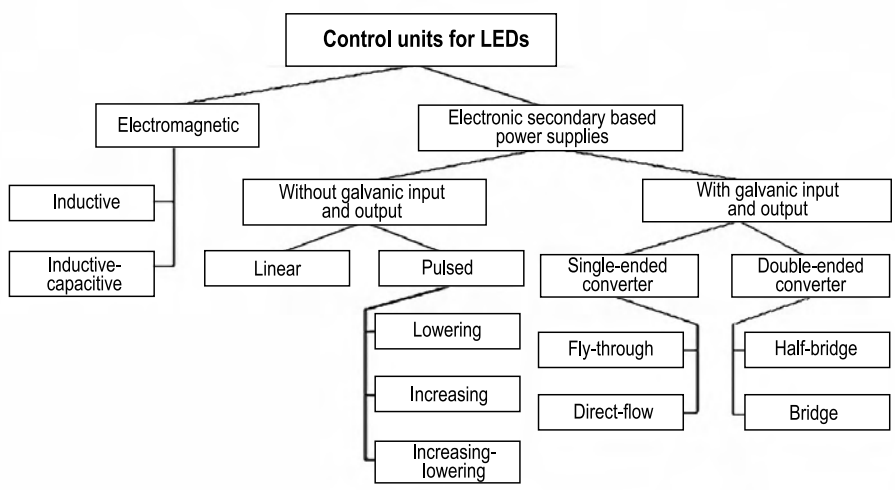

Fig. 6. Classification of LED drivers

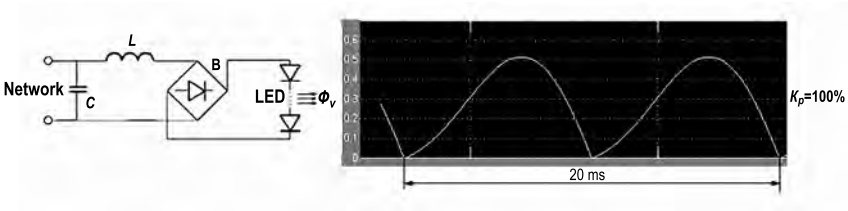

Fig. 7. Inductive scheme of connecting light-emitting diodes:
B – ballast, R – rectifier, C – compensating capacitor

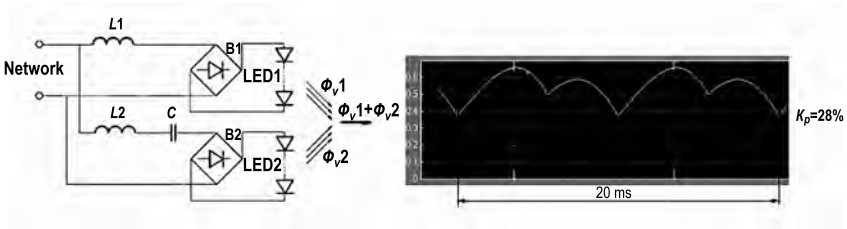

Fig. 8. Split phase scheme

connected to a driver. Options for connections are shown in Fig.5.

In the case shown in Fig.5a the LEDs are connected in series and a common current is running through them. A driver here shall have the features of a source of current. In specific cases, in order to eliminate extinction of a whole group when a single LED fails, the LEDs may be bypassed with relays (not shown in Figure) that complete the circuit when LED fails. For instance, *ON Semiconductor* active shunts may be used for this purpose [2].

In the case shown in Fig.5a several serial groups of LEDs are connected in parallel to the output of a driver. The driver here may be both the current source and the voltage source, but to balance current values in parallel circuits one shall use current limiting elements *T*. Up to 20 mA, resistors are being used for this purpose. Under higher currents it is reasonable to use linear current stabilizers (see below).

2.1. Classification of drivers

Classification of LED drivers is shown in Fig.6.

2.1.1. Electromagnetic drivers

In applications where luminous flux stability and flicker limitation are less of an issue, as well as the driver's weight, and where the major requirements are low price and high reliability – electromagnetic drivers may be used [3]. In addition to simplicity, low cost, reliability, and ability to operate under low temperatures (down to –60 °C) these drivers are environmentally friendly, since they can be totally recycled (remelted). In fact, electromagnetic drivers are just "the store of copper and steel placed at the ceiling", while electronic drivers end up as rubbish that cannot be recycled.

An additional advantage of electromagnetic drivers is their technological succession with respect to choke ballasts for discharge lamps which are underpinned by a developed manufacturing baseline.

Electromagnetic drivers are produced in two configurations – inductive (Fig.7) and inductive-capacitive with split phase (Fig.8).

Inductive scheme provides high power factor (>0,9), but at the same time – high flickering of luminous flux (flicker factor $K_п \approx 100$ %). To reduce pulsation, the split phase scheme is used, which operates two groups of LEDs (Fig.8).

It should be noted that the optimal performance for both schemes can be reached under m = 0.67, where m is the ratio between the voltage on the LEDs chain to the mains voltage. Under this condition the power transfer from the mains to the electric load reaches its maximum and output pulsation in the latter scheme is minimal (25–30 %), while the stability factor is at an acceptable level (1,5–1,75).

2.1.2. Electronic drivers

Electronic drivers are much more widely used in operating LEDs. In fact, they represent secondary power supply sources (in accordance with the

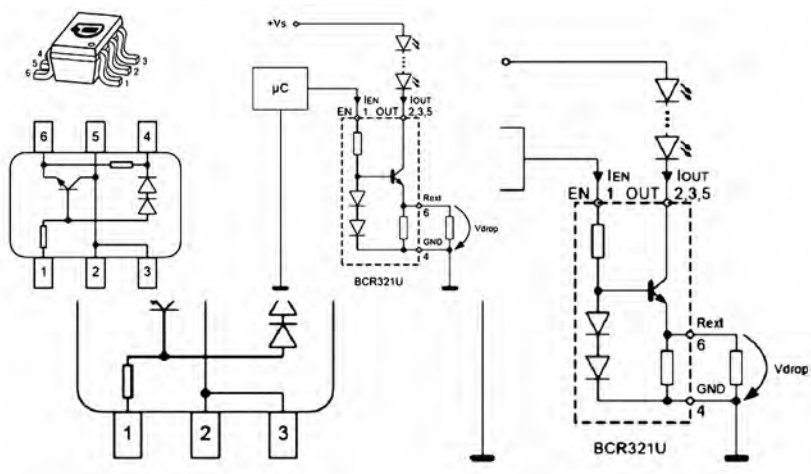

Fig. 9. Linear regulator *BCR321U*

definition accepted in converter engineering, this is a device designed to transform the electrical input of alternate or constant voltage into a power supply with requested features as an output) for operating such a specific load as LEDs.

Electronic drivers need to have functional capabilities that enable transforming power and provide optimal conditions to run and/or regulate LEDs, as well as to meet EMC (electro-magnetic compatibility) with the mains and other requirements of an end user.

Wiring diagrams of electronic drivers look very much like those for secondary power supply sources; in this way the design if the drivers reflects the achievements of contemporary converter engineering.

The most common wiring diagrams of LED electronic drivers are as follows (Fig.6).

2.1.2.1. Devices without galvanic isolation

Linear regulators are the simplest kind of electronic drivers that comprise only three elements: transistor, resistive sensor, and a source of threshold voltage. The transistor operates in an active mode and serves as a variable current-limiting resistor. It is reasonable to use linear regulators for current limiting elements *T* in LED circuits connected in parallel to the output of power supply source (Fig. 5, *b)*. In this case, in addition to aligning of current levels in parallel circuits, they play two more important roles: increase dynamic resistance of LED circuits (i.e. enabling a significant decrease in the requirements to the flickering of driver output voltage), and also make it possible to provide pulse-width regulation of a current in LEDs when a relevant digital input signal is applied. Such stabilisers are designed especially for LED circuits and manufactured in series.

For instance, *Infineon* company produces linear regulators under name of «*BCR*» for currents ranging from 10 mA to 2 A (with external transistor) and voltage up to 40 V. Fig. 9 shows the view of the product and its wiring diagram. The main features of this regulator are as follows: current – up to 250 mA, voltage – up to 24 V, maximal dissipating power – 1 W, housing SC74 *with* 6 pins, pulse-width regulation when a digital signal from outer controller is applied to the input *1*.

Pulse regulators are built on a single transistor key. They are cheap, compact, and used mainly in retrofit LED lamps with a screw base.

The scheme of the most widely spread product of that kind (operating as a decreasing regulator) is given in Fig. 10. The scheme comprises radio-interference filter, rectifier, passive diode-capacitor corrector of power factor, and pulse lowering power regulator. The latter is built on the base of highly efficient and not expensive pulse width modulation (PWM) controller *Supertex HV9910* (or *HV9961*), which is able to work under a voltage range from 8 V to 450 V. Brightness constancy of LEDs is provided by a stabilised output current either by its peak (*HV9910*) or average (*HV9961*) value. The direct output current has a saw tooth high-frequency flicker (20–100 kHz), the range of which is controlled by a choke *L2* and usually taken as 20–40 %. If required, the flickering can be reduced to several percent by connecting a capacitor in parallel to LEDs chain.

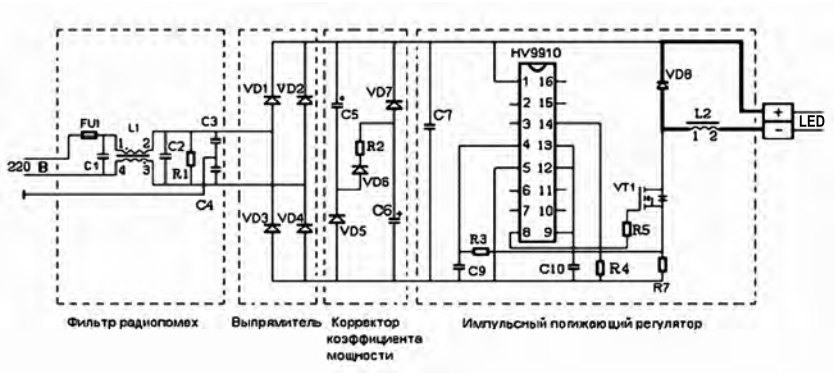

Fig. 10. Standard scheme of pulse decreasing regulators

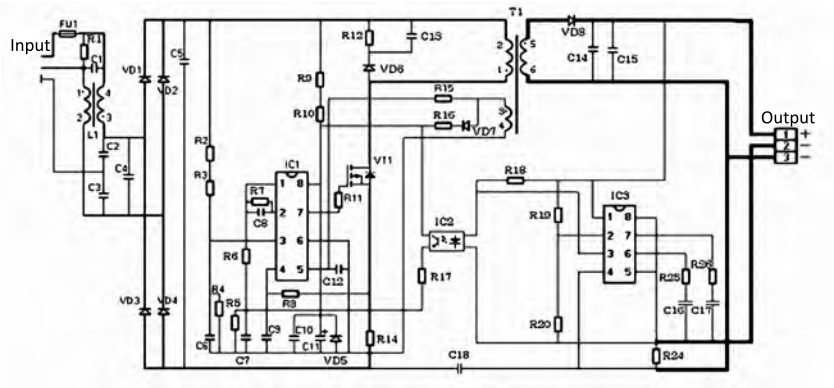

Fig. 11. Electronic ballast on reverse voltage converter

Other chips, e.g. *IRS2540* (*International Rectifier*), may be used as PWM controllers in that scheme. And active power factor corrector may be applied to provide a high power factor and a low value of harmonic distortion of a current consumed from the mains.

Electronic drivers based on pulse regulators are widely applied with a load up to several dozen Watts in condition that the galvanic separation between their input and output is not needed. In the opposite case, when galvanic separation is needed, other drivers are used, i.e. based on 1- or 2-stroke voltage converters (Fig.5).

2.1.2.2. Electronic drivers with galvanic separation between input and output

A distinctive feature of such drivers is the usage of transformers that provide galvanic separation between input and output.

One-stroke schemes are applied for powers up to 80W (*NXP Semiconductors* allows to use this kind of apparatus for powers up to 250W), and two-stroke schemes (half-bridge and bridge) shall be used for higher powers.

A device based on a reverse-stroke voltage converter, the scheme for which is shown in Fig.11 [4], is the most common product of this kind. Its scheme comprises radio interference filter, rectifier, and return-stroke voltage converter driven by a power factor controller *IC1.* This low cost 8-pin chip (*TDA4853* produced by *Infineon*) performs two important functions: first, it provides a high power factor and a low level of harmonic distortions of input current; second, depending on the type of feedback (either by voltage or load current), any output characteristic can be provided, thus a driver can be both a current source or voltage supply. To perform the second function, additional elements, i.e. current-voltage regulator *IC3* (*TLE4305 chip* produced by *Infineon)* and a decoupling optical transistor *IC2,* shall be introduced in the scheme. A signal proportional to input voltage is being delivered to the input of regulator *IC3* from a voltage divider *R19–R20*, while a signal proportional to output current is taken from a resistive current sensor *R24.* The device serves as a voltage stabilizer when a load is connected to its output terminals 1 and 3, and as a current stabiliser when connected to terminals 1 and 2.

Table 1. Power losses in ballasts for fluorescent lamps

Ballast class	Power losses, W, with lamp power		
	18 W	**36 W**	**58 W**
D	12	10	14
C	10	9	12
B2	8	7	9
B1	6	6	8

Table 2. HID ballasts parameters

Lamp power, W	Power losses, W	Power factor	Dimensions, mm			weight, kg
			L	***B***	***H***	
70	14,2	0,39	111	66	53	1,5
100	16	0,43				
150	19,5	0,42	133			2
250	28		135	85	70	3,15
400	29	0,5				3,18

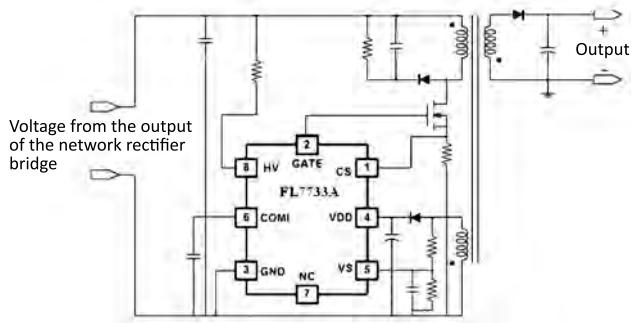

Fig. 12. One-stroke device scheme with regulation on the primary side

The device is attractive due to its relative simplicity and low cost, since it contains only one power switch *VT1* and one coil element *T1* (as well as the radio-interference filter coil) which performs a function of a cumulative throttle and transformer. Many other companies use the same scheme to produce drivers, only chips may differ. For instance, *Texas Instruments* applied *UCC28810* chip as a power factor controller, while *ST Microelectronics – L6562A/AT, ON Semiconductor – NCL30000,* and *NXP Semiconductors – SSL1750*.

The drivers of this group are being constantly improved. As an example, *Fairchild* company released controller *FL7733A* several years ago which manages operation of a reverse-stroke voltage to a converter by using feedback signal taken from the primary side of the scheme. The driver scheme became simple and low cost when previously used optrones, which transmitted information about current and voltage by taking signals from sensors on the secondary part of the scheme (Fig.12) [5] were rejected.

Direct-way devices are less common, since they have a degauss coil that makes a transformer more complex and, thus, more expensive.

There were numerous attempts to combine the direct and reverse schemes where during a direct move the power was transformed and released into the output circuit and during reverse move – the power accumulated in the transformer was released back into the same circuit. The corresponding wiring diagram (Fig.13) described in details in [6] was a result of such attempts. The diodes *8–9*, a choke *10* and capacitor *11* form the direct

Table 3. SON ballasts parameters

Lamp power, W	Power losses, W	Power factor	Dimensions, mm			weight, kg
			L	*B*	*H*	
70/50	14/9	0,39	111	66	53	1,5
100	16	0,43				
250	28	0,42	135	70	85	3,15
400	32	0,40	165			4,3
1000	55	0,43	196	105	90	10,0

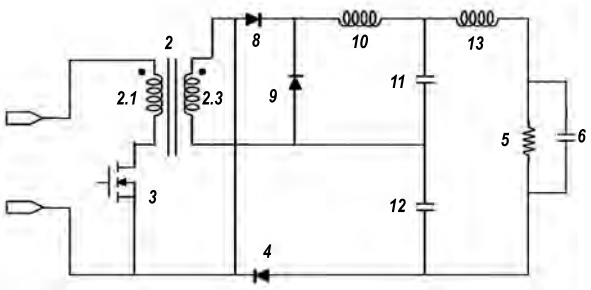

Fig. 13. Functional scheme of converter with a combination of direct and reverse circuits

scheme, while a diode *4* and capacitor *12* – the reverse scheme. Testing of this circuit showed that the voltage on transistor decreased by 1.3 times and heating of transformer – by (10–12) % in comparison with the scheme of the reverse converter.

Dealing with power greater than (80–100) W, the drivers shall be built by using the schemes of two-stroke voltage converters. For instance, the *Infineon* company implements the scheme in LED drivers for road luminaires with rated power exceeding 100 W. A scheme of such driver (Fig.14), [7] contains a radio interference filter *L*, rectifier *BR1*, half-bridge inverter based on transistors *MHS* and *MLS*. The latter brings into current and voltage agreement an isolating transformer T, an output rectifier, and a feedback block. Drivers of this kind are highly efficient and have practically no upper power limit.

3. FUTURE DEVELOPMENTS OF CONTROL GEARS AND DRIVERS

The future development of control gears and drivers totally depends on the market of light sources. The dynamics of the latter in Russia is given in Table 4 [8]. It shows that the production of discharge lamps will decrease by 10–100 times compared to 2013 levels in the nearest future, while production of LED products will increase 5–8 folds. That is why the new developments of electromagnetic and electronic ballasts for discharge lamps have been practically stopped. But since a lot of HID lamps (mainly, metal-halide and sodium) are still in use, the corresponding ballasts are in demand and will continue to be produced for a long time for such applications as road and horticulture lighting. A sufficient drop in production took place only in the following product groups: conventional ballasts for fluorescent lamps, integrated electronic ballasts for compact fluorescent lamps (retrofitted by LED lamps with screw base), and electromagnet-

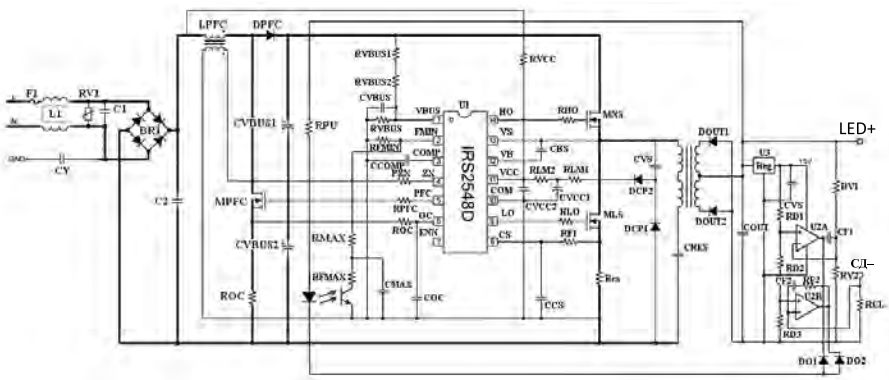

Fig. 14. Scheme of control unit based on two-stroke voltage converter

Table 4. Market trends for light sources in Russia (production and import), million pieces

Light source type	2013	2014	2015	2016	2017	2018	2019	2020
Fluorescent lamps	121	88,5	80	64	38	29(19)	22(10)	16(5)
Compact fluorescent lamps	124	106	58	37	18	4	3	2
High-pressure mercury lamps	9	6	2,5	1,5	0,5	0,3	0,2	0,1
High-pressure sodium lamps	2,4	2,2	1,4	1	0,8	0,6	0,4	0,2(0,1)
Metal-halide lamps	1,5	1,4	1	0,7	0,5	0,3	0,2	0,2
Light-emitting diodes	54	124	99	123	168	209(309)	240(375)	265(421)

Remark: values given in brackets are under discussion in the countries of the Eurasia economic union.

ic ballasts for high-pressure mercury lamps (HPL) replaced by sodium lamps (SON).

In contrast to ballasts for HID, the LED drivers are at the peak of development. The main directions of growth for these are as follows:

• New designs that correspond with the classification given in Fig.6;

• Use of new up-to-date components, namely, highly efficient semiconductor devices based on silicon carbide, gallium arsenide, etc.; special chips, planar high-frequency transformers and chokes, ceramic and film capacitors (instead of electrolytic);

• Since dynamic lighting systems are in great demand, the drivers shall be supported by wide range of analogue and digital interfaces in order to cooperate with lighting controls.

REFERENCES

1. Varfolomeev L.P. Elementary lighting technology. M.: Znak, 2008, 220 p.

2. Zvonarev E. NUD4700 – low cost solution for making LED luminaires more reliable // Electronics news, 2010, № 10, pp. 29–30.

3. Sergey A. Georgobiani, Leonid V. Gorev, Mikhail E. Klukov, and Elena A. Kovalenko

Electromagnetic Ballasts for Light Emitting Diodes// Light & Engineering Journal, 2013, V. 21, #4, pp. 81–87.

4. 40W LED. Street and Indoor Lighting Demonstration Board 2010, URL: http:// www.infineon.com (Date of the address 12.2016).

5. Design a High Power Factor Feedback Converter Using FL7733A for an LED Driver with Ultra-Wide Output Voltage, 2014. URL: https://www.fairchildsemi.com (Date of the address 12.2016).

6. Titkov C. New type of pulse converter // Modern lighting technology, 2016, № 4, pp. 16–18. URL: http://setilumen.ru/page62.html (Date of the address 12.2016).

7. Solomatin M., Avtushenkov K. Solutions of International Rectifier company for solid-state lighting // Modern lighting technology. 2013, № 5, pp. 58–64.

8. Gennady Ya. Vagin, Oleg Yu. Malafeev, and Mikhail V. Martynyuk Research into Light Sources Product Range, Assessment of Power Consumption and Electric Power Saving Potential in the Illumination Systems of Russia// Light & Engineering Journal, 2017, V.25, #1, pp.31–42.

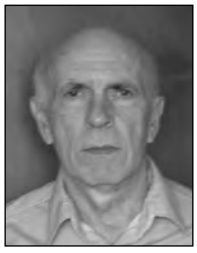

Mikhail E. Klykov,
Ph.D. He is graduated from Moscow Power Engineering Institute in 1963. At present, he is a leading specialist in VNISI Ltd. and involved in the study and designs of discharge lamps control gears and LED drivers

Tatyana A. Agafonova,
engineer, graduated from Moscow Power Engineering Institute in 1973. At present, she is a researcher in VINITI RAS and makes releases of abstract information on lighting technology and power converter devices

Light & Engineering
Vol. 25, No. 4, pp. 41-49, 2017

Svetotekhnika
No. 4, 2017, pp. 24–30

OPTOELECTRONIC COMMUNICATION IN THE ATMOSPHERE USING DIFFUSE LASER RADIATION: EXPERIMENTS IN THE FIELD

Vladimir N. Abramochkin, Vladimir V. Belov, Yury V. Gridnev, Andrei N. Kudryavtsev, Mikhail V. Tarasenkov, and Andrei V. Fedosov

The Institute of the Atmosphere Optics of V.E. Zuev of the Siberian Branch of the Russian Academy of Science, Tomsk
E-mail: belov@iao.ru

ABSTRACT

This article presents results of field experiments with bistatic optoelectronic communication systems (OECS) in the atmosphere using diffuse laser radiation. The work was performed in 2013–2016. The experiments were carried out in order to estimate communication quality (based on the control of probabilities and errors, as well as their root mean square deviations) and allow deriving the following conclusion: it is possible to create bistatic OECSs, which operate effectively in the atmosphere with hundreds of metres in UV and hundreds of kilometres in visible intervals of wave lengths, with orientation of the receiver axis both in a hemisphere containing the direction to the source and in a hemisphere containing the direction of propagation of non-diffused laser radiation.

Keywords: optoelectronic conmmunication, laser radiation scattering in atmosphere, time- pulse modulation, error probability

1. INTRODUCTION

The main questions associated with developing bistatic (over the horizon) optoelectronic communication systems (OECS) using diffuse laser radiation are discussed in [1] and a Monte-Carlo method choice was substantiated for the simulation of transmission characteristics of atmospheric bistatic channels. Published in the same journal in 2012, were a description of laboratory implementation of the experimental installation and an example of its test under real atmospheric conditions.

In 2013–2016, a series of field experiments was performed during the summer and autumn seasons to evaluate the possibility and quality of receiving information using bistatic optical communication channels under various atmospheric conditions and when changing the geometric parameters of the send-receive OECS circuit.

The work reproduces new and previous results of these studies performed at atmospheric routes in Tomskaya region.

2. EQUIPMENT, OPTICAL AND GEOMETRICAL CONDITIONS OF THE EXPERIMENTS

A flow chart of the bistatic OECS laboratory model, which is described in detail in [1], is given in Fig. 1.

Copper bromide vapour lasers [2] were used as a radiation source. They were developed in the IOA of the Siberian Branch of the Russian Academy of Science. They had the following characteristics: radiation wave length λ = 510.6 nm, pulse frequency repetition of (11–14) kHz, pulse duration Δt = 30 ns, average power P = (4–14) W, beam diameter on entering the atmosphere ∅ = 15 mm; radiation divergence Δv = 0.06 mrd.

The visual field angle of the receiving telescope was FOV = 2°. As a photodetector, a photoelectric multiplier (PEM) ФЭУ-84 was used. The op-

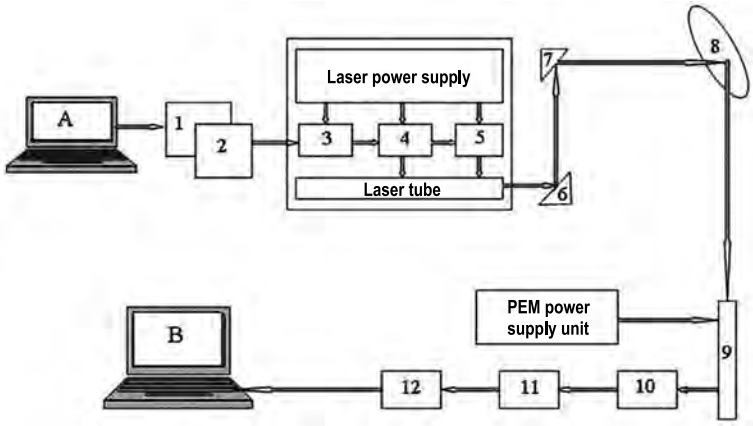

Fig. 1. A flow chart of the laboratory model of the communication system bistatic laser. Labels: A – "transmitting" computer, 1 – interface, 2 – data coding device, 3 – master generator of the laser, 4 – modulator, 5 – laser thyratron, 6 and 7 – alignment units, 8 – diffusing volume, surface, 9 – telescope + photoelectronic multiplier (PEM), 10 – signal amplifier, 11 – decoding device, 12 – interface, B – "receiving" computer

tical axis of the receiving telescope crossed the optical axis of the laser beam, and its inclination relative to the horizontal plane was set by α angle. The transmitting OECS was placed in the northern tower of the IOA building A at the height h_0 = 13 m from the ground surface, or 173 m above sea level. The direction of the laser beam axis was determined by altitude angle $5^o < \theta < 15^o$ and by azimuth angle – $10^o < \varphi +10^o$ in the horizontal plane from the direction to the receiving OECS. During experiments in 2013, the average power of the laser source was equal to 4 or 6 W, in 2016 it was equal to 8.5 or 14 W.

The laser beam passed (depending on the receiving optical system location) over the city of Tomsk and the Tom River (Fig. 2, direction 1), over Tomsk, Tom River and a suburb area (Fig. 2, direction 2), over Tomsk, Tom River and the town of Beryozkino (Fig. 2, direction 3), and over Tomsk, Tom River, forest areas, Ob River and fragments of the Ob swamp (Fig. 2, direction 4).

During the experiments, the time interval between the radiated laser pulse and clock pulse was measured. This modulation type of the radiation (pulse-time) exactly is used in the laboratory model of the bistatic OECS. During the experiments, by means of the Zond M active-and-pulse highly sensitive OECS [3] operating in a passive mode, the ray's diffuse trace in the atmosphere was recorded on video, selectively. Fig. 3 shows examples of these images.

A mobile OECS receiving office could be placed in any point accessible for vehicle transport. The first successful field experiments were made in 2013 when the OECS receiving office was placed at a distance of 9.9 km from the laser radiation source and the receiver height above sea level was 79 m. The main experiments were performed in 2013 when the receiving system was placed in a field behind the Tom River in the radiation direction 2 in Fig. 1. The source-receiver base was 8.77 km, the receiver height above sea level was 77 m. The maximum length of line sections from the source to the re-

Fig. 2. A scheme of laser ray directions to the points of placing the receiving OECS (green arrows) in 2013–2016

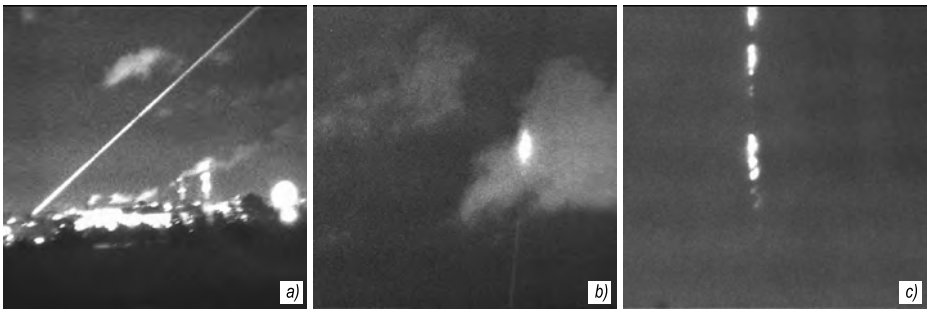

Fig. 3. Videos frames: (a) – of information laser ray diffused along a cloudless route in atmosphere, (b) – of diffused radiation passing a cloudy formation, and (c) – of radiation diffused on aerosol non-uniformities

ceiver through the intersection point of optical axes of the receiver and of the laser beam was 11 km (we name this distance the communication line length).

The experiments were made from August to October 2013 in a dark time under cloudy atmosphic conditions (separate cloud formations and solid cloud cover), as well as in a cloudless atmosphere and with precipitation. The information which was transmitted along the atmospheric bistatic channel for an evaluation of communication quality, was an image of graphic test signal in the form of a periodic triangular structure (without a horizontal leg).

Each experiment was carried out according to layout presented in (Fig. 4). One of two orientations of the transmitting laser beam with an altitude angle $\alpha \approx 5°$ and 15° was recorded at azimuth angle $\varphi \approx 0°$. The receiving telescope was oriented in the directions corresponding to the α angles (15–85)°. To control the communication operation, an additional transmitting laser beam orientation, corresponding to $\varphi \approx \pm 10°$, was carried out. Duration of each communication session at the stable experiment geometry depended on atmospheric conditions and was equal to between 7 and 30 min. Information (a graphic test signal) containing between 7,000 and 40,000 symbols was transmitted and registered in a computer. Each experiment lasted between one and three hours.

The control of the bistatic atmospheric communication channel under field conditions cannot be achieved completely. Therefore, to analyse the influence of weather and optical conditions on the quality of the OECS's work the following parameters were applied:

– Meteorological visibility range S_M, which was measured with an interval of 1 hour within the territory of the basic experimental complex of the IAO [4] located at a distance of 12 km from point S

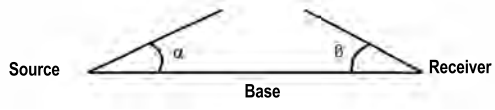

Fig. 4. Geometric experiment layout

(Fig. 2). The S_M measurement interval was limited from the top by S_M value equal to 30 km.

– Aerosol pressure, humidity and concentration (with particle size greater than 0.3 μ), which were measured on the TOP-station [5] placed at the High-rise station of the IAO (located at a distance of 400 m from the radiator of the bistatic OECS).

– Coefficient of atmosphic aerosol extinction β_{ext}^{a} at wavelength $\lambda = 0.5$ μ, which was determined along a horizontal route (coming from the building, where the OECS transmitting laser was placed) using the equipment and the technique described in [6–8].

3. RESULTS OF THE EXPERIMENTS

In order to estimate the quality of the communication, probability p and its root mean square deviation (RMSD) σ were used during communication sessions, when all geometrical parametres of the experiment setup were recorded. An algorithm of the real-time statistical characteristic calculation (i.e. at the time of carrying out the experiment) is described in detail [18].

It is clear from the information about the statistical characteristics of transmission quality that both atmospheric distortions, and changes of characteristics and send-receive optoelectronic units can be reasons for error, (for example, laser radiation power, photoelectronic multiplier (PEM) noise, etc.).

The error probability and error RMSD analysis has shown that some communication sessions have an ideal communication quality, i.e. $p = 0$ and $\sigma = 0$

Table 1. Selective values of communication error probabilities and their RMSD in the experiments of 10/1/2013.

Time	*P*	*σ*	Time	*P*	*σ*	Time	*P*	*σ*
8:35 p.m.	0.538	0.565	8:55 p.m.	0.053	0.065	9:08 p.m.	0.043	0.060
8:36 p.m.	0.277	0.308	8:56 p.m.	0.046	0.059	9:09 p.m.	0.035	0.069
8:37 p.m.	0.221	0.252	8:57 p.m.	0.054	0.065	9:11 p.m.	0.030	0.041
8:38 p.m.	0.143	0.163	8:58 p.m.	0.089	0.103	9:12 p.m.	0.041	0.054
8:39 p.m.	0.114	0.135	8:59 p.m.	0.103	0.120	9:13 p.m.	0.033	0.051
8:48 p.m.	0.043	0.061	9:02 p.m.	0.064	0.082	9:14 p.m.	0.026	0.035
8:49 p.m.	0.060	0.079	9:03 p.m.	0.055	0.063	9:15 p.m.	0.026	0.039
8:50 p.m.	0.068	0.086	9:04 p.m.	0.041	0.054	9:16 p.m.	0.029	0.043
8:51 p.m.	0.083	0.106	9:05 p.m.	0.039	0.060	9:17 p.m.	0.031	0.049
8:53 p.m.	0.069	0.081	9:06 p.m.	0.040	0.054	9:18 p.m.	0.030	0.047
8:54 p.m.	0.039	0.054	9:07 p.m.	0.035	0.046	9:20 p.m.	0.024	0.040

(for example, on September 4th), or close to it (for example, on September 11th). In other situations, *p* and σ values reached 0.8 and 0.9 respectively (for example, on September 29th).

To find out the reason for th variation in error probability *p,* aerosol concentration, transmittance coefficient, meteorological visibility range, temperature, humidity and atmospheric pressure were monitored.

The physical basis of bistatic communication is the diffusion effect, and both aerosol, and molecular components of atmosphere play their part. Therefore, we should first determine which of these processes affects communication quality more, or whether their influence is equal. With this end in sight, molecular diffusion coefficient β_{sct}^{m} values and aerosol diffusion β_{sct}^{a} values were compared. Aerosol scattering coefficients were determined using the *LOWTRAN-7* package [9], and molecular diffusion coefficients were calculated by the formulae given in [10] using the temperature and pressure data measured at the TOR-station [5].

It follows from this data comparison that aerosol diffusion coefficients considerably (almost by an order of magnitude) exceed molecular diffusion coefficients, i.e. one can assume that along cloudless routes, the aerosol component directly determines information transmission quality in bistatic OECS, at least, for a 510.6 nm wave length. The analysis has shown that there was no stable correlated relationship between error probabilitiy values and optical and meteorological atmospheric characteristics near the transmitting OECS.

As already mentioned, other sources of error in information transmission via atmospheric communication channels can be parameter change in the equipment of separate units. With the selected method of information modulation (pulse-time), the quality of information received is primarily influenced by the laser radiation power *P,* which in the experiments was changed within an interval of 4–6 W. When reducing *P*, we can expect a deterioration in communication quality, i.e. increase of error probability *p*. This is confirmed, for example, by a comparison of *p* values obtained diring experiments performed on September 16th (P = 6 W) and on September 25th, 2013 (P = 2 W). In these experiments, *p* equalled 0.01 and 0.572 respectively, air temperature was + 14.7 °C on September 25th, and – 4.3 °C on September 16th, meteorological visibility range S_M on September 16th and 25th exceeded 30 and 7 km respectively, and aerosol extinction coefficient β_{ext}^{a} restored from the 9 p.m. measurements was equal to 0.102 km^{-1} on September 16th and to 0.260 km^{-1} on September 25th.

Therefore, before specifying the main reason of the abrupt change in *p* errors (temperature, laser radiation power, or aerosol extinction), we will consider the influence of PEM temperature on the communication quality.

The results are presented in Table 1, where *p* and σ values are given depending on the time of the

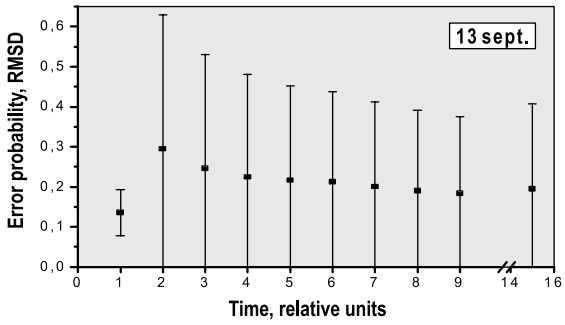

Fig. 5. Error probabilities and their root mean square deviations (RMSD) in the experiments of September 13th, 2016

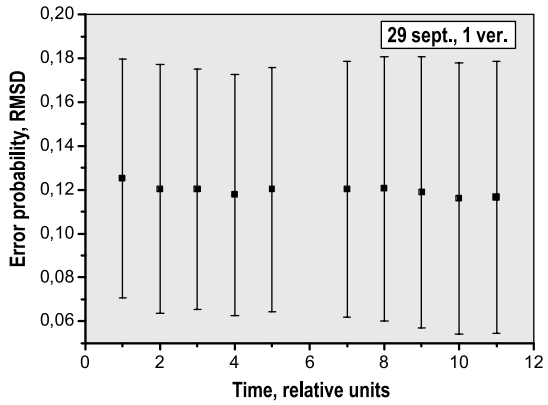

Fig. 6. Error probabilities and their RMSD in the experiments of September 29th, 2016

communication sessions in 2013. The first session was held without PEM forced cooling (beginning of the session was at 8:35 p.m.), and PEM temperature *T* corresponded to the ambient temperature, i.e. *T* = + 6.7 °C. The second and the next sessions were held with a switched-on cooling installation, which gradually cooled the PEM to a temperature of – 17C° over 30 minutes. As it can be seen, PEM temperature significantly influences the communication quality, and its change from + 6.7 °C to –17 °C leads to a reduction in communication errors by almost by an order of magnitude. This result confirms the known result of the influence of temperature conditions on PEM operation quality [11].

The first series of experiments in 2016 was performed at a laser source average power of 8.5 W and with the location of the receiving telescope near Berezkino settlement at a distance of 26 km from the laser radiation source (Fig. 2, direction 3, communication line length was equal to 26.12 km). The experiments were carried out under a cloudless firmament (along the laser beam propagation line). The angle of altitude of the telescope optical axis and altitude angle of the laser radiation axis were $\alpha \approx 5°$ and $\beta \approx 10°$ respectively. Fig. 5 shows an example of the real-time result evaluation of error probabilities *p* and σ in this experimental series.

On September 29th, 2016, an optoelectronic communication over the horizon, with diffuse laser radiation from 69.5 km and the length of the communication line at 69.83 km was carried out. The averaged power of the laser radiation source was 14 W. The receiver was placed in close proximity from the Tomsk-Novosibirsk road between Nashchekovo and Desyatovo settlements (Fig. 2, direction 4). The receiver captured the radiation, which was distributed over Tomsk, Tom River, Ob River, Ob swamp and forest area between the swamp and the road. The angles of altitude of the receiver optical axis and radiation axis were $\alpha \approx 10°$ and $\beta \approx 7°$ respectively.

In Fig. 6, results probability error evaluations and their RMSD for this experiment are given. The absence of results for the 5–7 time intervals in Fig. 6 is due to the fact that at this exact time interval a vehicle convoy drove the road with brigh headlamps, which diffused the radiation (there were no cutoff filters) and was registered by the PEM.

External limiting factors, such as the OECS's applicability area are noises connected with natural and artificial radiation sources in this wave length interval. Therefore, their use along atmospheric routes can be especially difficult in day time, or in night time if used close to intensive artificial sources (see Fig. 6, time interval 5–7).

This problem can be solved or rendered less significant, with the use of UV interval wave lengths lasers and, primarily, solar-blind wave length interval lasers as OECS radiation sources. This is evident from a growing body of theoretical research [12–15], which has expanded during the last decade.

In the experiments of 2016, a hardware implementation of the bistatic OECS was used as the baseline, which was tested in the visible wave lengths interval and was described in detail in [16–18]. A stationary copper bromide laser (wave length λ = 510.6 nm, of 10 W average power) was used as the primary source, the radiation of which was transformed to the radiation with wave lengths of λ= 255.3; 272.1 and 289.1 nm. A nonlinear transformation based on a *BBO* (BaB_2O_4) optical crystal was used. In the experiments considered below, radiation with wavelength 289.1 nm was used (0.3 W average power, 14 kHz frequency repetition pulses, 30 ns pulse duration). The beam cross section at the point of entry to the atmosphere was a square

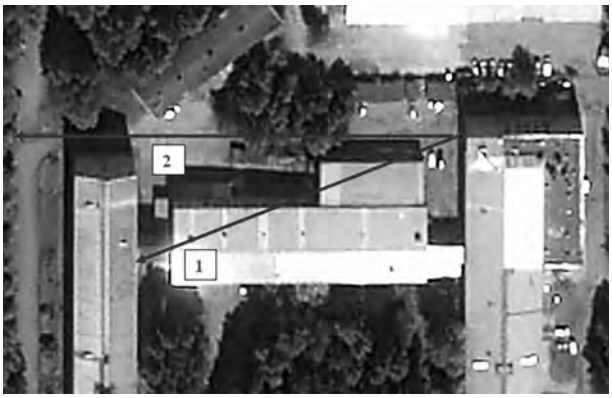

Fig. 7. A satellite picture of IAO cases of the Siberian Branch of the Russian Academy of Science and directions of radiation of a stationary laser UV source (arrow 1, 2)

of 2 mm side with full angular divergence by the sides equal to 2.5°. This wave length was selected based on the analysis of diffusing and absorbing atmosphere properties in the bottom layer. The receiving optical system was assembled using a refractor telescope scheme. Some its characteristics are as follows: the diameter of the light lens is 94 mm, the glass material is quartz glass КУ-1, uniformity class is 1, and focal length is equal to 300 mm. The field of vision of the receiving system is 2°. As a converter of optical radiation into the electric signal, PEM PhEM 142 was used. The experiments were made along routes 1 and 2, represented by a satellite photo of the IAO buildings given in Fig. 7. A stationary laser source was placed on the third floor of building A – north tower of the Institute (on the right in Fig. 7). In the first series of experiments, radiation was directed towards a receiver placed in the main building of the Institute (direction 1 in Fig. 8). Arrows 1 and 2 in Fig. 7 are horizontal plane projections of optical axes of the laser beams used in the experiments.

Fig. 8 shows geometrical schemes of three series of these experiments (side view). A receiving telescope was placed in a room on the second floor of the IAO building and was directed to the radiation source. The radiation was directed sequentially to points 1, 2 and 3. Point 1 corresponded to **n1** direction vector and was at a distance of 3 m over the receiver. The **n2** and **n3** direction vectors corresponded to points 2 and 3, and they were located at a distance of 4 and 8 m from point 1 respectively. This geometry excluded entering a non-diffused radiation into the lens of the receiving telescope. The length of the communication lines was equal to 96.2; 96.26 and 96.5 m.

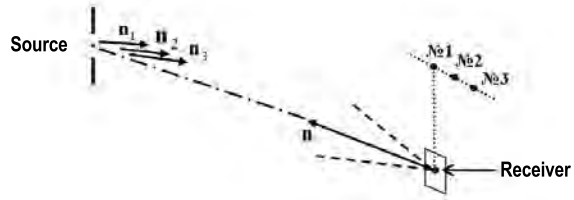

Fig. 8. Geometric diagrams of the first experiments

The second series of experiments was performed, where the laser radiation was directed into free atmosphere over the IAO main building at an angle of 2° to the horizon. The receiving telescope was placed on a site behind the main Institute building under ray 2 in Fig. 7. The receiver's optical axis was directed at angles between 15° to 110° to the horizon relative the source direction. The length of communication lines in these experiments was changed from 100 to 108 m.

In Fig. 9 as an example of error probabilities and their RMSD dependencies on the experiment series number are given. The experiments were performed on May 20th, 2016 according to the diagram in Fig. 8 for points 1 and 3. The squares and triangles designate the error probabilities, and horizontal intervals of different size designate upper and lower RMSD boundaries for points 1 and 2 respectively.

Probabilities and their RMSD corresponding to point 2 in Fig. 8 for all experimental series are between the values for points 1 and 3. It follows from a comparison of these results that the communication quality decreases with increasing communication line length (a sequential transition from point 1 to point 3). This conclusion is rather obvious, if we take into account that during the two hours, when the experiments were performed, optical conditions in near the ground atmosphere according to the TOR-station [5] did not change significantly.

Levels of communication error probabilities obtained in the experiments and their RMSD for the laser radiation propagation direction 2 in Fig. 7 are presented in Fig. 10. To illustrate the results obtained in these experiments, two situations were selected: (a): optical axis of the receiving system is directed to the hemisphere of directions from the source at an angle of 45° to the horizon, and (b): this axis is oriented into the hemisphere of directions from the source at an angle of 135° to the horizon. In Fig. 10, along the abscissa axis, relative time corresponding to the experiment series number for situations (a) and (b) is given.

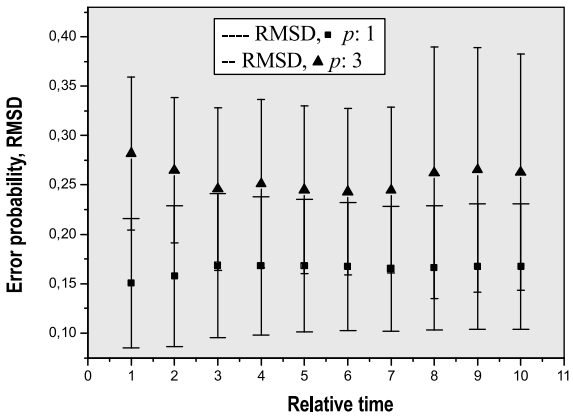

Fig. 9. An example of the estimated results of communication quality in the experiments according to the Fig. 8 diagram for points 1 and 3

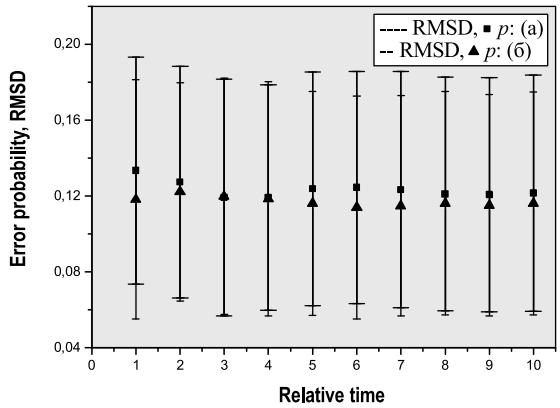

Fig. 10. An example of the evaluation results output of communication quality in the experiments for the laser radiation direction 2 in Fig. 7

The following conclusions can be drawn from the error probabilities and their RMSD comparison in Fig. 9 and 10. The values of these parameters in situations (a) and (b) are rather close. This can be explained by the fact that the prevailing radiation diffusion source at a wavelength of λ = 289.1 nm is molecular but not an aerosol atmosphere component, for which the diffusing indicatrix is symmetric relative to the directions of the front and to the back hemispheres. This leads to the fact that when the geometrical parameters of the communication lines correspond to situations (a) and (b), the fluxes diffused by air molecules become comparable.

A possible reason of this could be the fact that the experiments performed for series (b) were conducted 1.5 h later. All experiments were undertaken between 9 and 11 pm local time. We can assume that aerosol concentration decreased during this time, and since the moment of carrying out the experiment series for situation (a), it remained almost constant, and this is confirmed by the TOR-station data [5]. Therefore, error probabilities value variations as well and their RMSD in Fig. 10 (curve b) are somewhat lower. In particular, probability p variations in situation (a) did not exceed 0.014141, RMSD module – 0.01829, and in situation (b) p variations did not exceed 0.008889, RMSD module – 0.005541.

It is interesting to compare the quality of communication in visible and UV wavelength intervals. For this purpose we refer to [16], where examples of the evaluating error probabilities and their RMSD are given. These data were obtained in field experiments using a laboratory model of the bistatic OECS with diffuse laser radiation in the visible wavelength interval (λ = 510.6 nm) at communication line length of more than 10 km. This comparison shows that communication quality in the visible interval is significantly higher than in the UV interval. It would seem that the UV interval is preferable for high-quality communications, because solar radiation noise in this case is significantly lower.

However, if we remember that the experiments were conducted in twilight time and that the visible interval laser radiation power was higher than the UV interval power by more than 15 times, and that various PEMs were applied, then the comparison results are practically assured.

4. CONCLUSIONS

The field experiments conducted in 2013–2016 in order to evaluate the possibility and quality of information transmission along bistatic OECS using a diffuse laser radiation, allow formulating the following general and particular conclusions.

1. A high-quality bistatic optoelectronic communication in the visible wavelength interval can be implemented under both cloudy and cloudless atmospheric conditions.

2. In the case of a a cloudy sky, the communication can be accomplished via intromission and diffusion areas of laser radiation on the lower boundary of the solid cloud cover, or on the bottom and a side boundary of individual clouds.

3. Statistical characteristics of the quality if information transimission using bistatic atmospheric channels (error probabilities and their root mean square deviations) depend on laser radiation pow-

er (decreasing in proportion with its growth) and on PEM sensitivity. Cooling of the PEM (ФЭУ 84) used in the experiments from + 6.7 to – 17 °C led to a reduction of error probability almost by an order of magnitude.

4. An analysis of the influence of the optical and meteorological state of the atmosphere on statistical characteristics of communication quality at a wave length of 510.6 nm has showed that in the case of bistatic communication, when laser ray interception is accomplished by the receiving system in the surface layer of the atmosphere, it is determined by radiation diffusion, which generally depends on atmospheric aerosol concentration and on the fact that a maximum base, with which a stable communication with error probability at a level of 0.1, can exceed 70 km.

5. To exclude or reduce the influence of hardware failure during operation of an over the horizon OECS, field experiment carrying out conditions should provide for a guaranteed power stability of the radiation transmitter and constant temperature of the PEM.

6. The field experiments affirmed the possibility of developing and operating at a high level of quality bistatic multiple-address OECS in UV wavelength interval with an operating range exceeding hundreds of metres.

7. At basic distances up to hundreds of metres and more, optoelectronic UV interval communication is possible both with the receiving system optical axis orientation in the direction to the source of horizon angles at more than 10°, and in the direction from the source to the receiving system optical axis tilt angles to the horizon up to 30–40°.

8. The results presented by this research require a further replication and correction as part of subsequent pilot and theoretical studies in order to determine the main influences on communication quality and long-range operation areas of bistatic OECS according to their optical and geometric characteristics and parameters of their implementation versions.

The authors are grateful to Belov D.V. for participation in the experiments, as well as for the PEM cooling solution and to Protasova V.P. for engineer processing of the work.

REFERENCES

1. Belov V.V., Tarasenkov M.V., Abramochkin V.N., Ivanov V.V., Fedosov A.V., Troitsky V.O., Shiyanov D.V. Atmospheric bistatic communication channels with diffusion. Part 1. Study methods // Optics of atmosphere and ocean, 2013, V. 26, #4, pp. 261–267.

2. Dimaki B.A., Sukhanov V.B., Troitsky V.O., Filonov A.G., Shestakov D. Yu. A copper bromide laser with computer control of pulse-periodic, train and standby modes // Experiment devices and methods, 2008, #6, pp. 119–122.

3. Belov V.V., Matviyenko G.G., Pak R. Yu., Shiyanov D.V., Kirpichenko R. Yu., Kuryachy M.I., Pustynsky I.N., Shurygin Yu.A. Active TV systems of vision with selection of diffusion backgrounds // Sensors and systems, 2012, #3, pp. 25–30.

4. Zuev V.E., Belan B.D., Zadde G.O. Optical weather. Novosibirsk: Nauka publishing house of the Siberian Branch of the Russian Academy of Science. 1990. 192 p.

5. Arshinov M. Yu., Belan B.D., Davydov D.K., Ivlev G.A., Kozlov A.V., Pestunov D.A., Pokrovsky E.V., Tolmachev G.N., Fofonov A.V. Posts for monitoring greenhouse gases and for gases oxidising atmosphere // Optics of atmosphere and ocean, 2007, V. 20, #1, pp. 53–61.

6. Pkhalagov Yu. A., Uzhegov V.N. A statistical method of separating general extenuation coefficients of IR radiation into components // Optics of atmosphere and ocean, 1988, V. 1, #10, pp. 3–11.

7. Pkhalagov Yu. A., Uzhegov V.N., Shchelkanov N.N. A computer-aided multiwave measuring instrument of spectral transparency of ground atmosphere // Optics of atmosphere and ocean, 1992, V. 5, #6, pp. 667–671.

8. Uzhegov V.N., Rostov A.P., Pkhalagov Yu. A. A computer-aided route photometer // Optics of atmosphere and ocean, 2013, V. 26, #7, pp. 590–594.

9. Kneizys, F.X., Shettle, E.P., Anderson, G.P., Abreu, L.W., Chetwynd, J.H., Selby, J.E.A., Clough, S.A., Gallery, W.O. User Guide to LOWTRAN-7. – AR-GL-TR-86–0177. ERP 1010. Hansom AFB. MA 01731.

10. Bucholtz, A. Rayleigh-scattering calculations for the terrestrial atmosphere // Applied Optics, 1995, V. 34, # 15, pp. 2765–2773.

11. Soboleva N.A., Melamid A.E. Photoelectronic devices. Moscow: Vysshaya shkola, 1974. 376 p.

12. Pozhidayev V.N. Feasibility of the ultra-violet interval communication lines based on the effect of molecular and aerosol diffusion in atmosphere // Radio and the electronic engineering, 1977, V. 22, #10, pp. 2190–2192.

13. Ding, H., Chen, G., Majumdar, A.K., Sadler, B.M., Xu, Z. Modeling of non-line-of-sight ultraviolet scattering channels for communication // IEEE journal on selected areas in communications, 2009, V. 27, # 9, pp. 1535–1544.

14. Han, D., Fan, X., Zhang, K., Zhu, R. Research on multiple-scattering channel with Monte Carlo model in UV atmosphere communication // Applied optics, 2013, V. 52, #22, pp. 5516–5522.

15. Xiao, H., Zuo, Y., Wu, J., Li, Y., Lin, J. Non-line-of-sight ultraviolet single-scatter propagation model in

random turbulent medium // Optics letters, 2013, V. 38, # 17, pp. 3366–3369.

16. Belov V.V., Tarasenkov M.V., Abramochkin V.N., Ivanov V.V., Fedosov A.V., Gridnev Yu. V., Troitsky V.O., Dimaki V.A. Atmospheric bistatic communication channels with diffusion. Part 2. Field experiments of 2013// Optics of atmosphere and ocean, 2014, V. 27, #8, pp. 659–664.

17. Belov, V.V., Tarasenkov, M.V., Abramochkin, V.N. Bistatic Atmospheric Optoelectronic Communication Systems (Field Experiments) // Technical Physics Letters, 2014, V.40, #. 10, pp. 871–874.

18. Belov, V.V., Tarasenkov, M.V., Abramochkin, V.N., Troitskii, V.O. Over-the-horizon Optoelectronic Communication Systems // Russian Physics Journal, 2014, V. 57, #. 7, pp. 202–208.

Vladimir N. Abramochkin, Ph.D. Graduated from the Military and Air Engineering Academy of N.E Zhukovsky (1992). At present, he is senior research associate of the Institute of Optics of Atmosphere of V.E. Zuev of the Siberian Branch of the Russian Academy of Science, Tomsk. Field of scientific interest: optoelectronic communication

Vladimir V. Belov, Doctor, professor, an honoured scienctist of the Russian Federation, graduated from the Tomsk State University (1971). At present, he is a Head of the ROS laboratory of the Institute of Optics of Atmosphere of V.E. Zuev of the Siberian Branch of the Russian Academy of Science, Tomsk. Fields of scientific interest include: theory of optical radiation transport in diffusion and absorbtion environments, theory of laser probing, theory of vision, atmospheric correction of aerospace images of the Earth's surface, Monte-Carlo method and multiple diffusion

Yury V. Gridnev, graduated from the Tomsk Polytechnical University (1981). A fellow of the Institute of Optics of Atmosphere of V.E. Zuev of the Siberian Branch of the Russian Academy of Science, Tomsk. Scientific field of interest: system programming

Andrei N. Kudryavtsev, graduated from the Tomsk University of Radio Electronics and Control (2003), a leading electronics engineer of the Institute of Optics of Atmosphere of V.E. Zuev of the Siberian Branch of the Russian Academy of Science, Tomsk. Fields of scientific interest: measuring instruments of laser power, laser time strobing devices, electronic circuits, field programmable gate arrays, microcontrollers, sodars

Mikhail V. Tarasenkov, Ph.D. Graduated from the Tomsk Sate University (2007), a senior research associate of the Institute of Optics of Atmosphere of V.E. Zuev of the Siberian Branch of the Russian Academy of Science, Tomsk. Fields of scientific interest: analysis of principles of forming images via atmosphere, atmospheric correction of images in visible and UV intervals, theoretical study of communication channels out of direct visibility

Andrei V. Fedosov, graduated from the Radio assembly school, a technician of the Institute of Optics of Atmosphere of V.E. Zuev of the Siberian Branch of the Russian Academy of Science, Tomsk. His field of scientific interest is electronics

Light & Engineering
Vol. 25, No. 4, pp. 50-56, 2017

Svetotekhnika
No. 6, 2017, pp.45–49

AUTONOMOUS PHOTOVOLTAIC LIGHT-SIGNAL UNITS WITH BATTERIES: DEVELOPMENT AND FIELD TEST RESULTS IN THE MOSCOW REGION

Alexei B. Tarasenko and Oleg S. Popel

Joint Institute for High Temperatures, Russian Academy of Sciences
E-mail: o_popel@mail.ru

ABSTRACT

Photovoltaic systems are widely used for autonomous power supply in different branches of industry. In many countries, they are applied mostly for road, park and yard lighting and for signal lighting (road sign, traffic light). Some aspects of autonomous photovoltaic power application, concerned with the application of different types of battery are investigated under conditions typical for the Moscow region. Lithium-ion batteries are increasing storage capacity technology for different niches, including stationary, portable and electric transport. Lead-acid batteries are the traditional solution for back-up power and photovoltaic systems.

The storage unit usually has a significant influence on photovoltaic system costs and operational parameters. The possibility of decreasing capital costs and increasing the life cycle of photovoltaic autonomous systems due to lithium iron phosphate-based batteries is presented in this study.

Keywords: photovoltaic system, autonomous power supply, solar power units, lithium-ion battery

1. INTRODUCTION

Rapid development in renewable energy technologies [1] and primarily photovoltaic technologies has ensured the wide application of autonomous solar power units, usually with electrochemical battery energy storage, for light and road traffic control applications. One can see such power units on many roads all over the world. Many companies introduced into the market different versions of such power units and their components. In different regions of Russia, an interest in such solar power applications can be observed. For example in Moscow, several thousands of solar-powered signal-light units have been mounted on pedestrian crossings [2].

A typical solar-powered signal-light unit includes a photovoltaic module, a charge controller, a lead-acid battery (gel or absorbed glass mat type) and light emission diode backlight [3]. Cheapest samples use pulse-width modulation charge controller without maximum power point tracking. Sometimes a small wind turbine is also included as a part of the system [4]. The widest application such units has been seen in China and Germany. Due to their low cost, Chinese systems are actively spreading all over the world. Considering their construction features, all power units can be divided into two types: the first is the block-type, where the photovoltaic module covers the top part of the container and the light-diode unit is situated on its lower part. A charge controller and battery are placed inside the container, which itself is put on the mast. Another design can be characterized as set-type – a set of components (usually the photovoltaic module, light-diode unit and container with a charge controller and battery) each of which is mounted on a mast separately. The tilt angle of the solar panel is defined by the mounting construction.

It is worth mentioning that most of the units imported to Russia are designed for application in southern regions. Attempts to operate them

Table 1. Basic parameters of modern lithium-ion batteries [9]

	$LiCoO_2$|LiC_6	$LiFePO_4$|LiC_6	$LiMn_2O_4$|LiC_6	$LiNi_{1/3}Co_{1/3}Mn_{1/3}O_2$| $Li_4Ti_5O_{12}$
Specific energy capacity, Wh/kg	180	70–150	120–150	70–90
Cost, USD/Wh	≥3	0,7–1,2	≥1	≥3
Recommended depth of discharge,%	60	70	80	90
Cycle life, cycles	800	3000–5000	1500	≥6000
Operation cell voltage, V	4,2	3,3	3,7	2,1

Fig.1. Solar-powered autonomous signal-light unit

in regions at high and average latitudes, usually lead to failure in autumn and winter. In Fig.1, the first solar-powered light-signal unit mounted in Moscow in 2011–12 is shown [5]. Most of these systems were out of operation during the winter due to low photovoltaic power and a low tilt angle.

The second generation of solar-powered units in the Moscow region was characterised by an increase in photovoltaic module power (from 40–60 W up to 100–120 W) and a tilt angle closer to 90°. But the battery for electric energy storage was left as quite small due to its capital costs.

Photovoltaic power is used to feed the diode light unit and charge the battery during the day. At night, the light-signal unit is fed only from battery. The traditional type of battery used is lead-acid; lithium-ion and nickel-cadmium batteries are used much less often [6]. Lead-acid technology had a series of significant improvements, including the introduction of adsorbed in glass matrix electrolyte, tubular electrodes, special additives to the electrode material, increasing its lifetime. These measures slightly increased the depth of discharge and life cycle of lead-acid batteries. Another advantage of these batteries is their relatively low cost, but not for high-resource deep-cycle batteries with tubular electrodes [7].

Lithium-ion batteries have a longer life cycle and a greater depth of discharge than lead acid technology. In addition, they have better specific energy capacity that allows having less mass and volume of battery for thermal management in wintertime. But higher costs for lithium-ion batteries decrease their competitiveness against lead-acid technology in stationary applications. Another issue of lithium-ion battery applications is the need for a battery management system, which controls voltage and temperature on each cell in the battery and reacts on dangerous fluctuations, increasing battery lifetime, safety and costs [8].

Changes to the battery operational parameters at low environmental temperatures are the special problems. Some of lithium-ion systems as $Li_4Ti_5O_{12}$-based anode are more prone to low temperatures than lead-acid. This is very important for small-scale units (road signs, signal buoys, illuminating devices) where there is a lack of energy for battery container thermal management.

2. CALCULATION AND ANALITICAL STUDIES

Lithium-ion batteries, as well as lead acid ones, have different sub-types of technology, which is concerned with cathode and less anode material influence. Lithium cobalt, manganese oxides, mixed lithium oxides of cobalt, nickel, manga-

Table 2. Solar-powered signal-light unit optimal configurations

Battery type	Photovoltaic module		Battery					
	Area, m^2	Efficien-cy,%	Efficient energy capacity*, kWh	Nominal energy capacity, kWh	Efficien-cy,%	Minimal charge time**, h	Minimal discharge time **, h	Depth of discharge,%
Pb-Acid (AGM)	0,98	14,3	6,41	21	83	42,8	35,6	30
$LiFePO_4$	0,98	14,3	6,41	9	84	42,4	35,6	70

* considering recommended depth of discharge, ** considering maximum power flow through charge controller of 180 W

nese, aluminium and lithium iron phosphate are the main cathode materials for a lithium ion battery. Usually lithium graphite is used as an anode material, but several companies produce cells with $Li_4Ti_5O_{12}$-based anode, increasing the cost and cycle life and losing specific energy capacity. The main parameters of modern lithium-ion batteries are given in Table 1.

An energy balance calculation to evaluate autonomous solar-powered light-signal unit optimal configuration for conditions in the Moscow region was carried out.

NASA SSE monthly averaged solar radiation data was taken to estimate photovoltaic module productivity due to its availability and the possibility to obtain climate data for most parts of the Earth [10, 11, 12]. The relative error of solar radiation data is estimated as (10–15) % [11]. The energy balance calculation approach for different equipment configurations was close to that described in [13].

Two types of batteries were taken under consideration: lead-acid (absorbed glass mat type) and lithium-ion (lithium iron-phosphate cathode material), as the most cheap and widespread storage systems for the chosen battery technologies. EPSOLAR Tracer MPPT 1210 charge controller with maximum power point tracking was chosen for the lead-acid version of the solar-powered unit. Its main advantages are its low cost and the possibility to control the electric load (for example load can be fed not only the whole day and night, but also only in selected hours) [15]. Lithium iron-phosphate batteries were purchased from Winston Battery [16] as inexpensive version of lithium ion system, operational in a wide range of environment temperatures. Multi-crystal silicon photovoltaic modules TSM 140 (140 W peak power, JSC Telecom-STV, Zelenograd) were used in both configurations. For the lithium iron-phosphate battery, parameters of the EPSOLAR Tracer MPPT 1210 were chosen for calculation only, later an original controller was developed. A road sign “Crosswalk” with light-emission diode backlight 4 W was fed from the photovoltaic module and battery. Backlight was suggested to operate 24 hours per day during the whole year.

In the given conditions, the energy balance between generation, storage and consumption was estimated for different solar panel power and storage capacities. The optimisation criteria was minimum unit cost at backlight guaranteed operation during the whole year in the Moscow region. Calculated optimal configurations are shown in Table 2.

The guaranteed operational degree for such a unit was defined as the ratio of operated hours in the year to 8760 hours (the whole year).

For the configurations given in Table 2, guaranteed operational degree was about (97–98) % (operation of no less than 8500 h per year). The longest periods when the unit was out of operation in Moscow conditions were in January

3. EXPERIMENTAL APPLICATION

The main challenges for lithium-ion batteries in photovoltaic-based applications are:

– Development of a charge controller which are suitable for lithium-ion battery range of operational currents and voltages;

– Development of battery management system for the lithium-ion battery.

The first problem is concerned with the performance curve of the photovoltaic module. Having

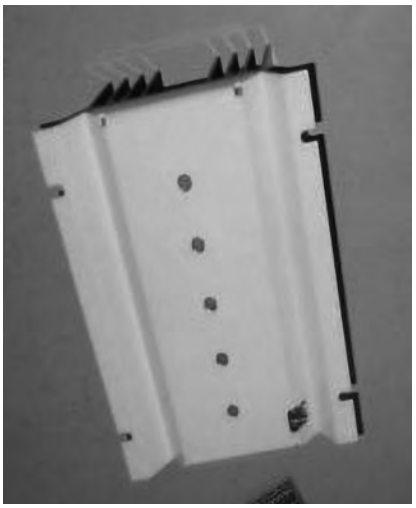

Fig. 2. Experimental charge controller for a lithium-ion battery

deeply discharged battery as a load, the photovoltaic module will be under current close to short circuit which leads to low voltage and efficiency. High current can also be also harmful for the battery, leading to decreased lifetime and possible overvoltage. So charge control is needed with current limitation and maximum power tracking for the solar panel to increase the charge process efficiency. Most of the charge controllers available on the market are adopted for operation with lead-acid batteries

Therefore, at the Joint Institute for High Temperatures a special charge controller for lithium-ion battery has been developed, Fig. 2. It is equipped with a battery management system of passive type to prevent battery overvoltage and maximum power point tracking using a P&O (perturb and observe) algorithm – the current from the photovoltaic module increases while the power increases or battery voltage reaches its upper limit. In case of a power drop after the current increases, the charge controller decreases the current. Current perturbations are generated every 3–5 minutes (due to slow solar radiation change dynamic)

Two solar-powered light-signal units were assembled according to the configuration presented in Table 2, and tested in the Joint Institute for High Temperatures, Fig. 3. Containers with lead-acid (a) and lithium-ion (b) batteries internal view is presented in Fig. 4. Both systems were tested from March to December 2016. Measurement system for data collection on currents and voltages in solar panel, battery and load circuits was built on OWEN data acquisition units. Data acquisition was carried

Fig.3. Experimental solar-powered light-signal units.

Fig.4. Internal view of battery container for lead-acid (a) and lithium-ion (b) batteries

out with a frequency of 0.2 Hz. Data obtained allowed to calculate the energy produced by the photovoltaic module, Fig. 5, stored in batteries and fed to the load. Zero voltage in the load circuit meant non-operational periods of the light-signal unit, so the sum of such periods allowed calculating the operational time during the whole test period and deriving a guaranteed operation degree.

During the whole test period, guaranteed operation degree of 89 % for lead-acid and 87 % for lithium-ion battery equipped solar powered units was obtained. The increased value of guaranteed operation degree was reached due to deep battery discharge – to 80 % instead of 30–40 %. A commercial charge controller only monitors voltage change in a battery, but for high capacity battery discharging by small current, voltage change is quite slow and does not represent correctly the depth of discharge. The developed controller also uses voltage as a control parameter, but the threshold voltage for load disconnect was preliminarily defined during tests on characteristic for photovoltaic applications of low currents. Greater depth of discharge leads to accelerated battery degradation.

Table 3. Capital costs and their structure for autonomous solar-powered light-signal units

Battery type	Capital costs		
	Components	**Costs, rub**	**Share,%**
Version A. Lead-acid battery (AGM)	Solar panel	7600	6,3
	Mounting construction	2800	2,3
	Charge controller	4500	3,7
	Battery	72000	60
	Cables, wiring, container	13000	10,7
	Construction works	20000	17
Total (for version A)		120000	100
Version B. Li-ion battery ($LiFePO_4$)	Solar panel	7600	8
	Mounting construction	2800	5
	Charge controller	7300	10,2
	Battery	55440	49
	Cables, wiring, container	12000	10,8
	Construction works	19000	17
Total (for version B)		112500	100

Experimental data deviation from the calculated results can be explained taking into account the shading of photovoltaic modules by nearby buildings in evening, which was not described during calculation.

4. ECONOMIC ESTIMATION

Cost shares for different experimental sample components in both configurations are given in Table 3.

Mass and dimensions estimates for both battery types are given in Table 4.

According to the relatively short lifetime of a lead-acid battery, one should estimate operational expenses which account for battery replacement over a 20 year period (averaged lifetime of modern solar panels). Manpower and transportation costs for battery replacement are estimated as 20 % of battery cost. Exact life cycle estimates at different depths of discharge is problematic, so a rough estimate is made, suggesting that 365 discharges down to recommended depth of discharge occur during the year. The calculation results for operational costs of battery replacement are given in Table 5.

Therefore, application of lithium-ion batteries is more competitive considering the whole period of the solar-powered light-signal unit's operation

5. CONCLUSIONS

1. Application of solar powered light and signal units with a high degree of guaranteed operation under the conditions of Russian regions requires a correct estimation of climate and geography factors. A high degree of guaranteed operation leads to an upscale of battery and solar panel and increased cost of the whole unit.

2. Application of a lithium-ion battery allows to decrease the cost of construction and operation of solar powered autonomous energy units due to its longer cycle life and greater depth of discharge than lead-acid batteries. A battery container can be made much more compact than for lead-acid batteries of the same efficient energy capacity. For today, application of lithium iron phosphate based batteries seems to be the most attractive.

3. For successful integration of li-ion batteries into solar powered systems efficient charge controllers with a solar panel maximum power point tracking algorithm, functions of voltage at each cell

Table 4. Battery type mass and dimensions estimates

Battery type	Mass, kg	Volume, m^3	Efficient energy capacity, W·h	Nominal energy capacity, W·h
Version A. Lead-acid battery (AGM)	855	0,8	6410	21367
Version B. Li-ion battery ($LiFePO_4$)	153	0,12	6410	9157

Table 5. Expenses for battery replacement for 20 years

Battery type	Capital costs, thousands of rub	Battery replacement for 20 years	Total costs over 20 years, thousands of rub
Version A. Lead-acid battery (AGM)	120	6	504
Version B. Li-ion battery ($LiFePO_4$)	112,5	2	230

of the battery and the battery depth of discharge, adequate controls must be applied.

ACKNOWLEDGMENT

This research is supported by Russian Scientific Foundation (project № 14–50–00124).

REFERENCES

1. Popel O.S. Fortov V.E. Renewable power in the modern world. Publishing house: MEI publishing house. 2015. 450 S. ISBN978–5–383–00959–8.

2. The Moscow parks can begin to cover at the expense of solar energy//power News. http://energo-news.ru/archives/31060.

3. Solar street lights. https://en.wikipedia.org/wiki/Solar_street_light.

4. Edensun Illumination. http://www.edensun-led.com/en/index.asp.

5. Internet resource: http://geliomaster.com/catalog/sunelectro/sunelectro_52039.html.

6. A.B. Tarasenko. Stores of electric energy for systems on the basis of RES: current state and prospects of development.//Materials of the eighth All-Russian scientific youth school with the international participation. Moscow. University book. 2012, pp. 148–185.

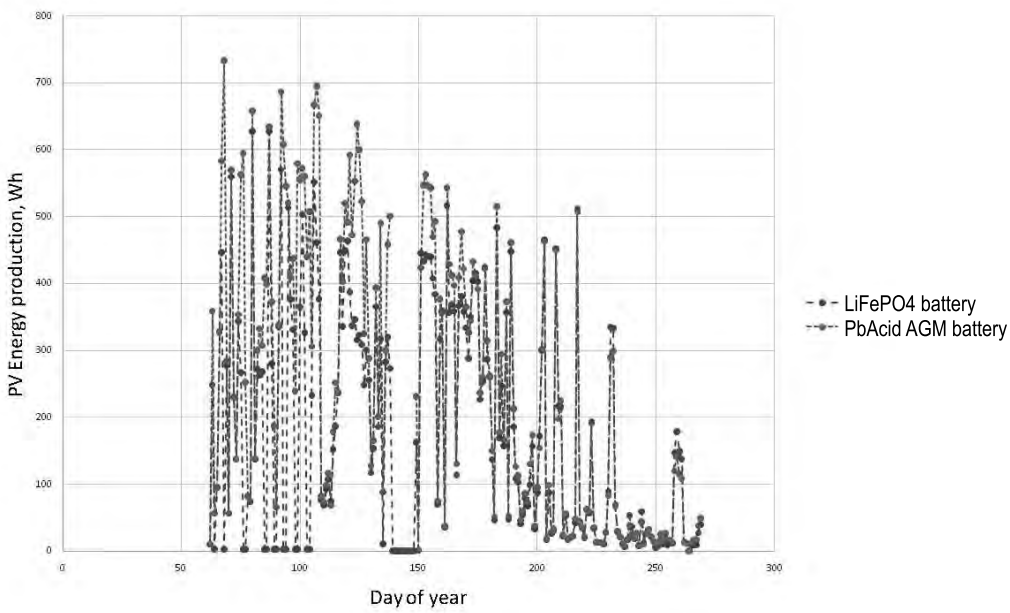

Fig. 5. Solar panel energy production for both experimental samples in 2016, March-December

7. John Baker, New technology and possible advances in energy storage // Energy Policy 36 (2008) 4368–4373.

8. A. Rykovanov. The systems of balance of lithium-ion batteries//the Force electronics, 1 (2009), S. 52–55.

9. Lithium batteries: Status, prospects and future, B. Scrosati, J. Garche //Journal of Power Sources 195 (2010) 2419–2430.

10. The NASA Surface Meteorology and Solar Energy Data Set http://eosweb.larc.nasa.gov/sse.

11. Popel O.S., Fried S.E., Kiselyova S.V., Kolomiyets Yu.G., Lisitskaya N.V. Climatic data for renewable power (base of climatic data). Manual. – M.: OIVT RAS, 2010. 56 p.

12. Popel O.S., Fried S.E., Kolomiyets Yu.G., Kiselyov S.V., Terekhova E.N. The atlas of resources of solar energy in the territory of Russia. – M.: OIVT RAS, 2010. 84 p.

13. N.A. Komarova, Yu.Y. Rafikova, A.B. Tarasenko and S.V. Kiseleva, Autonomous power supply using solar energy in Russian Far East regions // MATEC Web of Conferences **112** 10011 (2017), p. 1–6.

14. Yu.A. Shinyakov, Yu.A. Shurygin, V.V. Arzhanov, O.A. Teushchakov, A.V. Osipov, K.V. Arzhanov. Independent photo-electric power station.//News of the Tomsk Polytechnic University. 2012. T. 320. No. 4, page 133–138.

15. web-site Wiston Battery Ltd; http://www.thunder-sky.com/products_en.asp?fid=111&fid2=115.

Tarasenko Alexei B.
is the graduate of MEPhI, the senior research associate of the Joint Institute of High Temperatures of RAS (JIHT RAS), the leading expert of the company LLC TEEMP of the "RENOVA" group. Area of scientific interests is the photo-energy engineering, stores of electric energy, functional nanomaterials for stores, forecasting of operation of photo-electric power stations of autonomous and network application. The winner of the Award of the International academic publishing company «Science / Interperiodika» for the best scientific publication in the Heat and Power Energetic Journal (2011), the winner of a competition of the scientific and technical and research projects «Youth Innovations» (2016), the Winner of an award and medal of the academician V.M. Tuchkevich for work «Amorphous silicon: hetero-structure solar elements and power plants» (together with scientists from FTI after A.F. Ioffe). The author has more than 30 scientific publications in authoritative scientific publications

Oleg S. Popel,
Prof., Dr. of Tech. Sc., was graduated of the Moscow Power Institute, the deputy director of JIHT RAS for science, the Head of JIHT RAS Research centre «Physics and Technology Problems of Power», the winner of the Award of the Government of the Russian Federation in science and technology for work «Development and deployment of effective technologies of renewable and nonconventional power sources in small-scale power generation use « (2011), the author of 7 monographs and manuals, and more than 300 scientific publications. His areas of scientific interests are power, renewable energy source, energy saving, and thermo-physics

Light & Engineering
Vol. 25, No. 4, pp. 57-64, 2017

Svetotekhnika
No. 5, 2017, pp. 44–48

A STUDY OF THE CLASSICAL ARCHITECTURE FLOODLIGHTING

Wojciech Żagan and Rafał Krupiński

Warsaw University of Technology, Faculty of Electrical Engineering, Lighting Division
E-mail: rafal.krupinski@ien.pw.edu.pl

ABSTRACT

Designing historic building floodlighting belongs to fairly complicated tasks. Apart from a purely technical imagination and adherence to floodlighting principles and methods, aesthetic aspects should also be taken into account. Predicting the effect, which will be created, is a very difficult thing. It is often impossible for us to check, owing to the dimensions of the illuminated structures, number of the used lighting equipment and its installation capabilities. Here comes 3D computer graphics. The paper presents a case study of floodlighting Palace of the Commonwealth in Warsaw, Poland. A few concepts of illuminating the palace have been described, the analysis of effects has been made and the concept that after some consultations was selected for implementation has been demonstrated. All the floodlighting designs are shown in a form of the photorealistic visualization of lighting with a description of the intended and obtained effects. Apart from the visual evaluation, the level of the building luminance was carefully monitored under the project.

Keywords: illumination, floodlighting, lighting technology, computer graphics

1. INTRODUCTION – BUILDING DESCRIPTION

Palace of the Commonwealth in Warsaw is considered as one of the greatest examples of the baroque architecture in Poland. It is one of the most magnificent conceptions of a French style palace, *entre cour et jardin,* in Warsaw, with its main building called *corps de logis,* situated at the axis between the entrance court (*cour d'honneur*) and the garden at the back of the palace. The building was constructed according to the design by Tylman Gamerski in the years of 1677 and 1695 as a residence of Voivode of Płock, Jan Dobrogost Krasiński. Its structure is based on three avant-corpses as follows: one central five-radial and two side three-radial. Between the main and side avant-corpses there are pillar loggias. Both central avant-corpses, front and garden, are ended with tympana at whose tops there are statues. The basic dimensions of the palace are as follows: width of 76 m, height of 26 m representing 3 floors, roof and statues on tympanum as well as the depth of 28 m. At the back of the palace, there is a garden that was subject to revitalization while designing the palace floodlighting. The front façade is directed at Krasiński Square opposite a modern, glass-structured building of Supreme Court in Poland. Today Palace of the Commonwealth is a part of the Polish National Library's Special Collections Section (Manuscripts and Old Prints).

2. SCOPE OF PROJECT

In 2008, the façades of the palace were renovated, and the existing floodlighting, owing to the technical reasons, was partially disconnected and at present it does not perform (Fig.1). The design was implemented at the beginning of this century, and thus, based on the lighting solutions with economically inefficient light sources. As a result of these factors, there was a need to design a new concept to include and use modern lighting solutions, such as energy saving lighting equipment based on both

Fig. 1. Palace of the Commonwealth in Warsaw, Poland (front façade)

discharge lamps and light emitting diodes (LEDs). The aim of the new design was to floodlight the exterior façades of the Palace of the Commonwealth in Warsaw, meaning highlighting the façades of the building with light.

The conceptual scope of design covered working out a few concepts of the building floodlighting, selecting, positioning and directing the lighting equipment, making the lighting calculations, including the visualization of the floodlighting concept. For every lighting concept, the recommendations and guidelines related to the connection, control and maintenance system for floodlighting were described.

It was agreed that the spatial range of the floodlighting would cover all four façades of the palace: front, garden as well as south and north end walls. During the talks on the design with the building owners, it was agreed that the roof parts of front façade, seen from Krasiński Square, would also be lit.

In the course of designing the lighting solution for the building, the starting point was an analysis of a series of factors related to both palace and its surroundings [1–8]. The basic directions and points of observations, building surroundings in terms of its brightness and capabilities of mounting the lighting equipment were estimated, since its thorough modernisation had recently been carried out. Also, the architecture of the building, its details and function, which it performs, were taken into account. In that way, with the aid of computer lighting simulations, with all aspects of designing with this technique [8] a few concepts of floodlighting the front façade and one for the garden façade were analysed. All these designs were preceded with multiple changes in a type of the lighting equipment and locations of its mounting and directing. All created concepts of the palace floodlighting were complete in terms of design documentation. Apart from the visualization images, every project had the generated luminance distribution on the façades of the building that enabled assessing the design in terms of compliance with the CIE recommendations concerning the luminance of the buildings subject to floodlighting [9]. Also, the projects contained the

Fig. 2. Three-dimensional grid model of Palace of the Commonwealth in Warsaw

guidelines regarding the floodlighting maintenance system, including recommendations on a time period, after which cleaning the lighting equipment and replacing the light sources should be carried out.

3. UNDERTAKEN TECHNIQUE OF DESIGN FOR BUILDING FLOODLIGHTING

For such reasons as a prestige of the building, its dimensions, predicted number of the lighting equipment and necessity of analysing a large number of the lighting options, the only way to design the building floodlighting was to use the lighting simulation of its three-dimensional geometric model. There are many methods for designing the virtual 3D models dependent on both used computer application and designer's skills and knowledge in this field. However, the design basics are similar. On the basis of lines, profiles of the building and a series of functions available in the 3D applications, some sets of vertexes, edges and planes representing the virtual rendering of the real building are created. By convention, the authors calls these models a geometric representation of the building (Fig. 2).

Palace of the Commonwealth, as a relatively big building, is not easy to be reconstructed in the virtual space. Its structure is rich in architectural details and façade materials vary. However, in majority, the façade is plastered. As for the created three-dimensional representation of the building, the next step was to define all material features: colour, material texture, reflective properties.

The first two design stages are the most labour-intensive and time-consuming in this method for designing the lighting solution. However, on the basis of such a created virtual scene, the designer can analyse the unlimited number of floodlighting options. It means the options based on the real lighting equipment. Usually, luminaires are defined by lighting manufacturers in a form of luminous intensity distributions in the IES (Illuminating Engineering Society) format. The files uploaded to the software have defined basic lighting parameters: a luminous intensity distribution, maximum luminous intensity of a luminaire and luminous flux of a light source, whereas an appropriate colour temperature of light source should be assigned to them, and as far as a light strip is concerned, its length should be given.

The last stage of designing the lighting with this method is rendering. It is a calculation process, under which the geometry of the building is converted into an image after assigning the reflective and transmissive properties to it, and then, adding the light sources to a scene, as a result of the photometric and colorimetric calculations. On its basis, the designers can see and present their vision of illuminating the building as well as receive the technical, lighting data on their project. The luminance distribution on individual planes, enabling assessing this design should be recognised as the most important data (Fig. 9).

4. MULTI-OPTIONAL DESIGN FOR FLOODLIGHTING

Taking into account the points and directions of observing the building, option 1 was based on a mixed method, general and accent lighting [6]. 16 in-ground luminaires were installed in a distance of 3 m away from the façades evenly illuminating the front façade, with an increase in the luminance in its central part. For the accent lighting purposes, 107 spotlights and floodlights in total were applied. The arcades of the palace were highlighted with the

Fig. 3. Design of floodlighting front façade of palace (option 1 – visualization)

Fig. 4. Simulation of floodlighting garden façade of building

asymmetric light distribution floodlights placed inside them. The tympanum, three statues at its top, banister and pilasters were lit with a light strip system equipped with the light emitting diodes (LEDs). The other lighting equipment predicted for façade floodlighting was based on the metal halide lamps of colour temperature of 3000K. The roof surface of the front façade was illuminated with the rotary symmetric reflector spotlights with glass stretching the light beams horizontally. Due to the patina-covered roof surface, the light sources of a higher temperature (4200K) than for the façade were applied. Fig. 3 demonstrates the floodlighting design.

This option also had a few modifications illustrating an effect of floodlighting with the switched off lighting of the roof, banisters, pilasters and statues at the top of tympanum to show the influence of illuminating them on the final lighting effect.

Due to a different observation perspective, a decision on illuminating the garden and side façades only with the general light [6] was made (Fig. 4). One concept was created as a result of the early multiple changes to the types of lighting equipment and its positioning and directing. The project in this option assumed using 37 asymmetric distribution lighting fixtures equipped with the metal halide lamps mounted at the low bollards at a distance of 4m away from the façade. In order to highlight the depth, characteristic façades recession over the balcony, on their surfaces, 3 asymmetric floodlights each generating a higher luminance levels in these spaces were installed. Additionally, 13 LED linear luminaires to light the tympanum and 7 LED spotlighting fixtures to illuminate the statues at its top were applied.

The second option was a result of modification made to the first version. It assumed withdrawing from using the in-ground luminaires illuminating the front façade in favour of the asymmetric floodlights installed on the low bollards in front of the palace. Unfortunately, it was not a good solution – the lighting equipment was seen during the day time, however, owing to the existing bollards used in the former lighting system and power supply provided to them, a decision on analysing such a solution was made. The amount of lighting equipment was the same. The effects of floodlighting and luminance distribution for this option were similar to option 1.

The palace façade is characterised by the pilaster rhythm along its entire width. Thus, the third important modification to the lighting project assumed highlighting the rhythm of side, outermost avant-corpses, as well as emphasising the balcony banisters in the arcade part, with the light, together with the simultaneous reduction in luminance level in the upper parts of the building (Fig. 5). The effects were achieved thanks to the LED light strips. The number of the used lighting products grew to 160 pieces.

The next analysis was to switch off the arcades on the first floor and to accent the pilaster rhythm along the whole façade width from the palace side. Also, the luminaires illuminating the balcony banisters in the arcade part were left (Fig. 6). The total number of the lighting fixtures installed grew by the next seven pieces.

The last virtual lighting attempt was to emphasise the horizontal façade division by installing the light strips along the entire façade width, at the height of first floor, and to accent the pilaster rhythm in the central and side avant-corpses. The arcades, according to the recommendations regarding the building floodlighting, were lit with the asymmetric light distribution luminaires with the metal halide lamps from the inside. Fig. 7 illustrates the com-

Fig. 5. Visualization of floodlighting Palace of the Commonwealth (highlighting rhythm of pilaster avant-corpses)

puter simulation of the project. This option became the most spectacular, but also expensive. 201 luminaires in total number were installed.

5. FINAL CONCEPT OF FLOODLIGNTING

All the above mentioned concepts of floodlighting the building were initially presented only to its owner who selected option1 for the implementation – with modification meaning eliminating the luminaires mounted directly on the palace façade – on the central pilasters of avant-corps.

The design was also subject to evaluation by the conservation-restoration authorities for the aesthetics point of view [10, 11]. Unfortunately, as a result of the analyses and talks on both achieved effect and possibilities of mounting the lighting equipment, it was rejected. The conservator-restorer recommended using the general lighting method for all the building façades (Fig. 8). The lighting with the aid of two groups of narrow distribution spotlights from a long distance of 40 m away from the façade was recommended. A similar way of floodlighting was also proposed for the garden façade. A vast majority of the lighting products were supposed to be installed on the newly mounted bollards used in the lighting system of the park.

In total, to implement this option 34 spotlights and floodlights of the entire installed 4.2 kW were applied performing the average luminance value about 6 cd/m^2 (Fig. 9), which, thanks to the average surrounding brightness, can be found compliant with the recommendations concerning the building floodlighting [9]. The obtained lighting effect can be considered as consistent, since a nature of the building floodlighting with the general lighting method has hallmarks of rendering effect seen during a day. All floodlighting principles described in the literature of the subject [5, 6] can be also recognised as met. In the final option, 12 luminaires mounted on the three bollards relatively low (4m) were accepted for the installation purposes. In the extreme case there were 5 lighting fixtures of the narrow half-peak divergence of $\delta_{1/2}$ = 16 deg. The luminaire batteries with their size might not be so visible, however, it could be expected that their directing in the plane close to orthogonal to the building façade surface might cause a stronger light penetration into its interior [12, 13].

Fig. 6. Visualization of floodlighting palace (test on highlighting pilaster rhythm along front façade)

Fig. 7. Visualization of floodlighting Palace of the Commonwealth according to option 5

Therefore, there could be a risk of glare to the people walking around it, since the maximum luminous intensities of these luminaires are very high (around 200 kcd). The palace floodlighting with this method is also inefficient. There will also be a strong light pollution and glare to the observers. Yet, it will be possible to verify these parameters only after the implementation. At the current lighting design stage, the methods of discomfort glare risk occurrence evaluation [14, 15] are being worked out for the road lighting in particular, however, it should be expected that these methods can be adapted to the building floodlighting field.

6. ALTERNATIVE TO SIMULATION WAY OF DESIGNING FLOODLIGHTING

The building floodlighting design with the visualization method is a tedious process. The time required to generate a multi-optional lighting project is calculated in tens of working hours. A bigger burden of designing with this method is time needed to create a virtual light scene.

Carrying out the tests with the use of real lighting equipment under the real conditions is an alternative [16]. Also, for this building, the investor, upon the request from the conservator-restorer, did such a test. Unfortunately, it ended in failure. Despite a relatively small number of the lighting fixtures used for the final concept, none of the lighting companies managed to collect the number of specific types of the luminaires required under the project. However, it should be mentioned that generally, if it were possible to collect such an amount of equipment, the project evaluation during a short show would not be objective either, since it features a lot of disadvantages. It is hard to expect one-off decisions on a way of floodlighting to be made during the show, and it is also risky to rely on the possible analysis coming from the photo documentation of the floodlighting tests [17].

7. CONCLUSIONS

So far three building floodlighting methods have been known: accent, general and mixed. The choice of method mainly depends on a distance and location of the observation points. Taking into account the location of Palace of the Commonwealth, the points and directions of its observation as well as

Fig. 8. Final concept of floodlighting Palace of the Commonwealth (computer simulation)

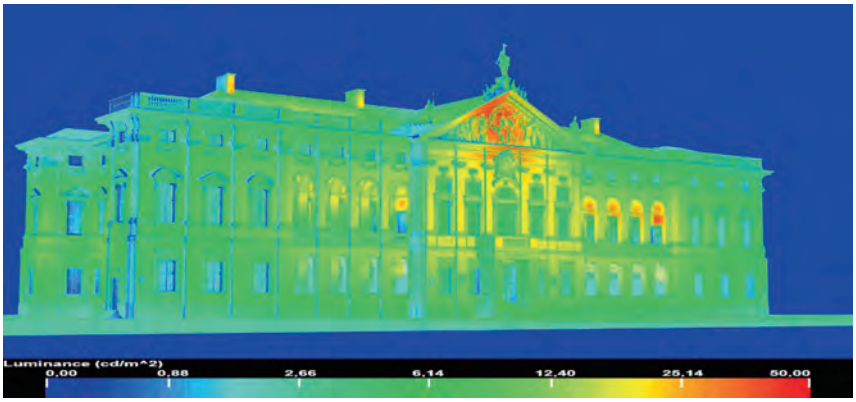

Fig. 9. Luminance distribution for option predicted for implementation

capabilities of its floodlighting, the use of mixed method was recommended from the lighting point of view. All options presented in the project were exactly based on this method. However, it is usually the conservator-restorer who has a decisive influence on floodlighting the building. His or her role is to take care of both building structure (lighting equipment mounting on the façade, drilling the holes, conducting the power supply cables, etc.) and its general appearance in the evening and at night – i.e. an appropriate floodlighting design. Apart from aesthetic reasons that should not be discussed, the final project for the palace to be implemented means, however, a lot of threats. The inefficiency of the final floodlighting option should be considered. After implementing the project, there will be a strong light penetration into the building interior, where there are a lot of collections of old prints and manuscripts. Also, a high light pollution should be taken into account. At present, the new building floodlighting method is being worked out in an attempt to reduce these threats to minimum. It is also possible to verify and change the described project, since while writing this paper the design is still being established.

Designing building floodlighting always requires multilayer approaches, analysing different solutions, both in terms of expected light effects and type of the used equipment. Without computer lighting simulations in 3D model, such an analysis is now difficult to be made. In this case, there are also some thoughts and tests in progress to find out how to solve this problem. It should be expected that in the nearest time the multi-optional floodlighting design on the basis of the real lighting equipment will not be so difficult and time consuming as it is now.

RETERENCES

1. Dugar A.M. „The role of poetics in architectural lighting design", Lighting Research & Technology 2016; 0: 1–13, DOI: 10.1177/1477153516664967.

2. Wang L. „Exploration of literary and artistic cultural values of large-scale landscape", Light & Engineering, 2016, Vol. 24, No. 3, pp. 6–9.

3. *Silkina M. A.* „Light reference points in a night city environment", Light & Engineering, 2015, Vol. 23, No. 2, pp. 29–33.

4. O'Farrell G. „External Lighting for Historic Buildings", English Heritage, 04/2007.

5. Żagan W., „Object Floodlighting Guidelines", Highlight WP 03/11.

6. Żagan W., Krupiński R. „Teoria i praktyka iluminacji obiektów (Floodlighting, theory and practice) ", Oficyna Wydawnicza Politechniki Warszawskiej, Warszawa 2016, ISBN978–83–7814–550–9.

7. Bojda P., Wachta H. „Usability of luminaries with LED sources to illuminate the window areas of architectural objects" Selected Issues of Electrical Engineering and Electronics (WZEE), 2016 13th, DOI: 10.1109/WZEE.2016.7800250.

8. Krupiński R. „Modelowanie 3D dla potrzeb iluminacji obiektów (3D modeling for floodlighting) ", Oficyna Wydawnicza Politechniki Warszawskiej, Warszawa 2011, ISBN978 83 7207 961 9.

9. Guide for Floodlighting, CIE94–1993, ISBN978 3 900734 31 2.

10. Revsina Y. E., Shvidkovsky D.O. „Illumination of classical architecture memorials in search of authenticity", Light & Engineering, 2016, Vol. 24, No. 1, pp. 24–30.

11. Malaska W., Wachta H. „Elements of inferential statistics in a quantitative assessment of illuminations of architectural structures", VI. IEEE Lighting Conference

of the Visegrad Countries, LUMEN, V4, DOI: 10.1109/LUMENV.2016.7745529.

12. European Standard EN12464–2 „Lighting of work places – Part 2: Outdoor work places".

13. Colchester Borough Council „External Artificial Lighting" Guidance Note: 2012.

14. Słomiński S., „Identifying problems with luminaire luminance measurements for discomfort glare analysis", Lighting Research & Technology, 48, ISSN1477–1535, pp. 573–588, DOI: 10.1177/1477153515596374.

15. Słomiński S., „Selected problems in modern methods of luminance measurement of multisource LED luminaires" Light & Engineering, 2016, Vol. 24, No. 1, pp. 45–50.

16. Krupiński R., „Visualization as alternative to tests on lighting under real conditions", Light & Engineering, 2015, Vol. 23, No. 4, pp. 33–40.

17. Słomiński S. „The correct image of illuminated object registration – problems arising from software capabilities and equipment limitation" Przegląd Elektrotechniczny, R. 89 NR8/2013 pp. 259–261.

Wojciech Żagan,
Prof. Since 1997, he is a Head of the Lighting Division of Warsaw University of Technology, author of more than one hundred of floodlighting projects in Poland, The Netherlands and Germany, author of books "Floodlighting of the objects" (2003) and "Floodlighting, theory and practice" (2016). He supervised thirteen doctors' theses in the area of lighting technology

Rafał Krupiński,
Ph. D., graduated from the Faculty of Electrical Engineering, Warsaw University of Technology in 2003. He is specialist of floodlighting using computer graphics simmulations methods. While making this method popular and implementing a few dozen floodlighting designs with its use over more than a decade of his work, he continues by improving it, he is the author of books „3D Modeling for floodlighting" (2011) and „Floodlighting, theory and practice" (2016). He is also lecture at the Warsaw University of Technology at the Faculty of Electrical Engineering, Lighting Division, where he occupies the post of an Assistant Professor

Fig. 1. Example of visualization of the space-angular luminance distribution by local estimates of the Monte Carlo method for the *Cornell Boxes* reference scene

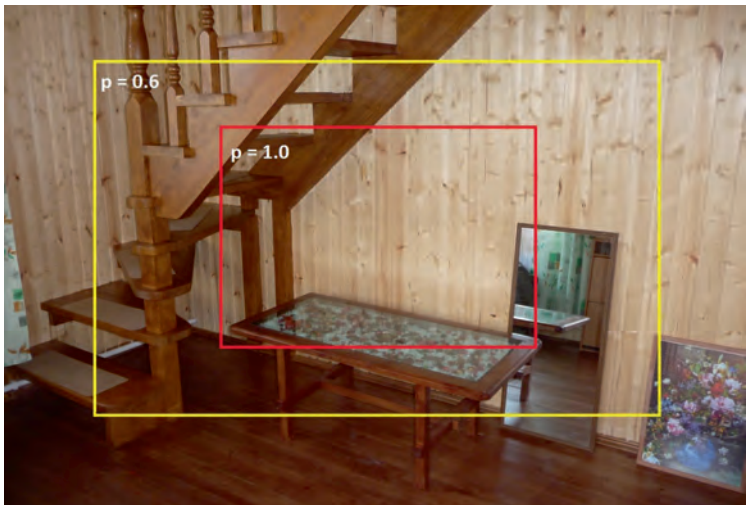

Fig. 2. Example of setting the weight coefficient *p* for different fields of view

Fig. 3. Example of determining the weight coefficient *h*, taking into account the lighting task

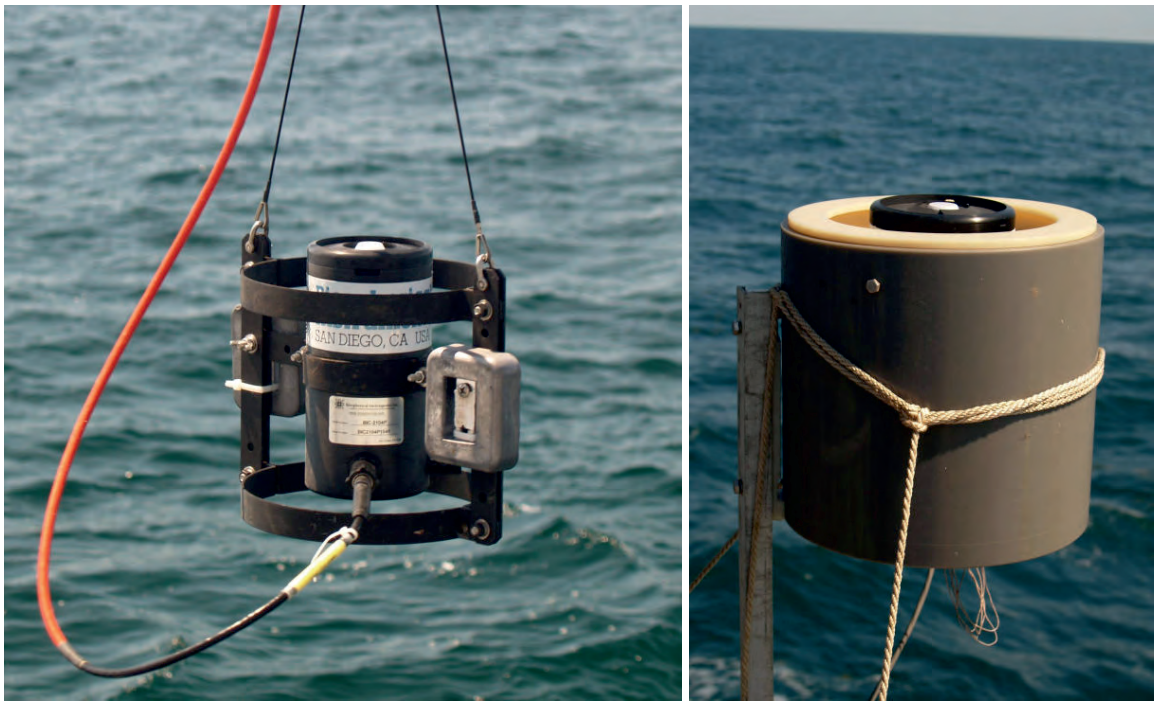

Fig. 4. A measuring instrument of light mode on the sea surface and in water thickness. On the left is an immersed detector, on the right is a deck-based detector

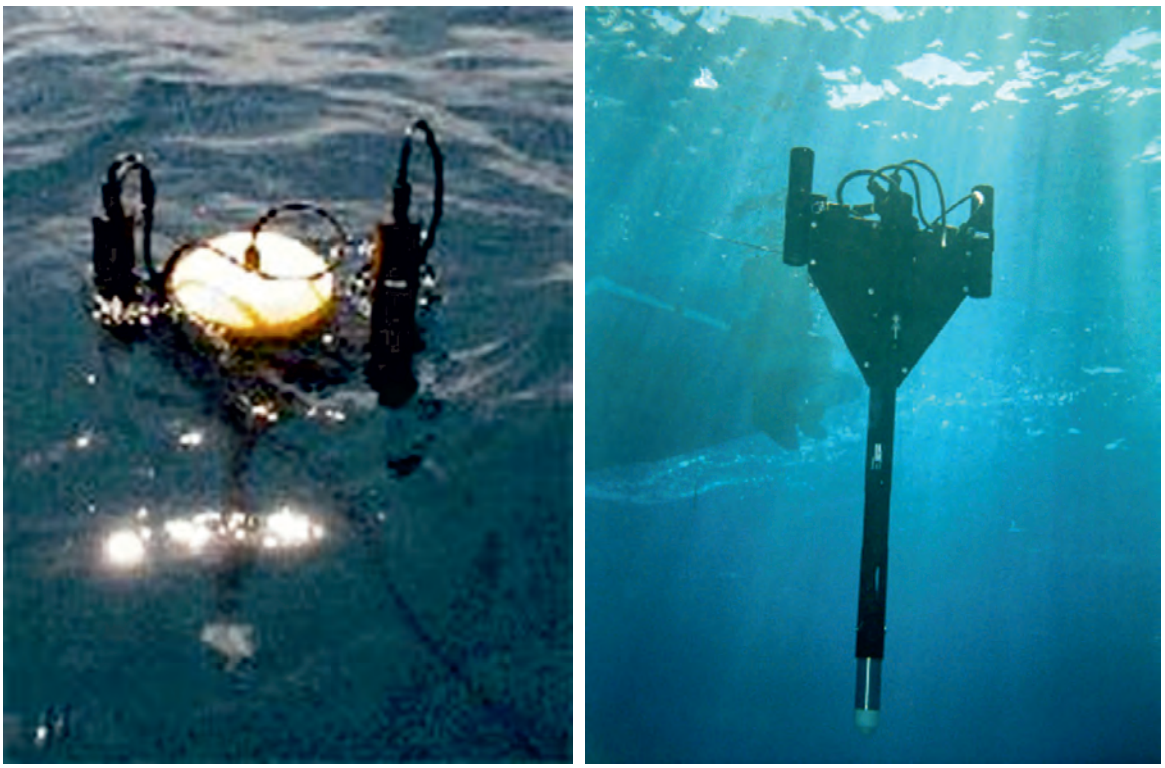

Fig. 6. The *Profiler II* measuring system developed by *SATLANTIC* Company [20] to measure luminance of ascending radiation and irradiance from the top in eight spectral channels. On the left is an example to measure in the buoy version; on the right – to measure in the free fall mode

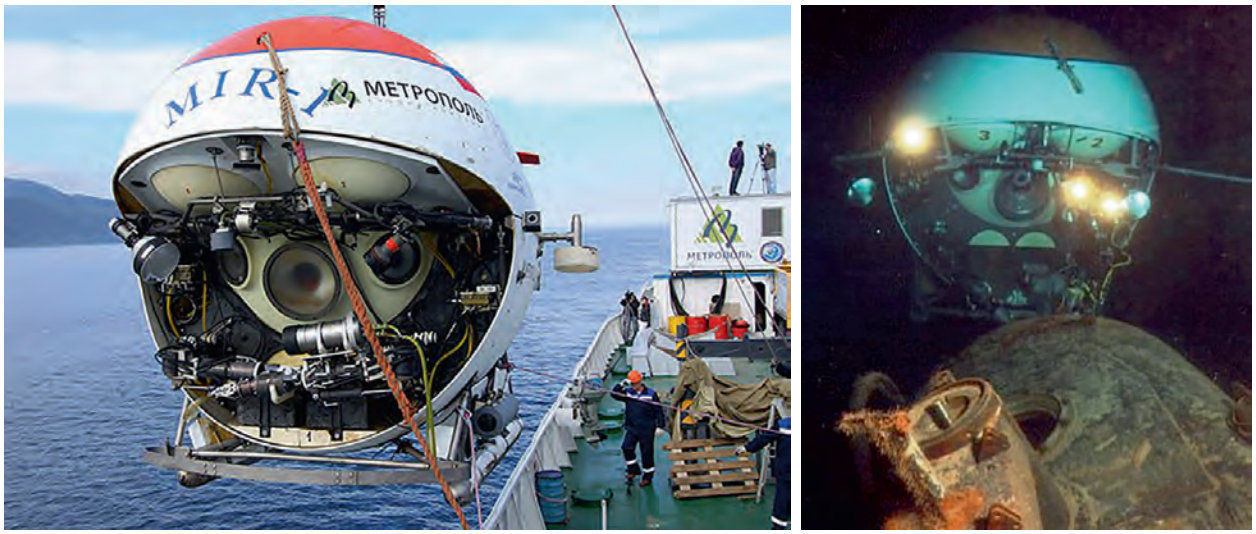

Fig. 8. Deep-water manned vehicle Mir: on the left – before immersion, on the right – investigation of a sunken submarine, Atlantic Ocean, depth is 5400 m

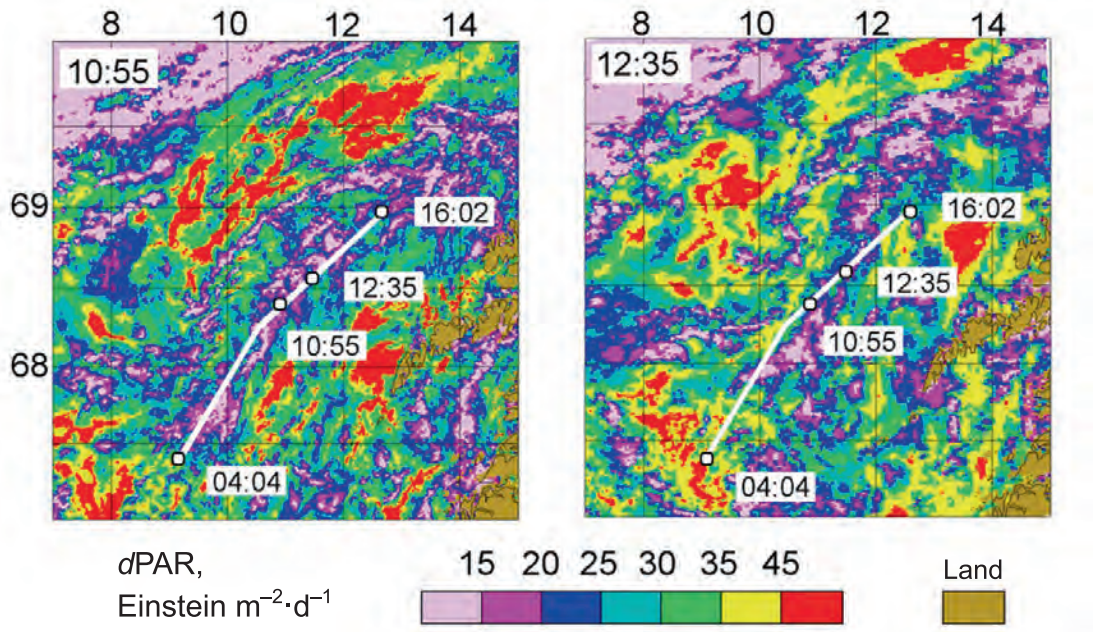

Fig. 10. Comparison of spatial distributions of daytime exposition of photosynthetically active radiation (400–700 nm) computed according to the *MODIS-Aqua* satellite scanner using IO RAS algorithm on August 1, 2014 at 10:55 am *GMT* (on the left) and at 12:35 pm *GMT* (on the right). The white line shows route of the boat, and figures nearby show the beginning (4:04 a.m.) and the end (4:02 p.m.) of the PAR measurements, as well as the boat position during the satellite flight [31]

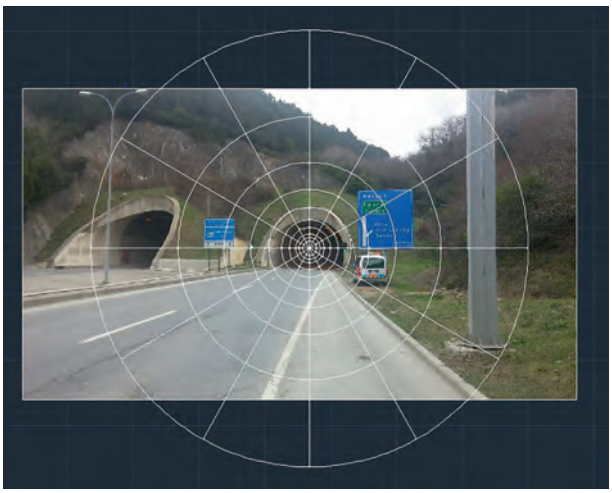

Fig.2. Circles drawn on the photograph of the Istanbul Beykoz tunnel entrance

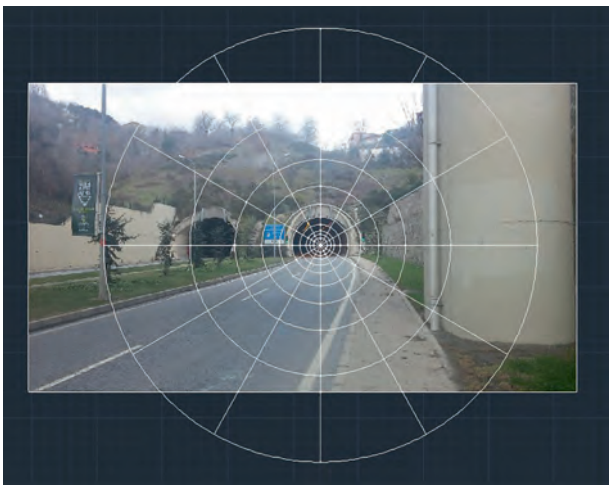

Fig.3. Circles drawn on the photograph of the Istanbul Kavacık tunnel entrance

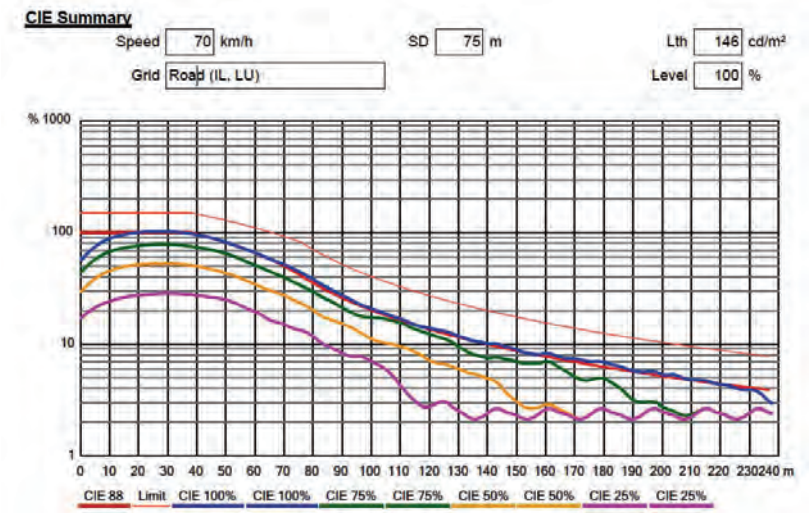

Fig.4. CIE088 curves for first tube

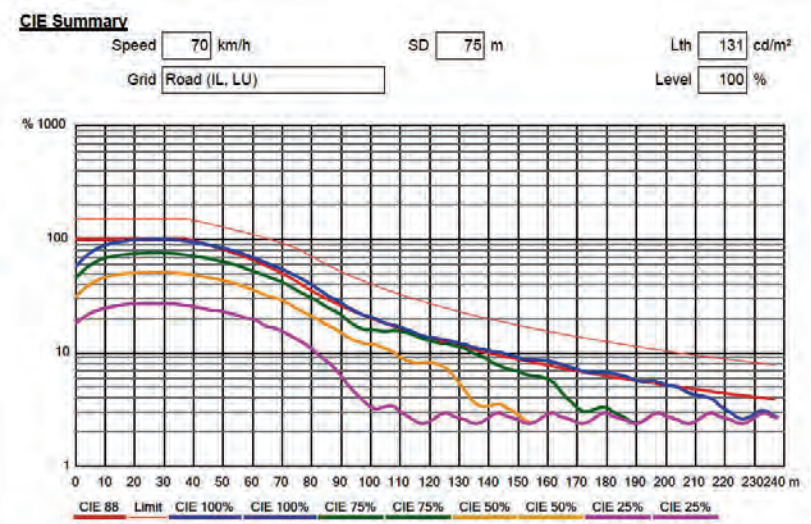

Fig.5. CIE088 curves for second tube

Light & Engineering
Vol. 25, No. 4, pp. 69-75, 2017

Svetotekhnika
No. 3, 2017, pp. 46–57

TUNNEL LIGHTING DESIGN WITH HIGH POWER LED LAMPS OF AN URBAN TUNNEL IN ISTANBUL

Canan Karatekin

Department of Electrical Engineering, Istanbul Technical University
E-mail: karatekin@itu.edu.tr

ABSTRACTS

In this study on tunnel lighting, a new lighting system was designed using high power LED lamps in an urban road tunnel. The automated LED lamp lighting system features a stepped lighting design created to provide variable luminance values. The study confirmed that the LED lamp lighting design conformed to the luminance values specified by the International Commission on Illumination (CIE088: 2004).

An urban tunnel in Istanbul was chosen to compare the energy efficiency change in cases of the high pressure sodium (vapour) lamps and the high power LED lamps using for tunnel lighting. The LED lamps were found to conserve 45.5 % more energy than the high- pressure sodium (vapour) lamps.

Keywords: tunnel lighting, high power LED lamps, high pressure sodium (vapour) lamp, energy efficiency

1. INTRODUCTION

Tunnels are extensively used for urban and intercity transportation, as they reduce the distances and provide ease of use and comfort. A driver's eye, which is adapted to expansive surroundings and bright light in the daytime, perceives the tunnel entrance as dark, and is therefore unable to fully see objects at the tunnel entrance [1]. At night, however, this issue does not pose a problem, as the eye is already adapted to the darkness. Tunnel lighting is therefore especially important in the daytime, when certain precautionary measures, particularly those related to the convergence zone of the tunnel, need to be taken to ensure that drivers are able to visually adapt to the dark tunnel. Tunnel lighting should provide the necessary minimum level of luminance required for the driver to travel safely and comfortably through the length of the tunnel. The safety features associated with the drivers' passage through the tunnel are determined by the International Commission on Illumination (CIE088:2004 Guide for the Lighting of Road Tunnels and Underpasses) [2]. This study is in accordance with these standards.

In the present study, a stepped lighting system, using automated high power LED luminaires was designed for an urban tunnel. In the tunnel, high pressure sodium vapor luminaires were used for the lighting. This study investigates the change in energy efficiency between the use of LED luminaires and sodium vapour luminaires.

The report "Energy Savings Potential of Solid State Lighting in General Illumination Application" released by the US Department of Energy indicated that the replacement of current light sources with LEDs could provide a savings of $250 billion in USA energy consumption over the next 20 years and decrease energy consumption for lighting by 50 % and reduce 1800 million metric tons of CO_2 emission [3].

The use of white LEDs in lighting systems is preferred to traditional lights because of its numerous advantages, such as higher energy efficiency, longer lifetime and, therefore, less maintenance, reduced size of the equipment, higher flexibility and

control of the level of light and colour variation, and low power consumption [4]. Lighting accounts for 20 % of total electricity use throughout the world today [5]. Using LEDs could reduce this figure to 4 % or less. As LEDs are expected to become the dominant light source over the next decade, the reduction of energy used and greenhouse gases emitted will benefit everyone, including consumers who will save hundreds of dollars every year from reduced energy use. The Tunnel Pass LED luminaire reduces energy consumption by up to 50 % compared to high intensity discharge (HID) fixtures and provides optimal lighting uniformity in tunnel and underpass applications while offering up to 100,000 hours of reliable operation.

A large part of the input power in high power LED chips transforms into heat, which needs to be directed away from LED lamps, while the remaining part of the power is transformed into light [6]. As a result, the operating temperature of LEDs is one of the most significant determinants of LED's reliability and strength. Continuous operation of LEDs at elevated temperatures hastens the decrease in luminous flux, thereby reducing the life span of LEDs. Therefore, as the generated temperature is the most significant problem associated with the use of high power LED lamps, this heat needs to be removed from the LED lamps via appropriate coolants.

High pressure sodium (vapour) lamps, fluorescent lamps and metal halogen lamps are used in tunnels. The use of LED luminaires in place of fluorescent lamps in railway tunnels was reported to provide energy savings and easy maintenance [7]. In another study, the performances of different luminaires, such as fluorescent, sodium vapour and metal halogen lamps, were compared at different heights according to their uses in submarine tunnels and other tunnels [8].

The drivers in the LED have dimming capability, allowing users to control the lumen output as desired. The fixtures are also available with optional lumen packages to maximize energy savings. Tunnel Pass LED luminaires can be ceiling or wall – mounted and are intended to be used to replace 100 W and 400 W high pressure sodium (vapour) lamps. In the present study, an investigation was conducted to compare energy efficiency in 150 W and 400 W sodium (vapour) lamps and LED luminaires. In the threshold luminescence zone of the tunnel, a counter beam illumination system was used, while a symmetric illumination system was used in the other zones of the tunnel. For safety purposes, an automated system was designed with the intent of preventing glares from occurring when drivers entered the tunnel from the outside.

2. THE DETERMINATION OF PARAMETERS FOR THE DESIGN

Tunnel lighting was performed using the tunnel v3 software, which is capable of making calculations, designs and reports in accordance with CIE088 standards, developed by the Schreder Company [9]. The Halit Ulukurt tunnel in Istanbul, which consists of two tubes, was used for the study. The first tube is 690 meters and second – 720 meters [10]. The total tunnel width is 10 meters, and each tube has two-lanes, with each lane having a width of 3.75 meters.

2.1. The Calculation of Stopping Distance Value

Stopping distance is the distance in which the driver of the car travelling at a constant speed can stop safely in the case of an object before them [2]. Two important parameters need to be known when calculating stopping distance:

1. Tunnel lighting design speed (TLDS);
2. The highest road slope value of the road within the tunnel design limits at the tunnel entrance and exit.

Calculation of stopping distance is shown below in expression (1). The first sum parameter indicates the distance elapsed from the time the driver notices the object ahead of them until the time the driver applies the brakes; the second sum indicates the distance covered by the car after applying the brakes and coming to a stop covers until stop.

$$SD = u \cdot t_0 + \frac{u^2}{2 \cdot g \cdot (f \pm s)}, \tag{1}$$

where,

- SD is stopping distance,
- u is tunnel lighting design speed [m/s],
- f is friction coefficient,
- t_0 is reaction time,
- s is road slope,
- g is gravitational acceleration [m/s^2].

The worst road slope for a sample tunnel stopping distance calculation, s = 0.5 %, and tunnel

lighting design speed, u = 70 km/h, was used. Friction coefficient f is taken as 0.35. Reaction time, t_0 is taken as 1 s. Stopping distance SD was calculated using equation (1):

$$SD = 75.25\text{m}, \tag{2}$$

2.2. The Calculation of the Threshold Zone Luminance Value

In all calculations related to tunnel lighting design, the determinant parameter is threshold luminance value (L_{TH}). This value is calculated by applying the perceived contrast method suggested by CIE088 publication [2]. This method involves first, drawing homocentric circles on the "special photograph", which is taken from a point designated to show length of stopping distance from tunnel entrance, to represent "driver's angle of view", and then conducting an evaluation of these measures in terms of luminescence. In this method, 10 homocentric circles need to be drawn on the special photograph [2].

Circles were obtained via graphical method by drawing the α angle at 2°, 3°, 4°, 5.8°, 8°, 11.6°, 16.6°, 24°, 36° and 56.8°, as shown in Fig. 1. Table 1 shows the calculated diameters of circles to be drawn based on the width of the tunnel entrance and the value corresponding to the photograph, with respect to the angle of the spaces.

Fig.2. shows the circles drawn on the photograph. The circle with the largest diameter was divided into parts by drawing 12 lines with a 30° angle passing through the centre. Perceived luminance values corresponding to these parts were calculated. The calculation of the luminance value was done based on the values in Table 2. Circles were numbered from 1 to 9, starting from the centre and moving outwards. Every outer circle, which was divided into 12 equal parts, was numbered from 1 to 12 in a clockwise direction starting from the top.

L_{seq} (total equivalent veiling luminance level, cd/m^2) is the function of the sum of luminance of the parts, except the largest two and smallest two parts obtained by drawing lines on 10 equivalent circles with an angle of 30°, since these parts are assumed to be outside of visual fields.

$$L_{seq} = 5{,}1.10^{-4} \sum L_{ije}, \tag{3}$$

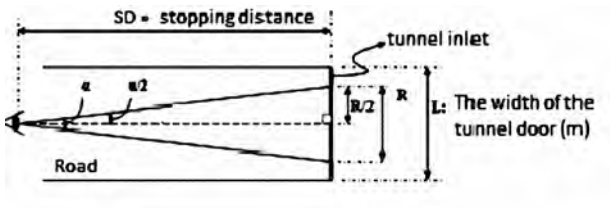

Fig 1. Top view of angle-diameter-tunnel entrance width

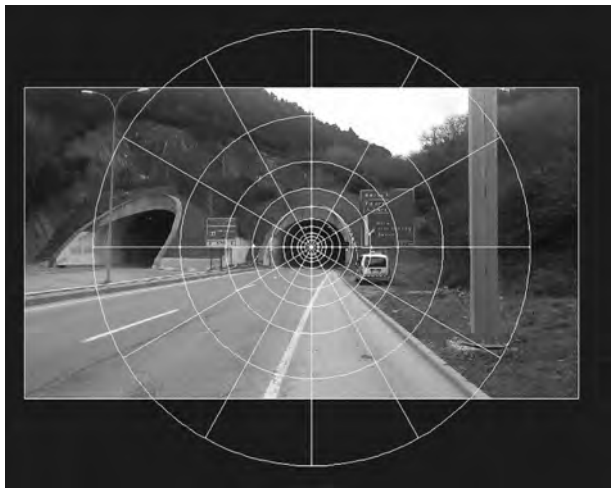

Fig.2. Circles drawn on the photograph of the Istanbul Beykoz tunnel entrance

Table 1. Diameters of circles

Angle α	Stopping Distance, *SD*, m	Diameters *R*, m	Calculated diameters of circles, m
2	75	2,62	13,09
3	75	3,93	19,64
4	75	5,24	26,19
5,8	75	7,60	37,99
8	75	10,49	52,45
11,6	75	15,24	76,18
16,6	75	21,88	109,41
24	75	31,88	159,42
36	75	48,74	243,69
56,8	75	81,10	405,52

$$L_{ije} = \tau_{ws}.L_{ij} + L_{ws}, \tag{4}$$

$$L_{TH} = \frac{L_M}{\frac{1}{C_m}\left(\frac{\rho}{\pi.q_c} - 1\right) - 1}, \tag{5}$$

Table 2. Examples of luminance at tunnel portals [2]

Driving direction (Northern hemisphere)	L_c (sky) kcd/m²	L_r (road) kcd/m²	L_e (environment) kcd/m²			
			Rocks	Buildings	Snow	Meadows
N	8	3	3	8	15 (V) 15(H)	2
E-W	12	4	2	6	10 (V) 15(H)	2
S	16	5	1	4	5 (V) 15(H)	2

$$L_m = \frac{\left(\tau_{ws}.L_{atm} + L_{ws} + L_{seq}\right)}{\left(\tau_{ws}.\tau_{atm}\right)}, \quad (6)$$

where

L_{seq} is the total equivalent veiling luminance level [cd/m²],

L_{ije} is the luminance of each part in front of the eye in the vehicle [cd/m²],

L_{ij} is the average luminance of each part measured in front of wind screen, outside of the vehicle [cd/m²],

L_{ws} is the "cover luminance" in the vehicle's wind screen [cd/m²],

L_m is the total luminance in front of the eye [cd/m²],

τ_{ws} is the transmission factor of the vehicle's wind screen,

ρ is the reflection factor,

q_c is the contrast revealing coefficient,

C_m is the perceived contrast value.

If the measurement was not able to be performed for the design part, values indicated by the CIE088 publication were accepted. Atmosphere permeability $\tau_{atm} = 1$, the permeability of wind screen $\tau_{atm} = 0.8$, and reflection factor of a dangerous object is equal to 0.2. "Contrast factor" can be "min 0.6" in an opposite direction system and "max 0.2" in a symmetric system. Luminensence values of the surrounding the environment are shown in Table 2. It is suggested that minimum value of perceived contrast value, C_m, be 28 % and have a negative value [2].

$$L_{ije} = \tau_{ws}.L_{ij} + L_{ws}\ , \quad (7)$$

$$L_{ije} = 146{,}58 \text{ cd/m}^2, \quad (8)$$

$$L_{seq} = 74{,}756 \text{ cd/m}^2. \quad (9)$$

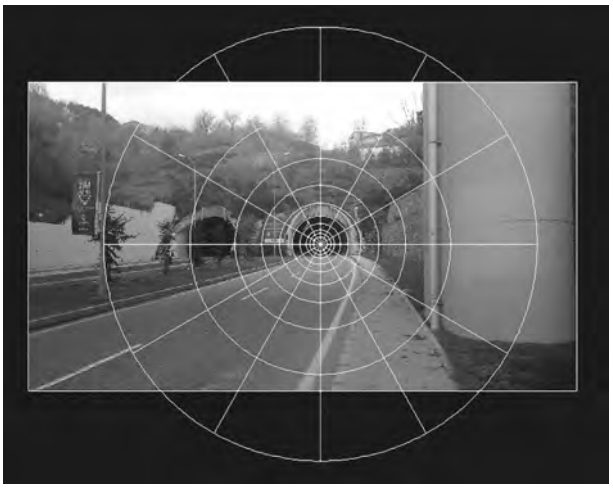

Fig.3. Circles drawn on the photograph of the Istanbul Kavacık tunnel entrance

Calculation of L_{TH} is performed after calculating L_{seq} value.

Using equation (6),

$$L_m = 320{,}94. \quad (10)$$

Using equation (5),

$$L_{TH} = 146{,}4 \text{ cd/m}^2. \quad (11)$$

Value of L_{TH} at the Beykoz tunnel entrance was found to be equal 146.4 cd/m². However, for the ease of the calculations, $L_{TH} \cong 146$ cd/m² was used. Likewise, in the calculation performed for the Kavacık tunnel entrance, $L_{TH} \cong 133$ cd/m² was used. Values obtained based on the calculations are listed below:

L_{th}: 146 cd/m² Beykoz tunnel entrance (First tube)

Table 3. The fifth step luminance value

Luminance	Average (A), cd/m²	Min/Avr, %	Max/Avr, %	Min, cd/m²	Max, cd/m²
Putative observer-1 (–60.00;1.88;1.50)	3,48	69,06	50,78	2,4	4,73
Putative observer-2 (–60.00;5.63;1.50)	3,48	69,06	50,78	2,4	4,73

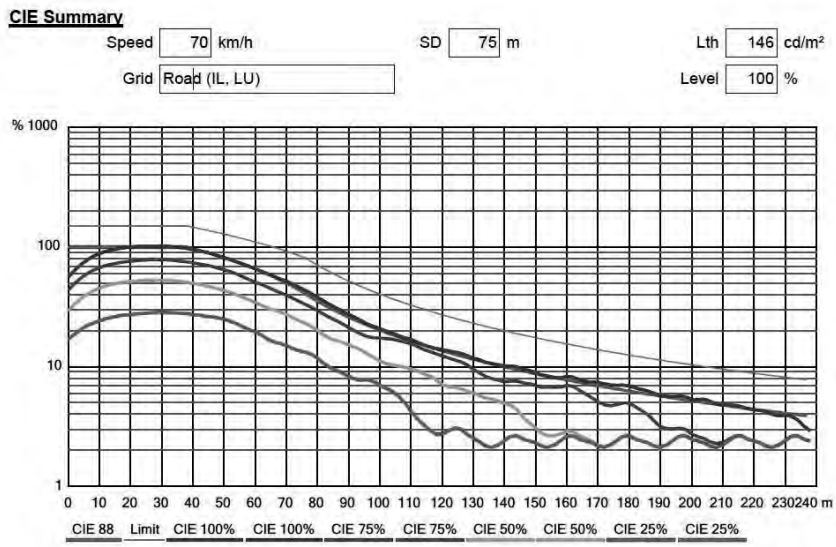

Fig.4. CIE088 curves for first tube

L_{th}: 133 cd/m² Kavacık tunnel entrance (Second tube)

$L_{interior\ part}$: 3.45 cd/m² (Interior Part Lighting Luminance Value)

L_{night}: 1.74 cd/m² (Night Lighting Luminance Value)

2.3. Luminance Values of Lighting Levels

The stepped system was designed for the provision of variable luminance values in the lighting of the tunnel. At the same time, the lowest level luminaires at the low luminance level were used to provide energy efficiency and obtain a desirable luminance value.

The design was composed of as six steps in accordance with CIE publication [2]. These steps are 100 %, 75 %, 50 %, 25 %, daytime and night steps. The step values of the first tube of the sample tunnel were as follows:

1. Step $L_{100\%}$: 146 cd/m²,
2. Step $L_{75\%}$: 109.5 cd/m²,
3. Step $L_{50\%}$: 73 cd/m²,
4. Step $L_{26\%}$: 36.5 cd/m²,
5. Step $L_{daytime}$: 3.45 cd/m²,
6. Step L_{night} : 1.74 cd/m².

Based on the standards, the Fifth Step $L_{daytime}$ is shown as 3.48 cd/m² (Table 3), and the Fifth Step luminance value in the sample tunnel was found to be 3.45 cd/m². Since 3.48 is larger than 3.45 cd/m², the latter value can be chosen for daytime step in accordance with the standards.

Based on the calculations, sixth step L_{night} was found to be equal to 1.74 cd/m², the same as the average value in Table 4.

The conformity to the CIE-088 standard of all steps was tested according to the CIE curves. The CIE-088 curve is highlighted in red and indicates the desired luminance level throughout the tunnel for the ideal design. The limit curve, highlighted in orange, is the maximum luminance level that should not be exceeded in any of the steps. In addition to the red and orange highlighted curves, the 100 % step, 75 % step, 50 % step and 25 % step are highlighted in blue, green, yellow and pink, respectively (see p.68). Luminance level curves obtained after applying the LED lamp design are given for the first tube and the second tube in Figs.4,5 respec-

Table 4. The sixth step luminance value

Luminance	Average (A), cd/m^2	Min/Avr, %	Max/Avr, %	Min, cd/m^2	Max, cd/m^2
Putative observer-1 (–60.00;1.88;1.50)	1,74	69,06	50,78	1,2	2,37
Putative observer-2 (–60.00;5.63;1.50)	1,74	69,06	50,78	1,2	2,37

tively. In both curves, as one-to-one luminance levels of the CIE088 curve at 100 % step were able to be obtained. It was determined that lighting design and luminaire numbers for both tubes were in accordance with the standards.

3. COMPARISON OF THE LUMINAIRES WITH HIGH POWER LEDs AND SODIUM VAPOUR LAMPS

The lighting design with high power LED luminaires was developed using Tunnel v3 Computer software.

At the completion of the design, it was determined that 140 and 128 LED lamps had 213 W power and 700 mA nominal drive current for the first tube and the second tube, respectively; 102 and 128 LED lamps had 75 W power and 500 mA nominal drive current for the first tube and the second tube, respectively. The unit energy consumption of luminaires using LED lamps with 700 mA nominal current was 213 W·h, while the unit energy consumption was 75 W·h using LED lamps with 500 mA nominal drive current.

In the sample tunnel, to date, high pressure sodium vapour lamps using 400W and 150W power have been used in luminaires. The number of luminaires using lamps having 400W is 64 and the unit energy consumption of such luminaires with ballast and blaster is 434.5 W·h. On the other hand, the number of luminaires using lamps having 150 W is 44 and the unit energy consumption of such luminaires with ballast and blaster is 170.6 W·h [10].

The comparison of the annual energy consumption of high power LED luminaires and the high pressure sodium vapour lamps used in the sample tunnel is shown in Table 5. Energy consumption values of the sample tunnel were obtained from the Istanbul Tunnel Management and Operations [10].

Based on the annual operation time, energy consumption is 207563 kWh when sodium vapor lamps are used, while it is 113096 kWh when LED lamps are used. From these results, it is clear to see that LED luminaires provide 45.5 % in energy savings, a significant figure, considering that most countries are in the process of trying to reduce as much as possible their energy consumption to very low values by applying energy efficiency programs.

The 45.5 % value achieved in energy savings with the use of LED luminaires in the sample tunnel is a considerably high number when taking into account the importance of conserving energy in today's world.

CONCLUSION

In the present study, a stepped lighting system, using automated high power LED luminaires was designed for an urban tunnel. The luminance values obtained from the design coincide with the CIE curves in the CIE088:2004 Guide for the Lighting of Road Tunnels and Underpasses. The results of the study found that the LED lamp based lighting design achieved the luminance values specified by the International Commission on Illumination.

Stopping distance was calculated as 75.27 m, while threshold luminance values were found to be 146 and 133 cd/m^2 for the first tube and the second tube, respectively.

In the study's sample tunnel, lighting is performed by high pressure sodium vapor lamps. Calculations were conducted in this study to determine the change in energy efficiency between the use of high pressure sodium vapour lamps and LED luminaires.

It was observed that the annual energy consumption would decrease by 45.5 % should the currently used high pressure sodium vapour lamps be replaced with high power LED lamps. As a majority of countries have sought to discover new ways to decrease their energy consumption and CO_2 emissions, the 45.5 % in energy savings achieved by LED lamps is considerably significant. LED lamps are a viable, easy- to- use alternative for tun-

Table 5. Energy consumption values based on the steps [10]

Steps	Annual Operation Time, h	Sodium Vapour Lamp		LED Lamp	
		Power, W	Consumption, kW·h	Power, W	Consumption, kW·h
Night	8760	399	82335	2925	25623
Daytime	4400	9399	41356	2925	12870
25 %	3500	8829	30902	7668	26838
50 %	2800	8828	24718	7542	21118
75 %	2000	8829	17658	8694	17388
100 %	1200	8828	10594	7716	9259
Total			207563		113096

nel lighting due to their longer life spans, higher colour rendering and higher efficiency factors compared to other lamps.

REFERENCES

1. Simons, R.H., Bean, A.R., Tunnel lighting. Lighting Engineering, Applied Calculations, 2001, pp. 402–410.

2. CIE International Commission on Illumination, Technical Report-88, Guide for the Lighting of Road Tunnels and Underpasses, 2004.

3. Navigant Consulting Inc., Energy Savings Potential of Solid –State Lighting in General Illumination Applications. U.S. Department of Energy, Office of Energy Efficiency and Renewable Energy, Building Technologies Program, Washington, DC, 2012.

4. Mottier P. LEDs for lighting applications, John Wiley& Sons, 2009.

5. Lenk, R., Lenk C. Practical lighting design with LEDs, John Wiley& Sons, 2011.

6. Ding X., Li Y., Li Z., Tang Y., Yu B., Yuan D. Application of heat pipe heat sink for high power LED lambs, Applied Mechanics and Materials, 2014, volumes 602–605, pp. 2713–2716.

7. Leung, H.M.S. LED lighting application in long railway tunnels, The Hong Kong Institution of Engineers Transactions, 2012, vol. 19, No.4, pp 42–46.

8. Cengiz, M.S., Rüstemli S. The relationship between height and efficiency and solution offerings in tunnel and sub-sea tunnels, Light& Engineering, 2014, vol. 22, No.2, pp. 76–83.

9. http://www.schreder.com.eg/en-egs/LearningCentre/Dossiers/Pages/Optimum-safety-for-LED-tunnel-lighting-solutions.aspx.

10. Istanbul Tunnel Management (ISBAK) http://tunel.isbak.com.tr/

Canan Karatekin,
Dr. of Electrical Engineering, graduated from Istanbul Technical University, Department of Electrical Engineering in 1993. At present, she is working at Istanbul Technical University as an Assistant Professor

Light & Engineering
Vol. 25, No. 4, pp. 76-79, 2017

Svetotekhnika
No. 4, 2017, pp. 65–67

POWERFUL PULSE IR SEARCHLIGHT

Boris I. Avdochenko, Yuri R. Kirpichenko, and Ivan N. Pustynsky

The Tomsk State University of Control Systems and Radio Electronics, Tomsk
E-mail: AvdochenkoBI@rzi.tusur.ru

ABSTRACT

The idea of upgrading serial continuously operating IR searchlights to work in pulse mode with a big relative pulse ratio is considered. A technique for establishing a maximum permissible pulse radiation flux without detriment to the searchlight's reliability is presented. An example of such upgrade is given. A 36-fold increase of the IR searchlight pulse radiation flux is obtained. This increase has essentially strengthened IR illumination (IR "local illumination") of television observation objects, on retention of the power supply output and reduction of optical noise influence. The main characteristics of the upgraded IR searchlight are as follows: pulse radiation flux is more than 460 W and pulse duration is (0.15–10) μs.

Keywords: IR searchlight, pulse mode, increase of radiation flux, technique of determining limit radiation flux

1. INTRODUCTION

Powerful pulse IR radiation sources are broadly used in dual purpose optical systems. Powerful pulse IR diodes (IRD), which have lately appeared with nanosecond switching time, are gradually forcing laser radiators out from the IR illumination devices group. The IRDs have a lower cost, longer life time, and allow obtaining better images of illuminated objects due to a lesser monochromaticity of the radiation. The use of an active pulse observation mode in this case gives considerable benefits when working under conditions of limited visibility and of strong optical noise, as well as providing increased stealth of observation.

The main problems of high power IR searchlight (IRS) development, which limit their application are forming a necessary radiation indicatrix for a large number of IRDs and the complexity of implementing as much as possible permissible radiation flux of every IRD with a preset radiation pulse duration.

To solve the first problem, focusing lens systems are used in IRD to summarise IRS radiation fluxes by selection of placing the latter and the distance between them and the lenses. Development of such complex focusing systems is reasonable for serial IRSs production, however, in some cases it is more practical to modify continuous operation serial IRSs with ready focusing systems for pulse operation mode.

To solve the problem of maximising pulse radiation flux (PRF), it is necessary to know the corresponding IRD watt-ampere characteristics in pulse operating mode, which are absent from the reference books. Manufacturers as a rule advertise the power consumption, pick-up range and IRS radiation indicatrix. The lack of information on reported characteristics and often their discrepancy with real values, makes it necessary to determine experimentally the maximum IRD PRF for a preset pulse duration.

The purpose of this paper is to assess the possibility of upgrading serial continuous operation IRSs for pulse mode work with as high as possible permissible PRF without detriment to the IRS's work. To achieve this purpose, a technique of determining possible limits of a specific IRD (1), pulse power supply circuit to obtain maximum PRF for

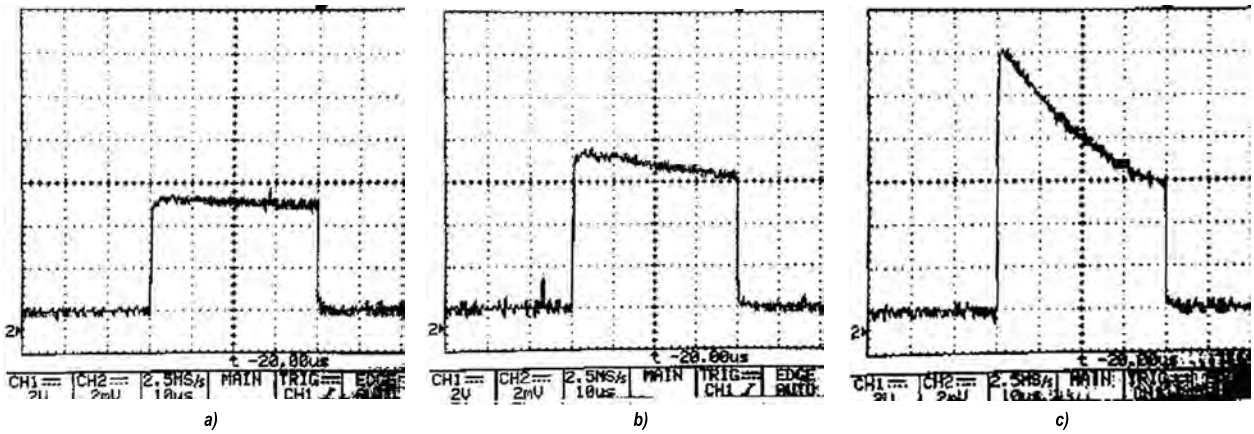

Fig. 1. Voltage oscillograms at the photodetector output:
a – a weak heating of the diode crystal, b – highest permissible heating of the diode crystal,
c – temperature of the crystal is higher than permissible

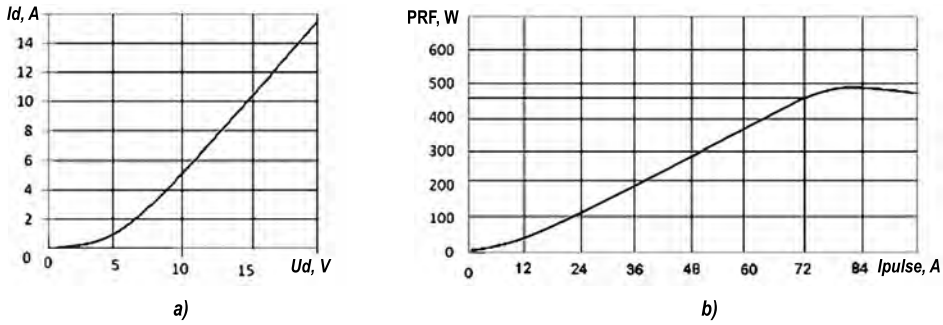

Fig. 2. Experimental characteristics of the pulse mode:
a – voltage-current characteristic of IR diodes, *b* – watt-ampere characteristic of IR searchlight

parallel-series IRD connection (2) and structure of modified IRS (3) are developed. The characteristics of the latter are also studied.

2. TECHNIQUE FOR DETERMINING DIODE PULSE IR RADIATION FLUX LIMIT

The radiation level of powerful IRDs increases linearly with growth of their forward current until a certain temperature increase of the crystal active area. In the continuous operation mode, IRD maximum radiation flux is limited by its active area resistance increase with the crystal warming-up, which reduces IRD efficiency down to several percent. In the case of power supply big relative pulse duration in the event of "quasicold" operation mode, IRD warming-up is almost excluded, and its peak PRF can be increased proportionally with relative a pulse duration of the forward pulse current by tens and hundreds times [1].

However, with excessive amplitudes and pulse duration of the power supply, IRD total failure is possible even in case of single pulse power supply.

The process of the IRD crystal warming-up can be visually observed in the change of the IRD PRF configuration when supplying pulse current. The decrease inefficiency as a result of the warming-up is connected with an increase of PRF peak decrease level, Fig. 1. The crystal temperature is close to its limit when this decrease achieves a critical level (30 % – 50 % depending on the IRD structure), though the IRD case temperature at a big relative pulse duration can be low. In such a mode, duration of the no-failure operation noticeably decreases.

It can be determined experimentally that the PRF oscillogram peak decrease level of (10–15)% allows obtaining PRF maximum output without detriment to the IRS lifetime and efficiency. With a preset duration of the optical pulse, such a decrease determines the limit pulse current of a specific IRD and its voltage. As an example, we will consider IRS upgrade of the PIK-10 type developed by Tireks Research-and-Technology Company, with

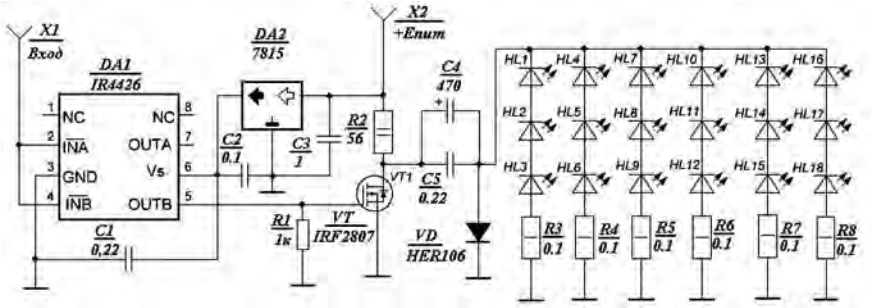

Fig. 3. Electric circuit of the searchlight with power supply switch

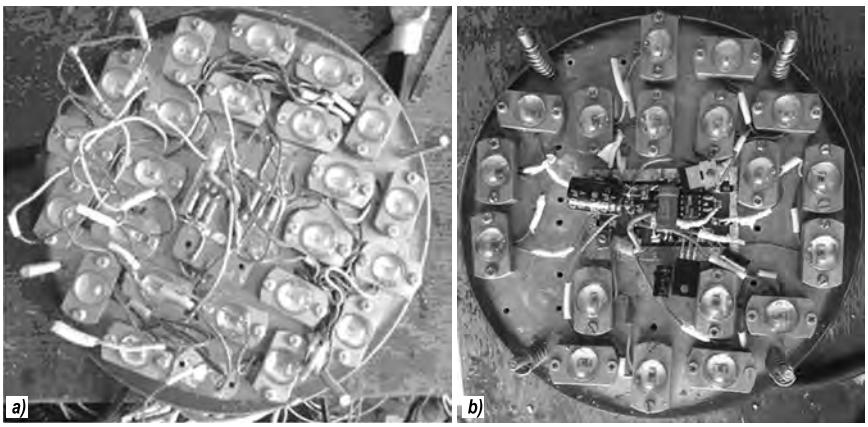

Fig. 4. Appearance of the searchlight with optical system removed before (a) and after upgrade (b)

a continuous radiation flux (wave length is 850 nm) of (700–800) mW power of every used IRD, with forward current of 800 mA and power consumption of 4 W. The device containing 24 IRDs provides (17–20) W radiation flux in a continuous mode. Experimentally measured current-voltage curves of separate IRDs in pulse mode with pulse duration of 10 μs, relative pulse duration of more than 100 and optical pulse peak decrease level of 20 % are given in Fig. 2a. Watt-ampere characteristics of the searchlight consisting of 18 IRDs in pulse mode are given in Fig. 2b. It can be seen from Fig. 2 that as a whole, in this case maximum power supply pulse current of a single IRD I_d amounted to 12 A with its voltage U_d of *17 V*, and IRS PRF in pulse mode was 460 W (general power supply pulse current I_p = 72 A), i.e. at a smaller IRDs number (18 instead of 24) it increased by an order of 36.

3. SEARCHLIGHT CIRCUIT

The modified IRS is manufactured as two units: a generator of control pulses and searchlight itself with a power supply switch (Fig. 3). The pulse generator consists of a network power supply, a pulse-train generator with repetition frequency tuning, a master pulse shaping unit, an electronic delay line and of a pulse duration shaping unit [2].

For PRF adjustment, to obtain a maximum object image contrast under different observation conditions, a switch supply voltage adjustment is used [3]. The highest permissible IRD pulse current with power supply voltage of 56 V, is 75A.

When upgrading the PIK-10 type IRS for pulse mode operation, special attention was given to minimising conductor inductance in the VT1 transistor output current circuit. The switch is installed into the IRS case at the current stabiliser place. To decrease the inductance, location of the switch elements was optimised, IRD conductors were shortened, and cross section of the printed circuit board conductors was increased by additional conducting bundle soldering. The lower side of the printed circuit board is metallised and connected to the general wire and to the IRS case. *DA1* microcircuit power supply leads are blocked with chip capacitors with a low inner inductance. IRS pictures with the removed optical system before and after the upgrade are given in Fig. 4.

A modified IRS view with installed optical system is shown in Fig. 5a, and a light spot configuration obtained using this system is shown in Fig 5b.

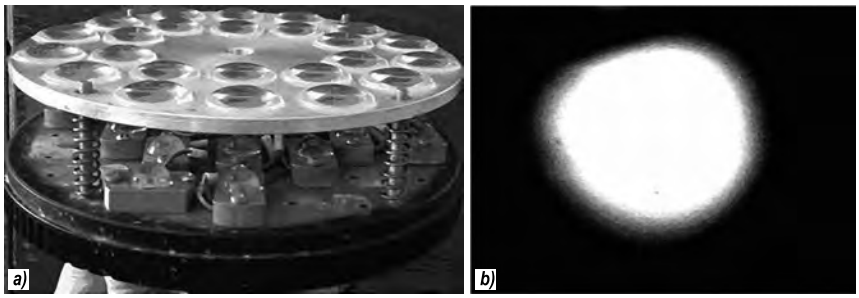

Fig. 5. Appearance of the searchlight with installed optical system and configuration of the light spot

The diameter of the light spot at a distance of 2m is 40cm, which corresponds to the rated indicatrix of the "initial" IRS radiation.

4. RESULTS OF THE SEARCHLIGHT UPGRADE

The modified IRS is used in an active pulse television observation system. The pulse parametres are adapted to the observation conditions using change of frequency, of input pulse duration and of puwer supply voltage. Radiation output pulse duration is adjusted within (0.15–10) μs, and PRF value – within (10–460) W. Maximum pulses repetition frequency is limited by their relative pulse duration and with pulse duration of 1 μs, it should not exceed 10 kHz. The radiation angle of the modified IRSs does not exceed 12°.

5. CONCLUSION

The presented technique allows obtaining a maximum PRF of the modified IRSs at radiation output pulse preset duration and repetition frequency with retention of operational reliability. A high PRF of the modified IRS allows replacing continuous operational IRSs with pulse IRSs in many application aspects and improving image quality of the illuminated (IK-highlighted) observation objects.

REFERENCES

1. Avdochenko B.I., Vilisov A.A., Pushkarev V.P., Teplyakov K.V., Yurchenko V.I. A source of powerful optical pulses using infrared interval wave length diodes // Semiconductor lighting engineering, 2010, #3, pp. 53–55.

2. Avdochenko B.I., Titov A.A., Pushkarev V.P. Generator of videopulses // Radiolubitel, 2008, #7, pp. 32–33.

3. Avdochenko B.I., Vilisov A.A., Pushkarev V.P., Teplyakov K.N., Yurchenko V.I. Pulse IR searchlights with controlled power / A collection of reports of the 18th International scientific and technical conference "Radio-location, Navigation and Communication (RLNC*2012) ", Voronezh, 2012, V. 1, pp. 190–195.

Boris I. Avdochenko, Prof., Doctor of Technical Science, graduated from the Tomsk Institute of Radio Electronics and Electronic Engineering (TIRET) in 1971. At present, he is the Professor of the Chair of Radio Electronics and Information Protection of the Tomsk State University of Control Systems and Radio Electronics (TUSUR)

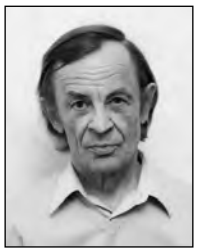

Yuri R. Kirpichenko, Ph.D. Graduated from the Tomsk Institute of Automated Control Systems and Radio Electronics, and at present – Associate Professor of the Chair of Television and Control of the Tomsk State University of Control Systems and Radio Electronics (TUSUR)

Ivan N. Pustynsky, Prof., Doctor of Technical Science. Graduated from the Radio Engineering Faculty of the Tomsk Polytechnic Institute in 1956. At present, he is the Professor of the Chair of Television and Controls of the Tomsk State University of Control Systems and Radio Electronics (TUSUR) and Honoured Worker of Science and Technology of the Russian Federation

Light & Engineering
Vol. 25, No. 4, pp. 80-85, 2017

Svetotekhnika
No. 4, 2017, pp. 14–18

PHOTOMETRY OF LED LIGHTING DEVICES

Tony Bergen

Photometric Solutions International Pty Ltd, Melbourne, Australia
E-mail: tonyb@photometricsolutions.com

ABSTRACT

LEDs have drastically changed the way that we do lighting. They are dynamic, versatile and colourful. They can easily be dimmed, tuned and pulsed; they are rugged; they have long lifetimes; and in different combinations they can make vivid and interesting shapes as well as engaging and vibrant illuminated scenes.

But they also create problems when it comes to measurement and standardisation. Not all of these problems are particularly new or unique, but they have become more significant or apparent with the advent of LED lighting and require careful consideration. This paper highlights some of the issues facing photometric laboratories in the testing of LED lighting devices and underscores the importance of standardization.

Keywords: photometry, LED photometry, LED standardization

1. SPECTRAL MISMATCH ERRORS

Fig. 1 shows the relative luminous efficiency *V (λ)* curve, which is the spectral luminous efficiency function for photopic vision. This function forms the basis for all photometry: it is representative of how our eyes see light, and photopic detectors such as luxmeters and luminance meters are designed to match this function. Also in Fig.1, an incandescent lamp spectrum which is indicative of the light source that we use to calibrate photometers (an incandescent source with a correlated colour temperature of 2856 K) is presented.

However, the spectrum of LED lamps is very different to the spectrum of the source used for calibrations. Because the spectral response of the photometer is never perfectly matched to the ideal *V (λ)* function this results in errors in the measurement which are called spectral mismatch errors. The size of the error depends on the spectral response of the detector and the spectrum of the source being measured.

Fig.2 (left) shows the *V (λ)* function along with the spectral response of a hypothetical detector that has a poor match in the blue part of the spectrum and the spectrum of a cool white LED. Although the spectral mismatch is high in the blue and there is a significant blue peak, the *V (λ)* function is low in the blue and so the contribution of the blue component to the luminous value is much lower than the longer wavelengths – approx. 1/17th – which

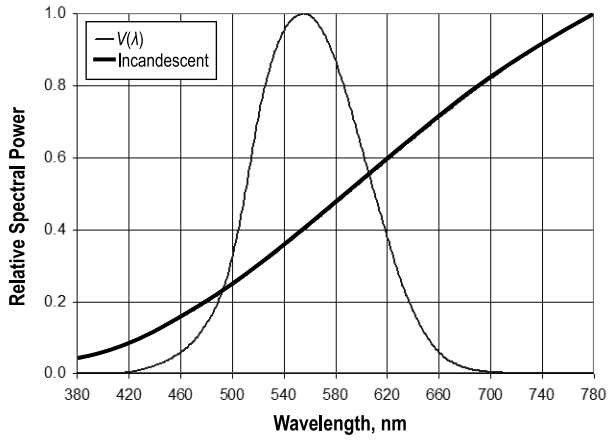

Fig.1. The *V (λ)* curve, which forms the basis of photometry, and the spectrum of an incandescent source usually used for photometer calibrations

limits the error and so in this case the error in measurement will be around 3 %. Another hypothetical detector, which is poorly matched in the red part of the spectrum, is shown in Fig.2 (b). Here the entirety of the spectral distribution is in the part of the spectrum where the detector is poorly matched and in this case the error in measurement will be around 20 %. This example highlights the fact that spectral mismatch is a much more significant issue for coloured LEDs compared with white LEDs, but still for best quality measurements we should take this into account and make corrections if possible for measurements of white LEDs.

More information regarding calibration of photometers, including determination of the spectral mismatch error, is given in reference [1]. Krüger and Blattner [2], offer a method of estimating the likely maximum spectral mismatch error that could be encountered for measurement of white LED sources based on the photometer's f_1' value.

2. PULSE-WIDTH MODULATED SOURCES

LED sources are often pulse-width modulated (PWM) for thermal management and output dimming control. While this is a nice innovation that is very useful for lighting designers, it can make life difficult for photometrists. The PWM effectively means that the source is being switched on and off rapidly many times per second and so, depending on the duty cycle, the instantaneous luminous intensity can be zero for a large proportion of the time. This has significant effect on the stability of our measurements if the measurement timing isn't precise. See for example the graph of instantaneous luminous intensity vs time for an LED torch with two levels of operation shown in Fig.3.

When the torch is operating in low power mode, its peak luminous intensity is actually higher than when it is operating in high power mode. This is likely because of thermal conditions – the output is only on for a short time in low power mode and it drops to zero in between. The measurements of these two modes of operation are shown in Table 1.

As Table 1 shows, even though the peak luminous intensity in low power mode is 24 % higher than the peak luminous intensity in high power mode, because the duty cycle is so low the amount of luminous energy emitted is smaller. When the

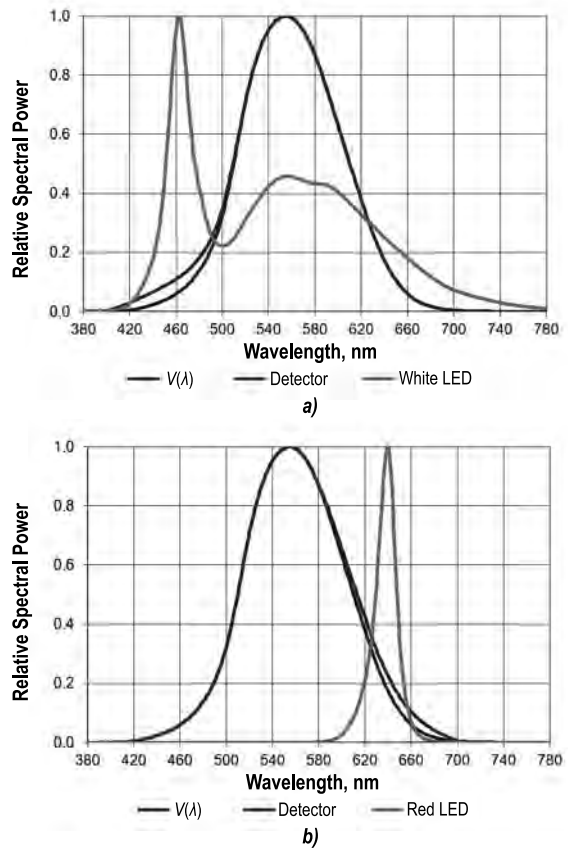

Fig.2. Examples of detectors, which are poorly matched to the *V (λ)* function with a white LED spectrum (a) and with a red LED spectrum (b)

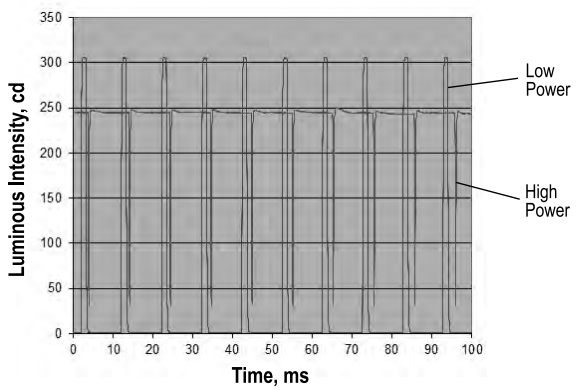

Fig.3. Graph of instantaneous luminous intensity vs time for an LED torch with two levels of operation

data is averaged over a 100 ms time interval it can be seen that the luminous energy of the output in high power mode is around six times higher than the output in low power mode, hence we see the high power mode as a brighter source.

Photometers are normally designed to measure light with measurement durations (integration times) that are an integer multiple of the period of the mains line power cycle. So in 50 Hz environ-

Table 1. Summary of measurements of the LED torch with output shown in Fig.3.

Parameter	Low Power Mode	High Power Mode
Peak luminous intensity:	306 cd	247 cd
Duty cycle:	13.1 %	98.2 %
Luminous energy over 100 ms interval:	3.94 cd.s	24.0 cd.s

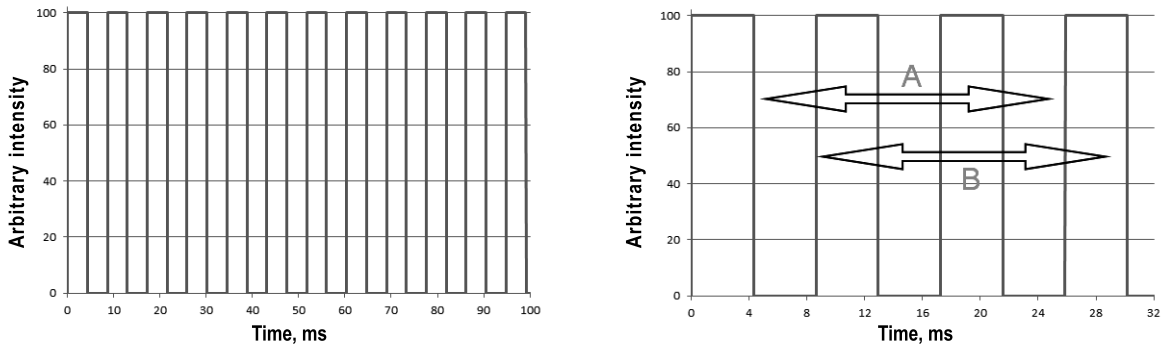

Fig.4. Hypothetical source with PWM frequency 116 Hz, 100 cd amplitude and 50 % duty cycle (left) and two measurements of this source with different starting times (right)

ments this will be 20 ms or 40 ms or 100 ms etc. Imagine that a photometer which has a 20 ms integration time is measuring a hypothetical source with a 116 Hz PWM frequency (period = 8.62 ms), 100 cd amplitude and 50 % duty cycle as shown in Fig.4 left.

Fig.4 right shows an expanded sample of the start of Fig.4 left along with two measurements of 20 ms integration time with different starting times. Measurement A would measure two complete pulses whereas measurement B would measure 2.6 pulses and so would be 30 % higher than measurement A, even though they are measuring the same source. We can analyse this further by dividing the 100 ms sample of Fig.4 left into five separate 20 ms readings, as shown in Table 2.

The average of the values shown in Table 2, which corresponds to a single measurement of 100 ms duration, is 51.7 cd. The true (long-term) average luminous intensity should be 50 cd (100 cd with 50 % duty cycle), so even a measurement of 100 ms duration has an error of 3.4 %.

The correct procedure in this case is to adjust the integration time of the photometer so that it matches the period of the source being measured. If the photometer integration time can be set to 8.62 ms or 17.24 ms or 34.48 ms etc. then it will be correctly sampling the source. Often a PWM frequency is not known and so the optimum integration time needs to be determined by experiment – adjust the integration time until fluctuations in measurements of the source are minimised.

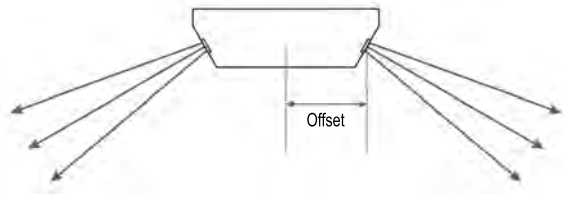

Fig.5. Mock-up of a road lighting luminaire consisting of separated LED modules

3. DIRECTIONALITY OF LED SOURCES

Measurements of luminous intensity distributions using far-field goniophotometers assume that the luminaire is "small" compared with the test distance. There are guidelines for what test distance should be used, for example CIE121:1996 [3] states that in general "the test distance should not be less than 15 times the maximum dimension of the light emitting area of the luminaire" (referred to as the 15: 1 rule) but this can be reduced to "5 times the dimension of the light emitting area parallel to the lamp axis" for sources with near-Lambertian (cosine) distributions (the 5: 1 rule).

However, Bergen and Jenkins [4] showed that even when we use these test distance guidelines when measuring LED luminaires made up of individual LEDs or modules or arrays separated by large

Table 2. 20 ms samples of the hypothetical source shown in Fig.4 left

Measurement time interval	Measurement result
0 ms to 20 ms	56.9 cd
20 ms to 40 ms	50.9 cd
40 ms to 60 ms	43.1 cd
60 ms to 80 ms	55.1 cd
80 ms to 100 ms	52.7 cd

non-luminous areas, we can encounter significant errors. Consider a mock-up of a road lighting luminaire shown in Fig.5. Even though this may seem to be an extreme case, the author has seen examples of road lighting luminaires like this, that have separate LED modules to produce highly directional beams in the direction of the intended throw of the luminaire on either side.

When it is being measured on a goniophotometer, the luminaire will be positioned so that its photometric centre is at the reference point of the goniometer. But when the goniophotometer is measuring the part of the beam in the direction of the arrows shown in Fig.5, the light is clearly coming from a distance closer to the detector than the reference position of the goniometer. This can create measurement errors which are more significant when the test distance is short, but even when using the 15: 1 rule for test distance, an error of up to 6.1 % in beam peak intensity could be encountered for a road lighting luminaire with a beam centre elevation angle of 60° [4].

There is a further error that can be encountered, and that is the determination of the cut-off angle or the beam centre angle of the luminaire; for this refer to Fig.6. The luminaire's cut-off angle is shown by the angle A in Fig.6, however, the goniophotometer will measure it at angle B. Although Fig.6 is highly exaggerated because the detector is very close, the errors encountered in practice can still be significant: when using the 15: 1 rule for test distance the error in beam centre elevation angle could be up to 0.96° [4].

Bergen and Jenkins [4] introduce the idea of a "D + S" in the determination of the minimum test distance required, where the maximum width of any non-luminous areas (S) is added to the luminous size of the source (D) when calculating the test distance. For the mock-up luminaires shown in Fig.5

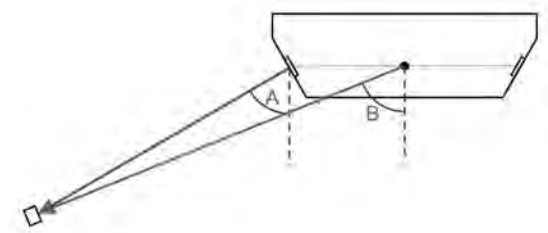

Fig.6. Mock-up of a road lighting luminaire showing incorrect determination of cut-off angle or beam centre angle

and Fig.6, the non-luminous space S is approximately equal to the total width of the light emitting area D and so the required test distance is practically doubled. This "D + S" concept is incorporated into the requirements for test distance for goniophotometry in CIE standard S025 [5] for photometry of LED lamps, LED modules and LED luminaires.

4. VARIATION OF COLOUR WITH ANGLE

Traditional sources, i.e. fluorescent, incandescent and HID lamps and luminaires containing such lamps, have an output whose colour is usually reasonably invariant with angle. This means that in a room full of luminaires with the same type of lamps, or in a roadway lit by an array of road lighting luminaires with the same type of lamps, the colour of the luminaires will look reasonably consistent. This is not always the case with white LEDs where, although there has been improvement in recent years, the output of an LED lamp or luminaire can vary considerably with angle and so the eye can often easily detect a colour variation when looking across a room lit by LED devices. Fig.7 shows

This variation in colour with angle means that it is now required to measure the chromaticity of LED

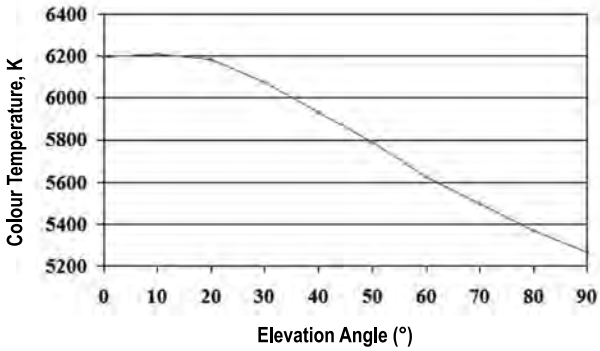

Fig.7. Example of how the correlated colour temperature of an LED lamp may vary with angle from the lamp axis

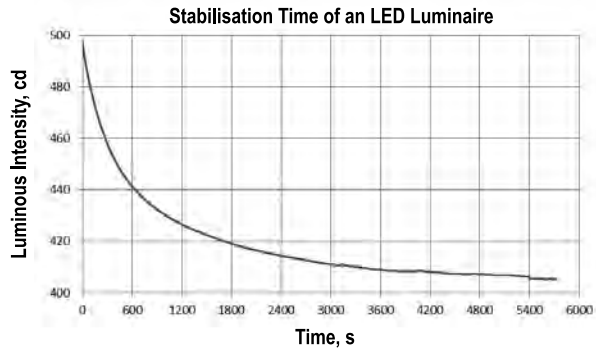

Fig.8. Decrease in luminous intensity of an LED lighting device as it warms up

lighting devices at different angles from the device in order to determine the colour spatial uniformity. Thus goniospectroradiometry has become more commonplace and now it is standard to install a spectroradiometer as well as a photometer in a goniophotometer. Methods of determining the colour spatial uniformity are given in, for example, CIE S025 [5] and IES LM-79 [6], although note that the method given in S025 is more rigorous (more correct) than that given in LM-79.

5. THERMAL EFFECTS

LED lighting devices are temperature-sensitive, i.e. their luminous output changes with the temperature of the device. After the device is switched on, its temperature increases as it stabilises and its output will normally decrease as the temperature rises. An example of this is shown in Fig.8, where an LED device takes over an hour and a half to stabilise and its output drops by around 20 % in that time.

It is therefore important that stabilisation conditions are well established and are followed when measuring an LED lighting device. CIE S025 [5] considers an LED lamp or LED luminaire to be stable when:

- It has been operating for at least 30 minutes and;
- Its variation in luminous output is less than 0.5 % over the past 15 minutes;
- Its variation in electrical power is less than 0.5 % over the past 15 minutes.

But in addition to the stabilisation time, there are other aspects which affect the device's output and which need to be considered, including:

- Ambient air temperature, which must be within standardised limits;
- Air flow, which may be caused by air conditioning or other draughts or by the device itself being moved by a goniophotometer;
- Thermal conduction, which may be caused by a lamp holder or other mounting jig touching the device and transferring heat away from it.

6. ABSOLUTE PHOTOMETRY

Parameters of luminaires, employing traditional light sources such as fluorescent lamps, HID lamps and other standardised replaceable sources of light, would be normally measured using methods of relative photometry. In these cases the luminous intensity data are pro-rated according to the luminous output of the lamp(s) in the luminaire and saved as candela per 1000 bare lamp lumens. The advantage of this is that a lighting designer or architect can then use the rated data for the type of lamp that they intend to use in an installation and scale the pro-rated data to what it will be in the actual installation.

But integrated LED luminaires do not use replaceable light sources – they are designed to be discarded and replaced at the end of their lifetime. It is not always possible, or accurate, to remove the LED modules and conduct relative photometry – and nor is it required, since the luminaire measured in the lab will be (nominally) the same as the luminaire installed in the room or roadway, or stadium etc. Therefore, measurements of LED luminaires are normally conducted using absolute photometry – the results reported are the results measured in the laboratory. Most laboratories are equipped to perform absolute measurement and so this doesn't necessarily create any difficulties in a measurement sense.

It is also worth noting that in these cases the light output ratio is effectively 100 %!

7. THE NEED FOR STANDARDISATION

Historically there were different testing methods produced for LED lighting devices in different regions around the world. This created trade barriers and made intercomparisons difficult, as the results measured according to the standard of one region may not be directly comparable to the results measured according to the standard of another region.

The International Commission on Illumination (the CIE) is an independent, non-profit organization recognized by the ISO and the IEC as an international standardization body in the field of light and lighting. In 2011 it established a technical committee, TC2–71 "CIE Standard on Test Methods for LED Lamps, Luminaires and Modules", with the goal of writing a standard test method for photometric, colorimetric and electrical measurements of LED lighting devices. It was globally representative, with 37 members from 16 countries in 5 continents.

The outcome of this was the CIE publication S025/E:2015 "Test Method for LED Lamps, LED Luminaires and LED Modules" [5]. S025 provides a unified global test method for harmonization of testing of LED lighting products. National and regional standardising bodies and regulators are encouraged to move to adopting S025 for LED measurement.

REFERENCES:

1. ISO/CIE19476:2014(E). Characterization of the Performance of Illuminance Meters and Luminance Meters.

2. KRÜGER, U., BLATTNER, P. (2013). Spectral mismatch correction factor estimation for white LED spectra based on the photometer's f_1' value. CIE x038:2013 Proceedings of the CIE Centenary Conference "Towards a New Century of Light", Paris, 2013.

3. CIE121–1996. The Photometry and Goniophotometry of Luminaires.

4. BERGEN, A.S.J., JENKINS, S.E. (2012). Determining the minimum test distance in the goniophotometry of LED luminaires, CIE x037:2012 Proceedings of CIE2012 "Lighting Quality and Energy Efficiency".

5. CIE S025/E:2015. Test Method for LED Lamps, LED Luminaires and LED Modules.

6. IESNA LM-79–08. Electrical and Photometric Measurements of Solid-State Lighting Products.

Tony Bergen
is a physicist who has been working in the field of photometry and radiometry for over 20 years, with specific expertise in goniophotometry, spectroradiometry, laboratory practice and measurement uncertainty. He is Technical Director of Photometric Solutions International, an Australian company which designs and manufactures photometric, radiometric and colorimetric testing and measurement equipment and has its own ISO 17025-accredited calibration and testing laboratory. He is also Secretary of CIE Division 2; President of CIE Australia; Australian Divisional Representative for CIE Division 2; Chair of CIE TC2–77 and TC2–78

Light & Engineering
Vol. 25, No. 4, pp. 86-91, 2017

Svetotekhnika
No. 4, 2017, pp. 42–46

TESTING EQUIPMENT FOR LED LUMINAIRE CONTROL DEVICES AND FLUORESCENT LAMP ELECTRON BALLASTS

Nikolai N. Bespalov, Mikhail V. Ilyin, and Sergei S. Kapitonov

Ogarev Mordovia State University, Saransk
E-mail: kapss88@mail.ru

ABSTRACT

A hardware and software system is presented, which was developed to test electron ballasts for low pressure (LP) fluorescent lamps of up to 40 W and for light emitting diode luminaire control devices (CD) of up to 200 W power. Structures of the system and of the operating control software are described. Test results of 8 W electron ballasts and of 30 W power control devices are presented. Conclusions are drawn on the possible applications of these products.

Keywords: hardware and software system, control device, electron ballast, test, diagnostics, *National Instruments*

Two main directions of trend can be observed in lighting equipment today: the transition to light emitting diode (LED) sources and replacement of electromagnetic ballasts for discharge lamps with electron ballasts [1].

The pursuit of these directions means development of new ballast devices for lighting products, which requires carrying comprehensive testing [2] to determine their electric parameters and characteristics.

Standard measuring equipment is usually insufficient for this purpose [3,4]. An additional requirement for modern test equipment is automation of the tests and documenting their results, which requires including information and measuring facilities.

National Instruments Company, a world leader in the information and measurement system industry [5,6], has developed the test equipment given below based on the hardware and software of this company.

Fig. 1. Appearance of the ADIP-SVET test hardware and software system

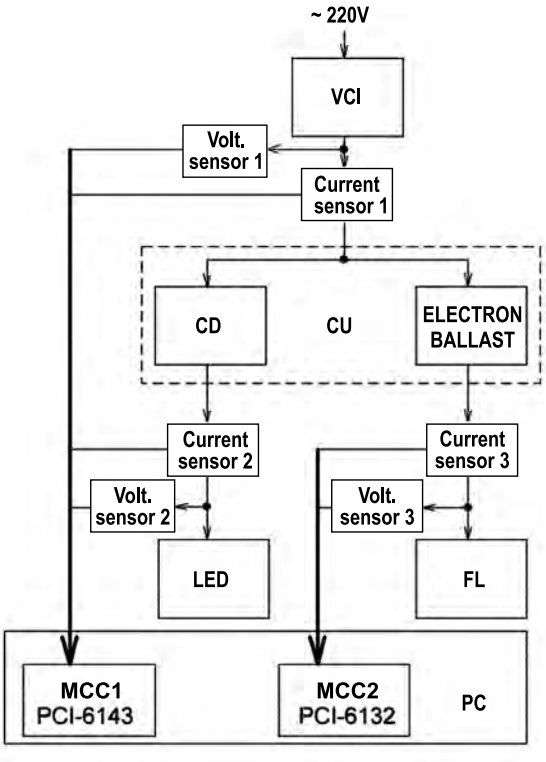

Fig. 2. A simplified structure of the hardware part of the test hardware and software system

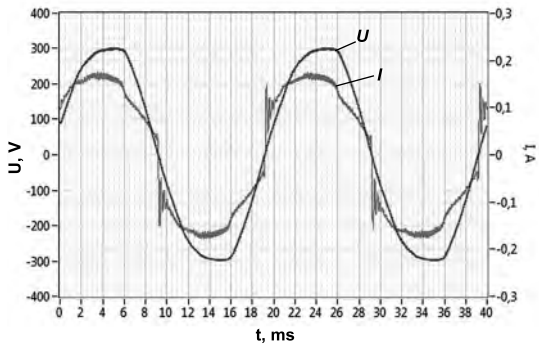

Fig. 4. Oscillograms of input voltage and current of the control device (CD)

The developed equipment being a measuring hardware and software ADIP–SVET system (MHSS) is intended to test electron ballasts for fluorescent lamps (FL) of up to 40 W power and for control devices ("drivers") for luminaires with LEDs of up to 200 W (Fig. 1)[1].

[1] The MHSS is developed according to the scientific and technological contract between the National Research of Ogarev Mordovia State University and the NIIIS of A.N. Lodygin State Unitary Enterprise of Republic of Mordovia to be operated in the latter.

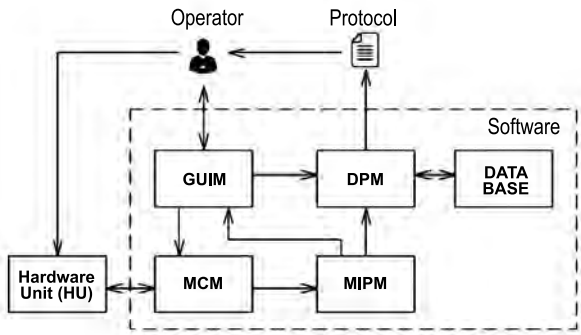

Fig. 3. Diagram of the interaction between software modules, as well as hardware unit and operator

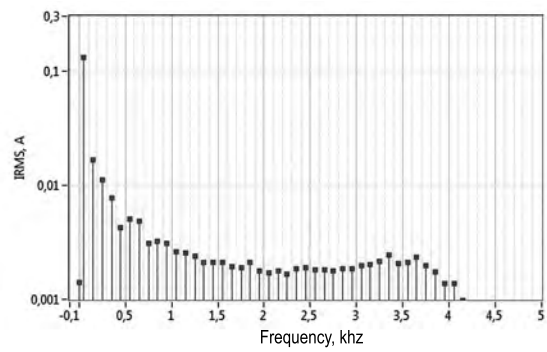

Fig. 5. CD input current range (root-mean-square *RMS* value)

The MHSS makes it possible to determine:

– Amplitude and root-mean-square values of input voltage and current;

– Effective power consumed from the circuit;

– Power factor;

– Amplitude and root-mean-square values of output electron ballast voltage and current;

– Average value of CD output voltage and current;

– Ripple factor of CD output voltage and current;

– Frequency of electron ballast output voltage;

– Effective power consumed by the load;

– Efficiency;

– Harmonic distortion factor.

During the test process, on the front panel of the virtual device besides the calculated parameters, oscillograms of input and output voltage and current are displayed, as well as spectral composition of the input and output current. In doing so, all measurement information is recorded in the computer memory as a database.

MHSS consists of the following units (Fig. 2): voltage control instrument (VCI); voltage sensors (ДН1, ДН2 and ДН3); current sensors (DT1, DT2 and DT3); commutation unit (CU); measurement

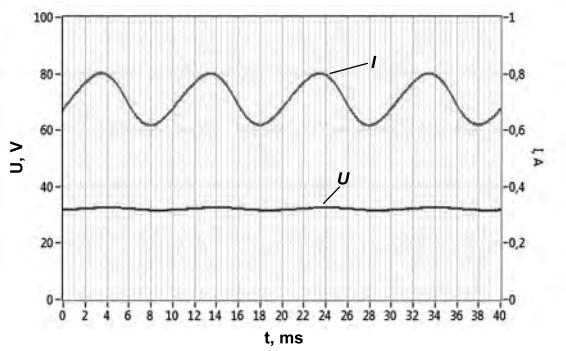

Fig. 6. Oscillograms of CD output voltage and current

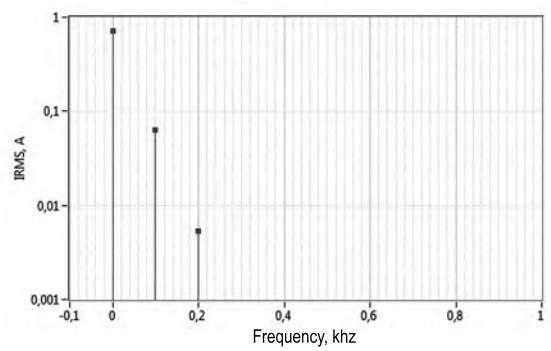

Fig. 7. CD output current range (root-mean-square *RMS* value)

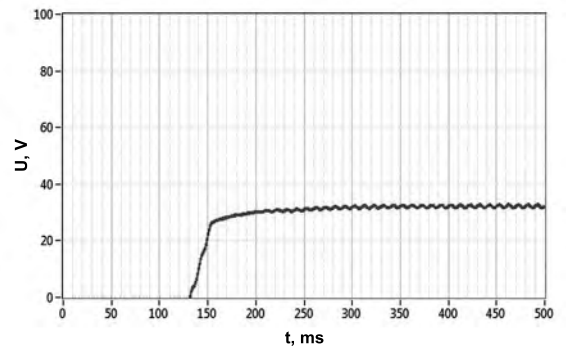

Fig. 8. Oscillogram of CD output voltage when switching on

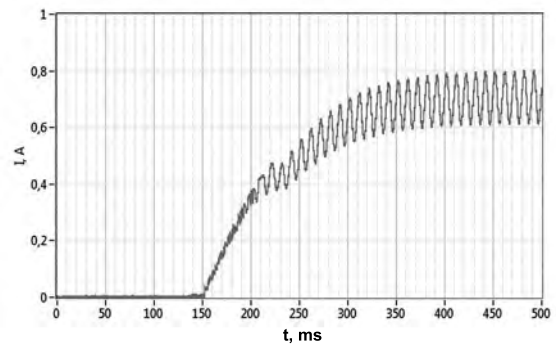

Fig. 9. Oscillogram of CD output voltage when switching off

and control cards (ИУП1, ИУП2); personal computer (PC); CD under test; electron ballast under test; luminaire LED light source (LED load); FL.

VCI allows testing CDs or electron ballasts within the whole working interval of input voltage. Using it, before the tests, a required voltage is set previously at the ballast input. In order to determine the VCI output voltage, which is input voltage for the ballast under test, DH1 is used. Signals from the latter are transmitted to the personal computer, and the operator can set a necessary voltage for the test according to indications on the front panel of the virtual device.

Voltage from the VCI unit output, via the DT1 sensor of input current comes to the commutation unit (CU). The latter is intended to connect the ballast under test and contains all necessary switching units. Ballasts under test in Fig. 2 are shown in the CU as CDs and ballast units. They are connected to an input voltage general bus and to different loads: LED light sources and LLs. When testing, one only device under test should be in the UC (CD or electron ballast).

To measure output current and voltage of the ballast under test, DH2 and DT2 are used. And to measure output current and voltage of the electron ballast, DH3 and DT3 are used.

Signals from all DH and DT sensor outputs are transmitted to the PC, which have ИУП1 and ИУП2 built in. ИУП1 is intended to measure CD input and output voltage and current, and ИУП2 is intended to measure the output voltage and current of electron ballast. ИУП2 contains analogy – digital converter (ADC) with a bigger sampling frequency than ИУП1, because output voltage frequency of the electron ballast is significantly higher than CD input and output voltage frequency. PCI-6143 and PCI-6132 cards of the National Instruments Company were chosen as measuring cards ИУП1 and ИУП2 respectively.

The MHSS software is developed in the LabVIEW graphical programming environment and intended to interact with the operator, to control the hardware in the test process, to store the test results and to create the test protocol.

It consists of the following main modules: 1) graphic user interface module (GUIM); 2) measuring and control module (MCM); 3) measuring information processing module (MIPM); 4) do-

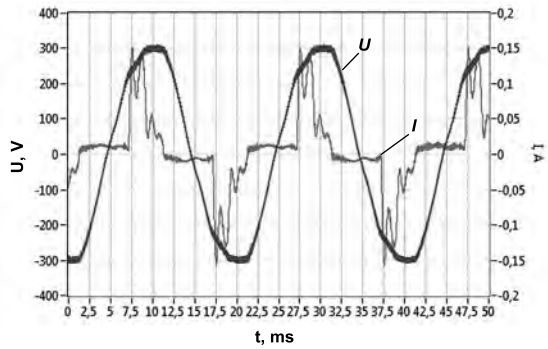

Fig. 10. Oscillograms of input voltage and current of electron ballast

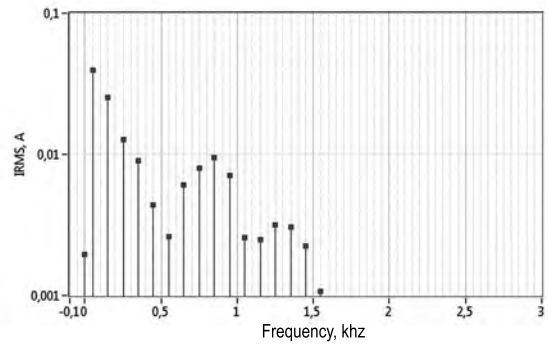

Fig. 11. Electron ballast input current range (root-mean-square *RMS* value)

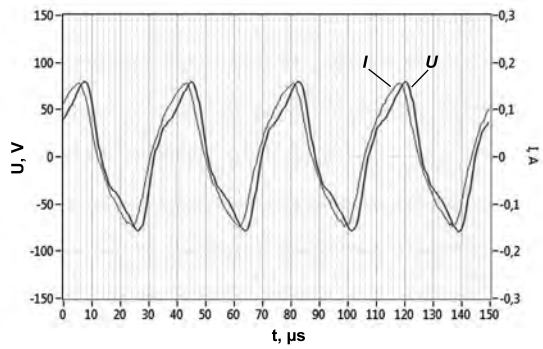

Fig. 12. Oscillograms of output voltage and current of electron ballast

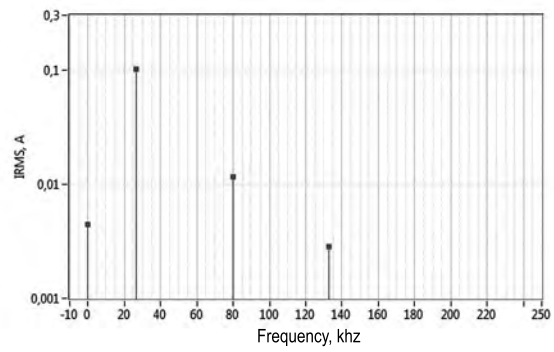

Fig. 13. Electron ballast output current range (root-mean-square *RMS* value)

cument and protocol module (DPM); 5) database (DB).

The interaction between the software modules and the MHSS hardware unit (HU) and with the operator is represented by the diagram in Fig. 3.

Based on the information entered through the GUI (type of device under test, rated electric parameters of the ballast under test, loading type of the device under test, rated electric parameters of the loading, as well as parameters of the protocol), the measure and control module (MCM) makes the decision on forming a control signal to connect a certain measuring channel and to switch on or switch off the device under test to the input voltage source. The main objects of MCM control are measuring and control HU cards. They are controlled by the specialised DAQmx CD.

The measuring information obtained from the MCM during the tests is recorded to the hard drive and transformed in parallel by the MIPM into calculated electric parameters and diagrams, which are displayed for the operator using the GUIM module.

Using the DPM, the operator can save the test results in the DB. For the storage convenience, the operator can group them as separate groups united in a single DB. And in doing so, for these groups separation convenience, an additional possibility exists to create new DBs.

After the test results are saved in a DB, the operator has an opportunity to form a test protocol.

In order to demonstrate the MHSS work, ballasts of Chinese production were tested: CDs of 30 W power and electron ballasts of 8 W.

In Fig. 4–9, diagrams obtained as the CD test results are shown. On the basis of these diagrams, the following calculated electric parameters of the driver under tests were obtained:

– Input voltage root-mean-square value: 220 V;
– Input current root-mean-square value: 133 mA;
– Amplitude of input current: 174 mA;
– Effective power consumed from the circuit: 29 W;
– Power factor: 0.97;
– Average output voltage: 32 V;
– 710 мA average output current: 710 mA;
– Amplitude of output voltage ripples: 1.46 V;
– Amplitude of output current ripples: 0.192 mA;
– Ripple factor of output current: 27 %;
– Root-mean-square power consumed by loading: 23 W;

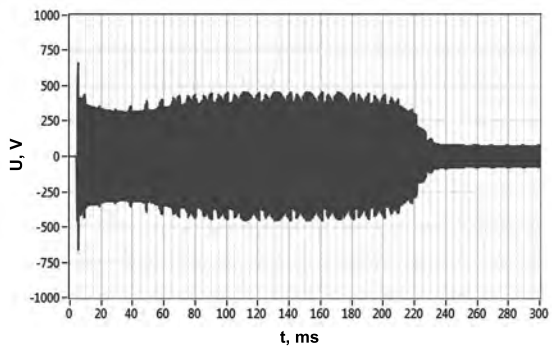

Fig. 14. Oscillogram of electron ballast output voltage when switching on

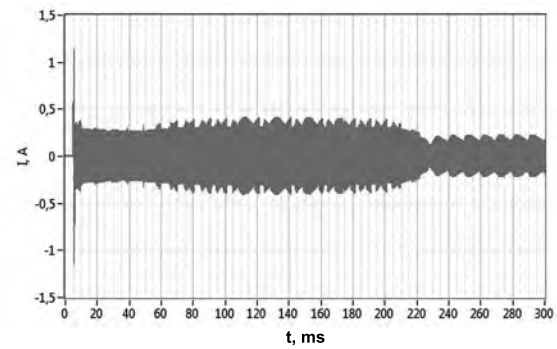

Fig. 15. Oscillogram of electron ballast output voltage when switching off

– Efficiency: 78 %;

– Harmonic distortion factor: 33 %.

Input current has an almost sinusoidal configuration (Fig. 4), and therefore the power factor is high (0.97). However, presence of high-frequency components (up to 4 kHz and more) in the input current is quite significant. Output current (Fig. 6) pulses rather strong (ripple factor is 27 %). Thus, in accordance with the Building regulations [7] the CDs under test, in luminaires with LEDs should not be used in the Russian Federation. Other measured electric parameter values of this CD presented corresponded to the declared (rated) levels.

Figs. 10–15 show the diagrams obtained as a result of electron ballast tests. Calculated parameters of the electron ballast under test are as follows: input voltage root-mean-square value is 220 V; input current root-mean-square value is 53 mA; input current amplitude value is 151 mA; effective power consumed from the circuit is 7.4 W; power factor is 0.64; output voltage root-mean-square value is 51 V; effective value of output current is 101 mA; output voltage amplitude value is 80 V; output current amplitude value is 0.157 mA; output voltage frequency is 26.6 kHz; effective power consumed by the load is 4.9 W; efficiency is 66 %; harmonic distortion factor is 95 %.

It can be seen from the test results that the electron ballast under test does not contain a power adjuster as the current consumed from the circuit is non-sinusoidal, which causes a low power factor (0.64) and a rather broad range of current and voltage.

Additionally, as can be seen from Fig. 14 and 15, this electron ballast lights FLs steadily but is not intended to provide additional modes to increase their life time.

Application of the ADIP-SVET MHSS by lighting companies will allow for:

1) Considerable reduction in test and diagnostics time of CDs for luminaires with LEDs and of electron ballasts for FLs;

2) Essential simplification of measurements, information processing and results visualisation due to the use of modern computer technologies;

3) Determining characteristics and values of all key CD and electron ballast parameters using one system (without any additional equipment);

4) Rejection of potentially unreliable CDs and electron ballasts and carrying out manufacturing quality control of these products;

5) Increased reliability and energy efficiency of FLs and luminaires with LEDs.

REFERENCES

1. Bespalov N.N., Kapitonov S.S., Kapitonova A.V. Research of processes in the LEDs luminaire in case of the voltage temperature coefficient of separate LEDs variation // Light & Engineering, 2016, Vol. 24, No. 4, pp. 72–75.

2. Kapitonov S.S., Kapitonova A.V. Simulation of thermal dependence of a powerful light emitting diode radiation flux // New university. The technical science series, 2015, issue #3–4, pp. 47–50 (Yoshkar-Ola).

3. Kapitonov S.S., Bespalov N.N., Kapitonova A.V., Ashryatov A.A., Kilmyamyatov Denis R., Kilmyamyatov Dias R. Development of light emitting diode electric model in the Multisim environment // The Scientific and technical bulletin of Volga region, 2015, issue #1, pp. 99–102 (Kazan).

4. Bespalov Nikolai N., Kapitonov Sergei S., Ilyin Michael V., Evishev Alexei V., Volkov Alexander G. Bespalov Nikolai N., Kapitonov Sergei S., Ilyin Michael V., Evishev Alexei V., Volkov Alexander G. Development

of electro-thermal model of LED in the Multisim / Young Researchers in Electrical and Electronic Engineering Conference (2017 ElConRus), St. Petersburg: IEEE, 2017, 221p.

5. Simulation of light emitting diode radiation characteristic in the Multisim environment // The Scientific almanac, issue #4 (6), pp.196–200 (Tambov: LLC Yukom Consulting Company).

6. Kapitonov S.S., Bespalov N.N., Kapitonova A.V., Ashryatov A.A. Study of a light emitting diode standard model in the Multisim environment // Collection of SWorld scientific works, 2014, issue 4 (37), V. 1, pp. 73–75 (Odessa: KUPRIYENKO CB).

7. Building regulations 23–05–95 “Artificial and natural illumination”.

Nikolai N. Bespalov,
Ph.D. Graduated from the Novosibirsk Electrotechnical Institute in 1974. At present – the Head of the Chair of Electronics and Nanoelectronics of the Ogarev Mordovia State University, Federal State Institution. Field of scientific interest: the study and development of LED light sources control systems

Mikhail V. Ilyin,
Ph.D. Graduated from the Ogarev Mordovia State University in 2004, at present, he is an Associate Professor of the Chair of Electronics and Nanoelectronics of the same State University, Federal State Institution. His field of scientific interest is the study and development of LED light sources control systems

Sergei S. Kapitonov,
Ph.D. Graduated from the Ogarev Mordovia State University in 2010 and now he is Associate Professor of the Chair of Electronics and Nanoelectronics of the same State University, Federal State Institution. Field of scientific interest: the study and development of LED light sources control systems

Light & Engineering
Vol. 25, No. 4, pp. 92-98, 2017

Svetotekhnika
No. 5, 2017, pp. 50–55

COMPARISON OF SINGLE PHASE BUCK-BOOST AND SEPIC LED DRIVER

Erdal Şehirli[1], Meral Altınay[2], Özgür Üstün[3], and Bekir Çakır[2]

[1]Kastamonu University; Kocaeli University[2]; İstanbul Technical University[3]; Turkey
E-mails: esehirli@kastamonu.edu.tr; meral.altinay@kocaeli.edu.tr; oustun@itu.edu.tr; bcakir@kocaeli.edu.tr

ABSTRACTS

This paper presents the comparison of LED driver topologies that include buck-boost and SEPIC converters. Both topologies are connected to grid over single phase diode rectifier and designed for 8W power. Furthermore, buck-boost and SEPIC converters operate with 63 kHz switching frequency and inductors of SEPIC are wounded as coupled. By means of the implementations, power factor (PF) and total harmonic distortion (THD) of current and voltage, power LED voltage and current are shown for both topologies. Comparison is also made between IEC61000–3–2 standard, buck-boost and SEPIC converters. Besides, electrical circuit model of power LED is derived by using its current-voltage characteristic.

Keywords: LED driver, PFC, buck-boost converter, SEPIC converter, power factor, THD

1. INTRODUCTION

Recently, power LEDs in illumination have been taking much attention due to their high efficiency feature with respect to other illumination methods such as fluorescent, incandescent and metal halide bulbs. However, power LEDs need dc power for their operation. This dc power can be mostly obtained after rectification process of single phase AC power. In this rectification process if uncontrolled rectifiers are directly used, this will cause harmonics on grid current and reducing power factor. Furthermore, grid current harmonics are limited by international standards such as IEC61000–3–2. To avoid this problem, high power factor or power factor correction (PFC) circuits can be used as a LED driver. Besides, PFC circuits in single phase can be realized by using any dc-dc converters after uncontrolled bridge rectifier. In literature, some studies are conducted on this topic as follows.

Using PFC converters as LED driver that include buck and buck-boost converter is designed in [1]. In [2], the implementation of Cuk converter based LED driver presented. LED drivers that consist of Flyback and SEPIC converter are realized in [3–4]. Also in [5], combination of buck and Flyback converters as an LED driver is implemented. AC-DC and DC-DC converters are used as an LED driver in [6]. PFC converters that include basic dc-dc converters are presented and compared by their advantages and disadvantages in [8–10]. Besides, detailed analysis, design and operation of dc-dc converters are clarified in [11]. Comparison of basic dc-dc converters that includes buck, boost, buck-boost, SEPIC and zeta with PFC for supplying high pressure sodium lamps is presented [12]. Also, another comparison in [13] is made for buck-boost, SEPIC, Cuk dc-dc converters that drive power LEDs.

In this paper, comparison of LED driver topologies that include buck-boost and SEPIC converters are presented. Both topologies are connected to grid over single phase diode rectifier and designed for 8W power. Besides, they operate with 63 kHz switching frequency and use easily found integrated circuits (IC). With implementations, PF and THD of grid current and voltage, power LEDs current and voltage are shown for both topologies. Furthermore,

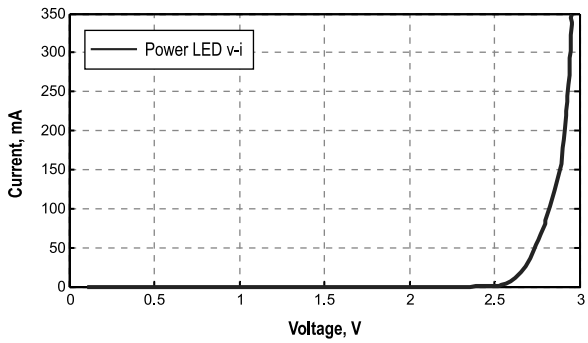

Fig.1. Voltage-current characteristic of power LED

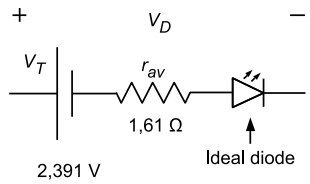

Fig.2. Electrical equivalent model of power LED

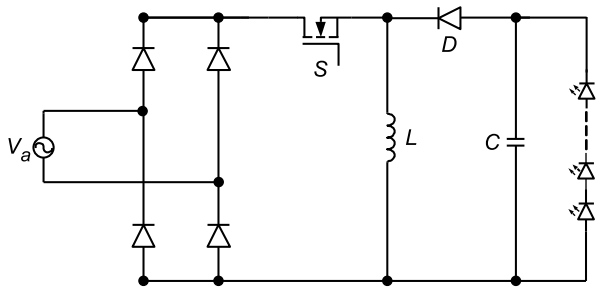

Fig.3. PFC Buck-Boost Converter

comparison between IEC61000–3–2 standard and results of implementations is made. Electrical circuit model of power LED is also derived.

This paper is organized as follows. Power LED current-voltage characteristic and electrical circuit model are derived in Section 2. LED driver topologies applied are reviewed in Section 3. Applications of LED drivers are presented in Section 4. THDs, power factor and power LED current-voltage of each topology are shown in Section 5. Some conclusions are given in Section 6.

2. POWER LED

In this chapter, current-voltage characteristics and electrical circuit model of power LED that are used for this study are derived by using Fluke 15B and Fluke 17B.

Fig.1. shows voltage-current characteristic of a power LED. The characteristic is obtained by increasing voltage on a single power LED and plotting voltages versus each current. It is seen from the figure that LED voltage and current has exponential relation and LED current increase extremely after LED conducts. Also, LED voltage doesn't change much after and up to 340 mA current [14].

By using Fig.1, electrical circuit model of power LED is derived as in Fig.2. It is understood by this model that threshold voltage and conductance resistance of power LED are 2.391 V and 1.61Ω, respectively.

3. LED DRIVER

In this chapter, PFC buck–boost and SEPIC converters as a LED driver are introduced. Both drivers are connected to grid over single phase diode rectifier. By changing duty cycle of each converter dc voltage on power LED can be set to the desired value while obtaining naturally high power factor on grid. Furthermore, both topologies can give lower or higher voltage with respect to input voltage.

A. Buck-Boost Converter

Fig.3. shows the buck-boost converter that consist of inductor L, capacitor C, diode D and S switch.

Buck-boost converter is connected to grid over diode bridge and with high frequency operation of the switch; dc voltage that feeds power LEDs is obtained. This converter works on principle of transferring energy of inductance and can

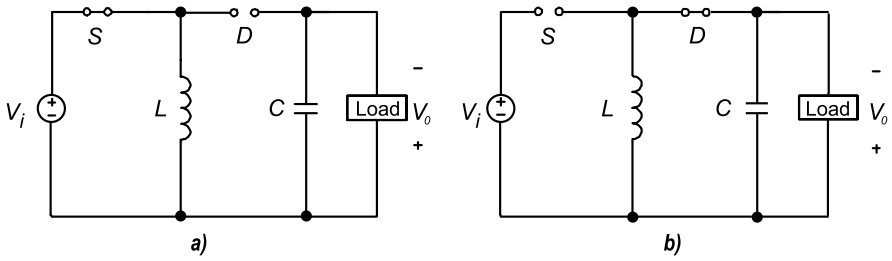

Fig.4. Switching state a) open, b) closed

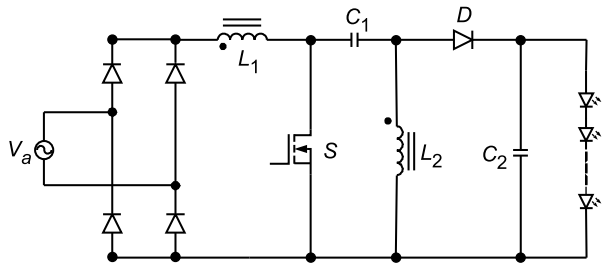

Fig.5. PFC SEPIC converter

be analyzed by the state of the switch that is seen in Fig.4. If the switch turned on, inductance stores energy and the switch turns off inductance transfer this energy to the load.

Furthermore, the voltage on power LEDs can be adjusted to less or more with respect to input voltage by changing pulse width modulation (PWM). Besides, high frequency operation also provides high power factor [8]. However, dc voltage on power LEDs is reverse polarity with input voltage and to avoid high frequency noise, input filter needs to be added.

Passive equipment can be chosen by using following equations (1–2) as in [11]. In equation (1), L_{max} is the maximum inductance value for discontinuous conduction mode (DCM) operation. R_{Lmin} is minimum load resistance. D_{max} is maximum duty cycle. f_s is switching frequency.

$$L_{max} = R_{Lmin}(1\text{-}D_{max})^2 \Big/ 2f_s \,. \tag{1}$$

$$C_{min} = D_{max}V_o \Big/ f_s.R_{Lmin}.V_{ripple} \,. \tag{2}$$

In equation (2), C_{min} is the minimum capacitor value, D_{max} is also maximum duty cycle, R_{Lmin} is again minimum load resistance, V_o is output voltage, V_{ripple} is the ripple voltage on output of converter and f_s is also switching frequency.

B. SEPIC CONVERTER

Fig.5. shows the PFC SEPIC converter circuit that has two inductors and two capacitors. Furthermore, inductors in SEPIC converter are wounded as coupled that means on the same core.

Switch states are shown in Fig.6 when S is turned on, L_1 is energized by power source, and L_2 is energized by C_1. When S is turned off, C_1 is charged by power source and L_1, also currents of L_1 and L_2

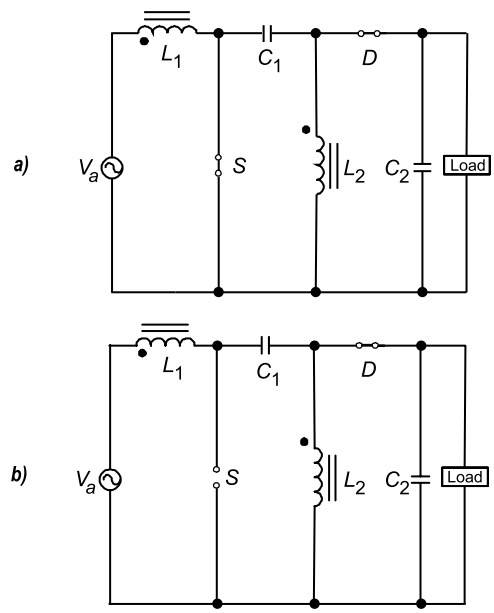

Fig.6. Switching state: a) open, b) closed

flow through D and load, C_2 is also charged [15–16]. Furthermore, by operating the switch with high frequency, PFC process is obtained naturally.

The most important advantage of SEPIC converter over buck-boost converter is to provide output voltage with the same polarity of input voltage. However, number of passive elements is more than buck-boost converter. But, having inductor on the input side provides continuous input current and helps the reduction of noise [15].

Passive elements in SEPIC converter can be chosen by using equations (3–5) as in [16–17]. In equation (3), L_{1min} and L_{2min} are the minimum L_1 and L_2 inductance values. D_{max} is maximum duty cycle. V_{in} is input voltage. ΔI_L is the ripple current on inductors. f_{sw} is switching frequency.

$$L_{1min} = L_{2min} = D_{max}.\, V_{in} \Big/ 2 \cdot I_L \cdot f_{sw} \,. \tag{3}$$

$$C_2 \geq I_{out}.D_{max} \Big/ V_{ripple}.f_{sw} \,. \tag{4}$$

In equation (4), C_2 is the value of C_2 capacitor, I_{out} is output current, V_{ripple} is the output voltage ripple, D_{max} is maximum duty cycle, f_{sw} is duty cycle.

$$C_1 = I_{out}.D_{max} \Big/ \Delta V_{C_1} \cdot f_{sw} \,. \tag{5}$$

In equation (5), C_1 is the value of capacitor C_1, I_{out} is output current, D_{max} is maximum duty cycle,

ΔV_{C1} is voltage ripple across C_1, f_{sw} is switching frequency.

4. APPLICATION

In this chapter applications of LED drivers that use buck-boost and SEPIC PFC as converter are realized. Fig.7. shows the experimental setup. Both converters are connected to grid over step down transformer 220/24 50Hz. Furthermore, as a load, three series connected power LEDs tied with two parallel branches. It is understood from Figs.1,2 that maximum 3V is required for best operation, therefore in applications, power LEDs are supplied up to 10V. Also, applications are conducted by easily found and cheap ICs that are SG3524, IR2117, TC4427 and LM317.

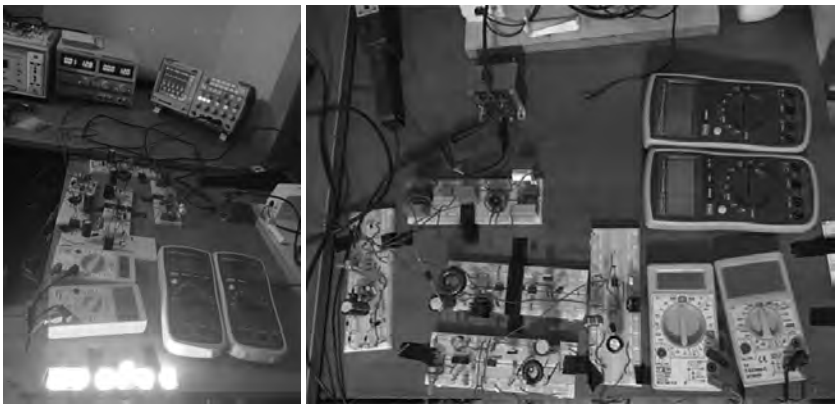

Fig.7. Experimental setup

4.1. PFC Buck-Boost Converter

Application circuit of buck-boost PFC based LED driver is shown in Fig.8. It is understood that open loop operation is realized and SG3524 IC is used for PWM signals. Besides, EMI filter, IRF540N Mosfet, IR2117 Mosfet driver, Mur460 fast diode, 100μH inductor, 1000 μF capacitor are included in the application circuit [18–21].

The duty cycle is changed by the potentiometer connected to SG3524 and PWM frequency is set to 63 kHz. To reduce high frequency noise and avoid discrete current on grid, π type of EMI filter is used as in [22]. Besides, passive elements are used after calculation by equations (1,2).

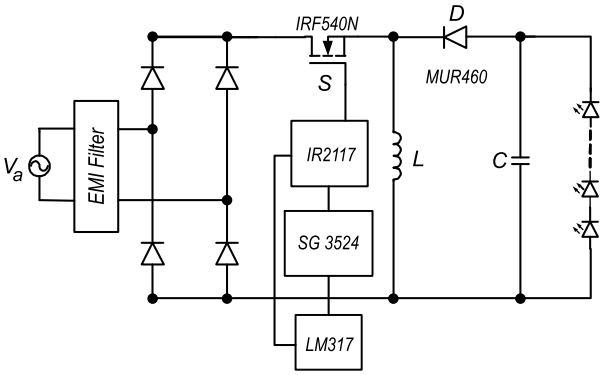

Fig.8. Application circuit of PFC buck-boost converter

4.2. PFC SEPIC Converter

Fig.9. shows the application circuit of SEPIC PFC based LED driver. This application is also realized by open loop algorithm. Furthermore, SG3524 IC is used for PWM signals and IRF540N Mosfet, TC4427 Mosfet driver, Mur460 fast diode, 100μH inductor, 1000 μF capacitor are used in the application circuit [18–23].

The duty cycle is also changed by the potentiometer connected to SG3524 and PWM frequency is again used as 63 kHz. The same load is used with buck-boost PFC LED driver. By using equations (4–5), passive elements are chosen. Without using an EMI filter, SEPIC PFC LED driver can give the desired results.

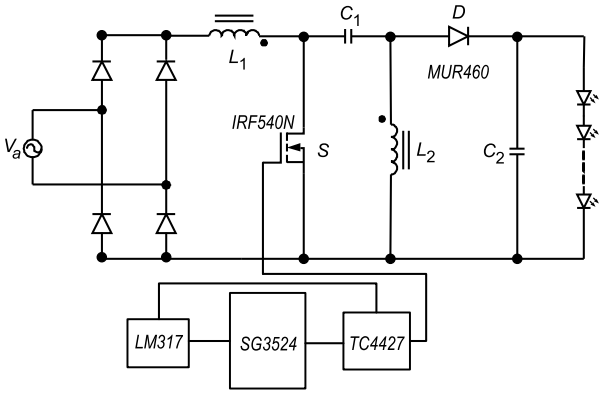

Fig.9. Application circuit of PFC SEPIC converter

5. MEASUREMENT RESULTS

In this section, THDs of grid current and voltage, power factors, power LEDs voltage and current are measured for both buck-boost and SEPIC based LED drivers. For measurement, TPS2024B oscilloscope and TPS2PWR1 power application software are used.

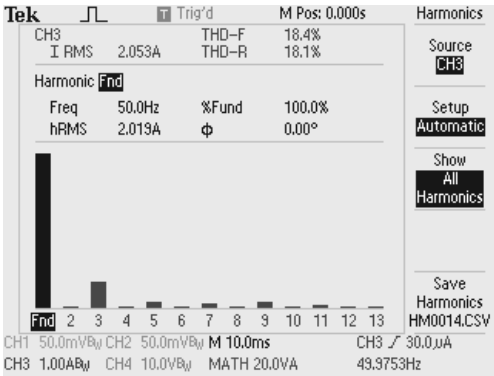

Fig.10. THD of grid current

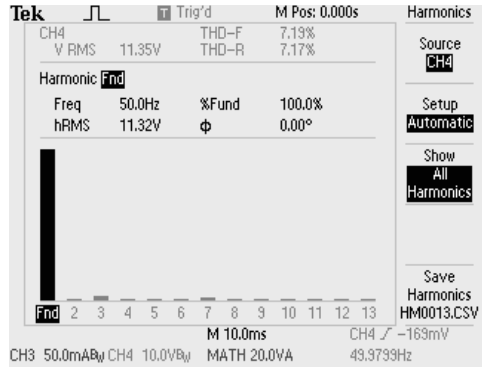

Fig.11. THD of grid voltage

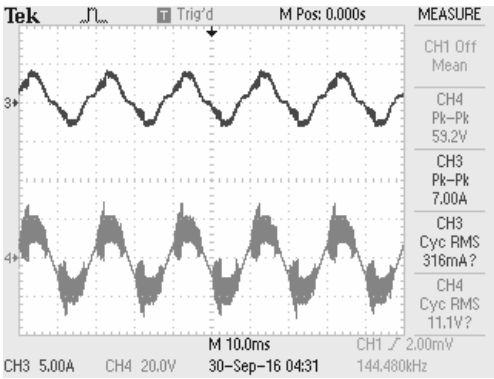

Fig.12. Grid current and voltage

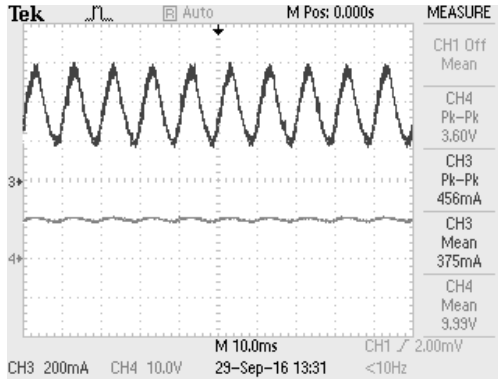

Fig.13. Power LED voltage and current

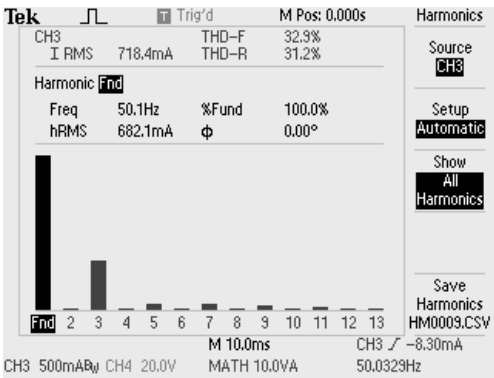

Fig.14. THD of grid current

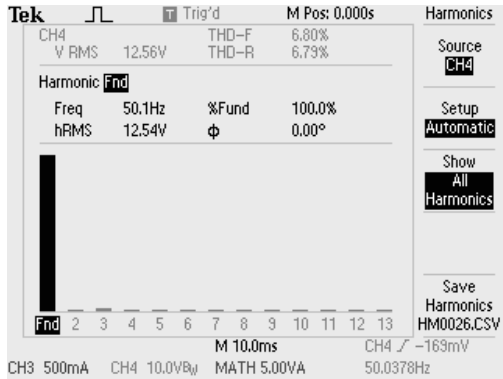

Fig.15. THD of grid voltage

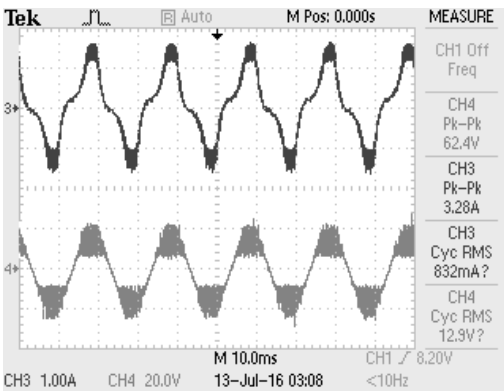

Fig.16. Grid voltage and current

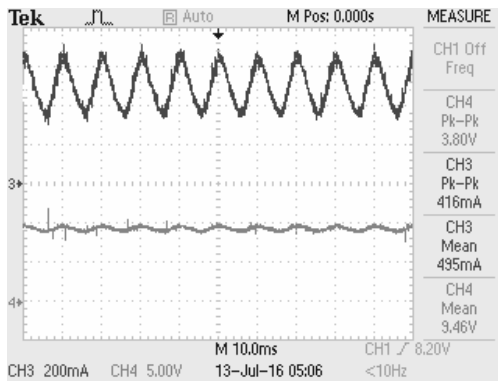

Fig.17. Power LED voltage and current

Table1. Comparison of grid Current THD's

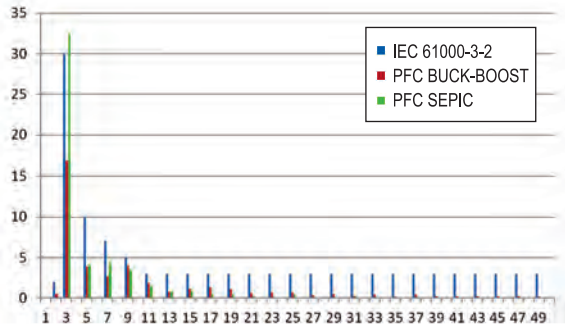

5.1. PFC Buck-boost Converter

Grid current THD of PFC buck-boost converter that is 18.4 % is shown in Fig.10. Also, PF is measured as 0.925. THD of grid voltage is measured as 7.19 % and shown in Fig.11.

Grid current and voltage are shown in Fig.12. The shape of grid current is similar to grid voltage, and they are both sinusoidal.

Power LEDs voltage and current are shown in Fig.13, and it is seen that LED current is not dc and it has oscillation with 400mA.

5.2. PFC SEPIC converter

Fig.14. shows grid current THD of PFC SEPIC converter that is 32.9 %. P.F. is also measured as 0.912.

THD of grid voltage is shown in Fig.15 and it is 6.80 %.

Grid current and voltage are shown in Fig.16. The shape of grid current is similar to grid voltage, and they are both sinusoidal.

Power LEDs voltage and current are shown in Fig.17, and it is seen that LED current has oscillation with 200mA.

6. CONCLUSIONS

This paper compares the LED drivers that include buck-boost PFC and SEPIC PFC converters. Also, voltage-current characteristics and electrical equivalent circuit of power LED are derived. With applications that are realized by using easily found and cheaper ICs, THDs of grid current and voltage, power factor, power LEDs current and voltage are measured. THD's of grid currents are 18.4, 32.9 % and THD's of grid voltages are 7.19 and 6.80 % for PFC buck-boost and SEPIC LED drivers, respectively. Furthermore, PF is also measured as 0.925 and 0.912 for buck-boost and SEPIC LED drivers, respectively. Besides, power LED current oscillations are 400mA and 200mA for buck-boost and SEPIC based drivers. PFC buck-boost converter provides IEC61000 3–2 standard C.

As a result, grid current THD and PF of buck-boost PFC are better than SEPIC PFC. However, grid voltage THD and oscillation level of power LED current in buck-boost PFC are worse than SEPIC PFC.

Furthermore, in Table1 comparison of grid current THD's between IEC61000–3–2 C class, PFC buck-boost and PFC SEPIC LED drivers is given. It is seen from that table, both LED drivers provides actual standard IEC61000–3–2. However, 3rd harmonic of PFC SEPIC is little bit higher than the limit of that standard. On the other hand, PFC SEPIC LED driver application is realized without using input filter. After adding an input filter, it is assumed that actual standard will be realized completely.

REFERENCES

1. Cheng H L, Lin C W. Design and Implementation of a High-Power-Factor LED Driver With Zero-Voltage Switching-On Characteristics. IEEE Transaction on Power Electronics, 2014. V29, #9, pp.4949–4958.

2. Mohammed L, Saudin N, Hamid N F A, Ramly N H, Isa Z M, Ahamad N B. Cuk Converter as a LED Lamp Driver. IEEE International Conference on Power and Energy, Kota Kinabalu Sabah, Malezya, pp.262–267.

3. Lamar D G, Arias M, Rodriguez A, Fernandes A, Hernando M M, Sebastian J. Design Oriented Analysis and Performance Evaluation of a Low-Cost High-brightness LED Driver Based on Flyback Power Factor Corrector. IEEE Transaction on Industrial Electronics, 2013. V60, #7, pp.2614–2626.

4. Ma H, Lai J S, Feng Q, Yu W, Zheng C, Zhao Z. A Novel Valley-Fill Sepic-derived Power Supply without Electrolytic Capacitors for LED Lighting Application. IEEE Transaction on Power Electronics, 2012. V20, #6, pp.3057–3071.

5. Paul E, Aleyas M V, Oommen A P. A Single Stage High Power Factor Supply Based on Integrated Buck Flyback Converter. International Journal of Advanced Research in Electrical, Electronics and Instrumentation Engineering, 2013. V2, #1, pp.680–688.

6. Arias M, Vazguez A, Sebastian J. An Overview of the AC-DC and DC-DC Converters for LED Lighting Applications. Journal for Control, Measurement, Electronics, Computing and Communications, 2012, V53, #2, pp.156–172.

7. Arias M, Vazguez A, Sebastian J. Integrated Double Buck-Boost Converter as a High-Power-Factor Driver for

Power-LED Lamps. International Journal of Scientific Engineering and Research, 2014. V2, #1, pp.74–77.

8. Grigore V. Topological Issues in Single-Phase Power Factor Correction. PhD thesis, Helsinki University of Technology, 2001.

9. Sharifipour B, Huang J S, Liao P, Huber L, Javanovich M M. Manufactoring and Cost Analysis of Power-Factor-Correction Circuits. IEEE APEC98, Anaheim, Canada, pp.490–494.

10. Zhang J, Javanovich M M, Lee F C. Comparision Between CCM Single Stage and Two Stage Boost PFC Converters. IEEE APEC99, Dallas, USA, pp.335–341.

11. Kazmierczuk M K. Pulse Width Modulated DC-DC Power Converters. Wiley, 1st edition, Singapore, 2008.

12. Costa M.A.D., Marchesan T.B., Da Silveira S.J., Seidel R.A., Do Prado R.N., Alvarez J.M.A. Integrated Power Topologies to Supply HPS Lamps: Comparative Study. IEEE Transactions on Power Electronics, 2010. V25, #8, pp.2124–2132.

13. Cabral H.G., Marques A.R., Pedrollo G.R., De Faria P.F., Dos Reis F.S., Performance Comparison of Buck-boost Family Converters for Driving LED Lamps. 2014 11th IEEE/IAS International Conference on Industry Application INDUSCON, Cascatinha, Brazil.

14. Sehirli E., Altınay M., Cakır B. Comparison of a Single Phase Linear and Buck-boost LED Driver. Light&Engineering, 2015. V23, #3, pp.78–84.

15. Url-5 < http://www.switchingpowermagazine.com/downloads/Sepic%20Analysis.pdf >, Visit date, 21.05.2016.

16. Url-6 <http://www.ti.com/lit/an/slyt309/slyt309.pdf>, Visit date, 21.05.2016.

17. Url-7 <http://www.ti.com/lit/an/snva168e/snva168e.pdf>, Visit date, 21.05. 2016.

18. Data sheet SG3524. Regulating Pulse-Width Modulators. Texas Instrument, 2003.

19. Data sheet IRF540N. IRF540N Power Mosfet. International Rectifier, 2001.

20. Data sheet MUR460. Ultrafast Plastic Rectifier, Vishay General Semiconductor, 2012.

21. Data sheet IR2117. Single Channel Driver, International Rectifier, 2007.

22. User Guide for FEBL7732_L28U008A, "8.4W LED Driver at Universal Line Using Buck-Boost Featured Fairchild Product FL7732, Fairchild, (2012).

23. Data sheet TC4427. 1.5 A Dual High-Speed Power Mosfet Drivers, 2014.

Erdal Sehirli
received the B. Sc. degree from Gazi University, Ankara, Turkey, in 2006, and the M. Sc. degree from Kocaeli University, Kocaeli, Turkey, in 2009. He is a currently Ph.D. student and lecturer at Kocaeli University, and Electronic Technology Department of Kastamonu Vocational High School, Kastamonu University, respectively. His current research interests include LED drivers, electrical machines and drives, voltage source rectifiers and nonlinear control

Meral Altınay
received the B. Sc. degree from Marmara Univeristy, İstanbul, Turkey, in 1994 and the M. Sc. and Ph.D. degrees from the Kocaeli University, in 1998 and 2005, respectively. In 1996, she joined the Department of Electrical Education, Faculty of Technical Education, Kocaeli University as a Research Assistant. Since 2006, she has been an Assistant Professor with the Technology Faculty, Kocaeli University. Her research interests include modelling, control design of switching mode-power converters, power quality

Özgür Üstün
received the B. Sc., M. Sc. and Ph.D. degrees from Istanbul Technical University, Turkey, in 1990, 1993 and 2000 respectively. He is currently working as an Associate Professor in Istanbul Technical University. His research interests are power electronics, electrical machinery and energy conversions

Bekir Çakır
received the B. Sc. and M. Sc. degrees from the Berlin Technical University, Germany, in 1986 and 1990, respectively and Ph.D. degree from both Yıldız Technical University and Kocaeli University, Turkey, 1995. In 1991, he joined Kocaeli University, Engineering Faculty as a Research Assistant. He was first Assistant Professor, then Associate Professor in Kocaeli University, 1995 and 2002 respectively. Since 2006, he has been a Professor with the Engineering Faculty, Kocaeli University. His research interests are embedded system design, power electronics driver circuits, renewable energy production systems and smart grids

Light & Engineering
Vol. 25, No. 4, pp. 99-108, 2017

Svetotekhnika
No. 4, 2017, pp. 51–59

DEVELOPMENT OF CCT TUNABLE LED LIGHTING SYSTEM USING RED-BLUE-WHITE LED

Rajib Malik, and Saswati Mazumdar

Jadavpur University, Kolkata, India
E-mails: rajib.diara@gmail.com; saswati.mazumdar@gmail.com

ABSTRACT

This study proposed a CCT tunable LED lighting system, which comprises of Red-Blue-White (RBW) LED luminaire, LED driver and Dimming-controller-unit (DCU). Here, first RGB LED at different intensity was blended with Warm-White (WW) LEDs to produce variable CCT. To achieve higher CCT than WW colour, it was found that only blue LED blended with WW LEDs is sufficient. On the other hand, for lower CCT range, red LED mixed with WW LEDs is enough. This new algorithm is capable to produce CCT ranging from 2700K to 9723K. Measured maximum deviation from set point value was found 18K for Red LEDs and 344 K for Blue LEDs blending respectively. The LED driver is designed to operate in voltage protection mode and in current control mode for a typical dimming cycle. The current control mode is implemented using an op-amp based PI (proportion-integral) controller.

Keywords: DCU, LED driver, RGBW LED, current control, PWM dimming, variable CCT

1. INTRODUCTION

Due to rise of energy price researcher are trying to develop new technology and lighting systems to utilize the electrical energy efficiently [1]. Now a days Light Emitting Diode (LED) gradually becomes a popular alternative light source over all other conventional light sources because LEDs are very energy efficient, start instantly, operate in cold temperature, have very low UV emission, as well as long life, compact size, light weight, breakage resistance, again they are easily controllable and environment friendly [1, 2,13] also.

To save electric energy, artificial light may be integrated with natural daylight. The colour of the artificial light source should match with that of natural daylight. The CCT of day light varies throughout a day, starting from 2000 K at sunrise through 5000 K for direct daylight at noon and can exceed 10 000 K in overcast conditions [3]. So, to create an exact visual sensation colour tuneable artificial light source should be introduced for daylight harvesting. Apart from daylight harvesting, colour tuneable light source may be used for mood lighting, which affects the emotional feeling of human [4].

It is well known that the three primary colours of visible light red (R), green (G) & blue (B) can be mixed to get a wide range of colours. In some of the previous studies, monochromatic RGBY (Red-Green-Blue-Yellow) LED was mixed to get different colour combination of white light [3]. But CCT of monochromatic light cannot be measured and CRI of the produced light is also poor. In this study RGB LED at different intensity is blended with Warm-White (WW) to produce variable CCT. Finally an algorithm is proposed to vary the CCT using only red and blue LED with warm white LED.

2. RGBW LED LIGHTING SYSTEM

The experimented RGBW (Red-Green-Blue-White) LED lighting system consists of one Dimming-Controller-Unit (DCU), four LED drivers and a RGBW LED module. The four LED drivers are

used to drive each of the LED string at four independent current. The DCU is responsible to generate four independent PWM duty ratios, which will ensure four independent current through each LED string. A block diagram of the developed system is shown in Fig. 1.

2.1. Basics principle of CCT control

The basic principle of the CCT control can be explained by CIE1931 (*x, y)* chromaticity diagram, any colour sensation can be represented by a couple of (*x, y*) coordinates. The colour temperature of a light source is the temperature of an ideal black-body radiator that radiates light as comparable with white light source. Lower the CCT value (2700K-3000K) is called warm white and higher the CCT (5000K-6000K) is called cool white.

Grassman law states that the superposition of colour is a linear phenomenon. So, when colour coordinates (x_k, y_k) of n primary emitters are known, any colour coordinates (*x, y*) lies inside the CIE1931 colour space diagram can be defined by eqn.(1) and eqn.(2) [5]. Y_K is the luminous flux of primary emitters.

$$\frac{x=\sum_1^n x_k \cdot \frac{Y_k}{y_k}}{y=\sum_1^n \frac{Y_k}{y_k}}, \quad (1)$$

$$\frac{x=\sum_1^n y_k \cdot \frac{Y_k}{y_k}}{y=\sum_1^n \frac{Y_k}{y_k}}, \quad (2)$$

2.2. Prototype luminaire design

Placement of RGBW 3528 LED strip on the bakelite board is shown in Fig.2. Each LED string has 14 number of parallel path and each parallel path consists of 3 series connected LEDs.

3. DESIGN OF LED DRIVER

In this article a switch mode power supply (SMPS) based LED driver is designed using fly-back topology and the hardware circuit has been implemented on a printed circuit board (PCB). Linear power supply has a poor efficiency as semiconductor device operates in active region. By switching (either ON or OFF) of active devices the efficiency of the converter can be made high than the linear power supply.

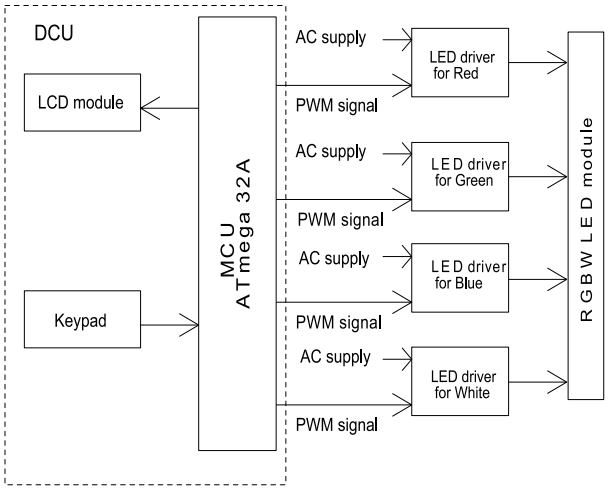

Fig.1. Block diagram of CCT controllable LED lighting system

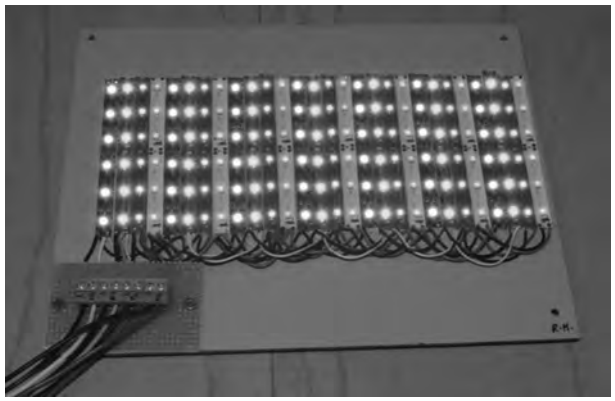

Fig.2. Prototype of RGBW luminaire

MOSFET 2N60 is used as a switching device which is 2A, 600V N-channel MOSFET.

3.1. Principle of designed LED driver

At first AC power is converted to DC by using rectifier, and then the DC is converted to the desired level of DC to drive the LED using a high frequency switch & a transformer. The logical block diagram of LED driver is shown in Fig.3

The self-oscillating fly back converter is a popular circuit for cost-sensitive applications due to its simplicity and low component count [6]. A detailed design-oriented steady-state analysis and a small-signal model of the self-oscillating fly-back converter has been found already [6].

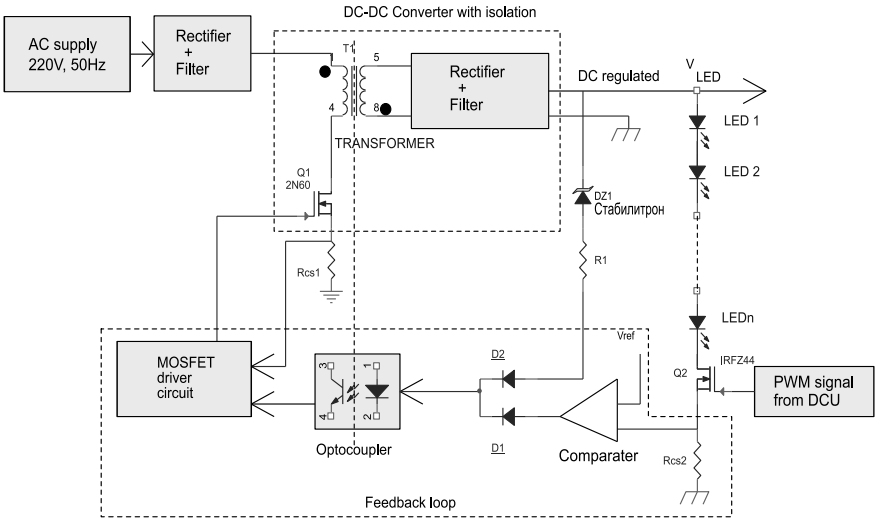

Fig.3. Block diagram of the LED driver

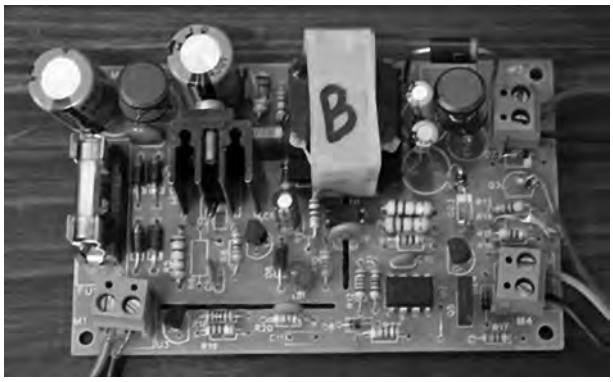

Fig.4. Prototype of the LED driver

So in this work a self-oscillating fly-back converter topology is designed and the circuit has been implemented to drive the LED strip. When the MOSFET Q_1 turns ON, current starts flowing through the primary coil of the transformer, and the energy is stored in the primary coil. The primary current I_p can be measured across a low value resistance R_{CS1} which is connected between MOSFET's source and ground terminal. In absence of feedback, the peak value of primary current I_p*R_{cs1} reaches base-emitter threshold voltage of an NPN transistor, which reduce the gate-source voltage of MOSFET Q_1. Because of regenerative action Q_1 rapidly turns OFF and the primary stored energy 1/2 L_p*I_p is transferred to the secondary, where L_p is the primary inductance. In the presence of voltage or current feedback the value of I_p*R_{cs1} is modified so that the required secondary voltage or current is modified.

The MOSFET driving circuit will rapidly turn ON and turn OFF the MOSFET Q_1 according to feed back signal or primary current. Opt coupler was used to isolate the secondary coil of the transformer from primary coil. Fig.4 shows the developed prototype of LED driver.

Table 1. Specifications of LED driver

Specifications	Values
Nominal input voltage, V_{in}	230V,50Hz AC
Nominal output voltage, V_{out}	16 *V*
L1 Primary inductance	430 μH,
L2 secondary inductance	8 μH
Rated LED current, I_{LED}	312mA
LED type and number of LED	LED strip 3528 (Red, Green, Blue, White)
Dimming frequency, F_{Dim}	244Hz
Current Sense resistor	0E5

Table 1 shows the different specification and component value used to design the LED driver.

3.2. Control mode of the LED driver

The control circuit at the secondary is designed to operate in voltage protection mode and in current control mode. In a typical cycle of PWM for dimming the secondary control signal goes through voltage protection mode and in current control mode. In a cycle during turns ON of MOSFET Q_2 the current control loop will be activated to protect the LED and during turns OFF voltage control loop will be activated to protect the MOSFET Q_1.

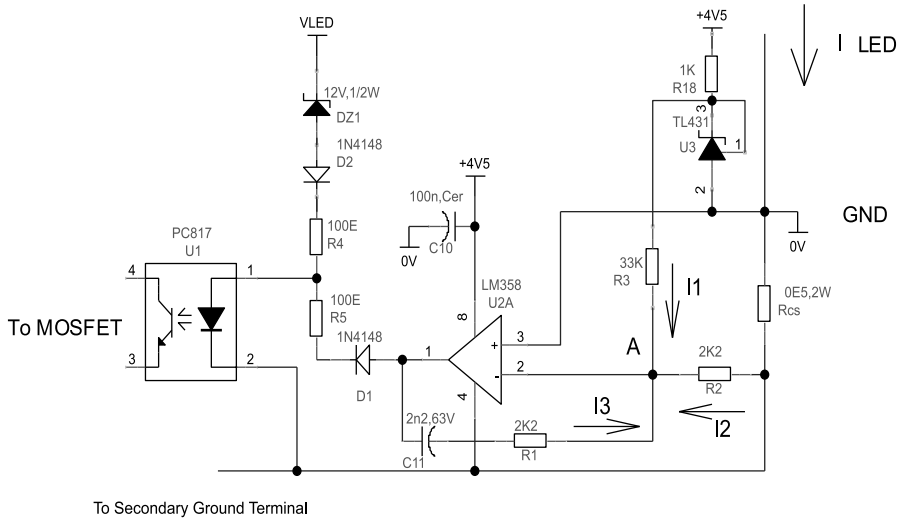

Fig.5 Circuit diagram of the PI controller based current control

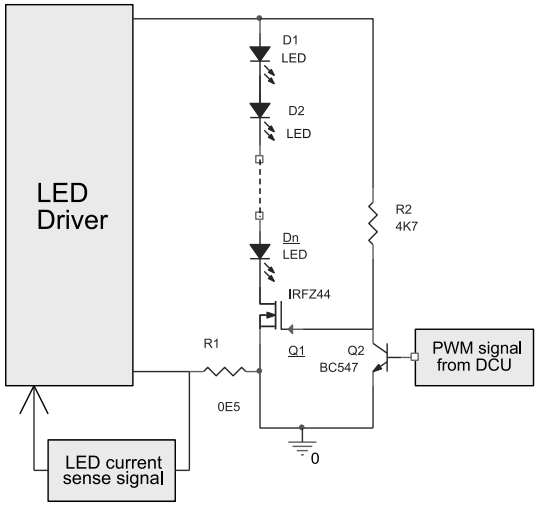

Fig.6. Schematic of series connected switch for dimming

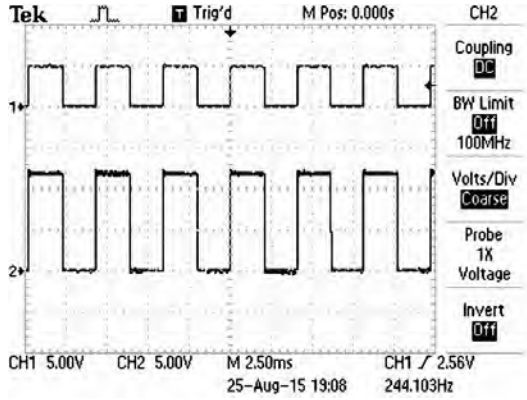

Fig.7 DCU signal (CH1–5V/div), Drain to source signal (CH2–5V/div) at 50 % duty cycle. Time scale-2.5 mS/div

3.2.1. Current Control mode

As LED is a current driving semiconductor device, its brightness is proportional to the current which will flow through it. The current control mode is implemented using a PI controller as shown in Fig.5. This control loop will work when the output terminal gets shorted or LED gets shorted, or load exceeds maximum allowable current.

The feedback control scheme of the secondary is implemented through a resistance divider and then the scaled voltage is amplified by using a transconductance type amplifier (TL431) [6].

In this article the feedback control scheme is modified by using A PI controller, which is required to control the LED current preciously.

Applying KCL at node A of Fig.5

$$I_1+I_2+I_3 = 0 \tag{3}$$

$$I_1 \frac{V_{ref}}{R_3}, \tag{4}$$

$$I_2 = -\frac{I_{LED} \cdot R_{CS}}{R_2}, \tag{5}$$

$I_3 = 0$ at steady state.

The maximum driving current that will be delivered by the LED driver can be calculated by using eqn.(6).

$$\text{So, } I_{LED} = \frac{R_2 \cdot V_{ref}}{R_3 \cdot R_{CS}}. \tag{6}$$

So limit of maximum current can be set by varying any parameters R2, Vref, R3, R_{CS}. Operation-

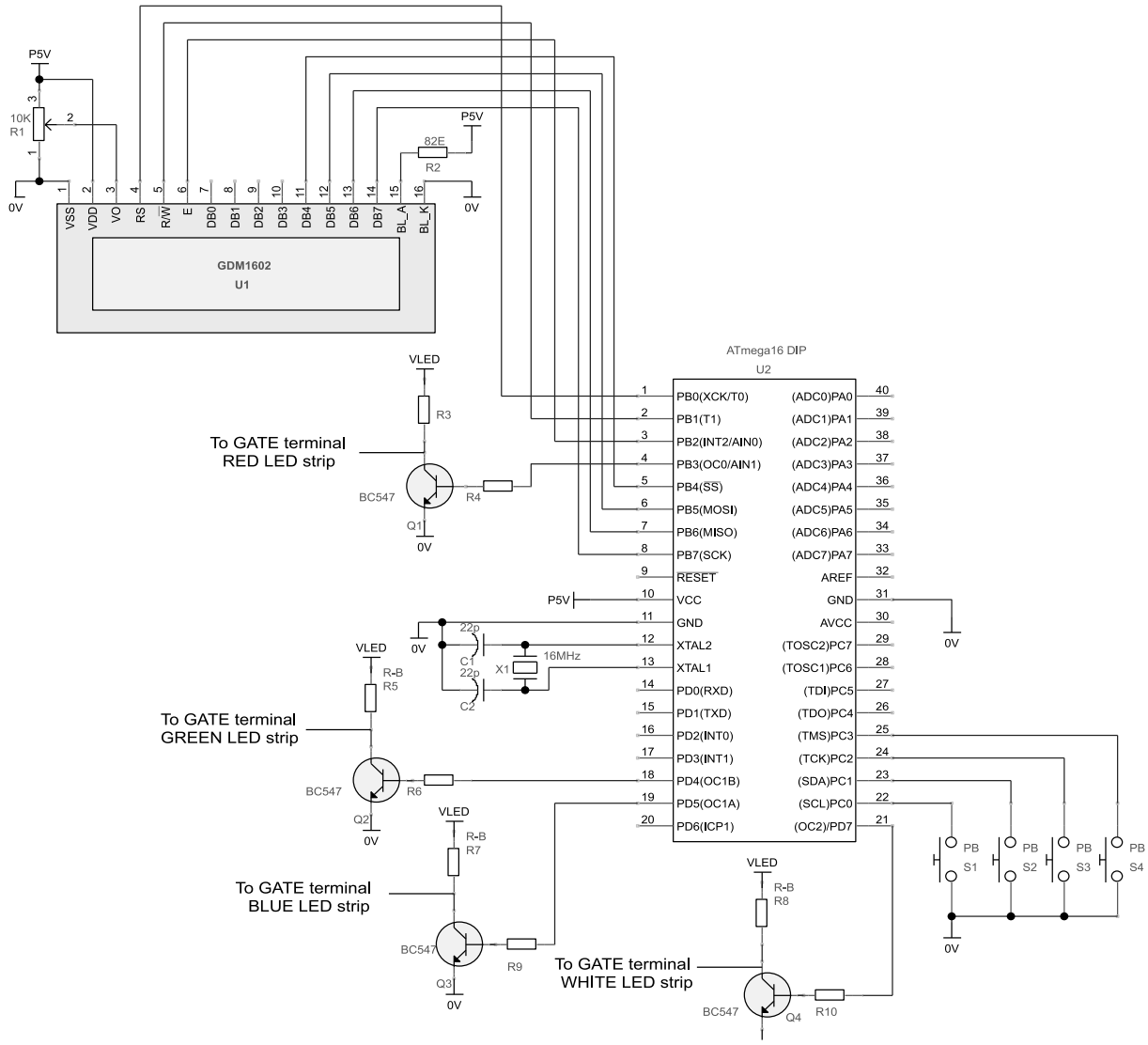

Fig.8. Pin connection of LCD and keypad to Microcontroller

al-amplifier (OP-AMP) LM358 is used to compare between reference voltage and driving current. I_{LED} can be calculated from eqn.(6). It is equal 312 mA. The reference voltage 2.5V is generated by using a precision shunt regulator TL431. In current control mode $I_1<I_2$, so output of the comparator will be high.

3.2.2. Voltage Control mode

In voltage control mode $I_1>I_2$, and output of the comparator will be low.

LED terminal voltage V_{LED} will be decided by voltage drop of zenor diode DZ_1, D_2 and opt coupler diode. The output voltage at LED terminal must not go beyond the supply voltage of LED under any circumstance.

4. DESIGN OF DCU (DIMMING-CONTROLLER-UNIT)

A DCU is used to generate four independent PWM signals. The DCU comprises of ATmega32A microcontroller from Atmel Corporation, a 16X2 LCD display and a 4X1 keypad module. The PWM dimming frequency generated from the DCU must be higher than 100Hz to avoid flickering as described by [7, 8,14]. It was set to 244Hz for RGBW channel to avoid flicker.

4.1. Principle of LED dimmer

As LED is a current driving semiconductor device, its brightness is proportional to the current, which flows through it. The light output of LED can

Fig.9. Test set up for CCT measurement by Konica-Minolta colorimeter

be varied by modulating the amplitude of the current. However, this type of linear dimming is not recommended for RGB colour dimming as chromaticity changes with amplitude of the current and with varying junction temperature [9]. For semiconductor device most flexible way of dimming is to use a pulse-width modulated (PWM) current signal on the LED array with varying duty cycle. It will change the illuminance value without changing the peak current of LED's string. PWM dimming technique has some advantages over analogue or amplitude dimming like stability of chromaticity during 0–100 % dimming and it has also linear relationship between duty cycle & light intensity of LED. From the previous study it can be concluded that PWM dimming is most suitable for this purpose as analogue dimming changes the colour of LEDs [9]. So, a PWM based dimming technology is implemented as one most suitable for this purpose.

A semiconductor switch is used in series with each of the RGBW LED string to turn ON and OFF LED's individually, according to the duty ratio. The average current that will be supplied by LED driver to LED can be expressed as eqn. (7)

$$I_{avg} = \frac{I_{LED} \cdot T_{on}}{T_{on} + T_{off}}, \tag{7}$$

I_{LED} is equal to maximum allowable current through LED, can be calculated from eqn. (6).

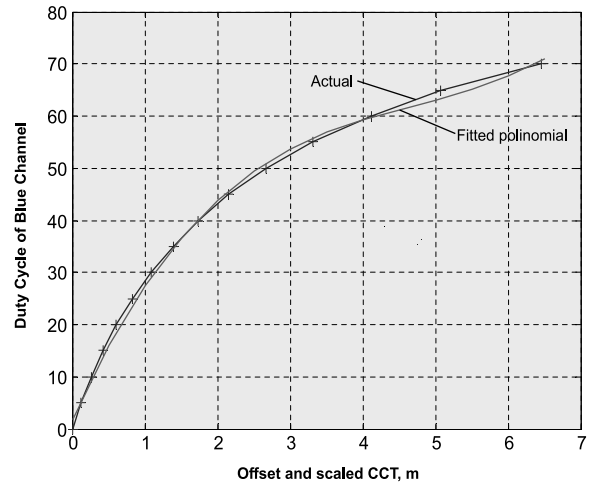

Fig.10. Scaled CCT vs duty cycle for blue channel

T_{on} and T_{off} is the turned ON and OFF time of LED respectively. Duty cycle can be varied from 0–100 %, so light output from the LED will vary also from 0–100 %. The schematic diagram of series connected switch is shown in Fig.6. The switch Q2 is an N-channel power MOSFET IRFZ44. To ensure proper turn ON and turn OFF of the series dimming MOSFET (IRFZ44) Q_2 a NPN transistor Q_3 (BC547) is used to provide the necessary GATE current for Q_2.

Fig. 7 shows that when DCU signal is high, drain terminal of Q2 is also high as GATE terminal of the MOSFET Q2 is grounded through Q3 and when DCU signal is low the gate terminal of Q2 will be high, so LED string will be ON during low DCU signal

4.2. PWM signal generator

ATmega32A is a low-power CMOS8-bit microcontroller based on the AVR enhanced RISC architecture. It has the following features like, 32 Kbyte of In-system programmable flash memory with read-write capability, Four PWM channel, 32 Programmable I/O line, speed 0–16MHz, 1024Kbyte EEPROM, 32 General purpose resistors etc. [10] By enabling Timer 0, Timer 1, Timer 2 of ATmega32A four PWM signals are generated.

The program for PWM generation, keypad and LCD module interfacing program is written in Atmel Studio 6.2 software (from Atmel Corporation) [11] and the HEX file is loaded into the ATmega32A microcontroller using USBASP AVR Programmer.

Register TCCR0 of Timer0 of ATmega32A is used to set the different modes and frequency selection. OCR0 register is used to set the duty cycle of the generated wave by comparing OCR0 and TCNT0 register value.

Frequency of the generated wave can be calculated by using eqn. (8) [10]:

$$F_{generated\ wave} = \frac{F_{oscillator}}{256 \cdot N}, \qquad (8)$$

N is the prescaler value that may be (1/8/64/256/1024) the value of the prescaler chosen 256, oscillator frequency is equal to16 MHz. So, $F_{generated\ wave}$ will be 244.14 Hz.

Now the duty cycle of the duty cycle of the generated wave can be calculated as eqn. (9) [10].

$$\text{Duty cycle } = \frac{OCR0+1}{256} \cdot 100, \qquad (9)$$

Value of OCR0 may vary from 0 to 255. Value of OCR0 register can be set through keyboard according to the RGBW mixing ratio. The percentage of duty cycle corresponding to each RGBW LED string is displayed in LCD screen for user interfacing. Same could be repeated for Timer1 and Timer2.

Duty cycle can be varied by setting OCR0, OCR1A, OCR1B, OCR2 register of ATmega32 through a keypad module for RGBW LED string respectively.

4.3. Keypad and LCD module

Key pad module is used to change the duty cycle of the individual channel according to blending ration.

Pin connection of LCD, keypad and dimming signal to the microcontroller is shown in Fig .8.

JHD162A LCD module is used to display the dimming parameters (i.e. percentage of blending ratio), which is capable to display 16 Characters and 2 Lines [12]. The keypad interfacing program is written in such a way that the keyboard debounces or multiple key presses can be restricted.

5. EXPERIMENTAL RESULT

Here CCT is measured by varying the intensity of Red, Green and Blue LED individually with respect to WW LED. Various CCT produced by the

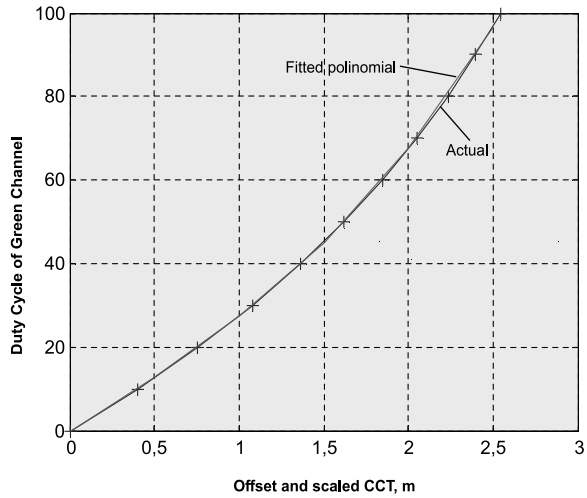

Fig.11. Scaled CCT vs duty cycle for green channel

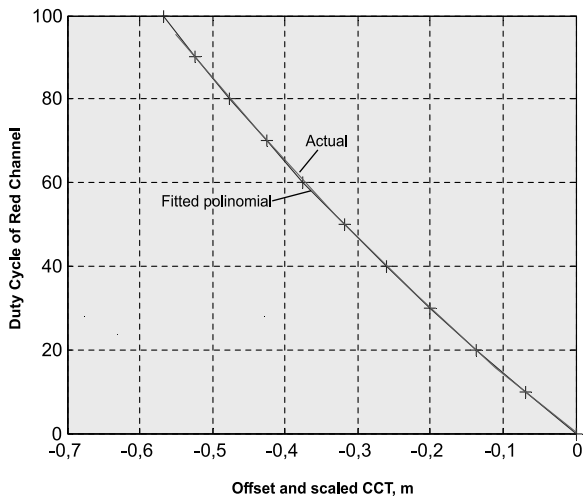

Fig.12. Scaled CCT vs duty cycle for red channel

RGBW luminaire is measured using Konica-Minolta CL200A Chroma Meter. The experiment has been carried out in a windowless dark-painted room at Electrical Engineering Department of Jadavpur Univertsity, and the Chroma Meter is placed 1 meter below the RGBW light source. The experimental set-up is shown in Fig.9.

As CCT of Warm white LED (3268 K) does not change so much throughout the 0–100 % dimming, the reading has been taken keeping the warm white LED at 100 % brightness, which will also increase the illuminance level. To achieve different illuminance level, duty ratio of the white channel can be varied. CCT is measured up to 70 % duty cycle of the blue channel, because beyond this, CCT cannot be measured by the Konica Minolta CL200A Chroma Meter as blue content is very high. The measured CCT with respect to duty cycle of blue channel is given in Table 2.

Table 2. CCT vs duty cycle of blue LED

Sl. No	Blue channel duty cycle, %	CCT, K
1	0	3268
2	5	3394
3	10	3539
4	15	3692
5	20	3880
6	25	4100
7	30	4360
8	35	4664
9	40	4996
10	45	5420
11	50	5940
12	55	6581
13	60	7389
14	65	8341
15	70	9723

Based on Table 2 above we can automate the process of producing white light of a certain CCT. A new variable, m, representing an offset and scaled value of the CCT as defined below

$$m = (\theta\,(\Delta_B) - \theta\,(0))\,/\,1000, \qquad (10)$$

where θ (Δ_B) is the CCT of the white-blue composite array at a duty cycle Δ_B of the blue channel, is used below.

The variable ΔB is now plotted as a function of *m*. Using MATLAB®, a cubic polynomial is then fitted through this graph. Actual varying CCT of blue channel and fitted polynomial is shown in Fig.10.

The polynomial equation is given by

$$\Delta_B = 0.4132 * m^3 - 5.8318 * m^2 + 31.0856 * m + 1.8145. \qquad (11)$$

An increase in the order of the polynomial was avoided for two reasons. The first is that it did not provide any higher accuracy throughout the range. The second reason is that it increases the computation time of the method described below.

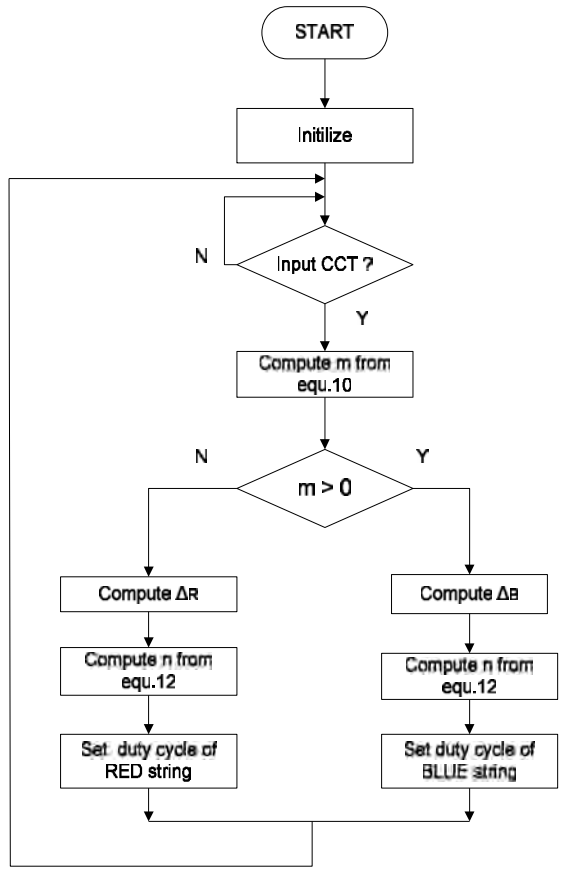

Fig.13. Flow chart of CCT varying algorithm

PWM width selection registers OCR0, OCR1A, OCR1B and OCR2 of ATmega32A are 8 bit register. So for 0–100 % dimming corresponding register value will vary from 0–255.

So, the register value n can be calculated as eqn. (12)

$$n = 2.55 * \Delta_B, \qquad (12)$$

where Δ_B is the calculated duty cycle from eqn.(11).

Proposed algorithm to select the proper duty cycle of blue channel with respect to desired CCT as described below:

Step1: – Set the desired CCT value ranging from 3230° K to 9723° K;

Step2:– Compute m from eqn.(10);

Step3: – Compute Δ_B from eqn.(11);

Step4: – Compute n from eqn.(12);

Step5: – Set the 8 bit register OC1A of ATmega32A by computed value of n to achieve desired CCT.

For an example to produce CCT 4100° K using blue and WW LED duty cycle of blue channel will

Table.3 CCT vs Duty cycle of red and green LED

Sl. No.	Duty cycle of G/R LED, %	CCT, K for green blending	CCT, K for red blending
1	0	3268	3268
2	10	3673	3198
3	20	4025	3132
4	30	4192	3067
5	40	4350	3008
6	50	4628	2950
7	60	4887	2893
8	70	5316	2842
9	80	5502	2791
10	90	5665	2745
11	100	5813	2700

be 25 % and the corresponding OCR2 register value will be 64.

Same process could be repeated for Red and Green channel. The measured CCT ranges for WW-G and WW-R LED blending are 3268–5813K and 3268–2700K respectively, where duty cycle of green and red LED varied from 0–100 %. The measured CCT with respect to duty cycle of green and red channel are given in Table 3.

The fitted polynomial equations for green and red channel are given by eqn. (13) and eqn. (14).

$$\Delta_G = 2.2750 * m^3 - 0.4693 * m^2 + 25.7082 * m - 0.1606. \quad (13)$$

$$\Delta_R = 75.2395 * m^2 - 132 * m + 0.3191. \quad (14)$$

The fitted polynomials using MATLAB® are shown in Figs.11,12 respectively.

By observing Table.2 and Table.3 it can be concluded that to achieve higher CCT than WW LED, only blue LED may be blended and on the other hand for lower CCT range red LED may be used. To automate the process, an algorithm is proposed and the flow chart of the proposed algorithm is shown in Fig.13.

Now the CCT is set in the interval of 500K by using a keypad and measured by the Konica Minolta CL200A Chroma Meter. Table 4 shows maximum deviation of 18 K and 344 K for red and blue blending from set point value respectively. This algorithm can select automatically blue LED for higher CCT and red LED for lower CCT with respect to WW CCT.

Table 4. Measured CCT and error

Sl. No.	Set CCT, K	Measured CCT, K	CCT error, K
1	2700	2718	–18
2	3000	3011	–11
3	3500	3493	7
4	4000	3946	54
5	4500	4470	30
6	5000	5022	–22
7	5500	5601	–101
8	6000	6114	–114
9	6500	6620	–120
10	7000	7039	–39
11	7500	7370	130
12	8000	7745	255
13	8500	8170	330
14	9000	8656	344
15	9500	9433	67

6. CONCLUSION

To vary CCT of light from 2700K – 9723K, it is understood that only WW, red and blue LEDs are sufficient. To change CCT only from 3268k up to 5813k, green and WW may be used. So, to get the effect of natural light, only RBW LEDs are needed instead of RGBW LEDs. It reduces the cost of total number of LEDs. Here, this work does not take care about the illuminance available on a working plane. Research is being carried out to select the CCT and Illuminance both simultaneously in a similar type of lighting system.

REFERENCES

1. Kim JK, Schubert EF. Transcending the replacement paradigm of a solid-state lighting. Opt Express, 2008. V16,#26, pp.21835–21842.

2. Protzman JB, Houser KW. LEDs for general illumination: the state of the science. LEUKOS, 2006. V3,#2, pp.121–142.

3. Gilman JM, Miller ME, Grimaila MR. A simplified control system for a daylight-matched LED lamp. Lighting Res Technol, 2013. V45,#5, pp.614–629.

4. Lin K-C, Linb C-S. The study of a novel control method of the mood lighting emulator. Optics Communications Elsevier, 2015. 350, pp.71–76.

5. Buso S., Spiazzi G.. White light solid state lamp with luminance and colour temperature control. Power Electronics Conference (COBEP); Brazilian, 2011, pp. 837–843.

6. Irving Brian T. and Jovanović Milan M. Analysis and Design of Self-Oscillating Flyback Converter. APEC Seventeenth Annual. Con. IEEE, 2002, V2, pp. 897–903.

7. Bullough JD, Hickcox K Sweater, Klein TR, Narendran N. Effects of flicker characteristics from solid-state lighting on detection, acceptability and comfort. Lighting Res Technol, 2011. V43,#2, pp. 337–348

8. Wu C–$5, HuN – C, Chen J – N, Chang H – I. Parameterised LED current regulator for pulse width modulation switch delay for accurate color mixing in multi-LED light sources. Lighting Res Technol, 2014. V46,#2, pp.171–186.

9. Dyble M, Narendran N, Bierman A, Klein T. Impact of dimming white LEDs: chromaticity shift due to different dimming methods. P Soc Photo-Opt Ins, 2005. 5941, pp.291–299.

10. 2015. Atmel ATmega32A [DATASHEET]. <http://www.atmel.com/images/atmel-8155–8-bit microcontroller-avr-atmega32a_datasheet.pdf > Accessed 2015 December 11.

11. 05/2014. Atmel Studio 6.2 [RELEASE NOTES].<http://www.atmel.com/images/astudio6_2_1153-readme.pdf > Accessed 2016 January 23.

12. JHD162ASERIES datasheet <http://pdf1.alldatasheet.com/datasheetpdf/view/127934/ETC1/JHD162A.html > Accessed 2016 January 23.

13. S. Golder, S. Mazumdar, Ray K. A high efficiency DC to DC boost converter for white LED based lighting systems- An energy-efficient, cost-effective approach for rural application, 2007. V15,#2, pp.53–58.

14. R.Malik, S. Saha, S. Mazumdar, "Development of Discrete Component based LED Driver with RGB PWM dimming" Published in the Proceedings of LUX Pacifica 2015, Kolkata, 27–29 November, pp.635–641.

ACKNOWLEDGMENT:

Special thanks to Prof. (Dr.) Kalyan Kumar Ray for his extensive technical support throughout the research work.

Rajib Malik
is Ph.D. fellow at Electrical Engineering Department of Jadavpur University. He received his M.E. degree in Illumination Engineering in 2013 and B.E. degree in Applied Electronics & Instrumentation Engineering in 2010. His research interests include Solar based Smart Lighting system, electronics converters for lighting application and colour control of light

Saswati Mazumdar,
Ph.D. and Professor at Electrical Engineering Department and Former-Director of School of Illumination Science and Engineering & Design in Jadavpur University. She has 29 years of experience in Lighting Research and Teaching, developed a modernized Illumination Engineering laboratory in Electrical Engineering Department of Jadavpur University, have founded two Masters' Courses: one Illumination Engineering and another on Illumination Technology & Design in Jadavpur University, executed a large number of R&D and consultancy projects on Illumination and allied fields

Light & Engineering
Vol. 25, No. 4, pp. 109-113, 2017

Svetotekhnika
No. 1, 2018

DESIGN OF A SELF-ADAPTED LED DESK LAMP BASED ON TCS3414CS

Jingyu Chen, Aiming Ge*, Rulong Hao, Ling Zhu, and Xinran Tao

Department of Light Sources & Illuminating Engineering,
Fudan University, Shanghai 200433, China
**E-mail: amge@fudan.edu.cn*

ABSTRACT

In this paper, a design of a self-adapted LED desk lamp is presented. The illuminance on the work plane and colour temperature of the hybrid light are measured by the multi-channel colour sensor TCS3414CS. The MCU embedded in the lamp will adjust the LED drivers' output to maintain constant illumination. Experimental results show that, no matter how the ambient light changes under different scenes, the lamp can still provide satisfactory lighting condition with both illuminance and colour temperature adjusted to a predefined value, leading to a more comfortable user experience.

Key words: LED desk lamp, illumination, CCT, colour sensor, dimming control

1. INTRODUCTION

With the rapid development of LED technology, people are paying more and more attention on quality, comfort and environmental friendliness of illumination rather than brightness and cost. Desk lamps are the most widely used supplementary lighting devices in our daily life. There are two main types of LED desk lamp in current market [1]: traditional lamps without dimming function and smart lamps whose brightness and colour can be manually set. However, once ambient light changes, the former cannot maintain a constant illumination on the work plane. And because the adjustment solely depends on users' intuitive feelings, the latter type may provide a too high or too low lighting level, causing damage to human's eyes if it is used for a long time. And the by-hand adjustment is contrary to the intelligent, humanized and low-carbon design concept of modern household appliances. Besides, users have various colour temperature preferences and colour requirements are not always the same in different scenarios. For example, warm light is more suitable for leisure time reading, while light with high colour temperature can keep people's mind active when they are working [2]. In order to better meet the needs for quality lighting, this paper design a self-adapted LED desk lamp capable for both illuminance and colour temperature adjustment. When the environmental light changes, the lamp is able to adjust the LED output to provide a constant illuminance level and keep the correlated colour temperature of the hybrid light (ambient light & LED) to a predefined value in the meantime.

2. DESIGN OVERVIEW

The hardware design of the desk lamp consists of a micro controller, LED drivers, a colour sensor

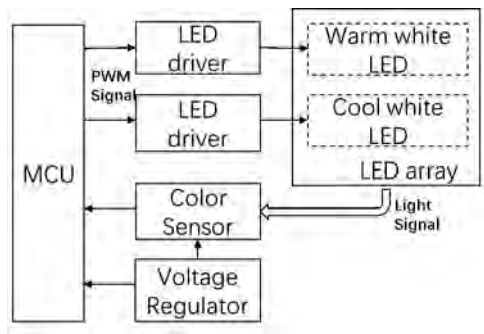

Fig.1. Overview of the desk lamp

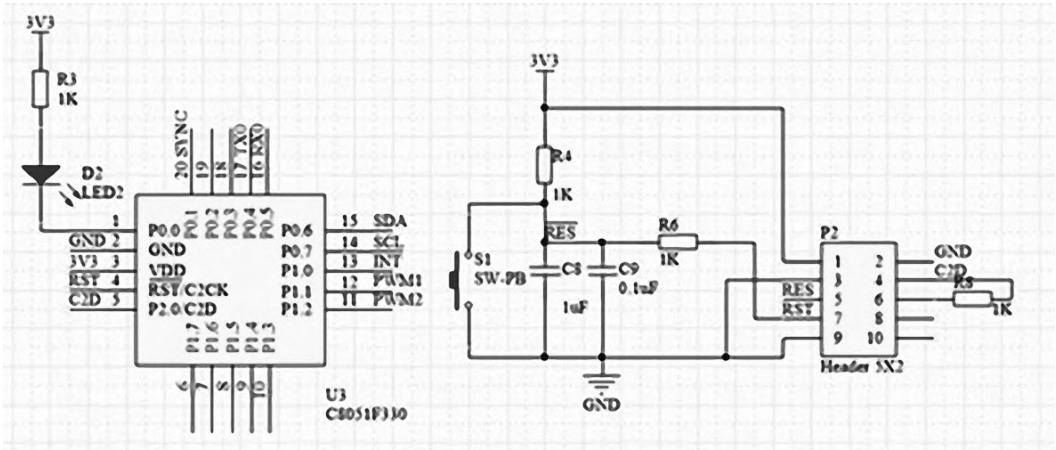

Fig. 2. MCU circuit and its programming interface

[3,4], voltage regulators and a LED array, as Fig. 1 shows.

The LED array is comprised of 2 kinds of LED with different colour temperature in order to implement the CCT adjustment feature. To extend the range of light colour control as well as meet the output flux requirement, Cree XLamp XPE series is selected for its spectra diversity and high performance. In this design, we choose 2600K and 6500K LED whose power can be up to 2W per chip.

The colour sensor located on the lamp holder can receive the hybrid light, and send the information to the MCU. Then the MCU will calculate the hybrid light CCT and illuminance on the work plane, and compare the results with preset values to adjust the LED output to realize adaptive control.

For the sake of safety, the input voltage of the desk lamp is restricted to 12V with an external AC-DC adapter. Since the rated voltage for both the

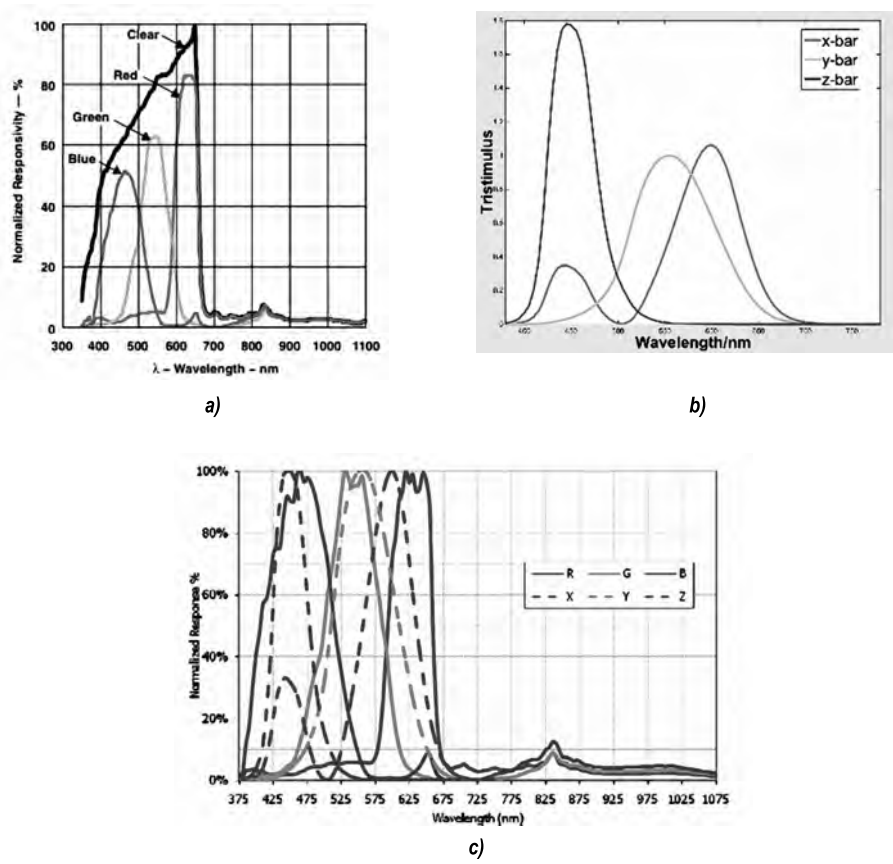

Fig. 3. (a) Response curves of TCS3414CS; (b) Tristimulus of human eyes; (c) Normalized curves comparison

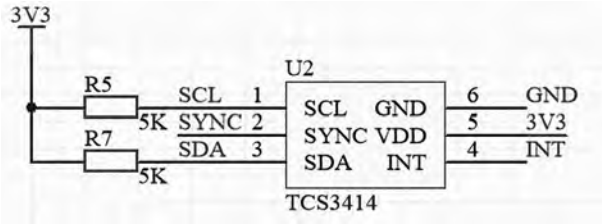

Fig. 4. Colour sensor TCS3414CS

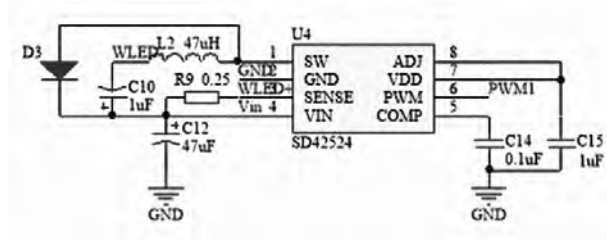

Fig.5. LED driver

MCU and the colour sensor is 3.3V, extra voltage regulators are implemented in the PCB board.

3. HARDWARE DESIGN

3.1. Control circuit

As the core of the hardware design, the controller is responsible for PWM signals generation, communication with the colour sensor and output adjustment based on the control algorithm. In this design, we choose Silicon Laboratories' 8-bit MCU8051F330, which contains a high-speed pipelined 8051-compatible microcontroller core and various peripherals, Fig.2. Apart from many kinds of digital interfaces such as SMBus, UART and SPI integrated, C8051F330 is rich in counter resource and able to generate 4-independent-channel PWM signals, which meets our design requirements perfectly.

3.2. Colour sensor

In order to obtain the illuminance on the work plane and CCT of hybrid light, a 4-channel digital colour sensor, TCS3414CS, produced by AMS, is used in this design. This sensor includes an 8×2 array of filtered photodiodes, analogue-to-digital converters, and control functions on a single monolithic CMOS integrated circuit. Of the 16 photodiodes, 4 have red filters, 4 have green filters, 4 have blue filters, and 4 have no filter (clear). Fig. 3(a) shows the spectral responsivity of TCS3414CS, Fig. 3(b) is the tristimulus curves of human eyes and Fig. 3(b) is the comparison of the normalized curves.

Since the response curve have very similar peak wavelength and FWHM with tristimulus curve, MCU can solve for CCT and illuminance by Matrix operations and use the results as the regulation basis. Equation 1 shows the calculation of illuminance and Equation 2–5 illustrate how to acquire CCT value [5,6]. Where *R, G* and *B* are the integral response of the filtered channels of TCS3414CS respectively.

$$E = (-0.32466)R + (1.57837)G + (-0.73191)B. \quad (1)$$

$$\begin{cases} X = (-0.14282)R + (1354924)G + (-0.95641)B \\ Y = (-0.32466)R + (1..57837)G + (-0.73191)B, \\ Z = (-0.68202)R + (0.77073)G + (0.56332)B \end{cases} \quad (2)$$

$$\begin{cases} x = X / (X + Y + Z) \\ y = Y / (X + Y + Z) \end{cases}, \quad (3)$$

$$n = (x - 0.3320) / (0.1858 - y), \quad (4)$$

$$CCT = 449n^3 + 3525n^2 + 6823.3n + 5. \quad (5)$$

The MCU communicates with the colour sensor through I^2C bus as Fig. 4 shows. The sampling integration time is set to 154 ms.

3.2. LED driver

The LED driver plays a significant role in the desk lamp design. General requirements for LED drivers are high efficiency and good control accuracy [7]. In this design, we take advantages of Silan's high performance step-down PWM control LED driver, SD42524, to modulate the light output. With the 12 V DC input voltage, the LED drivers can achieve 1A continuous output current with thermal shutdown protection and current restriction. Two SD42524 chips are used for independent adjustment of the two different color temperature LEDs. To simplify the control algorithm, the sampling resistance of the LED drivers are tuned to make the total flux of 2600K LEDs equal to that of 6500K LEDs when the duty cycles are set to 1 for both. Fig. 5 is the circuit of LED driver.

4. DIMMING STRATEGY

A two-stage dimming strategy is adopted in this design to provide target illuminance on work plane, adjust the CCT of hybrid light to a certain degree and keep stable lighting condition.

First of all, the MCU will acquire the current illuminance through the colour sensor and compare it with the target value.

$$e = E_m - E_t. \tag{6}$$

Where E_m and E_t are the target and measured illuminance. If the absolute value of e exceeds the threshold, the MCU will increase (when e>0) or decrease (when e<0) the output power of both LED drivers by same percentage simultaneously. Usually after several rounds of negative feedback regulation, the gap between measured illuminance and target value will be narrowed down to the threshold.

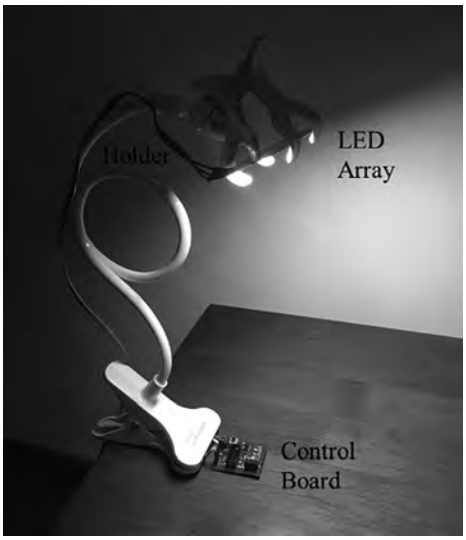

Fig. 6. The testing experiment

Table 1. The illumination and CCT values under different scenes in Experiment 1

Scenes	Illuminance, lx (LED Off)	CCT, K (LED Off)	Illuminance, lx (LED On)	CCT, K (LED On)
Turn off all other lights at night	0	N/A	495	4033
Turn on the remote fluorescent lamp	208	3123	506	3965
Turn on the nearby fluorescent lamp	385	3353	497	3950
Open windows at noon	244	4698	513	4076

Once the illuminance requirement is met, the dimming strategy goes into the next stage to realize a constant CCT value of the hybrid light. Similarly, the error between real CCT value and preset value is solved out first. Then if it goes beyond the CCT threshold, the MCU will adjust the output of the two LED drivers by same percentage but in opposite direction. For instance, if the measured CCT is higher than the target, the output of warm white LEDs will increase while the cool white ones are turned down and vice versa.

Proportion control algorithm is adopted for both illuminance and CCT adjustment [8] to fulfil smoothly modulation. Taking illuminance regulation as an example, the control object is the duty cycle of the PWM signal and it is calculated according to the following equation:

$$D(n+1) = D(n) + P \times e. \tag{7}$$

$D(n)$ is the current duty cycle, $D(n+1)$ is the duty cycle for the next moment and P is the proportionality factor. The P value can't be set too high or too low, because it will cause the output unstable or make the MCU takes more rounds to hit control targets. In this design, we used the empirical equation below to solve out the P value.

$$P = \frac{0.0002(E_t - E_a)}{E_{LED}}. \tag{8}$$

Where E_a is the illuminance of ambient light, which can be measured before LEDs are turn on. And E_{LED} is the maximum illuminance that one single channel LEDs can produce on the work plane. The same proportionality factor is used for CCT control algorithm.

Table 2. The illumination and CCT values under different scenes in Experiment 2

Scenes	Illuminance, lx (LED Off)	CCT/K (LED Off)	Illuminance, lx (LED On)	CCT/K (LED On)
Turn off all other lights at night	0	N/A	746	5023
Turn on the remote fluorescent lamp	200	3221	756	5095
Turn on the nearby fluorescent lamp	392	3307	743	4952
Open windows at noon	256	4701	771	5026

5. SIMULATION EXPERIMENT AND RESULTS

Two sets of simulation experiments were conducted to verify the control function. As shown in Fig. 6, the LED array is clamped by an adjustable holder. The control board is placed near the holder on the desk. And the distance between the LED array and the colour sensor mounted on the PCB board is around 50 cm, which is equal to typical reading distance.

Experiment 1:

Target illuminance: 500 lx, threshold: 50lx;

Target CCT: 4000K, threshold: 100K

The test results are shown in Table 1.

Experiment 2:

Target illuminance: 750 lx, threshold: 50lx;

Target CCT: 5000K, threshold: 100K

The test results are shown in Table 2.

From the test results, we can figure out that the fluctuation of illumination is restricted within 3 % and the CCT shift is limited to 2 % under different situations. The output will be stable within 20 rounds of feedback regulations, that is, in less than 3 seconds.

6. CONCLUSION

A design of a self-adapted LED desk lamp is presented in this paper. The illuminance on the work plane and correlated colour temperature of the hybrid light are measured by the multi-channel colour sensor TCS3414CS. Based on the sensor reading, the embedded MCU will adjust the LED drivers' output to maintain constant illumination. Experimental results show that, no matter how the ambient light changes under different scenes, the LED desk lamp can still provide satisfactory lighting condition with both illuminance and correlated colour temperature adjusted to a predefined value, leading to a more comfortable user experience. The specific mechanical structure of the lamp is not designed in this paper. In actual production, the control board can be enveloped in the lamp base with a small hatch over the colour sensor, and then the light can be measured.

Aiming Ge thanks the China Scholarship Council (CSC) for financial support No. 2010610538 of his research study at Utah State University and University of California, Merced, USA. This Study was also supported by the Natural Science Foundation of Shanghai Municipality, China (Grant No. 15ZR1402400).

REFERENCES

1. Cong-Hong L I, Yan Y. A new design of the intelligent LED table lamp[J]. Information Technology, 2013.

2. Chou C W, Chiang Y H, Tu H W, et al. Effect of LED desk lamp for working efficiency[C]. International Conference on Electrical and Control Engineering. IEEE, 2011:5868–5872.

3. Caicedo D, Li S, Pandharipande A. Smart lighting control with workspace and ceiling sensors[J]. Lighting Research & Technology, 2016.

4. Anandan M. Color sensor integrated light emitting diode for LED backlight: US, US20070170449[P]. 2007.

5. Smith J. Calculating Color Temperature and Illuminance using the TAOS TCS3414CS Digital Color Sensor[J]. Intell. OPTO Sens, 2009 (25): 1–7.

6. Ohno, Yoshi, Hardis, Jonathan E. Four-Color Matrix Method for Correction of Tristimulus Colorimeters[C]// Color Imaging Conference – Color Science, Systems and Applications. 1997:65–68(4).

7. Chiu H J, Lo Y K, Chen J T, et al. A High-Efficiency Dimmable LED Driver for Low-Power Lighting Applications [J]. Industrial Electronics IEEE Transactions on, 2010, 57(2):735–743.

8. Mahdavian M, Wattanapongsakorn N. PID controller tuning and optimizing for greenhouse lighting application considering real-time pricing in the smart grid[C]// International Computer Science and Engineering Conference. 2013:85–90.

Chen Jingyu,
Master in Optoelectronic System and Control Technology from Dept. of Light Sources & Illuminating Engineering, Fudan University. She got her Bachelor degree in Electrical Engineering and Automation in 2012. Her research topics are intelligent lighting control systems and relevant optics designs. At present, she is working on the integration of a LED/sunlight hybrid lighting systems

Ge Aiming,
visiting scholar, Associate professor of Fudan University, Post-doctoral in physics, Ph. D in optical engineering, mainly engaged in the theory and technology of Optoelectronic system, the design of optical system for imaging and illumination, the precise measurement and measurement technology, etc.

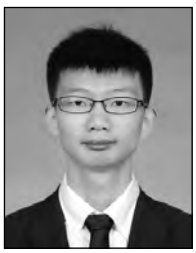

Rulong Hao
is a Ph.D. student at Fudan University. He is mainly engaged in imaging and illumination optics and system design of new methods of research. His research interests focus on imaging optical design and hybrid lighting system using collecting sunlight, transmitting light and rearranging light to satisfy indoor space

Zhu Ling
She works mainly on the novel design of the optical devices and system based on Freeform surface. She takes part in the research work in the guidance of Professor Ge and works on the efficient system of automobile lamps such as the reversing lamp

Xinran Tao
is a postgraduate student at Fudan University. At present, she is mainly engaged in research for optical elements with gradient refractive index materials and new methods of system design. Her research focuses on how to achieve optical elements with specific characteristics using gradient refractive index materials and theoretical design methods

Light & Engineering
Vol. 25, No. 4, pp. 115-122, 2017

Svetotekhnika
No. 5, 2017, pp. 62–68

EFFECTS OF LED LIGHTING ON THE LUMINANCE COEFFICIENT[1]

Pablo R. Ixtaina and Braian D. Bannert

Laboratorio de Acústica y Luminotecnia Comisión de Investigaciones Científicas LAL–$5IC Gonnet, Argentina
pixtaina@yahoo.com

ABSTRACT

The application of luminance technique in road lighting requires the knowledge of the reflection properties of the road surface. The effect of LEDs radiation spectra on these reflection properties is analyzed in the present paper. On this topic, CIE publication No 30–2 notices that road surfaces are not completely spectrally unselective, nevertheless, the effects on reflection of luminous sources spectra used on the road are usually disregarded. A spectral study on samples of Argentinean draining road surfaces is shown in this paper. Size standardized samples were measured under the standard observation angle, for three different light incidence angles. A focused spectrometer was used as detector. A standard high pressure sodium lamp (HPS) and a cool street LED luminaire were used as light sources. A specially built diffuse surface was used as reference in order to compare the spectral differences in reflection.

As a result, colour selectivity was found. The spectral samples selectivity produced a photopic absorption about 5 to 10 percent greater in HPS lamps spectra than LED sources.

Keywords: LED, road lighting, road reflection, spectra

I. INTRODUCTION

In road lighting, the visual perception of the driver is conditioned by the luminance distribution on the surface of the lit road. In this model, known as Luminance Technique, reflection properties of the road surface are characterized by the luminance coefficient "*q*", proportionality factor, for each road point, between its illuminance and the luminance reflected in the observation direction. The integer of luminance coefficient "q" on a solid angle that underlies a road element is called average luminance coefficient *Qo*, useful factor for evaluating the degree of "lightness" of the road surface.

The surface *Qo* impacts directly on the energetic efficiency of the installation. A "lighter" surface

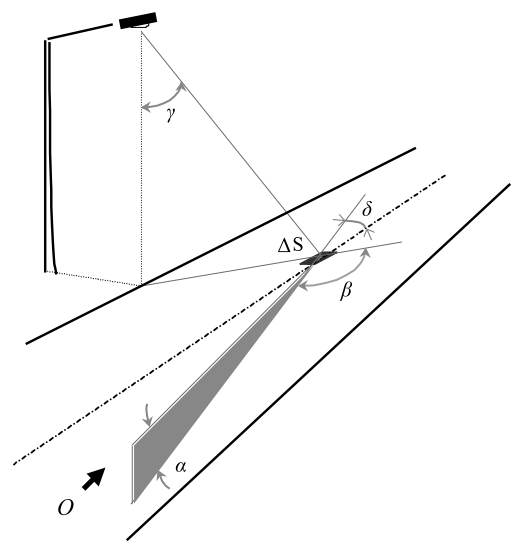

Fig.1. Basic geometry for the vision analysis in roads

[1] On basis of report at the European Lighting Conference LUX EUROPA 2017, September 18–20, 2017, Ljubljana Slovenia

will result in greater luminances in direction to the observer for a same distribution of illuminances. As *Qo* is a property mainly determined by the type of asphalt mixture or the kind of concrete, as well as the building methods used, its value can change regionally or by zones. This effect has already been observed for asphaltic concretes of a same area, with different compounds or application techniques [1]. It is then worth studying if this "degree of lightness" can change with the spectrum of light sources used in the lighting system. Particularly, and in the light of the current technological changes, our present work will focus on the possible effects of "spectral selectivity" that influence the reflection of white LEDs light.

1.1. Luminance coefficient

The luminance L of an elementary surface ΔS on the road (Fig. 1) is determined by equation (1):

$$L = \frac{I(C,\gamma)}{H^2} q(\alpha,\beta,\delta,\gamma) cos^3(\gamma), \tag{1}$$

where $I(C,\gamma)$ is the lighting intensity of the luminary in direction to the point where luminance is calculated, H the height of the luminary installation and q is the road luminance coefficient.

The luminance coefficient depends completely on the road surface: basic material, binder composition, application method final texture, time of use, etc. Far from being a constant, its value depends on the positions of the observer and on the lighting source with respect to the point under consideration. Studies showed that a valid simplification is to fix the observation angles: it has been standardized the driver's vision line parallel to the road axis ($\delta = 0^o$) and its elevation so that it has an impact on the vision point with a slope $\alpha = 1^o$. Thus, the standardized conditions for vision on road consider q dependent only on β and γ [2].

If E is the exact illuminance on the road, (1) can be rewritten as:

$$L = q(\beta;\gamma)E. \tag{2}$$

The luminance coefficient complies with the function of proportionality factor, for each road point, between illuminance and luminance. Thus, it is defined the average luminance coefficient Qo, which quantifies the degree of "lightness" of the road surface:

$$Q_0 = \frac{1}{\Omega_0} \int_{\Omega 0} q d. \tag{3}$$

In (3), Ωo represents the solid angle that underlies the element Δs in Fig. 1. As it was mentioned in the previous paragraphs, higher values of *Qo*, associated with "lighter" surfaces, will allow obtaining an increase of average luminance for the same system of lighting (thus, increasing the installation efficiency).

1.2. Coefficient *Qoo*

If there is an enough amount of simultaneous evaluations of accurate luminances and illuminances on several sections of a road surface, it is possible to use factor *Qoo*, relationship between average luminance and average illuminance as an empirical approximation of the road degree of lightness:

$$Q_{00} = \frac{Lm}{Em}. \tag{4}$$

Although there is no theoretical relationship between *Qo* and *Qoo* coefficients, the low dispersion obtained in the analysis of an important number or luminance and illuminance evaluations allows inferring a good performance of this coefficient as marker of the road lightness degree [1–3].

The study described in [1] verified significant differences in the "lightness" degree of surfaces in access and urban motorways of Buenos Aires

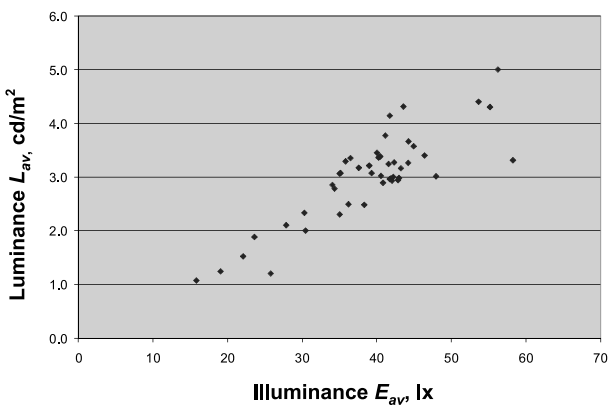

Fig. 2. Example of luminance-illuminance relationship, [1]

Table 1. Assessed LED Installations

Motorway	Measurements	*Qoo* (average) [cd/m^{2}lx]	Standard uncertainty [cd/m^{2}lx]
La Plata – Bs AS City. Section 1	8	0,0860	0,006
La Plata – Bs As City. Section 2	4	0,1080	0,010
Bs As City Urbans motorways	6	0,0828	0,005
Panamericana	2	0,0640	——

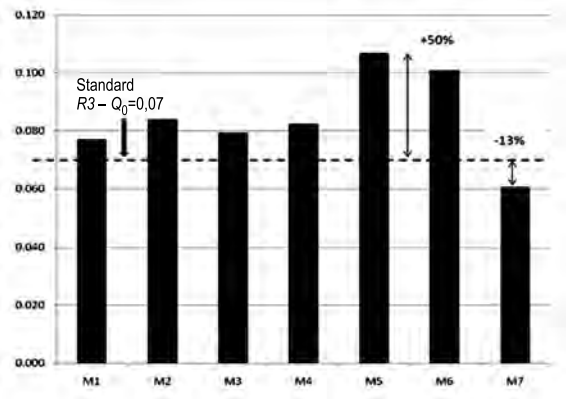

Fig.3. *Qoo* values, [1]

City (Argentina). Such work had as basis more than 300 simultaneous evaluations of luminance and illuminance, carried out in motorways close to Buenos Aires City for the time period 1998–2012. All measurements were carried out following the standardized procedures according to the Argentinean recommendations [4]. The studied installations used HPS vapor lamps and the following rules were met:

- The collected data were grouped by sections with the same kind of asphalt (composition and application technique);
- Time periods only without recoating or changes of surfaces were considered;
- Lighting installations were kept without changes for each assessed zone, except for cleaning, repairs and lamp changing.

Fig. 2 shows an example of luminance-illuminance relationship of an assessed zone. For the studied cases, a clear correlation *E-L* was observed, and this justified the definition and use of *Qoo*.

Comparing the different studied sections, it can be observed substantial differences in the lightness degree of their surfaces. Besides, the study shows a significant discrepancy between the *Qoos* of the actual surfaces and the *Qo* of the standard surface of CIE R3, used as almost exclusive reference of local designs. Fig. 3 summarizes the results obtained in the mentioned study. In this figure, M1, M2, etc. correspond to different sectors or motorways with homogeneous surfaces.

2. DEGREE OF LIGHTNESS UNDER LED LIGHTING

The aim of the present work is to verify if there is any change in the average luminance coefficient assignable to white LED light. In other words, it is intended to find some kind of spectral selectivity in the reflection from the surface.

2.1. Background.

Ekrias [5] studied the spectral reflection of eleven types of asphaltic compounds from Finland, combining samples of "natural" surfaces and with aggregates of colour pigments for clarifying them. His measurements were based on circular samples, of 100 mm in diameter, incidence angles *b*= 20º and elevation *g*=55º. The observation angle *a* was 35º, larger than standard CIE of 1º. Fig. 4 allows observing some samples used in such research. In the image, it can be observed an important size of stone, with a much smaller proportion of binding asphaltic compound than that of surfaces in use in our coun-

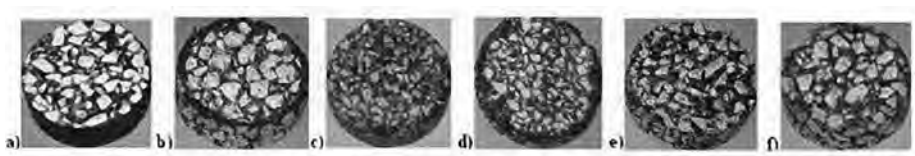

Fig. 4. Samples of surfaces used in [5]

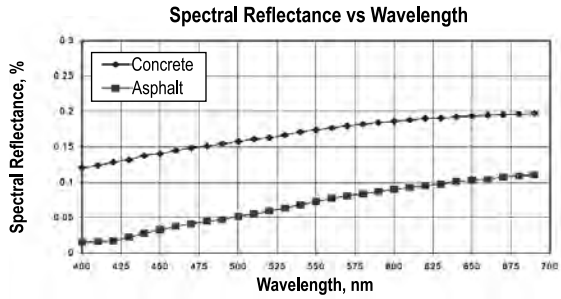

Fig. 5. Results of Adrian's spectral studies

try. Besides, some of the samples presented a reddish tone, possibly due to colouring aggregates.

The mentioned tone is shown in the spectra obtained by Ekrias, which evidence a slight increment in their reflectance towards the red zone of the spectrum.

Adrian's studies [6] show similar results. In this case, the studied samples were asphaltic concretes or concretes, without specifying the use of any type of colouring aggregate. Fig. 5, extracted from [6], shows a growth in the reflectance for growing wave lengths, similar to that found in [5].

American studies [7] show an increase in the reflectance towards the red, more evident on surfaces worn out due to several years of use (Fig. 6). It is noteworthy the coincidence among studies from distant places (USA – Europe), despite the high regional influence on the surface composition and the use or non-use of colouring aggregates.

2.2. *Qoo* with LED Lighting

Following the model of the experience described in [1], luminance and illuminance simultaneous measurements were analyzed in motorway installations with LED lighting, extracted from the database of the laboratory for the period 2013–2016.

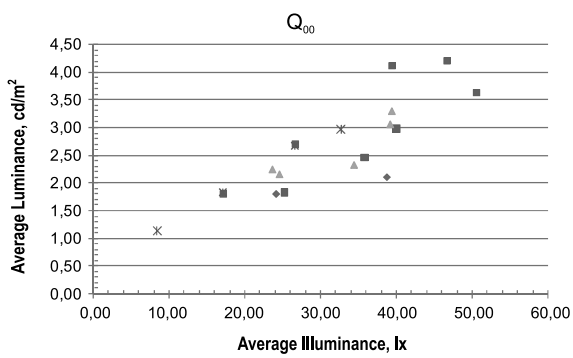

Fig.7. Luminance / illuminance relationship for the studied sections with LED

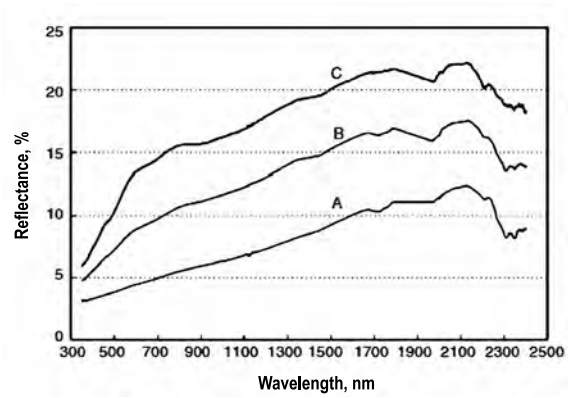

Fig.6. Herol's studies (USA). C surface with over ten years of use

The assessed cases were installations reconverted to LED (15 measurement areas) and tests of LED devices. The latter were based on measuring "witness" sections, formed by the replacement of at least 4 consecutive columns of luminaries in a motorway section. The assessment area was placed in the central reservation (5 cases). All considered tests had their correlation with HPS devices and were counted for the test [1]. Likewise, care was taken to include only those evaluation areas without extreme changes on the road surface. Table 1 summarizes the analyzed cases.

The standard uncertainty considering only that assignable to type A component, was evaluated following [8].

Although the considered cases were limited, the uncertainty was of the same order of magnitude as in the test [1] and that is why *Qoo* estimations for LED lighting can be considered representative for each type of surface. The last case is an excep-

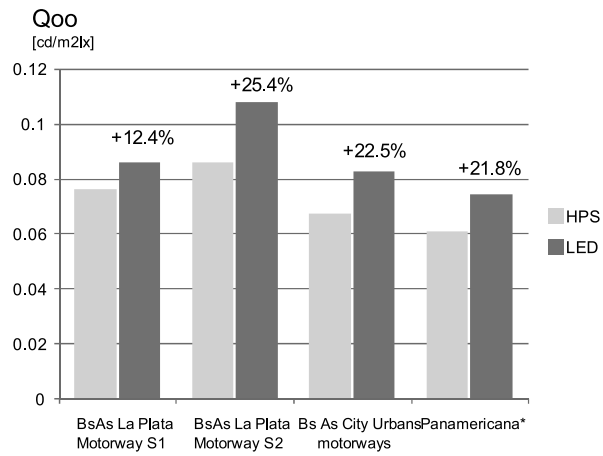

Fig.8. Comparison of *Qoo* obtained for installations with HPS lamps and LEDs

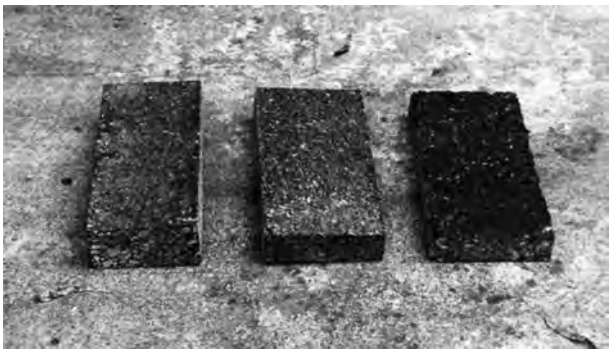

Fig. 9. Samples of draining surfaces, similar to the surfaces of the studied motorways

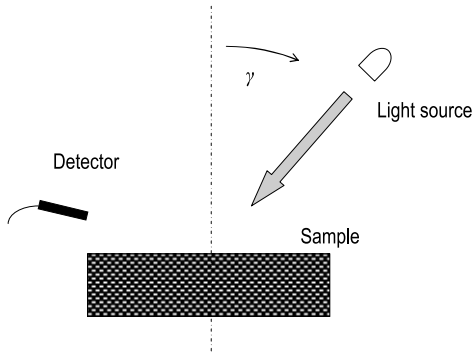

Fig.10. Diagram of measurement system

Fig.11. Aspects of the experience, detector

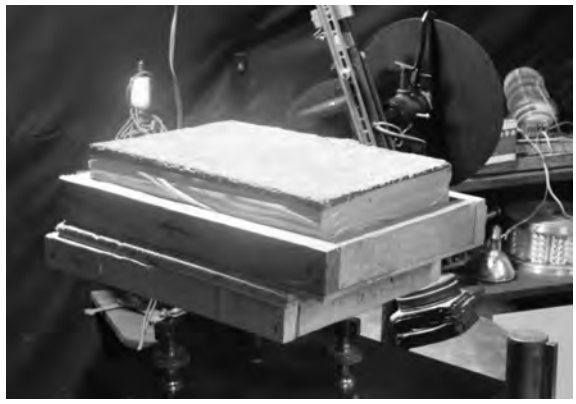

Fig. 12. Aspects of the experience, sample

tion with only two measurements, which are included just as an illustrative example.

2.3. Results

Fig. 7 shows the average luminance and average illuminance relationships for each studied sections.

In Fig. 8, the *Qoo* values obtained with traditional lighting (HPS lamps) and the new LED luminaires are compared for each zone.

The obtained results indicate an increase in the "lightness degree" of each road surface for the LED spectrum. In a first analysis, this result coincides with the background mentioned before. As the qualitative fact of source spectrum influence on the average reflection of surface is that reflection cannot be considered achromatic. However, the link between the *Qoo* increment for the LED spectrum with the "reddish" tone of the surfaces studied by Ekrias, Adrian and Herold is not clear. This trend combined with the blue prevailing spectrum of LED suggests an opposite result to that found in our study. Coherent with this last idea in [5], it is mentioned an improvement in *Qo* for surfaces lit with HPS lamp with respect to the same surface under white light (high pressure mercury).

On the other hand, we cannot affirm that European or American surfaces of the mentioned research can be comparable to those currently in use in Argentina, and which were studied here. Fig. 9 shows samples of such surfaces of the "draining" type. It can be observed a granulometry and different colours from those presented in Fig. 4. It is evident that the comparison between photos has only a relative descriptive value, but shows a higher density (at least superficial) of binder and smaller stone size for the local surfaces. Besides, the images do not show evidence of reddish tones.

3. SPECTRAL STUDY

3.1. Measurement diagram

Works were carried out on a sample similar to those shown in Fig. 9, of standardized dimensions for evaluation of samples [2], assembled on equipment for measuring r-table of LAL (Sample Reflectometer). The light source was placed in b=0º, and

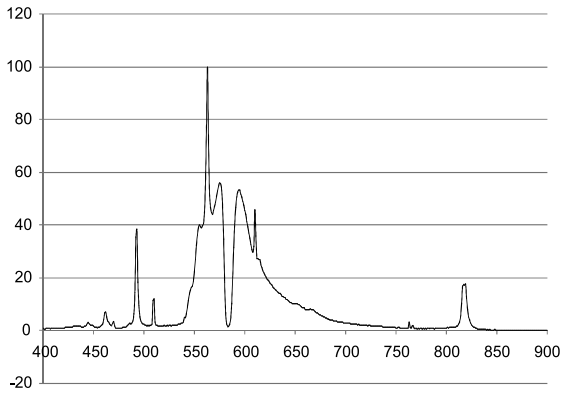

Fig. 13. Spectrum of used HPS lamp

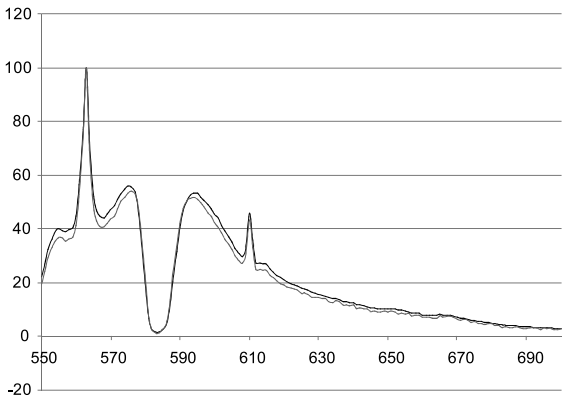

Fig. 15. Direct and reflected spectrum for HPS

three angles of vertical incidence: g = 0º, 15º and 30º were used.

The spectrum reflected by the sample was recorded with a spectrometer Avantes Starline, AvaSpec 2048 [9] with observation angle of standard CIE, a=1º.

Fig. 10 shows a diagram of the measurement system, in Figs. 11 and 12 are aspects of the experience.

Two light sources were compared. On one hand, HPS lamp, tubular clear bulb type, which spectrum is shown in Fig. 13.

A plate with Surface Mounted Devices (SMD) LED components, without refracting lens, chromatic features *x= 0.362, y= 0.366, CCT= 4500 K* was used as LED source. Its spectrum is shown in Fig. 14.

3.2. RESULTS

Comparison of direct and reflected spectra was carried out from re-scaling them to percentage values of their respective maximums. Overlapping of both curves should indicate (in the case of no coincidence) the zones with differences in spectral absorption. Fig. 15 compares spectra for HPS lamp

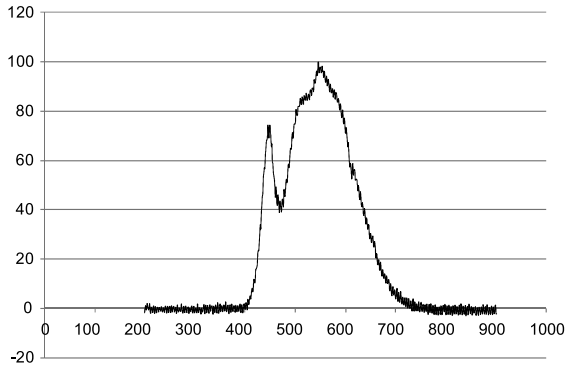

Fig.14. Spectrum of used LED source

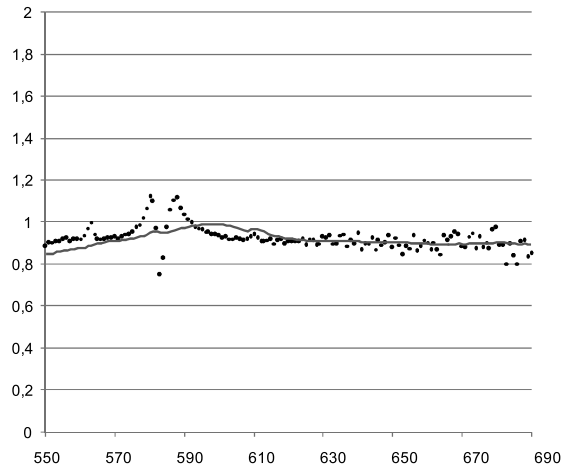

Fig. 16. Reflected/direct spectrum relationship and tendency line

with incidence g of 30º and it is representative of g 0º and 15º. It has been highlighted the spectrum region with greater differences being outstanding the region 560–580nm and 590–630 nm, which present a greater absorption than in the rest of the spectrum.

In the mentioned zones, the quotient of both curves (which should be centred in 1 due to re-scaling) is prone to locate near 0.9 what may indicate 10 % more of absorption in this part of the spectrum (Fig.16).

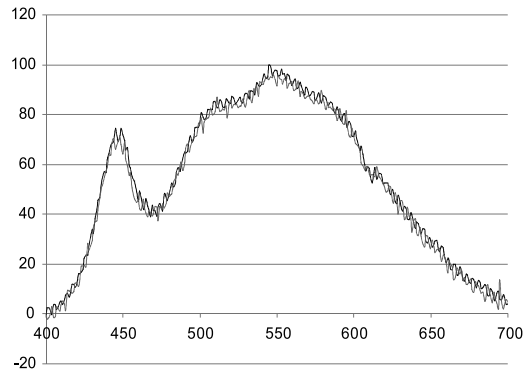

Fig.17. Direct and reflected spectrum for LED

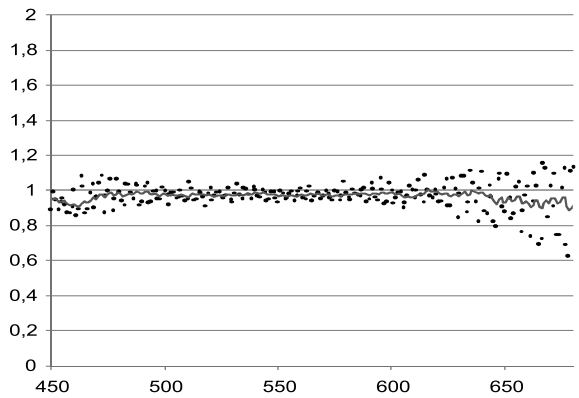

Fig.18. Reflected/direct spectrum relationship and tendency line

Fig. 17 shows overlapped direct and reflected spectra for LED source. Except for a little difference in region 450–500 nm and around 650 nm, both curves seem overlapped, showing slighter discrepancies than for the sodium case. Fig. 18, which presents the relationship reflected to direct spectrum, shows more thoroughly this phenomenon.

In the spectrum visible zone, Fig. 18 shows a trend line very close to 1.

For evaluating the "photopic" effect of these differences and being able to quantify with a unique number, representative of the average reflection in the visible zone (value only valid for the measuring conditions: a= 1°, b= 0° and d= 30°), factors F1 and F2, proportional to emission and photopic reflection, were calculated and defined as:

$$F1 = \int Gdir(\lambda)V(\lambda)d\lambda. \quad (6)$$

$$F2 = \int Gref(\lambda)V(\lambda)d\lambda. \quad (7)$$

In (6) and (7), $V(\lambda)$ is the standardized curve of the spectral sensitivity of the human eye and $G(\lambda)$ are the measured spectra, "*dir*" direct and "*ref*" reflected by the sample in the already mentioned conditions. Fig.19 shows, as example, $Gref(\lambda)$, $V(\lambda)$ and the product, for the sodium lamp case.

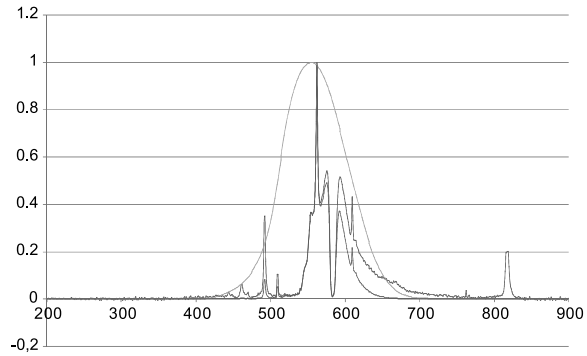

Fig. 19. HPS reflected spectrum and curve $V(\lambda)$

Table 2 summarizes the result of the performed calculation. It is observed a difference in favor of LED reflection ("gain") close to 4 % for the studied surface, for the observation and lighting conditions already mentioned.

4. CONCLUSIONS

The results found are in agreement with previous studies carried out in this laboratory and the research performed in Europe and USA regarding the existence of a soft dependence of the reflection on surfaces with the incident light spectrum. This implies a slight colouring towards reddish green that appears in all studies despite the different research techniques used and the type and composition of surfaces studied.

The study with actual surfaces, in use in the metropolitan area of Buenos Aires allowed correlating this "spectral selectivity" with an increment (gain) in the lightness degree when LEDs are used compared to the HPS lamp spectrum. The *Qoo* improvement found in motorways were of an order of 20 % average, whereas in the spectral study on a sample, the increment could be estimated around 4 %. It is worth mentioning here that in the last case the sample was a surface not necessarily similar to the

Table 2. Results of Photopic Comparison

Spectrum	$F = \int G(\lambda)V(\lambda)d\lambda$	Relative difference (F2-F1)/F1	LED to HPS reflected gain
Direct HPS lamp	25,00	–5,92 %	3,8 %
Reflected HPS lamp	23,52		
Direct LED	85,30	–2,12 %	
Reflected LED	83,49		

actual ones in use nowadays. However, the agreement, at least in the tendency, indicates a new advantage of LED technology and its link to energy efficiency.

ACKNOWLEDGEMENT

The authors are thankful to the CIC PBA, where Pablo Ixtaina is a member of the Scientific and Technological Researcher Career and Braian Bannert is professional member.

REFERENCES

1. Ixtaina, Pablo R; Vidal, Pedro A., *Road Surface Lightness and Energy Efficiency inroad Lighting,* 12th European Lighting Conference "LUX EUROPA 2013, Poland, 2013.

2. Publication CIE Nº 30–2 (TC-4.6), *C*alculation and measurement of luminance and illuminance in road lighting. Vienna, 1982.

3. Ixtaina P, Armas A, Bannert B, *Use Effects on the Reflection of Macro Textured Surfaces*. Journal of Applied Engineering Sciences ISSN: 2247–3769 / e-ISSN: 2284–7197, VOL(6), ISSUE1/2016, pp51–56, May 2016.

4. Instituto Argentino de Racionalización de Materiales, IRAM AADL J 2022–2, Alumbrado Público, Vías de Tránsito – Clasificación y Niveles de Iluminación. Buenos Aires, 1995 J.

5. Ekrias A, Ylinen A, Eloholma M, Halonen L, Effects of Pavement Lightness and Colour on Road Lighting Performance.CIE International Symposium on road surface photometric characteristics: Measurement Systems and Results, Italy, 2008.

6. Adrian W., Jobanputra R, Influence of Pavement Reflectance on Lighting for Parking Lots. Portland and Cement Association, PCA R&D Serial No 2458, 2005.

7. Herold, M. *R*emote Sensing of Impervious Surfaces, Ch. 12 – Spectral Characteristics of Asphalt Road Surfaces, Wageningen University, DOI: 10.1201/9781420043754, 2007.

8. International Organization for Standardization ISO, "Guide to the expression of uncertainty in measurements", Switzerland, 1993.

9. http://www.avantes.com/products/spectrometers/starline.

***Pablo R. Ixtaina*,**
Prof., Universidad Nacional de La Plata Electrical Engineer, Professor of Electrical Measurements and Lighting for degree and postgraduate careers at National and Technological La Plata Universities. Researcher of the Comisión de Investigaciones CIentíficas (Buenos Aires, Arg.), he has carried out postgraduate studies, improvement work and scientific visits at the National University of Tucumán, La Plata National University, Optical Research Center Ciop, LMT Laboratory (Berlin, Germany), Philips Lighting Application Center (Eindhoven, Holland). He is Director of the Laboratorio de Acústica y Luminotecnia, LAL, Buenos Aires Official Research Center in Light and Sound. He is member of the "Public Lighting" Commission of the Argentinean National Standards (IRAM). He has about 40 publications in Scientific and Technical Journals and Congress reports

Braian D. Bannert
is in staff of the Universidad Nacional de La Plata Engineer in Electronics. He belongs to Comisión de Investigaciones CIentíficas (Buenos Aires, Arg.) scientific staff. He currently participates in studies related to the area of lighting technology

Light & Engineering
Vol. 25, No. 4, pp. 123-129, 2017

Svetotekhnika
No. 3, 2017, pp. 29–41

A COMPARATIVE ANALYSIS OF FUNCTIONAL CHARACTERISTICS OF SUN-PROTECTIONS MEANS FOR CIVIC BUILDINGS IN SUNNY CLIMATE CONDITIONS

Sergei V. Stetsky

Moscow State Civil Engineering University, National Research University
E-mail: agpz@mgsu.ru

ABSTRACT

The functional qualities different means of protecting buildings from excessive sunlight are compared. Summertime and external spaces in the solar climates are considered. Devices for protection from the sun are considered, specifically stationary and adjustable sunscreens. A comparative analysis of their main functional characteristics is given.

Conclusions are drawn about the need for a comprehensive application of sunscreens of various types in a "clear sky" environment, typical for regions with the sunny climate characteristics. Stationary sunscreens contribute to an increase in indoor daylight due to the reflection of the sun's rays from them and redistribution of rays within interiors.

Keywords: sun-protection means, functional characteristics, comprehensive application, summer and communication premises, stationary and regulated sun-protection devices, aesthetic qualities of sun-protection

In a hot and sunny climate, the insolation of premises should be minimised, and in summer it should be excluded altogether, because in these climate conditions, it causes considerable overheating of rooms and light discomfort [1–5].

The effective protection of premises against thermal and light exposure to sunlight when using natural (passive) methods of creating a microclimate environment in the premises can be categorised as means of sun-protection, the main of which are [1–8]: 1) the compass orientation of rooms; 2) the planning solution of buildings; 3) the shading effect of the surrounding buildings; 4) elements of large-scale facade architecture; 5) summer and communal outdoor areas; 6) sun-protective devices (SPD).

SPD, which can be external and internal, stationary and dynamic, often aesthetically improve the architectural quality of the facades of the buildings. In addition, some summer recreational and communal outdoor areas (loggias, balconies and galleries) can be considered as stationary SPD, due to the external horizontal and vertical shading elements which are part of their design, Fig. 1, [1–5, 8–12]. In this case, arcades, galleries, loggias, balconies and verandas are important means of sun protection for windows, walls and open spaces.

Table.1 shows the characteristics of the main sun-protection means, the analysis of the effectiveness of which should be based on a comparison of their functional qualities, which, in addition to limiting insolation, include lighting and aesthetic aspects, Table 2.

In this case, in particular, the role of horizontal elements of external stationary SPD in the sunny climate conditions is considered to be very positive in the lighting industry, which has been convincingly proved in a number of papers [2–7, 13–17].

In Fig. 2, it is shown that the generally accepted understanding of the shading effect of horizontal SPD based on the standard (normative) theory of diffuse outdoor lighting does not "work" in the sunny climate and clear sky, since the sun's rays reflected from the ground's surfaces and below-lo-

a – A cult buildings in Dar-es-Salaam, Tanzania;
b – An administrative building in city of Zanzibar, Tanzania;
c – A residential building in Lattakia, Syria;
d – An educational building in Lattakia, Syria.

Fig.1. Traditional design solutions of summer and communal outdoor spaces, typical for sunny climate regions

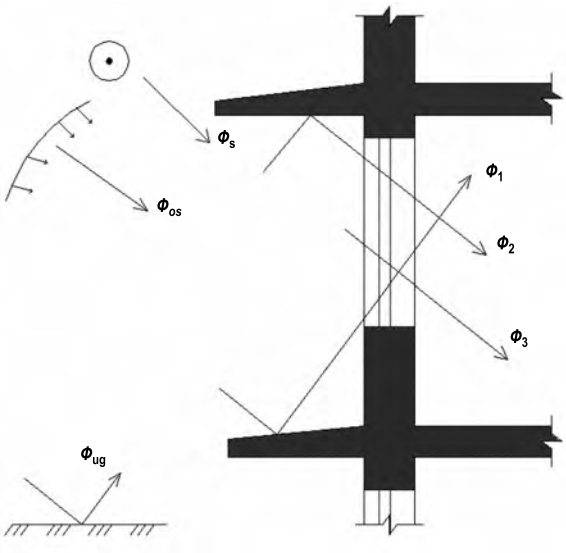

Φ_s - Luminous flux from the sun;
Φ_{os} - Luminous flux from an overcast sky;
Φ_{ug} – Light, reflected from the ground's surface;
Φ_1 - Luminous flux from top surface of a canopy;
Φ_2 - Luminous flux from bottom surface of a canopy (awning);
Φ_3 – Luminous flux, penetrating in a premise directly from sun and sky.

Fig. 2. Luminous fluxes coming into interiors from side natural lighting and implementation horizontal canopies awnings as SPD

cated SPD increase the levels of daylight factor *D* in the premises. As practice shows, this *D* increase can be as high as 10 % – 30 % in the zones furthest from the window, which is extremely important from the point of view of comparison of calculated and normalised values of *D* for natural side illumination, which are determined in the most distant point from the windows [1–6, 18].

The studies that determined the increase in *D* when using stationary SPD in clear-sky conditions during the last decade were conducted at the Department of Architecture of Civil and Industrial Buildings (now the Department of Design of Buildings and Structures) at the Moscow State University of Civil Engineering [7, 13–17, 19–20]. Studies of the internal light environment in residential buildings in Beirut, Lebanon [13, 14] concerned premises without SPD, where temporary layouts of combined SPD were installed over the windows. These consisted curved visors and narrow side screens. This made it possible to determine the *D* both in the presence and in the absence of a SPD, both under clear sky conditions and diffuse outdoor lighting on the basis of calculated and full-scale studies,

Table 1. Architectural, structural and urban development aspects of sun protection, in hot and sunny climate conditions

№№	Major methods of sun protection and explanatory diagrams	Details
1	2	3
1	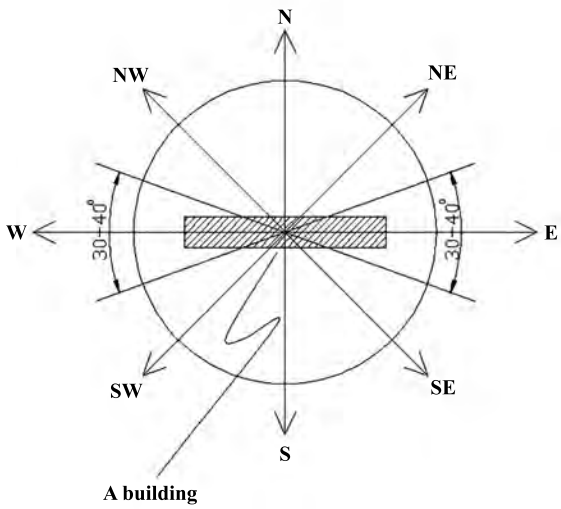	Orientation Latitude orientation is optimal, i.e. with southern and northern window aspects. Longitudinal axis of the building runs east – west (± 15 ÷ 20°). The most efficient sun protection is on the south facade in the form of stationary horizontal sun-protection devices, such as canopies (awnings).
2	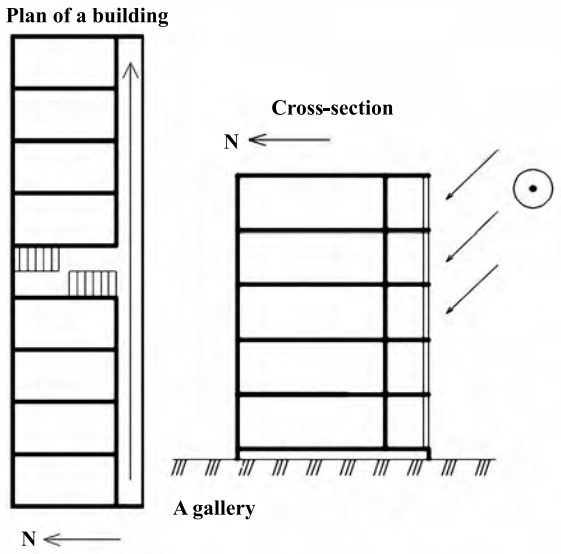	Planning solution The most efficient are buildings with galleries or loggias, wherein communal and leisure functions are combined with sun-protection functions of horizonal stationary SPD.

3	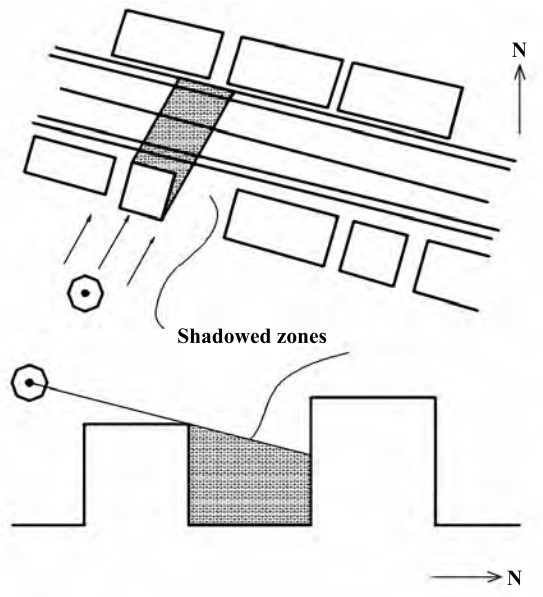	Shadowing effect of the surrounding development Under low sun-position in the case of dense development, narrow streets and opposite – development, a shadowing effect for certain surrounding buildings with surrounding occurs. Such an effect functionally adds some efficiency to the action of stationary SPD.
4	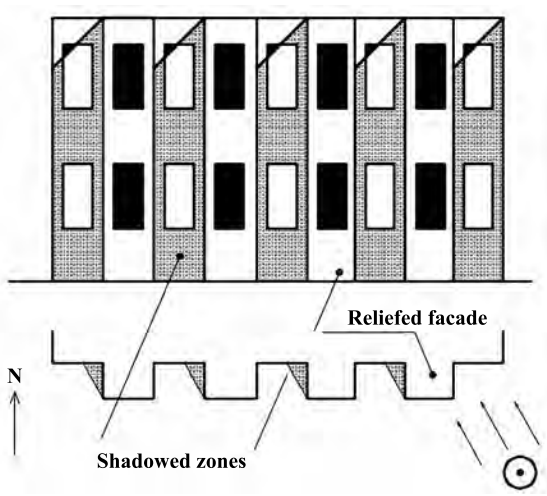	Reliefed facades. Under latitude orientation of buildings low rays of rising or dawning sun may be effectively screened with elements of facades architecture, which act as vertical sun-protective screens.
5	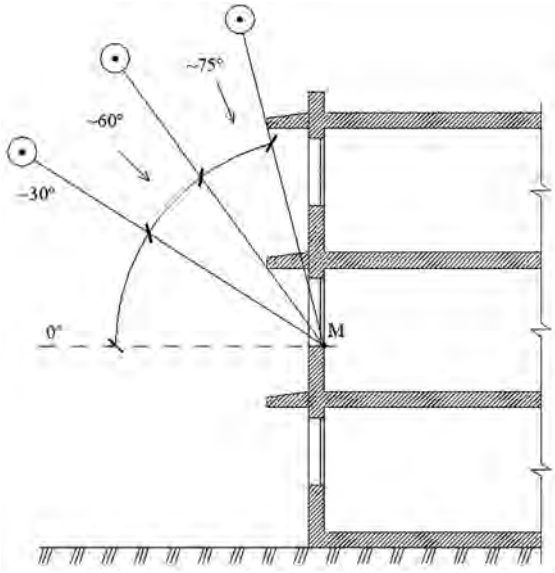	The universal horizontal stationary SPD: it ensures the sun-protection functions to be fulfilled in summer and transition seasons. Passive heating of interiors due to solar radiation in cold season is carried out under the sun height from 30º to 60º

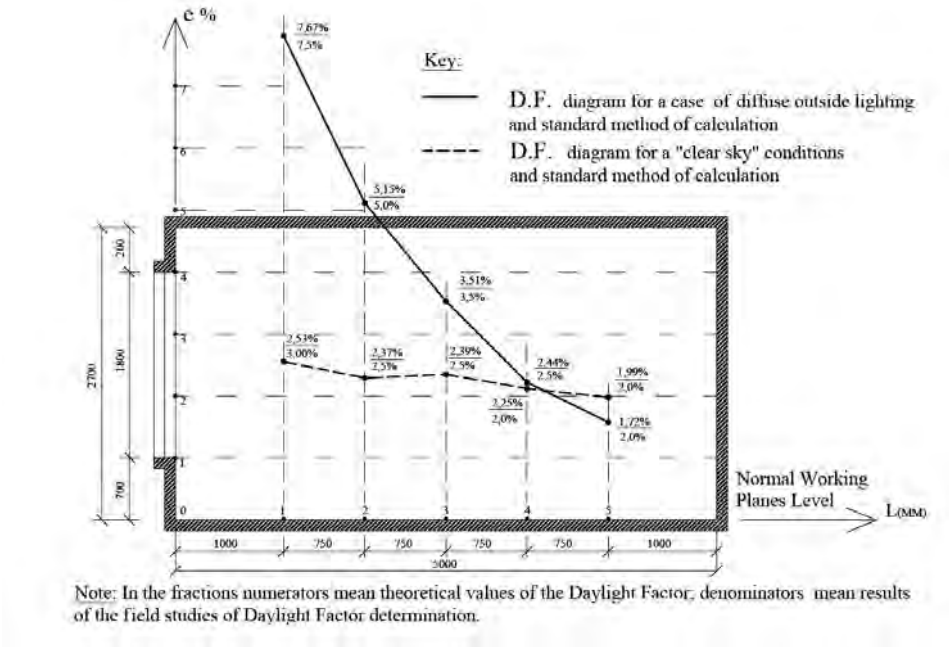

Fig. 3. Daylighting factor diagrams in a room without combined SPD

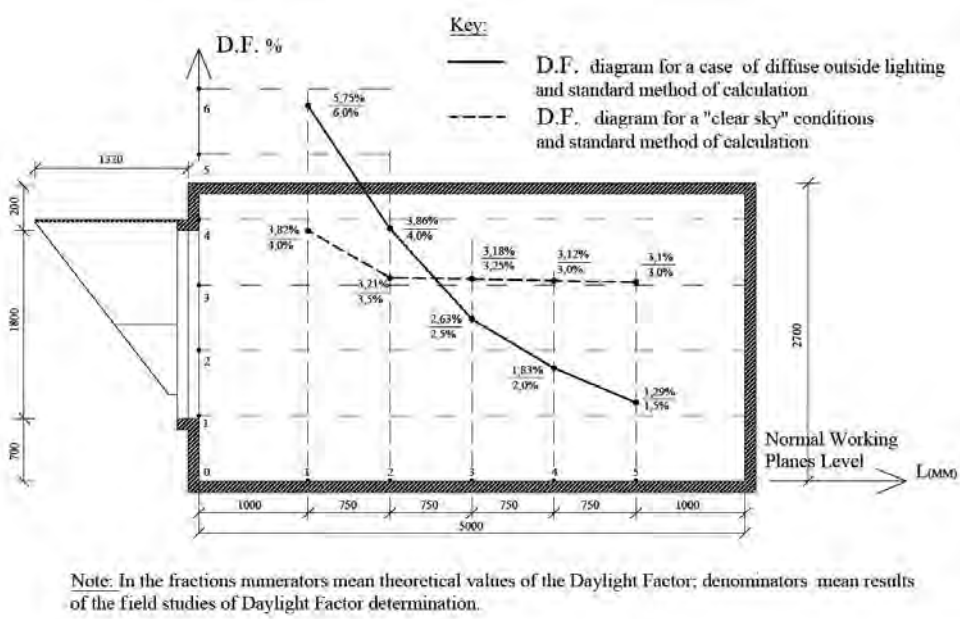

Fig. 4. Daylighting factor diagrams in a room with combined S.P.D

Fig. 3. The results of the studies showed a significant positive effect of outdoor SPD on daylight coefficient levels inside premises in regions with a sunny climate and the nature of outdoor lighting corresponding to clear sky conditions. At the same time, there was a decrease in *D* when using the SPD in conditions of diffuse outdoor lighting, which is expected due to the smaller reflected luminous fluxes from the SPD to the interiors of rooms under a cloudy sky than under a clear one.

CONCLUSIONS

1. A comparative analysis of the functional characteristics of various sunscreen products that meet the basic requirements for their physical, technical and aesthetic qualities shows that the most effective sunscreens in hot and sunny climates are both different types of SPDs and various summer and communal external spaces. In part, these requirements are met by the elements of large-scale facade clad-

Table 2. Comparative functional characteristics of different types of sun-protection means

№№	The versions of sun-protection means.	Factors under consideration		
		Sun-protection	Natural lighting	Aestetics
1	2	3	4	5
1	Orientation of premises on the horizon sides (aspect)	●	◓	○
2	Planning solution of buildings	◓	◓	◓
3	Shadowing effect of a surrounding development	●	◓	○
4	Relief facades	◓	◓	◓
5	Summer and utility outdoor premises	●	●	●
6	Sun - protection devices	●	●	●

Key:

● Maximum efficiency of the resource ◓ Medium efficiency of the resource ○ Minimum efficiency of the resource

ding, and the geometry of the objects surrounding the construction.

2. The analysis confirms the conclusion that the optimal ratio of functional and aesthetic qualities of sunscreening means is possible only with the optimal combination of stationary and regulated SPD with elements of large facade cladding and with summer and communal external areas (taking into account their aesthetic qualities).

3. A significant positive effect of external stationary SPD on *D* levels in rooms in regions with a sunny climate was determined both in full-scale studies and in theoretical studies using the "clear sky" technique. Moreover, in diffuse external illumination, the SPD weakens the internal illumination more than the lower SPD amplifies it with a small reflection of the luminous fluxes.

REFERENCES

1. Gusev N.M. "Fundamentals of building physics", Moscow, Stroyizdat, 1975, 438 p. (in Russian).

2. Soloviev A.K. "Environmenal physics " Moscow, ASV, 2008, 341p. (in Russian)

3. Obolensky N.V. "Lighting research aspects of Insolation and sun-protection in building construction" Ab-

stract of the Doctor of Sciences thesis, Moscow, 1983, 29 p.

4. Obolensky N.V. “Consideration of direct sunlight flows in buildings design in southern regions” / / Industrial construction, 1965, № 1, pp. 12–14.

5. Obolensky N.V., Volkov U.A. “Lighting and plastic expression of industrial elements of buildings “ // Architecture of the USSR, 1976, № 7, pp. 54–55.

6. Stetsky S.V. “Stationary sunscreening means as a factor of architectural expression of buildings and ensuring comfortable internal microclimatic regimes in their premises for a hot and sunny climate” // Nauchnoe obozrenie, 2014, № 7, pp. 572–579. (in Russian)

7. Stetsky S.V. “Aesthetics of civil buildings when using stationary sunscreen means in them under conditions of hot climate “ PGS, 2015, № 7, p. 76–80. (in Russian)

8. Stetsky S.V., Salo M.A. “Accounting of influence of sun – protection devices in natural lighting design in the southern regions with clear sky conditions” // SMOT of XXI century, 2004, № 10, pp. 64–65. (in Russian)

9. Stetsky S.V. Amhaz H. “The role of sun – protection devices in creation of comfortable lighing environment in administrative buildings offices for conditions of Beirut “ // SMOT of the XXI century, 2004, № 12, pp. 52–53.(in Russian)

10. Stetsky S.V., Suliman S. “Rising of a natural lighting levels in premises of civil buildings with side natural lighting system for the conditions of hot sunny climate. // SMOT of the XXI century, 2005, № 5, pp. 82–84. (in Russian)

11. Stetsky S.V., Porublev S.A. “Methods of natural lighting design with respect of light, reflected from sun shelves.” // SMOT of the XXI century, 2011, № 4, pp. 34–37. (in Russian)

12. Stetsky S.V., Khodeyr V.A. “Indoor lighing environment in residential buildings with use of combined sun – protection devices” // Vestnik MGSU, 2012, № 8, pp. 39–45. (in Russian)

13. Stetsky S.V., Khodeyr VA “Efficient sun – protection devices in civil building construction in regions with hot sunny climate” // Vestnik MGSU, 2012, № 7, pp. 9–15. (in Russian)

14. Harkness E., Mehta M. “Solar radiation control in buildings” // STROYIZDAT, 1984, 176 p. (Translated from English)

15. Soloviev A.K. “Assessment of lighting environment of industrial premises under clear sky conditions” Svetotechnika, 1987,№ 7, pp. 12–14. (in Russian)

16. Soloviev A.K. “Accounting the influence of reflected light in design of natural lighting in industrial buildings with systems of roof lights under non-uniform light distribution,” A digest of scientific works of Architectural Chair of Moscow Civil Engineering institute, 1974, pp. 73–82. (in Russian)

17. «Solar shading for low-energy buildings» European Solar-Shading Organization, Belgium. February 2012, 34 p. (in English)

18. «External Blinds-Performance requirements including safety» European Standard, 2004, 43 p. (in English)

19. «Blinds and Shutters-Thermal and Visual Comfort-Performance Characteristics and Classification» European Standard, 2005, 57 p. (in English)

20. «Understanding overheating-where to start» (an introduction for house builders and designers) NHBC Foundation, 2012, Great Britain, 34 p. (in English)

Sergei V. Stetsky,
Ph.D. Associate Professor at the chair “Buildings and structures design” of Moscow State University of Civil Engineering. Graduated from Moscow Civil Engineering Institute in 1970 with a specialty in Civil Engineering, author and co-author of more than 60 scientific articles, textbooks, study manuals

Light & Engineering
Vol. 25, No. 4, pp. 130-133, 2017

Svetotekhnika
No. 3, 2017, pp. 42–45

ENERGY EFFICIENCY REQUIREMENTS, LABELLING AND ECODESIGN OF LIGHTING PRODUCTS: EUROPEAN EXPERIENCE

Marina L. Abrashkina[1] and Eugene A. Sysoeva [2]

[1]NIIIS LLC of A.N. Lodygin, Saransk
[2]The Ogarev Mordovia State University, Saransk
E-mail: sysoewa@mail.ru

In the future the unit of currency will be the kilowatt-hour
Arthur Clark

ABSTRACT

The main European laws regulating the energy efficiency, labelling and eco-design of lighting products are considered in the article.

Keywords: energy efficiency, labelling, eco-design, directive of the European Union, regulation of the European Union, lighting products, classes of energy efficiency, eco-labelling

The main objectives of the European Union's (EU) uniform energy policy are the transition towards renewable energy sources, the increase in energy efficiency, the decrease of greenhouse gas emissions, the creation of a uniform energy market and support of the development of competition within it.

In December 2008, an EU summit affirmed the program on abatement of climate change for 2013–2020, developing the 20–20–20 goals. This plan includes a 20 % growth target for energy renewable sources in the overall power consumption landscape by 2020, a 20 % reduction in polluting greenhouse gas emissions compared to 1990 levels and a general reduction in energy consumption of 20 %. The 20–20–20 plan aims to make EU economies energy efficient and reduce fuel consumption.

In January 2014, the EU began the implementation of a new programme of work, focusing on scientific and technological innovation, called "Horizon 2020", which combines framework programmes of the EU on scientific research and development, on competitiveness and innovation. Priority is given to high efficiency eco-, nano-, bio- and info-technologies aimed at solving social and environmental problems. These include safe, clean and efficient power generation, climate change, efficient use of resources and raw materials.

The EU applies an integrated approach to building a legislative base in the energy efficiency, labelling and eco-design fields. The main legislative instruments of the EU are Directives and regulations issued by the European Parliament and EU Council, which regulate product standards for all producers in EU member states. Adopted Directives and regulations are increasingly targeting electronic devices, including lighting products. In this context, it is impossible to implement an effective energy saving policy in Russia without commiting to the standards set by EU Directives and regulations.

An important factor, which can assist consumers in correctly choosing high-efficiency lighting products out of the existing product line, is energy efficiency labelling. Labelling influences a product's competitiveness, because the label also indicates quality and reliability.

Over the last few years, the European Parliament has introduced some additions and changes into the adopted directives on energy efficiency, labelling and eco-design of household electrical appliances.

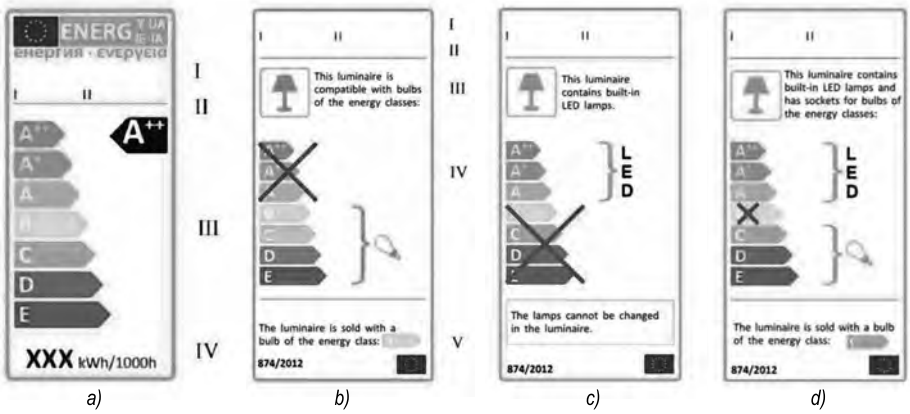

Fig. 1. Examples of labels [3]. a – for electric lamps; b – for luminaires compatible with lamps of power consumption classes *B, C, D, E* equipped with energy efficiency lamps of class *E*; c – for luminaires compatible with built-in non-interchangeable LED lamps; d – for luminaires containing built-in LED lamps and sockets for replaceable lamps of power consumption classes A^{++}, A^{+}, *A, C, D, E* equipped with power consumption lamps of class *N*

The new Energy Labelling Directive 2010/30/EU [1], which replaces directive 92/75/EEC [2] from June 18, 2010 on labelling power-consuming products, with an energy efficiency label and replaces EU regulation 874/2012 on labelling electric lamps and luminaires, with an energy efficiency label [3] supplementing directive 2010/30/EU, establishes that energy efficiency labels are necessary for all electrical household appliances on the EU domestic market. According to these documents, energy efficiency information on the labels depends on the product's energy efficiency level: *from* A to G. Relevant information on the energy efficiency labels of household lamps sold in European shops helps buyers choose the products.

According to EU regulation #874/2012 on labelling, the energy efficiency label of electric lamps and luminaires establishes two more energy efficiency classes for products, which meet the highest market standards for energy parameters: A^{+} and A^{++}. If luminaires have the highest class of energy efficiency (A^{+} or A^{++}), then the lowest classes (*E*, *F*, *G*) for such luminaires should be excluded from the label by means of their lining through in the label. And otherwise, in case luminaires cannot have energy efficiency class higher than class B, then highest classes (A^{+} and A^{++}) are lining through in the label[1].

Fig. 1 presents examples of labels [3] for electric lamps and luminaires, which should be presented at point of sale.

EU regulation 2015/1428/EU [4] establishes a requirement, based on which luminaires placed on the EU market should be compatible with high-efficiency lamps of class A^{+}. After adoption of regulation 2015/1428/EU and amendments to EU regulation 1194/2012 [5], it can be expected that further EU directives and regulations will be adopted, which will determine a list of indices for energy efficiency classes A^{+} *and* A^{++} for high-efficiency light sources, including LED products, as well as developing methods of determination of energy efficiency classes for such light sources.

In 2005, the EU Commission adopted directive 2005/32/EU [6] and the correspondent regulations #244/2009 [7] and #245/2009 [8] establishing requirements for environmentally friendly power-consuming products. According to this directive, the manufacturers should undertake measures for energy consumption reduction and to decrease other negative impacts on environment at all stages of the product's service life. This approach was named ecodesign. Ecodesign is a new concept in EU countries, which aims to decrease the energy consumption of household electrical appliances. Ecodesign establishes requirements for the structure and operating parameters of electrical household appliances, in order to avoid harmful impacts on environment (limitation of application and reduction of toxic substances in production) and to be energy efficient. According to directive #2005/32/EU, a manufacturer must include information concerning environmental friendliness of the product and its level of energy efficiency on the packaging, which allows consumers to compare products before purchase. Electrical household appliances, which includes

[1] As for the Russian Federation, in 2011, a project of the Engineering regulation of the Customs union was developed "About informing consumers on energy efficiency of electric power-consuming devices" (http://www.eurasiancommission.org/ru/act/texnreg/deptexreg/tr/Pages/InformEnergy.aspx) but it has not been adopted yet. In the territory of the RF, GOST P 54993–2012 "Household Lamps. Indices of energy efficiency" is valid, within which classes A^{+} *and* A^{++} are not provided for. – Editor's note.

Table 1. Luminous flux of energy efficient lamps and power of the equivalent incandescent lamps [7]

Luminous flux, lm			Power of equivalent incandescent lamp, W
Compact fluorescent lamps	Halogen incandescent lamps	Light-emitting diode and other lamps	
125	119	136	15
229	217	249	25
432	410	470	40
741	702	806	60
970	920	1 055	75
1 398	1 326	1 521	100
2253	2 137	2 452	150
3 172	3 009	3 452	200

lighting products, impact the environment during their service life. The impacts include raw materials and natural resources used in their production, packaging, transportation, sale, operation and utilisation. Besides, ecodesign ensures reducing energy resource consumption, which is an important component of the EU policy. And it should be noted that in [7] for the first time, a requirement was officially formulated, according to which " If equivalence with an incandescent lamp is claimed on the packaging, the claimed equivalent incandescent lamp power (rounded to 1 W) shall be that corresponding in Table 6 to the luminous flux of the lamp contained in the packaging. The intermediate values of both the luminous flux and the claimed incandescent lamp power (rounded to 1W) shall be calculated by linear interpolation between the two adjacent values".

To expand the scope of directive #2005/32/EU, directive EU2009/125/EC [9] concerning requirements for ecodesign of directional light luminaires, LED lamps and the accompanying equipment was adopted in 2009. According to the mentioned directive, for each service life stage of a product, ecological aspects should be estimated including the following parameters: expected consumption of raw materials and other material as well as resources and energy; expected lifecycle emissions into the atmosphere, water, or soil; pollution including noise, vibration, radiation, electromagnetic fields; potential for material recycling and utilisation. In Directive 2009/125/EU ecodesign requirements cover the full extent of lighting products' design (mercury concentration and emission, carbon dioxide emission into atmosphere, electromagnetic compatibility, etc.). And the existing requirements for product energy efficiency labelling, as well as a voluntary deposition of the ecological label are applied along with the requirements established by ecodesign directives.

A voluntary ecolabelling of light sources is established by EU decision #2002/747/EU. Manufacturers can display the EU Flower (Fig. 2) awarded to products most the favourable environmental credentials, if they meet requirements [10] on eco-labelling. To obtain the right to eco-labelling, products must meet certain conditions:

– The product should correspond to a high class of energy efficiency, at least to class A;

– Use of toxic substances should be limited in the product. For example, mercury concentration in discharge lamps should not exceed values stipulated by directive 2002/95/EU [11].

Furthermore, certain operational parameter requirements must be met, such as lifetime, luminous flux, as well as other parameters determining lamp quality.

The European experience shows that energy efficiency requirements for lighting products change significantly with time, becoming more stringent,

Eco LABEL

Fig. 2. EU eco label

which is confirmed by continuing adoption of new directives and regulations, as well as amendments made to current regulatory documents.

Continuously monitoring the directives and regulations which exist in the EU will allow Russian lighting product manufacture to consider all of the requirements of the European market, including energy efficiency, labelling and ecodesign, which will eventually facilitate an increase in lighting product export.

REFERENCES

1. DIRECTIVE2010/30/EU OF THE EUROPEAN PARLIAMENT AND OF THE COUNCIL of 19 May 2010 on the indication by labelling and standard product information of the consumption of energy and other resources by energy-related products // Official Journal of the European Union. 18.06.2010, L 153, pp. 1–12.

2. COUNCIL DIRECTIVE92/75/EEC of 22 September 1992 on the indication by labelling and standard product information of the consumption of energy and other resources by household appliances // Official Journal of the European Union. 13.10.1992, L 297, pp. 16–19.

3. **Commission Delegated Regulation (EU) No 874/2012 of 12 July 2012 supplementing Directive 2010/30/EU of the European Parliament and of the Council with regard to energy labelling of electrical lamps and luminaires** // Official Journal of the European Union. 26.09.2012, L 258, pp. 1–20.

4. COMMISSION REGULATION (EU) 2015/1428 of 25 August 2015 amending Commission Regulation (EC) No 244/2009 with regard to eco-design requirements for non-directional household lamps and Commission Regulation (EC) No 245/2009 with regard to eco-design requirements for fluorescent lamps without integrated ballast, for high intensity discharge lamps, and for ballasts and luminaires able to operate such lamps and repealing Directive 2000/55/EC of the European Parliament and of the Council and Commission Regulation (EU) No 1194/2012 with regard to eco-design requirements for directional lamps, light emitting diode lamps and related equipment // Official Journal of the European Union.27.08.2015, L 224, pp. 1–9.

5. COMMISSION REGULATION (EU) No 1194/2012 of 12 December 2012 implementing Directive 2009/125/EC of the European Parliament and of the Council with regard to eco-design requirements for directional lamps, light emitting diode lamps and related equipment // Official Journal of the European Union.14.12.2012, L 342, pp. 1–22.

6. Directive 2005/32/EC of the European Parliament and of the Council of 6 July 2005 establishing a framework for the setting of eco-design requirements for energy-using products and amending Council Directive 92/42/EEC and Directives 96/57/EC and 2000/55/EC of the European Parliament and of the Council // Official Journal of the European Union. 22.07.2005, L 191, pp. 29–58.

7. COMMISSION REGULATION (EC) No 244/2009 of 18 March 2009 implementing Directive 2005/32/EC of the European Parliament and of the Council with regard to ecodesign requirements for non-directional household lamps // Official Journal of the European Union. 24.03.2009, L 76, pp. 3–16.

8. COMMISSION REGULATION (EC) No 245/2009 of 18 March 2009 implementing Directive 2005/32/EC of the European Parliament and of the Council with regard to ecodesign requirements for fluorescent lamps without integrated ballast, for high intensity discharge lamps, and for ballasts and luminaires able to operate such lamps, and repealing Directive 2000/55/EC of the European Parliament and of the Council // Official Journal of the European Union. 24.03.2009, L 76, pp. 17–44.

9. **Directive 2009/125/EC of the European Parliament and of the Council of 21 October 2009 establishing a framework for the setting of ecodesign requirements for energy-related products //** Official Journal of the European Union. 31.10.2009, L 285, pp. 10–35.

10. Decision 2002/747/EC (OJ: L242/44/2002) establishing revised ecological criteria for the award of the Community eco-label to light bulbs and amending Decision 1999/568/EC // Official Journal of the European Union.10.09.2002, L 242, pp. 44–49.

11. **Directive 2002/95/EC of the European Parliament and of the Council of 27 January 2003 on the restriction of the use of certain hazardous substances in electrical and electronic equipment** // Official Journal of the European Union. 13.02.2003, L 37, pp. 19–23.

Marina L. Abrashkina is graduated from the MSU of N.P. Ogarev in 1981. At present, she is a Head of the laboratory of standardization at NIIIS by A.N. Lodygin. Her scientific field of interest is the study of standardisation problems for lighting products

Eugene A. Sysoeva, Doctor of Economics. She is graduated from the Ogarev Mordovia State University in 1998. At present, she is a Professor of the Chair of statistics, econometrics and information technologies in management of the same university. Field of scientific interest: study of quality and competitiveness problems of lighting products

Light & Engineering
Vol. 25, No. 4, pp. 134-140, 2017

Svetotekhnika
No. 3, 2017, pp. 23–28

SHIPBOARD LIGHTING FACILITIES OF CARRIER-BASED AIRCRAFT

Dmitri V. Vasilyev[1], Andrei A. Grigoryev[2], and Alexander I. Laryushin[3]

[1] *Ramensk Instrument-making Factory JSC, Moscow Oblast, Ramensk*
[2] *The Moscow Power Energy Institute, National Research University (NRU)*
[3] *Polyus Scientific Research Institute JSC of M.F. Stelmakh, Moscow*
E-mail: vasilievd1969@yandex.ru

ABSTRACT

The article is dedicated to the development of shipboard lighting facilities of take off and landing operations for aircraft from the deck of carrier-capable ships, undergoing transition to modern semiconductor radiation sources: high power light emitting diodes and laser diodes. A method of calculating far-field parameters of light signal systems (AC), visual analyser threshold and statistical models for the evaluation of the parameters of light fields under formation and application of the radiation transfer equation for evaluation of a possibility to be oriented by diffuse light ray are analysed. Development prospects for near-field beacon systems (YO) based on the projective principle of information formation are considered.

Keywords: monochromatic sector, light field, AS beacon system, YO beacon, threshold model, statistical model, visual analyser, radiation transfer equation, radiation semiconductor source

1. INTRODUCTION

Take off and landing operations of carrier-based aircraft on air-capable ships is the most emergency prone part of flight. Transmitting visually perceived information to the pilot on a safe movement trajectory and in position on take off and landing site (TOLS), in situations when a sip may be rolling considerably, increases the need for safety. Quality of light-signal information directly depends on the type of light source used. In the YO beacon systems, application of hyper-luminous light emitting diodes (LED), has become a global trend. In the AS beacon systems, electric lamps with light filter units were used until recently, which provided low contrast, a limited range of operation and wherein key light field parameters were difficult to control. During the last decade, a gradual transition to hyper-luminous LEDs in these systems has occurred. A similar process has been observed with take-off direction pointers, the development of which is connected with solid-state, and lately with semiconductor lasers. In view of the requirements of carrier-based aircraft lighting systems, the following sections present solutions for the development of light field parameter calculation methods for AS beacon systems, and their evaluation based on the threshold and statistical models of the visual analyser. Use of the radiation transfer equation in a diffusing environment to determine energy parameters of radiation sources is also involved. Perspectives of replacing existing YO beacon systems with projective systems capable of significantly expanding the scope of information provided and to make perception more comfortable are considered.

2. THE CALCULATIONS

Take off and landing operations of carrier-based aircraft largely depend on the orientation of the visual light field of the shipboard light-signal equip-

ment as sight provides the most reliable information, especially under the rapidly changing conditions.

Light-signal shipboard systems (Fig. 1) can be divided by the following conditions:

– By their placement (aircraft carriers, mixed types, helicopter carriers of single and group deployment);

– By application stage: AS beacon (colour-flashing dotted and position), or YO beacon (position, indicative, restrictive, illumination);

– By orientation method (direct radiation and radiation of collimated light ray diffused in the atmosphere);

– By location (deck or bulkhead);

– By mobility degree (immovable, low-mobile, mobile).

The most strict requirements are applied to the light fields of an AS beacon because of the need to exactly position an aircraft, which is related to the high risks associated with the low height of the final flight stage. An exact stableglide path and course trajectories from the moment of capture of the final approach track is provided by visual orientation using colour-flashing lights.

All AS beacon systems are sector navigation systems (SNS), forming fields of several monochromatic sectors with different flashing characteristics. Each sector is formed by a group of independent radiators, which use hyper-luminous monochromatic LEDs as a radiation source. Radiator fields are identical by their parameters and orientation and superimposed on each other in space with a high degree of accuracy (deviation from the sector optical axis is no more than one angle minute). The method to calculate light fields uses the sector diagram parameters and the method of determining a transitional area width between sectors is used. Due to the specific nature of the task, a new method needed to be developed. Calculation of distributing illuminance in a cross section of the sector diagrame requires a simultaneous accounting radiation source (LED) and optical system parameters, as well as parameters of atmosphere, observation conditions (including radiation luminance of the observed light diffused in the atmosphere), and of the detection probability [1]. As a result, configuration of the monochromatic sector diagram is determined, within which AS beacon light is perceived with a probability not lower than the preset. The method is based on interpreting the light field as a radiation source of several images, based

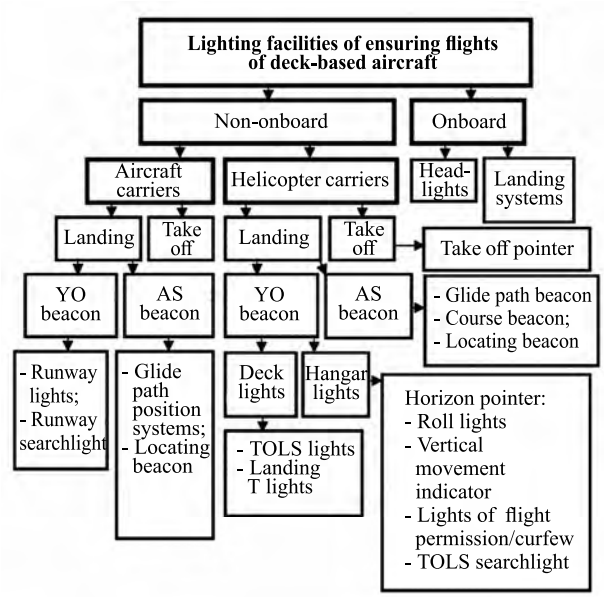

Fig. 1. Lighting facilities to ensure air-capable ship flights

on which the sector diagram is plotted, at different distances from the system. Illuminance spatial distribution is dedermined by the expression:

$$E_i(x_i, y_i, d_i) = \frac{1}{d_i^2} \int\int_{-\infty}^{\infty} g'(v_x', v_y') \cdot$$

$$\cdot exp[-i2\pi(v_x' x_i \frac{1}{d_i} + v_y' y_i \frac{1}{d_i})] dv_x' dv_y',$$

where $g'(v_x', v_y') = g(v_x, v_y)\Pi_{i=1}^{n} D_i(v_x, v_y)$ is the image spectrum; v_x, v_y are spatial frequencies; $g(v_x, v_y)$ is source spectrum; $D_i(v_x, v_y)$ is the optical transmission function (OTF) of the optical system, of diffusing and turbulent atmosphere. ($D_{oc}(v_x, v_y)$ is proportional to the coupling factor of the aberration level with structure data of the optical system K_{os}, m^{-3}); d_i is distance from the optical system to the image plane (x_i, y_i).

The angular luminance distribution of the observed light radiation diffused in the atmosphere is determined by the expression:

$$L_\alpha = \int_{p_i} \frac{f(\beta_i)\alpha' E_i(x_i, y_i, d_i) e^{-\varepsilon p_i}}{4\pi \cos\beta_i} dp_i,$$

where ε is the atmospheric radiation attenuation index; $f(\beta_i)$ is indicatrix of radiation diffusion in volume dV; α' is diffusion index.

Parameters of $f(\beta i)$ for different meteovisibility values S_m are given in Table 1.

Table 1. Diffusion indicatrices for various states of atmosphere ($f(\beta_i)$)

β_i, grade	Ideal atmosphere, S_M = 50 km	Clear atmosphere, S_M = 20 km	Sea haze, S_M = 4 km	Coarse foggy sea haze, S_M = 1km	Sea fog, S_M = 0.2 km
0	1.49	4.72	22.2	69.2	408.16
10	1.4	4.36	12.44	24.86	33.98
20	1.31	4.0	6.94	8.88	2.79
30	1.202	3.312	3.89	3.19	0.233
40	1.094	2.624	2.17	1.14	0.019
50	0.986	1.936	1.214	0.41	0.0016
60	0.9495	1.6045	0.68	0.146	
70	0.913	1.273	0.38	0.053	
80	0.8765	0.9415	0.21	0.019	
90	0.84	0.61	0.12	0.0067	

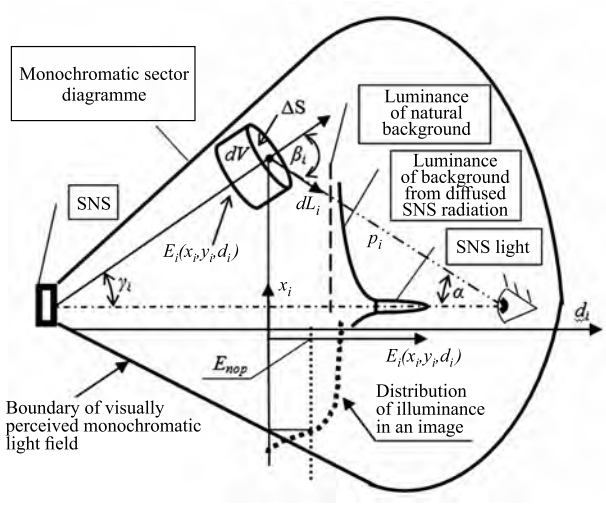

Fig. 2. Formation of the light information field monochromatic sector diagram for sector navigation system (SNS)

Angular radiation luminance distribution of the system light diffused in atmosphere has values considerably different from 0 within 15 angular minutes only. With S_m increase, luminance of diffuse radiation quickly decreases. The process of forming the sector diagram and of background luminance is explained in Fig. 2.

When simulating the light fields of light-signal systems, two visual analyser models are used: a threshold model operating with the established illuminance levels for transport types [2], and a visual analyser statistical model developed at the Light and Engineering Chair of the Moscow Power Institute NRU, which considers the processes inside the human eye more completely [3].

Evaluation of visual perception is implemented accounting for additional background luminance caused by diffusion of the observed light in radiation atmosphere. The influence of this factor increases with reduced meteovisibility, and it is especially potent when making observations over the surface of the water when the atmosphere is saturated with aerosols.

In the case of background luminance $L_f > 10^{-3}$ cd/m^2, the probability of SNS colour light detection (P_o) against the colour background with an arbitrary luminance distribution over the light and background surface is determined by a visual analyser statistical model as follows:

$$P_o = 0,5 + \frac{1}{\sqrt{2\pi}} \int_0^y exp(-\frac{t^2}{2})dt;\ y = \frac{m_\Lambda - \ln \Lambda_n}{\sigma_\Lambda},$$

$$m_\Lambda = \iint_\Omega \begin{bmatrix} X_0(\eta,\theta)\ln\left(\frac{X_0(\eta,\theta)}{X_b(\eta,\theta)}\right) - \\ -X_0(\eta,\theta) + X_b(\eta,\theta) \end{bmatrix} d\eta d\theta,$$

$$\sigma_\Lambda = \left(\iint_\Omega X_0(\eta,\theta)\ln^2 \frac{X_0(\eta,\theta)}{X_b(\eta,\theta)} d\eta d\theta \right)^{0,5},$$

where θ and η are angular co-ordinates of SNS background and light points, angular minutes; Ω is vision field, str; Λ_n is the threshold likelihood ratio; t is the parameter of normal distribution; $X_o(\eta, \theta)$ and $X_b(\eta, \theta)$ are mathematical expectations of an-

Table 2. ΔL of colour lights for sector boundaries of the light field

Observation conditions	*ΔL*, cd/m² (night, twilight)	*ΔL*, cd/m² (day time)
Red	7.23 (on green)	107.1 (on white)
Green	11.41 (on red)	168.9 (on white)
Green	11.78 (on yellow)	174.3 (on white)
Yellow	15.94 (on green)	235.9 (on white)

gular density of an eye receptor output signals when sighting SNS light and background respectively.

The general expression for $X(\eta, \theta)$ (min^{-2}) calculation is given by equation

$$X(\eta,\theta)=\frac{a_1}{a_2}(1+1,3\ln a_3)\ln a_3,$$

where

$$a_1=83,4\left[\begin{array}{c}0,04+0,68exp\left(-\left(\frac{R}{26}\right)^2\right)+\\+0,28exp\left(-\frac{R}{100}\right)\end{array}\right],$$

$$a_2=1,0524/\left[0,0524+exp\left(-\frac{R}{6}\right)\right],$$

$$a_3=1+0,00025a_2a_4L,$$

$$a_4=79,5[5-3\text{th}(0,4\cdot\lg L_{str})]^2,$$

$$R=\sqrt{\eta^2+\theta^2},$$

L and L_{str} are observed luminance and average observed luminance of SNS light and background when determining $X_o(\eta, \theta)$ and $X_b(\eta, \theta)$ respectively, η and θ are in angular minutes, L is in cd/m², $X(\eta, \theta)$ is in min^{-2}.

The result of applying the statistical model is the determination of luminance difference ΔL between colour light and background, at which light is made evident with a preset probability. For the boundaries of red, green and yellow sectors of the system light fields, the result is given in Table 2 (P_o = 1) and in Fig. 3.

It follows from the obtained results that the angular width of transitional areas does not depend on the time of day. And at night, background luminance is determined by the diffusion of light radiation in the atmosphere. At day time it is determined by diffused sunlight.

The proposed calculation method is applied for the simulation of the monochromatic sector diagram at different detection probabilities, different meteovisibilities and degrees of atmospheric turbulence: (low, when structural constant of refraction index C_n^2 = 10^{-15} m$^{-2/3}$), average (10^{-14} m$^{-2/3}$) and high (10^{-13} m$^{-2/3}$) and different background luminances (time of day). A shift of the sector boundary caused by atmosphere turbulence at an expansion distance of d_i is characterised by a dispersion σ_r^2 (index r means shift in a perpendicular direction to the radiation expansion), by mean-square deviation σ_r (uncertainty of visual SNS positioning is about $2\sigma_r$), which is determined by the following expression [2]

$$\sigma_r=\sqrt{\overline{\left(r-\bar{r}\right)^2}}=135C_n\lambda^{-1/12}d_i^{17/12},$$

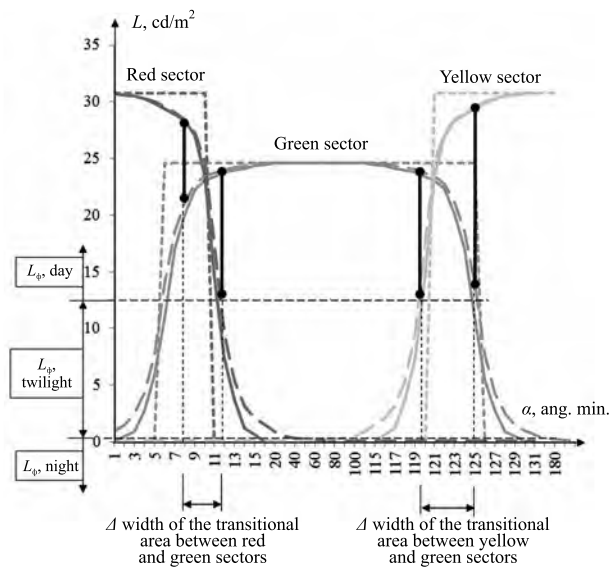

Fig. 3. A cross-section of a multi-coloured light field formed by SNS taking into account diffusion of SNS radiation in the atmosphere (observation distance is 230 m, meteorological visibility range is 200 m)

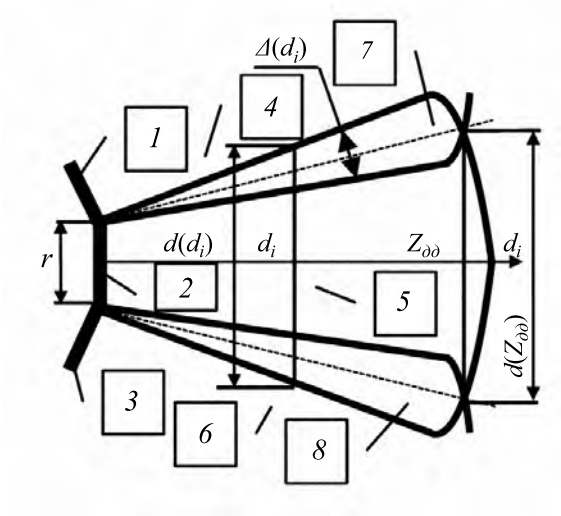

Fig. 4. Determining the width of the transitional area: *1*, *2* and *3* are radiator groups with λ = 505, 590 и 625 nm respectively; *4*, *5* and *6* are sector diagram with λ = 505, 590 and 625 nm respectively; *7* and *8* are transitional areas between sectors with λ = 505, 590 nm and 590, 625 nm respectively

where r is the current shift of the sector boundary, $\bar{r}$ is average shift of the sector boundary.

The calculation results for the working interval of wavelength of (505–630) nm show that the influence of turbulence is almost not selective, and the mean-square deviation value is only determined by the degree of turbulence. The spatial shift of the monochromatic sector boundary is no more than 10 % of the transitional area width, and within this sector, turbulence does not influece light perception. The simulation results for various weather conditions and time of day allow drawing an important conclusion that sector angular dimensions and diagram configuration do not change when the visibility range is changing: this is necessary to form the sector information field and provide a high precision of visual orientation.

Current width of transitional areas between sectors is characterised by a smooth change of colour and determined by the following expression [1] (designations are according to Fig. 4):

$$\Delta(d_i)=\left(d(d_i)-\frac{d_i}{z_{44}}\left(d(z_{44})-r\right)-r\right)\times$$

$$\times\frac{z_{44}}{\sqrt{z_{44}^2+0,25\left(d(z_{44})-r\right)^2}},$$

where r is the linear size of radiating surface of a radiator group.

The calculation results of the transitional areas and of the experiments (number of observers was 3–5, number of observations at the specified range for each observer was 5) are given in Table 3. These results show that the width of the transitional areas between the light field sectors remains within 5–7 anglular minutes regardless of external conditions, which corresponds to the flight requirements and is confirmed by the results of experiments. Formation of the sectors by radiator groups ensures an absence of dazzle when observing light at short distances because of the separate perception of the radiators, which is of a current concern for air staff.

When taking off at night, a visually perceived movement trajectory is necessary. For this purpose, a take off direction pointer is used, which generates a light ray stabilised in space, by which diffusion of visual orientation occurs. Its efficiency is determined by atmosphere's influence on the ray expansion: by absorption of radiation and diffusion in the environment thickness. A calculation of passing optical radiation through a thickness of a muddy environment is based on the solution of the radiation transfer equation (RTE) using the Green function method. RTE Green function used in most cases at the transfer analysis, is calculated either with approximation of one or two diffusion multiplicity, or within a low-angle approximation, which significantly limits its field of application. The first approximation is limited by a small optical distance area, and low-angle approximation is only correct for environments with maximum anisotropic radiation diffusion, when almost the whole luminous flux is diffused by an environment volume element concentrated in angle range from 0 to (10–15)°. However atmosphere over 90 % of time is either in haze state with no more than (20–30) % of diffuse luminous flux, or in foggy haze state, when 50 % of diffuse luminous flux is concentrated in the specified angle interval [4].

With the calculation difficulties overcome, the Green function takes the RTE solution obtained within low-angle approximation only, neglecting dispersion of diffused photons, which allows obtaining a universal method for calculating optical radiation transport through a muddy environment [4] and determining an observer's eye illuminance E_{vi} by radiation diffused in the atmosphere (Fig. 5):

Table 3. Width of the transitional areas between sector diagrams (with p = 0.5)

	d_i, m		200	500	1000	2000	4000	6000	8000	9000	9500	10000
λ_1/λ_2, nm	$S_м$, km	Time	$\Delta(d_i)$, м									
505/590	50	night	0.34 0.33*	0.87 0.72*	1.7	3.31	5.91 6.23*	9.16	13.31 13.78*	5.75	0	0
590/625			0.33 0.35*	0.81 0.79*	1.64	3.25	5.88 6.55*	8.92	13.67 14.02*	11.94	7.92	0
505/590	5	night	0.34	0.87	1.76	3.36	0					
590/625			0.34	0.83	1.73	3.34	0					
505/590	0.8	night	0.41 0.57*	0.95 1.02*	0							
590/625			0.53 0.68*	0.92 1.06*	0							
505/590	50	twilight	0.32 0.34*	0.78	1.55	3.14	5.34 5.87*	8.57	0			
590/625			0.3 0.35*	0.71	1.43	3.22	5.47 6.24*	8.8	0			
505/590	50	day	0.31 0.34*	0.75	1.56 1.51*	0						
590/625			0.3 0.35*	0.87	1.38 1.72*	0						

$$E_{vi} = \frac{\varepsilon \Lambda x(\pi) \Omega_{\text{eye}} \tau_{\text{cg}}}{4\pi S_{\text{vi}}}$$

$$\int_{a\cdot\text{tg}(\beta_{\text{vi}}-\frac{a_{\text{vi}}}{2})}^{a\cdot\text{tg}(\beta_{\text{vi}}+\frac{a_{\text{vi}}}{2})} E_{\omega}(\hat{r}, \hat{n}_0 \to \hat{r}) e(\hat{r}, \hat{r} \to -n) S_{\text{ray}}(\hat{r}) dL(\hat{r}),$$

where $\hat{n}_0$ is the unit vector of the radiator beam axis; $\sigma(\pi) = \varepsilon\Lambda x(\pi)$ is the backward diffusion of the environment; $x(\pi)$ is the diffusion indicatrix value at an angle of 180°; Ω_{eye} is solid angle of an observer's eye field of vision (at the tome of take-off); τ_{cg} is the cabin glass transmission factor; a is basic distance; is the unit vector of the visual analyser direction; E_ω is the illuminance of spatial distribution; $-n$ is the direction reverse to the direction of radiation beam expansion; S_{vi} is visual analyser (eye) pupil area; S_{ray} is the ray of the cross-sectional area.

When calculating, the following parameters were used: a ten-fold excess of illuminance threshold for the night sight level of reliable recognition; wave length of 540 nm; meteovisibility interval of 0.2–5 km; basic distance of 30 m. The obtained power of the light ray at the take off direction pointer output is above 2 W.

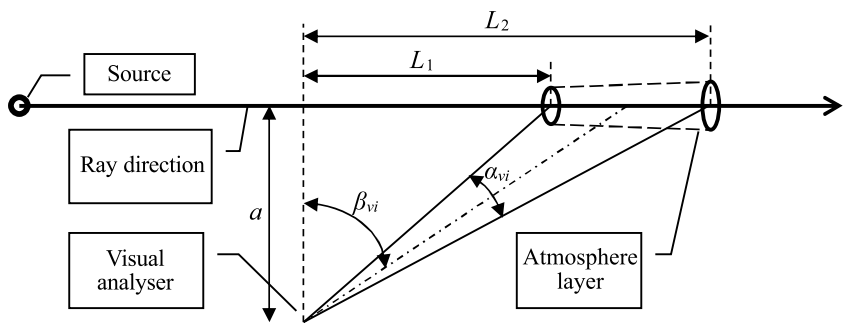

Fig. 5. Determination of an observer's eye illuminance created by diffused radiation. (Here "Source" is a device forming light rays)

When approaching and hovering of an aircraft over TOLS, visual orientation is possible due to the YO beacon lights, i.e. by extended light sources, for the perception analysisof which it is most practical to use a statistical model of the visual analyser.

To perceive lights from different directions from distances less than 200 m, their spatial light distribution should have axial luminous intensity of 0.2–0.3 cd and a radiation angle not less than 120° (i.e. luminous intensity at radiation angle sides equal to the axial half).

3. DEVELOPMENT PERSPECTIVES

Already today lighting equipment on air-capable ships, which illuminates take off and landing operations has been developed into quite advanced systems, which give the pilot a minimum necessary scope of visually perceived information. A new direction of the systems development relative to the YO beacon can be an improvement of the information delivery method. Taking into consideration the rapid development of light-projection facilities, many YO beacon lights (lights of roll, vertical movement and landing T indication) can be replaced with their projected pictures on the bulkhead elements of a ship. This will provide pilots with more comfortable conditions for their observation when hovering over the deck, when the collection of the large information on the movement of the ship TOLS is necessary.

4. CONCLUSION

The expressions presented in the article to determine parameters of the light fields and energy characteristics of radiation sources and be combined with the visual analyser threshold and statistical models applied for the analysis allow simulating systems. The AS and YO beacon can be analysed using these methods in order to determine the parameters, which most fully met the flight support requirements of carrier-based aircraft on air-capable ships.

REFERENCES

1. Vasilyev D.V., Laryushin A.I., Kormakov A.A. Optimisation of process of designing optical systems of LED and laser complexes to solve tasks of transport visual navigation // Electronics and electric equipment of transport. 2007, #2, pp. 40–44.

2. Batusov S.V. Light-signal installations. Moscow: Energiya, 1979, 120 p.

3. Grigoriev A.A., Koshchavtsev N.F. Determination of detection probability of non-uniform background objects // Writings works of the Moscow Power Energy Institute. Issue 316. Theoretical and applied questions of lighting engineering: Topic collection, 1977, Moscow: The Moscow Power Engineering Institute Publishing House, pp. 15–18.

4. Budak V.P., Savenkov V.I. Transport of an optical image in active–pulse location systems // Writings of the Moscow Power Energy Institute. Issue 602. Applied physical optics: Topic collection, 1983, Moscow: The Moscow Power Energy Institute Publishing House, pp. 24–30.

Dmitri V. Vasilyev,
Ph.D. Graduated from the Moscow Power Energy Institute in 1993. Deputy chief designer of Ramensky Instrument-making Factory JSC

Andrei A. Grigoriev,
Doctor of Technical Science, Professor, graduated from the Moscow Power Energy Institute in 1972. Deputy of the Head of the Chair "Light and Engineering" of the MPEI

Alexander I. Laryushin,
Doctor of Technical Sciences, Professor, graduated from the Ulyanovsk Polytechnical Institute in 1968. A scientific consultant of Polyus Scientific Research Institute of M.F. Stelmakh JSC

Light & Engineering
Vol. 25, No. 4, pp. 141-144, 2017

Svetotekhnika
No. 6, 2017, pp. 75–77

ELECTROLUMINESCENT LIGHT SOURCE EMISSIVITY SIMULATION

Alexander M. Kabyshev, Evgeny N. Kozyrev, Igor N. Goncharov,
Roman O. Askerov, and Vladimir V. Urumov

The North Caucasian Mining and Smelting Institute (State Technological University), Vladikavkaz
E-mail: asker2005@rambler.ru

ABSTRACT

Characteristics that define luminous and electrical features of flexible electroluminescence light sources (ELLS) are discussed. A computer model of ELLS in combination with a power supply unit was designed. A serial RC-circuit served as a load in the model. The model is highly adequate to the real object and that was proved by measured oscillograms of voltage and current.

Keywords: electroluminescent light source, luminance, phosphor, computer simulation, electric capacity, RC-circuit, timing diagram of voltage and current

1. INTRODUCTION

Electroluminescent light source (ELLS) is an up-to-date highly efficient source of uniform optical radiation which may have large area and generate light of various wavelengths. This product may be used to illuminate instrument panels of different steady-state and mobile devices; in signalling and long-lasting emergency lighting systems; in advertising displays with wide composing abilities. An ELLS may light from below an image printed on a transparent film and provide a picture with a quality and brightness similar to monitor display.

An ELLS is a solid-state source of optical radiation, which transforms electrical power into light with an efficacy of 80 %. Rather simple design, thinness, diversity of dimensions and shapes, low power consumption, resistance to vibration, damp, cuts and punctures – are additional benefits of ELLS. Its main characteristics are as follows: supply voltage U (about 150V); supply frequency ($f \approx$1000Hz); luminance B (reaching 45cd/m^2 under f=50Hz and U =220B, and 200 cd/m^2 under f=1000 Hz and U=150 V).

2. TEST DESCRIPTION

A luminous panel consists of two main layers located between plane electrodes. As a matter of fact, electroluminescent panel is a capacitor with two transmitting (transparent and non-transparent) surfaces, i.e. electrodes. A layer of zinc sulphide phosphor with binder and dielectric sheet are placed between the electrodes. The ZnS luminescent solid D512C-GG was made in China and radiated a turquoise light. The second dielectric sheet comprised a thin plate of porous aluminium oxide in an epoxide binder mixed with a barium titanate BaTiO3 ferroelectric taken in a weight ratio of 2.5: 1, and a wetting agent – hydroxyethyl phenol OP-10.

The luminescence of this source follows the Lambert law, i.e. its luminance does not depend on the viewing direction. The glow starts when an alternating voltage is applied to two conducting layers. This is an electroluminescence process (Destrio effect). The phosphor emits light quanta during both half periods of voltage, and its instant luminance is a periodic function of time [1, 2, 4]. The ELLS luminance depends on the magnitude, shape, frequency, and duration of current pulses running through the panel. Thus it is related to the operation of power supply unit, which has to provide an advantageous combination of amplitude and fre-

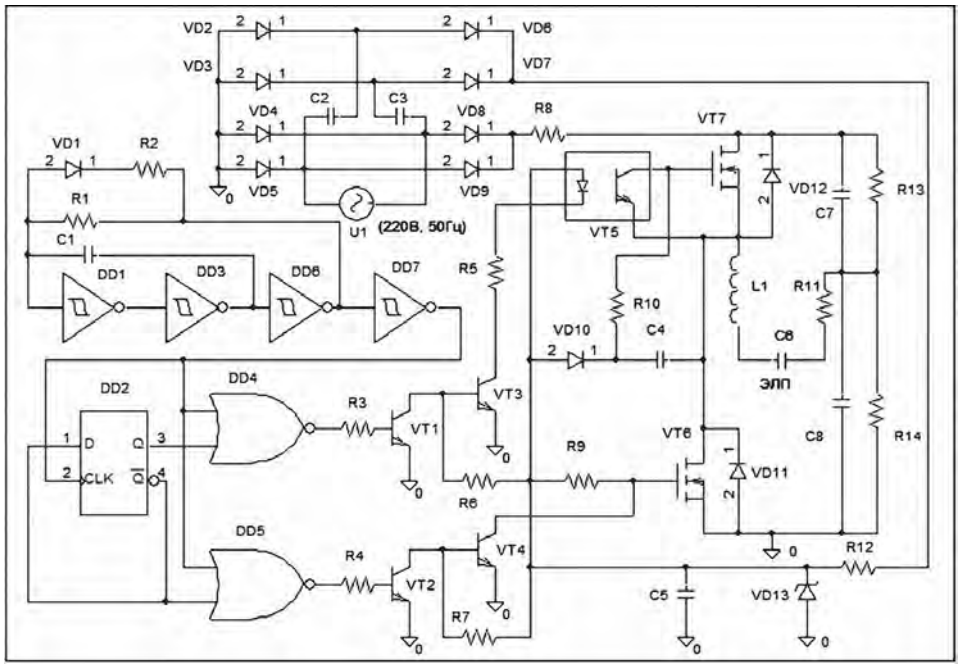

Fig. 1. Computer model of power supply unit

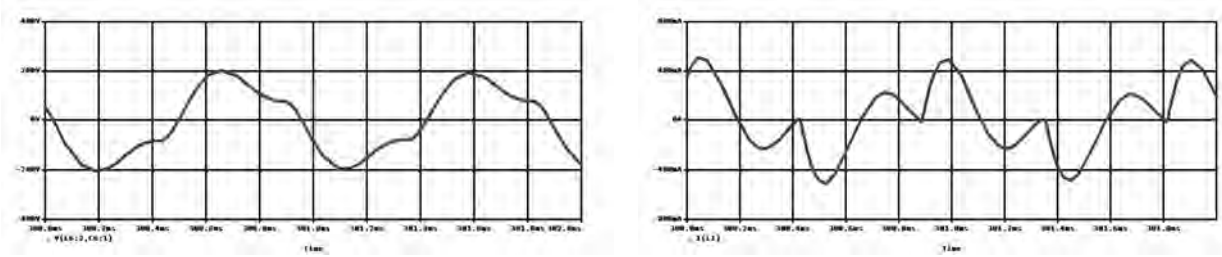

а) Voltage time chart ***б)*** Current time chart

Fig. 2. Time charts of voltage and current

quency of voltage, and optimum shape and duration of pulses [1,2].

Since ELLS is a plane capacitor, electric capacity *C* is its main feature. Let us derive the equation for calculating capacity *C*.

Ignoring leakage current of ELLS, the complex resistance may be equal to the resistance of equivalent capacitor X_C:

$$X_C = \frac{1}{2\pi fC} = \frac{U}{I}, \qquad (1)$$

where *f* is a frequency of alternating current, Hz, *I* – a current running through ELLS, A.

The value of C may be expressed as follows:

$$C = \frac{I}{2\pi fU}. \qquad (2)$$

The capacity makes a significant effect on the magnitude and shape of running current, and hence, on the luminance of a panel and operating modes of power supply unit [3].

Knowing the capacity C of a panel, phase shift φ between current and voltage, one may determine the active resistance of luminescent layer:

$$R = \frac{1}{2\pi fc \cdot tg\phi}. \qquad (3)$$

For example, if panel capacity calculated from the equation (1) equals to 0.24 mkF, then under *f*= 1000 Hz and $\varphi = 66^0$ the active resistance of fluorescent layer in ELLS is 290 Om.

Fig. 1 shows circuit diagram of designed converter for power supply of ELLS. The diagram is adapted for computer simulation within OrCad software.

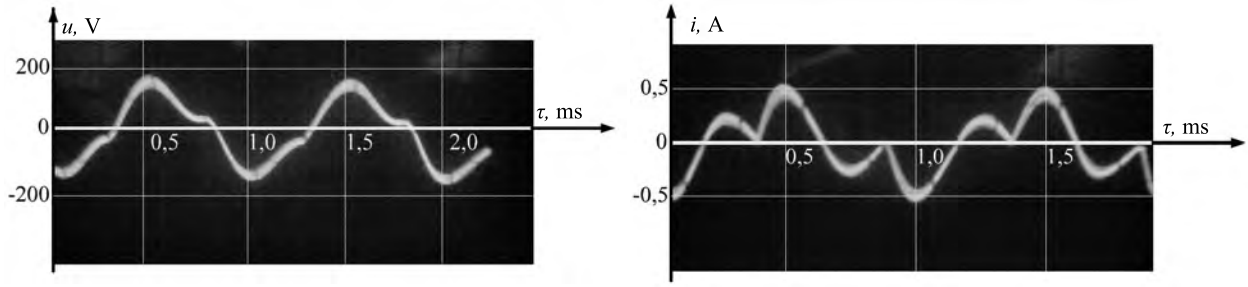

а) Oscillogram of voltage ***б)*** Oscillogram of current

Fig.3. Oscillograms of voltage and current under *L*1=16 mHn

The scheme elements: VD2 – VD9, C2, C3 are the part of a rectifier (R). Stand-alone voltage inverter is built on the base of transistor switches VT1 – VT6 and capacitors C7, C8. The control system consists of generator of rectangular pulses based on "not"-logic elements (DD1, DD3, DD6, DD7), pulses distributor (DD2 trigger) and "or-not" logic elements (DD4, DD5) that provides the time period ("dead period") when the transistor switches VT6, VT7 are closed. Variation of the resistance R2 enables to change time interval and generator pulses duty cycle and thus to control the shape of the current running through ELLS.

One of the main elements of the circuit that determines its weight, dimensions, and running parameters, is a choke with inductance L1. The choke is designed to limit and smooth pulses of alternating current (AC) of ELLS and thus to provide the optimal luminous and thermal mode of operation of a panel.

At the circuit (see Fig.1.) capacitor C6 and resistor R11 serve as a load and take into account the panel capacity and fluorescent layer resistance.

Fig. 2 shows the time charts of voltage and current resulted from computer simulation.

The charts correspond to operational mode of power supply unit with a load (ELLS) having the following parameters: capacity – 0.25 mkF, resistance of fluorescent layer – 290 Om, inductance of a choke L1–16 mHn.

To validate the results of computer simulation we obtained the oscillograms of voltage and current running through ELLS (see Fig.3) while operating with a real power supply unit made by the scheme shown in Fig.1. The electrical capacity of the panel was 0.24 mkF.

A comparative analysis of results obtained from computer simulation and measurements (oscillograms) gives reason to make a conclusion that the computer model of power supply unit and ELLS (as a serial RC-circuit) corresponds to real physical objects.

It is possible to derive from calculated and measured oscillograms under given input electrical parameters of luminous structure the following output characteristics: actual voltage – 130 V, actual current – 300 mA, thus, according to data from [1] the luminance of ELLS with A3 dimensions will be about 140 cd/m^2 under the temperature of 35 °C.

ACKNOWLEDGMENT

The work was carried out under support of the Ministry of Education and Research of the Russian Federation (ID RFMEFI57715X0196).

REFERENCES

1. Goncharov I.N., Kabyshev A.M., Kozyrev E.N., Maldzigati A.I. Design and optimization of power supply unit for flexible electroluminescent panels. Svetotekhnika. 2016, № 6, pp.39–42.

2. Goncharov Igor N., Kabyshev Alexander M., Kozyrev Evgeny N., and Maldzigati Alan I. Development and Optimisation of a Power Supply for Flexible Electroluminescence Panels. Light & Engineering Journal, V. 25, #2, 2017, pp.126–130.

3. Goncharov I.N., Kabyshev A.M., Kozyrev E.N., Maldzigati A.I. Power supply unit for electroluminescent panels. Radio and Electronics Journal, 2017, V.62, № 6, pp.1–3.

4. Gusev A.I., Samokhvalov M.K. Electrical characteristics of thin-film electroluminescent indicators. Ed. Samokhvalov M.K. Ulyanovsk: USTU, 2006, 125 p.

Alexander M. Kabyshev,
Ph.D. He is a senior lecturer of the Industrial electronics chair of the North Caucasian Mining and Smelting Institute (State Technological University). Fields of scientific interest include converters of electric energy

Igor N. Goncharov,
Doctor of Technical Science, Professor of the Electronic Devices Chair of the FSBEI, North Caucasian Mining and Metallurgical Institute (State TechnologicalUniversity). Scientific interests: modern sources of optical radiation, optical quantum generators, image converters

Evgeny N. Kozyrev,
Doctor of Technical Science, Doctor of Economics, Professor, Academician of the Russian Academy of Natural Sciences, Academician of the International Academy of Ecology, Health and Safety, Head of the Electronic devices Chair of the FSBEI North Caucasian Mining and Metallurgical Institute (State Technological University). Scientific interests: theoretical and experimental studies of photoelectronic, electron beam, solid-state and microwave devices

Roman O. Askerov,
assistant of the Electronic Devices Chair of the FSBEI of Higher Education, the North Caucasian Mining and Metallurgical Institute (State Technological University). Scientific interests: modern sources of optical radiation and electric energy converters

Vladimir V. Urumov
At present he is an eengineer-designer at JSC "Gran", which is a plant specializing in the production of electro-optical converters for night vision devices, post graduate student, and his scientific interests are optoelectronic devices and instruments, industrial electronics

Light & Engineering
Vol. 25, No. 4, pp. 145-148, 2017

Svetotekhnika
No. 5, 2017, pp. 65–67

IMPROVING RELIABILITY AND SHORT-CIRCUIT PROTECTION OF POWER LINES FOR ROAD LIGHTING
(INTERCHANGE OF EXPERIENCE)

Akilya A. Galimova

The Samara State Engineering University, Samara
E-mail: akilya@mail.ru

ABSTRACT

A technique for choosing circuit breakers for the effective protection of outdoor illumination power lines on highways against short circuits and to increase power supply reliability is presented. The technique is based on the principle of electric circuit sectioning.

The technique allows determining places to install protection devices graphically and using calculations in long lines of road lighting illumination.

Keywords: outdoor illumination power line, road lighting and highways lighting, electric power supply system, short circuit protection

1. INTRODUCTION

Road safety is directly connected with the reliable and effective operation of outdoor illumination power lines (EIPL). A review of publications on this subject has confirmed the relevance of increased EIPL reliability and of ensuring high performance of light source characteristics for luminaires with an uninterrupted power supply [1–7].

Methods exist for choosing conductors and placing protection devices (PD) in power lines of high and low voltage [8] but they are effective for power supply systems and electric power lines connecting a transformer substation (TS) with the loading. In long power lines with a distributed load, especially of low power, this technique does not allow choosing an effective short circuit protection. EIPLs of highways are among such lines. Such EIPLs are, as a rule very long, up to several kilometres, and have low power distributed along the whole length. Short circuit (SC) mode in EIPLs on highways has a feature: SC current at the end of the line is, as a rule, less or closer to the loading current at the end of the line. In this case, automatic circuit breakers installed in the 0.4 kV distributing device at the TP do not disconnect the loading, if SC occurs at the end of the line.

In this article, a technique for selecting PD on long power lines with a distributed loading is given. The technique is based on sectioning of the lines. The whole power line is divided into sites (sections), each of which is protected by its own automatic circuit breakers.

2. FORMULATION OF THE PROBLEM

When developing the technique, the first task was to compute CS current at point *i* of the line at a distance of l_i from TP and to find node *j* of the connected loading at a distance of *lj* from TP, where it is possible to install a PD for effective protection of the line section $l_j - l_i$. For this technique, two conditions should be met:

– To provide an acceptable PD response time, CS current should be not lower than the PD rated current of a preset multiplicity:

$$I_{sc} \geq K I_{rp}; \quad (1)$$

– the PD rated current should be not lower than the loading rated current in node *j*:

$$I_{rp} \geq I_{rj}.$$

3. CALCULATION METHOD FOR THE SOLUTION

SC current is calculated in accordance with a national standard (GOST) [9]. The replacement circuit of the electric power supply system contains a TP transformer and power line replacement circuits. When calculating complex impedance of the replacement circuit, resistance of switching devices, contacts and other elements which comprise the electric power supply system are also taken into consideration.

Active and reactive resistances of the transformer's positive sequence are calculated based on the rated values, for example according to the formulae given in [10]. Negative sequence resistance of the transformer and positive as well as negative sequence resistance of other replacement circuit elements are selected in accordance with GOST [9].

In 0.4 kV networks, minimum currents appear at non-symmetric SCs. Therefore as a criterion for PD choice, single-phase SC current $I^{(1)}{}_{sc}$ is accepted:

$$I^{(1)}{}_{cs} = \sqrt{3}\, U_{av} / \\ / \sqrt{(2R_\Sigma + R_0)^2 + (2X_\Sigma + X_0)^2}, \quad (2)$$

where U_{av} is the average value of low voltage, which for a 380 V circuit is equal to 400 V; R_Σ and R_0 are total active resistances of positive and negative sequences of the electric power supply system replacement circuit, Ohm, respectively; X_Σ and X_0 are total reactive resistances of positive and negative sequences of the electric power supply system replacement circuit, Ohm, respectively.

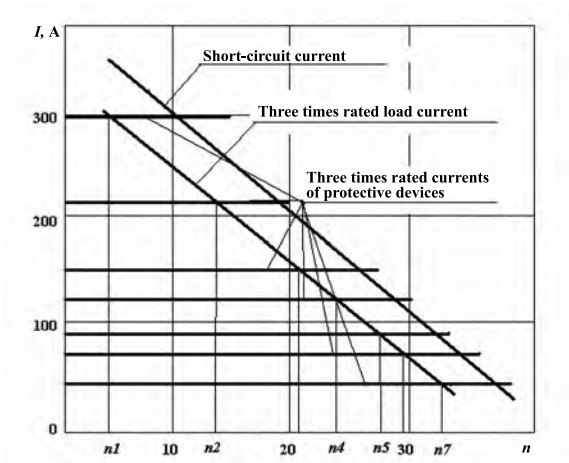

Fig.1. Distribution of short circuit and loading currents in power line nodes

To determine node *j* for PD installation, formula (1) is used. After right part of formula (2) is substituted into the left part of formula (1), the following inequality is obtained:

$$\sqrt{3}\, U_{av} / \sqrt{(2R_\Sigma + R_0)^2 + (2X_\Sigma + X_0)^2} \geq KI_{rp}.$$

If loading rated current is expressed in it using node *j* power, the following inequality will be obtained:

$$\sqrt{3}\, U_{av} / \sqrt{(2R_\Sigma + R_0)^2 + (2X_\Sigma + X_0)^2} \geq \\ \geq (3P_{rj} n) / \sqrt{3}\, U cos\varphi, \quad (3)$$

where P_{rj} is power in *j* node, W; *n* is node number from the connection point in the TP to node *j*; cos*φ* is a power factor. When designing, the power factor is accepted to be equal to 0.85; *U* is rated voltage of the electric power supply system, 380 V.

The result of solving the inequality (3), after substituting parameters of the electric power supply system and replacement circuit into it, the loading node (n), in which PD should be installed, can be determined. Assuming the solution of this inequality, distance from SC point in node *i* to PD *j* unit, such a calculation will be at possible. Node choice errors for PD installation using inequality (3) are caused by the fact that PD rated current is selected of a standard number of currents of automatic switches or of automatic circuit breakers manufactured for use in electric circuits. If the difference between loading rated current I_{pj} in node *j* and standard rated current I_{rp} in a PD is essential, KI_{rp} value can exceed SC current. Substitution of the PD rated current into the right side of inequality (3) is also not practical as there will be no relation in the inequality with loading parameters. Using the considered technique, the author proposes the following solution. Node number from TP to node *j*, in which PDs should be installed, is determined as follows:

$$n = \left(P_\Sigma - I_{rp}\sqrt{3}\, U cos\varphi\right) / P_{rj}, \quad (4)$$

Table 1. Results of choosing installation node and parameters for protection devices of an outdoor illumination power line

Highway #1					
Length of highway sections, km	0.585	1.193	1.73	2.566	3.055
Wire cross-section, mm^2	150		120		
Phase-zero loop resistance, Ohm	1.314	2.44	3.67	4.63	6.69
Rated current, A	87.7	70,9	55	38.4	17
SC current, A	527	284	189	150	103
Automatic circuit breaker current, A	100	80	60	50	25
Support numbers for automatic circuit breakers to be installed	89	72	56	39	17

where P_{Σ} is total loading of the electric power supply system, W.

PD rated current is selected as follows: CS current is calculated at the end of the line, PD rated current is chosen to be no more than 1/K of CS current. After the selected protection rated current value is substituted into formula (4), the value of *n* can be determined. A final choice of node *j* is made using inequality (3): if it is not met, then the value of *n* should be corrected. An experience of solving these tasks has showed that if inequality (3) is not met, the value of *n* should be reduced by choosing node *j*-1. Further CS current in node *j* is calculated, the node for PD installation is selected, and the protection interval is determined. Calculation for the whole power line is performed in this manner. The last node for PD calculation and installation is the TP low voltage switch-gear device.

4. A GRAPHIC METHOD FOR SOLVING THE TASK

The node choice task for PD installation of a power line site can also be solved graphically.

SC currents and threefold rated current in distributed loading nodes for automatic circuit breakers with characteristic *A* are presented in Fig.1. In Fig.1, lines corresponding to the least acceptable number of SC currents for switches with characteristic *A* are also presented. The intersection point of PD threefold rated current line with dependence line of threefold loading current in nodes corresponds to the *n* value, which is a lower boundary for the node, where PD installation is practical. And maximum permissible PD installation node is the point of intersection of the lines corresponding to PD threefold rated current with an SC current line. The effective range of a PD installed for example in n_1 point is up to n_2 point, etc. The loading node for a protection device has to be installed, should be selected between the two above mentioned dependencies to have a sufficient SC response safety factor and a reserve for a small overload in the node. If the graphic method of the task solution is used, the line is plotted according to the selected PD as CS response time is regulated by the Rules of Electrical Facilities Maintenance and by characteristic of the selected PD.

5. PRACTICAL IMPLEMENTATION OF THE TECHNIQUE

The technique was applied when designing and constructing a EIPL of a highway 6 km long, part of the city road network of Samara. The EIPL has four highway sites, each about 3 km long. As a result of the sectioning, each site is separated into 4–5 sections, each of which is protected by an automatic circuit breaker group with rated currents corresponding to the response conditions.

Calculation results for one section are given in Table 1. The sections are connected using mast contact breakers, in which automatic circuit breakers with parameters selected according to this technique are installed. As a result of the sectioning, each EIPL section with luminaires is protected against CS currents by its own automatic circuit breakers. Besides, in case of CS emergence in the

middle or at the end of the line, the main part of the luminaires will work, because only some of the luminaires will be switched off, which are in the CS current coverage area.

6. CONCLUSION

The technique considered in the article allows achieving the following:

1. To determine places for PD installation by graphic and calculation methods in a long EIPLs of highways;
2. To increase PD efficiency when appearing SC in a EIPL;
3. To increase the working reliability and efficiency of electric equipment for highway EIPLs;
4. To ensure the normal functioning an EIPL in case of an accident at the EIPL end.

Efficiency and performance ability of the technique proposed in the article is confirmed by an implemented project: a highway EIPL successfully operating in Samara.

REFERENCES

1. Bukatov A.S., Kirichok A.I. Functional energy-effective illumination of the capital outdoor spaces: state and trends of the development // Svetotekhnika, 2012, #6, pp. 38–41.

2. Aizenberg Yu. B., Matveeva E. Yu., Yushkov D.D. On state of outdoor illumination of cities of the country // Svetotekhnika, 2012, #6, pp. 42–43.

3. Nemet-Vidovsky A., Shanda J. Road illumination and photometry in the conditions of twilight sight // Svetotekhnika, 2012, #6, pp. 44–48.

4. King B. Development of a method of comprehensive evaluation of road and town illumination // Svetotekhnika, 2012, #2, pp. 27–31.

5. Dehoff P. Illumination quality and energy efficiency do not contradict each other // Svetotekhnika, 2012, #3, pp. 64–68.

6. Budak V.P., Ilyina E.I.. Choice of efficiency parameters of utilitarian outdoor illumination luminaires at the development stage // Svetotekhnika, 2012, #5, pp. 45–50.

7. Gardin A.I., Sharygin M.V., Shevchenko A.S. On calculation of electric networks of street illumination using lighting devices working in a preset power consumption maintenance mode // Svetotekhnika, 2011, #4, pp. 22–25.

8. Karpov F.F., Kozlov V.N. Handbook on calculation of wires and cables. Second edition, Moscow, Leningrad: Energiya, 1964, 224 p.

9. GOST 28249–93. Short circuits in electric installations. Calculation methods in alternating current electric installations up to 1 kV.

10. Electrotechnical handbook. V.1. Under the general edition of P.G. Grudinsky, et al. The fifth revised edition, Moscow: Energiya, 1974, 776 p.

Akilya A. Galimova,
Ph.D. (1998). She graduated from the Electro-technical Faculty of the Kuibyshev Polytechnic Institute with a specialisation in Electric Systems and Networks in 1987. At present, she is an Associate Professor of the chair “Theoretical and general electrical engineering» of the Samara State Power University.
Her fields of scientific interest are: electric power supply systems of outdoor illumination power lines on highways and substations of 0.4–35 kV

CONTENTS

VOLUME 25 NUMBER 1 2017

LIGHT & ENGINEERING

CONTENTS

VOLUME 25 **NUMBER 2** **2017**

LIGHT & ENGINEERING
(SVETOTEKHNIKA)

CONTENTS

VOLUME 25 **NUMBER 3** **2017**

LIGHT & ENGINEERING
(SVETOTEKHNIKA)

Vol. 25, No.3, 2017 is devoting to the selected papers from the partnership of Light&Engineering Journal from CHINA, which are focused in the scope of the journal.

PARTNERS OF LIGHT & ENGINEERING JOURNAL

Editorial Board with big gratitude would like to inform international lighting community about the Journal Partners Institute establishment. The list with our partners and their Logo see below. The description of partner's collaboration you can found at journal site *www.sveto-tekhnika.ru*

BL GROUP holding

ЛИТ

REFLUX HID Lighting systems

PHAROS-ALEF

VS LIGHTING SOLUTIONS

enercom® СОЗДАЕМ ЛИДЕРОВ В ЭНЕРГОСБЕРЕЖЕНИИ

ГСТЗ г. Гагарин

FAGERHULT

Светотехнический завод ВЛАДАСВЕТ

TS TENZOSENSOR

СВЕТОВЫЕ СИСТЕМЫ

СОЛАР® МАГИЧЕСКИЙ СВЕТ

ВНИСИ

ЦФ

НИИ